CORONARY ARTERY DISEASE

Assessing the development and treatment of coronary atherosclerosis

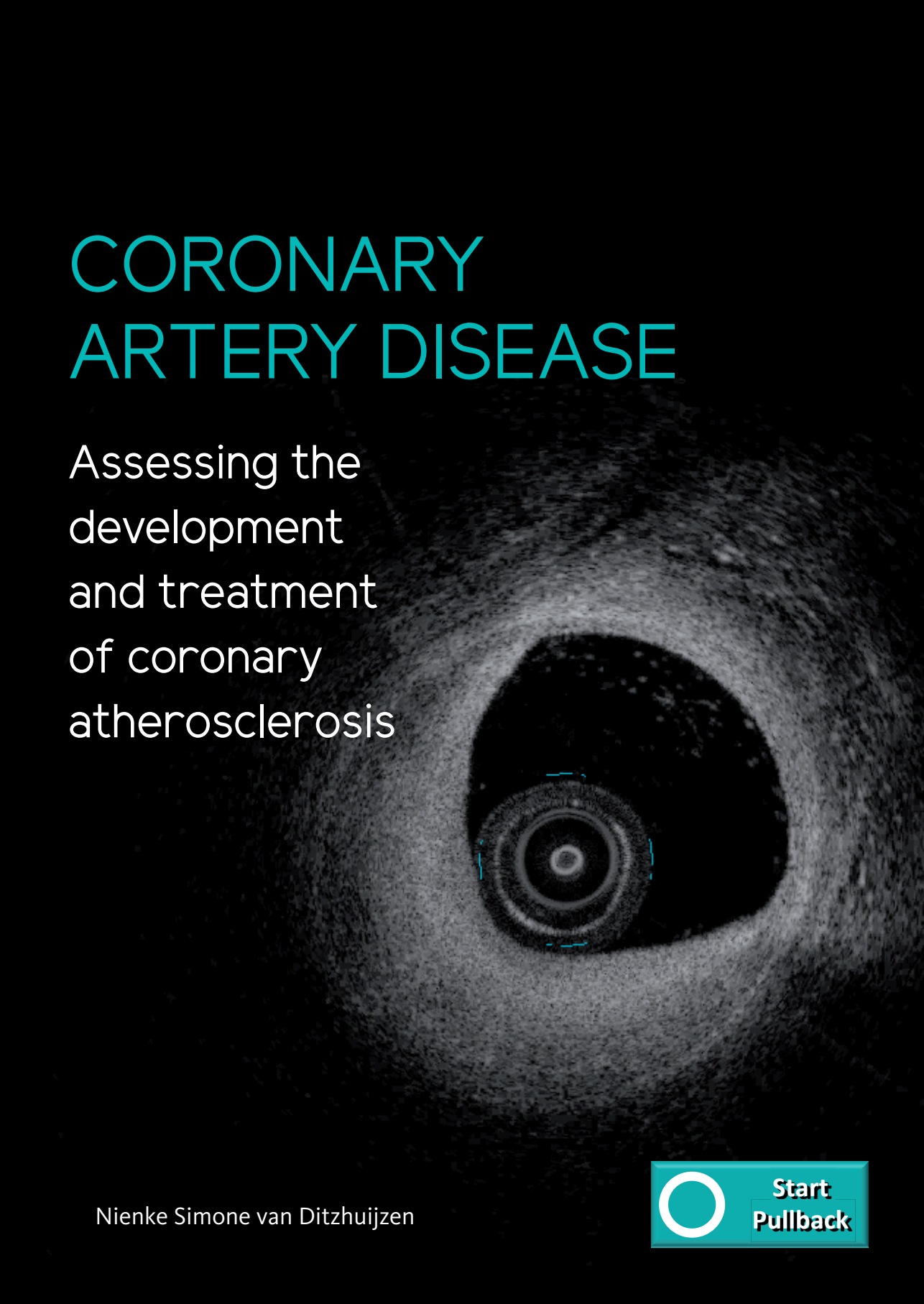

Nienke Simone van Ditzhuijzen

Coronary Artery Disease

Assessing the development and treatment of coronary atherosclerosis

Nienke Simone van Ditzhuijzen

Layout: Ridderprint BV - www.ridderprint.nl
Printed by: Ridderprint BV - www.ridderprint.nl
ISBN 978-94-6299-585-7

Coronary Artery Disease
Assessing the development and treatment of coronary atherosclerosis

Coronair Vaatlijden
Het beoordelen van de ontwikkeling en behandeling van coronair atherosclerose

Proefschrift
ter verkrijging van de graad van doctor aan de
Erasmus Universiteit Rotterdam
op gezag van de
rector magnificus

Prof.dr. H.A.P. Pols

en volgens besluit van het College voor Promoties.

De openbare verdediging zal plaatsvinden op
dinsdag 9 mei 2017 om 15:30 uur

door

Nienke Simone van Ditzhuijzen
geboren te Utrecht

Erasmus University Rotterdam

Promotiecommissie

Promotoren	Prof.dr. F. Zijlstra
	Prof.dr. D.J.G.M. Duncker
Overige leden	Prof.dr.ir. A.F.W. van der Steen
	Prof.dr. C. von Birgelen
	Dr. M. Sabaté
Co-promotor	Dr. E. Regar

The studies in this thesis have been performed at the Erasmus Medical Center at the department of Cardiology and the Laboratory for Experimental Cardiology, Rotterdam, the Netherlands. Financial support by the Erasmus University is gratefully acknowledged.

Financial support by the Dutch Heart foundation for the publication of this thesis is gratefully acknowledged.

Table of contents

Abbreviations and acronyms

3D	Three-dimensional
ACS	Acute coronary syndrome
ALAT	Alanine aminotransferase
AMI	Acute myocardial infarction
ASAT	Aspartate aminotransferase
AUC	Area under the curve
BK	Bradykinin
BMS	Bare metal stent
BVS	Bioresorbable vascular scaffold
CA	Coverage area
CABG	Coronary artery bypass graft
CAD	Coronary artery disease
CCTA	Coronary computed tomography angiography
CMD	Coronary microvascular dysfunction
CSA	Cross-sectional area
CRC	Concentration response curves
CVD	Cardiovascular disease
DES	Drug-eluting stent
DM	Diabetes mellitus
ECG	Electrocardiography
EDHF	Endothelium-derived hyperpolarizing factors
ET	Endothelin
FD	Fourier-Domain
FF	Fast-food fed
FIT	Fibrous intimal thickening
GPC	Gel permeation chromatography
HDL	High density lipoprotein
HE	Hematoxylin-eosin
HFD	High fat diet
IB-IVUS	Integrated backscatter intravascular ultrasound
ICC	Intra-class correlation coefficient
IVUS	Intravascular ultrasound
IV-OCT	Intravascular optical coherence tomography
LA	Lumen area
LAD	Left anterior descending coronary artery
LCBI	Lipid core burden index
LCP	Lipid core plaque
LCX	Left circumflex coronary artery
LD	Lumen diameter
LDL	Low density lipoprotein
LL	Lipid-laden
LM	Left main
M	Month
MACE	Major adverse cardiac events
MI	Myocardial infarction
MLA	Minimal lumen area
MLD	Minimal lumen diameter
N	Number
NDM	No diabetes mellitus
NIRF	Near-infrared fluorescence
NIRS	Near-infrared spectroscopy
NO	Nitric oxide
NPV	Negative predictive value
NSTEMI	Non-ST-segment elevation myocardial infarction
OCT	Optical coherence tomography
OFDI	Optical frequency domain imaging
ORO	Oil-red-O
PB	Plaque burden
PCI	Percutaneous coronary intervention
PLLA	Poly-L-Lactid Acid
PPV	Positive predictive value
PSR	Picrosirius red
PS-OCT	Polarization-sensitive optical coherence tomography
QCA	Quantitative coronary angiography
QUICKI	Quantitative insulin sensitivity check index
RCA	Right coronary artery
ROC	Receiver-operator characteristic
ROI	Region of interest
SA	Scaffold area
SD	Scaffold diameter
Sens	Sensitivity
SMC	Smooth muscle cell
SNAP	S-nitroso-N-acetylpenicillamine
Spec	Specificity
STEMI	ST-segment elevation myocardial infarction
T	Time point
TC	Total cholesterol
TCFA	Thin cap fibro-atheroma
TD	Time-Domain
QCA	Quantitative coronary angiography

General Introduction

1

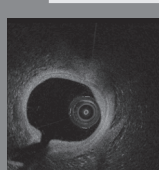

General introduction

Coronary artery disease (CAD) is a major cause of mortality and morbidity worldwide.[1, 2] CAD is a progressive, multifactorial disease, characterized by the formation of atheromatous plaques in the arterial vessel wall, causing lumen narrowing and subsequently leading to limitations in coronary blood flow and myocardial oxygen supply.[3-5] Patients with diabetes mellitus (DM) have a 2-6 fold increased risk for adverse events associated with CAD than non-diabetic patients.[6] With an expected worldwide DM epidemic, adequate understanding of the development and treatment of CAD, e.g. by coronary stent-implantation, seems inevitable.[7]

Animal models have been instrumental in improving our understanding of etiology and pathophysiology of CAD.[8] However, the vast majority of our knowledge is derived from transgenic or knock-out mouse, rat or rabbit models, rather than large animal models that resemble the human situation more accurately.[9] Furthermore, limited knowledge is available regarding the development of CAD in a background of DM. To study human-like coronary atherosclerosis in a background of DM, the porcine model seems most suitable. Moreover, swine reach blood lipid profiles that are similar to humans and swine are known to develop atherosclerotic lesions spontaneously and in response to a high-fat diet, at anatomical locations similar to those in humans.[10, 11,12] In addition, swine can be rendered diabetic, while their large size allows intracoronary imaging, and implantation of stents in the coronary circulation, resembling the human clinical situation and allowing adequate assessment of the development and treatment of CAD.[13]

Traditionally, the development and treatment of CAD has been evaluated using coronary angiography. However, the introduction of intravascular ultrasound (IVUS) imaging, and the subsequent introduction of other new intravascular imaging techniques including optical coherence tomography (OCT) and near-infrared spectroscopy (NIRS), have yielded new insights into the development and treatment of CAD.[14-16] These techniques are highly complementary, as OCT enables high-resolution imaging of stents and the coronary morphology, whereas NIRS allows for the assessment of the chemical composition of the coronary vessel wall.[15, 16]

Currently, the gold standard for the treatment of CAD is the implantation of a drug-eluting stent (DES). Compared to coronary angioplasty, stents provide a sustained solution to acute vessel obstruction.[17] Compared to bare metal stents (BMS), DES reduce neointimal hyperplasia, overcoming the problem of in-stent restenosis and thereby lowering the need for repeat revascularization.[18-21] However, metallic stents have sev-

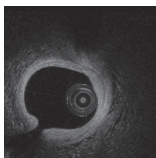

eral disadvantages, including permanent caging with or without malapposition, jailing of side branches and late stent thrombosis.[22, 23] Bioresorbable vascular scaffolds (BVS) may overcome these limitations by enabling restoration of coronary vasomotion and allowing late luminal enlargement.[24] The advantage of BVS in more complex patient populations, such as patients with DM, remains however unclear as only up to 20% of the patient population in whom BVS were investigated suffered from DM.[25, 26]

Scope of this thesis

This thesis will elaborate on the assessment of the development and treatment of coronary atherosclerosis.

Specifically, the aim of this thesis is to:

- Provide an overview of the various invasive imaging techniques that can be employed for the evaluation of coronary atherosclerosis and discuss the safety and methodological considerations of intracoronary OCT imaging (**Part I: Chapter 2, 3 and 4**).
- Evaluate micro- and macrovascular coronary dysfunction in swine with diabetes mellitus and coronary atherosclerosis development in swine with and without diabetes mellitus using experimental in-vivo and ex-vivo techniques (**Part II: Chapters 5, 6 and 7**).
- Describe the intracoronary assessment of various bioresorbable vascular scaffolds and assess the vascular response to the Absorb BVS in a clinical and experimental setting (**Part III: Chapters 8, 9 and 10**).

References

1. Roger VL, Go AS, Lloyd-Jones DM, Benjamin EJ, Berry JD, Borden WB, Bravata DM, Dai S, Ford ES, Fox CS, Fullerton HJ, Gillespie C, Hailpern SM, Heit JA, Howard VJ, Kissela BM, Kittner SJ, Lackland DT, Lichtman JH, Lisabeth LD, Makuc DM, Marcus GM, Marelli A, Matchar DB, Moy CS, Mozaffarian D, Mussolino ME, Nichol G, Paynter NP, Soliman EZ, Sorlie PD, Sotoodehnia N, Turan TN, Virani SS, Wong ND, Woo D, Turner MB, American Heart Association Statistics C, Stroke Statistics S. Heart disease and stroke statistics--2012 update: a report from the American Heart Association. Circulation 2012;125(1):e2-e220.
2. Murray CJ, Lopez AD. Mortality by cause for eight regions of the world: Global Burden of Disease Study. Lancet 1997;349(9061):1269-76.
3. Stary HC, Blankenhorn DH, Chandler AB, Glagov S, Insull W, Jr., Richardson M, Rosenfeld ME, Schaffer SA, Schwartz CJ, Wagner WD, et al. A definition of the intima of human arteries and of its atherosclerosis-prone regions. A report from the Committee on Vascular Lesions of the Council on Arteriosclerosis, American Heart Association. Circulation 1992;85(1):391-405.
4. Stary HC, Chandler AB, Glagov S, Guyton JR, Insull W, Jr., Rosenfeld ME, Schaffer SA, Schwartz CJ, Wagner WD, Wissler RW. A definition of initial, fatty streak, and intermediate lesions of atherosclerosis. A report from the Committee on Vascular Lesions of the Council on Arteriosclerosis, American Heart Association. Circulation 1994;89(5):2462-78.
5. Stary HC, Chandler AB, Dinsmore RE, Fuster V, Glagov S, Insull W, Jr., Rosenfeld ME, Schwartz CJ, Wagner WD, Wissler RW. A definition of advanced types of atherosclerotic lesions and a histological classification of atherosclerosis. A report from the Committee on Vascular Lesions of the Council on Arteriosclerosis, American Heart Association. Circulation 1995;92(5):1355-74.
6. Norhammar A, Malmberg K, Diderholm E, Lagerqvist B, Lindahl B, Ryden L, Wallentin L. Diabetes mellitus: the major risk factor in unstable coronary artery disease even after consideration of the extent of coronary artery disease and benefits of revascularization. J Am Coll Cardiol 2004;43(4):585-91.
7. Fox CS, Evans JC, Larson MG, Kannel WB, Levy D. Temporal trends in coronary heart disease mortality and sudden cardiac death from 1950 to 1999: the Framingham Heart Study. Circulation 2004;110(5):522-7.
8. Badimon L. Atherosclerosis and thrombosis: lessons from animal models. Thromb Haemost 2001;86(1):356-65.
9. Bentzon JF, Falk E. Atherosclerotic lesions in mouse and man: is it the same disease? Curr Opin Lipidol 2010;21(5):434-40.
10. Swindle MM, Makin A, Herron AJ, Clubb FJ, Jr., Frazier KS. Swine as models in biomedical research and toxicology testing. Vet Pathol 2012;49(2):344-56.
11. M.M. Swindle DCMaLDP. *Swine as Models in Biomedical Research*: Iowa State University Press, IA; 1992.
12. Dixon JL, Stoops JD, Parker JL, Laughlin MH, Weisman GA, Sturek M. Dyslipidemia and vascular dysfunction in diabetic pigs fed an atherogenic diet. Arterioscler Thromb Vasc Biol 1999;19(12):2981-92.
13. Granada JF, Kaluza GL, Wilensky RL, Biedermann BC, Schwartz RS, Falk E. Porcine models of coronary atherosclerosis and vulnerable plaque for imaging and interventional research. EuroIntervention 2009;5(1):140-8.

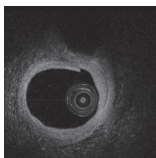

14. Hodgson JM, Graham SP, Sheehan H, Savakus AD. Percutaneous intracoronary ultrasound imaging: initial applications in patients. Echocardiography 1990;7(4):403-13.
15. Huang D, Swanson EA, Lin CP, Schuman JS, Stinson WG, Chang W, Hee MR, Flotte T, Gregory K, Puliafito CA, et al. Optical coherence tomography. Science 1991;254(5035):1178-81.
16. Gardner CM, Tan H, Hull EL, Lisauskas JB, Sum ST, Meese TM, Jiang C, Madden SP, Caplan JD, Burke AP, Virmani R, Goldstein J, Muller JE. Detection of lipid core coronary plaques in autopsy specimens with a novel catheter-based near-infrared spectroscopy system. JACC Cardiovasc Imaging 2008;1(5):638-48.
17. Serruys PW, de Jaegere P, Kiemeneij F, Macaya C, Rutsch W, Heyndrickx G, Emanuelsson H, Marco J, Legrand V, Materne P, et al. A comparison of balloon-expandable-stent implantation with balloon angioplasty in patients with coronary artery disease. Benestent Study Group. N Engl J Med 1994;331(8):489-95.
18. Sousa JE, Costa MA, Abizaid AC, Rensing BJ, Abizaid AS, Tanajura LF, Kozuma K, Van Langenhove G, Sousa AG, Falotico R, Jaeger J, Popma JJ, Serruys PW. Sustained suppression of neointimal proliferation by sirolimus-eluting stents: one-year angiographic and intravascular ultrasound follow-up. Circulation 2001;104(17):2007-11.
19. Morice MC, Serruys PW, Sousa JE, Fajadet J, Ban Hayashi E, Perin M, Colombo A, Schuler G, Barragan P, Guagliumi G, Molnar F, Falotico R, Lesions RSGRSwtS-CBVB-ESitToPwdNNCA. A randomized comparison of a sirolimus-eluting stent with a standard stent for coronary revascularization. N Engl J Med 2002;346(23):1773-80.
20. Moses JW, Leon MB, Popma JJ, Fitzgerald PJ, Holmes DR, O'Shaughnessy C, Caputo RP, Kereiakes DJ, Williams DO, Teirstein PS, Jaeger JL, Kuntz RE, Investigators S. Sirolimus-eluting stents versus standard stents in patients with stenosis in a native coronary artery. N Engl J Med 2003;349(14):1315-23.
21. Stone GW, Ellis SG, Cox DA, Hermiller J, O'Shaughnessy C, Mann JT, Turco M, Caputo R, Bergin P, Greenberg J, Popma JJ, Russell ME, Investigators T-I. A polymer-based, paclitaxel-eluting stent in patients with coronary artery disease. N Engl J Med 2004;350(3):221-31.
22. Serruys PW, Garcia-Garcia HM, Onuma Y. From metallic cages to transient bioresorbable scaffolds: change in paradigm of coronary revascularization in the upcoming decade? Eur Heart J 2012;33(1):16-25b.
23. Ong AT, McFadden EP, Regar E, de Jaegere PP, van Domburg RT, Serruys PW. Late angiographic stent thrombosis (LAST) events with drug-eluting stents. J Am Coll Cardiol 2005;45(12):2088-92.
24. Simsek C, Karanasos A, Magro M, Garcia-Garcia HM, Onuma Y, Regar E, Boersma E, Serruys PW, van Geuns RJ. Long-term invasive follow-up of the everolimus-eluting bioresorbable vascular scaffold: five-year results of multiple invasive imaging modalities. EuroIntervention 2016;11(9):996-1003.
25. Scheen AJ, Warzee F, Legrand VM. Drug-eluting stents: meta-analysis in diabetic patients. Eur Heart J 2004;25(23):2167-8; author reply 2168-9.
26. Serruys PW, Onuma Y, Dudek D, Smits PC, Koolen J, Chevalier B, de Bruyne B, Thuesen L, McClean D, van Geuns RJ, Windecker S, Whitbourn R, Meredith I, Dorange C, Veldhof S, Hebert KM, Sudhir K, Garcia-Garcia HM, Ormiston JA. Evaluation of the second generation of a bioresorbable everolimus-eluting vascular scaffold for the treatment of de novo coronary artery stenosis: 12-month clinical and imaging outcomes. J Am Coll Cardiol 2011;58(15):1578-88.

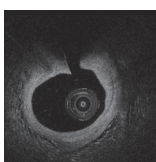

Part I

Intracoronary Imaging

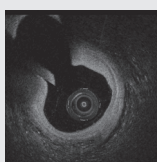

Invasive imaging of the coronary atherosclerotic plaque

van Ditzhuijzen NS, van Beusekom HMM, Ligthart JM, Regar E

Minerva Cardioangiol. 2012 Jun;60(3):305-29

2

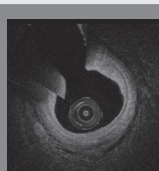

Abstract

Coronary atherosclerosis has a high prevalence and is known as the leading cause of death worldwide. Clinically, coronary atherosclerosis is routinely evaluated by coronary angiography, which provides a luminogram of the coronary artery and allows for recognizing lumen narrowing. However, angiography does not allow for the direct assessment of the disease process within the coronary vessel wall. Today, a number of catheter-based imaging methods can overcome this shortcoming and provide physicians with additional information on specific morphological components of atherosclerotic lesions. This article discusses the abilities of intravascular imaging techniques such as intravascular ultrasound (IVUS), IVUS-VH, iMAP, integrated backscatter-IVUS, intravascular optical coherence tomography, near-infrared spectroscopy and angioscopy, to diagnose coronary atherosclerosis and their potential to guide clinical decision-making.

Despite current advances in the treatment and prevention of cardiovascular disease (CVD), cardiovascular disease remains the main cause of death worldwide with a high prevalence and incidence.[1] Coronary artery disease (CAD) is the most prevalent manifestation of CVD and is associated with high mortality and morbidity.[1] It is a progressive disease that generally begins early in life and manifests clinically in late adulthood. In the clinically apparent, symptomatic stage, atherosclerosis within the vessel wall produces lumen narrowing, causing limitations in coronary blood flow and myocardial oxygen supply. CAD can present clinically as either a stable syndrome with patients suffering from angina pectoris in circumstances of elevated myocardial oxygen demand (e.g. during physical exercise), or as acute coronary syndrome (ACS). ACS encompasses unstable angina, non-ST segment elevation (NSTEMI) and ST-segment elevation myocardial infarction (STEMI), and is characterized by a sudden onset of potentially life-threatening myocardial ischemia [2], necessitating invasive treatment.[3] While coronary atherosclerosis has been described already centuries ago, the mechanisms of disease progression and the development of ACS in apparently healthy subjects was poorly understood.[4] An important reason for this relative paucity of knowledge was the lack of imaging methods that allowed direct visualization of the coronary artery vessel wall and its atherosclerotic changes. Over the last two decades, a number of catheter-based technologies have been developed to overcome this limitation and to enable direct assessment of the coronary artery wall in vivo. This review discusses the principle and the diagnostic value of currently clinically available intravascular imaging techniques in patients with coronary artery disease.

The morphology of coronary arteries

Normal coronary artery

The wall of a coronary artery consists of three distinct layers: the tunica intima, tunica media and the tunica adventitia.[5] The intima is the innermost layer of the coronary artery. The intima is defined as the region of the arterial wall extending from the lumen to the luminal margin of the media, and includes the endothelium, a surface layer that consists of a monolayer of endothelial cells, and the subendothelium consisting of microfibrils such as collagen IV and von Willebrand factor. The internal elastic lamina, considered part of the media, denotes the border between intima and media.[6] The media primarily consists of smooth muscle cells (SMCs). The external elastic lamina consists of multiple layers of elastin and denotes the end of the media. It is part of the adventitia, and contains connective tissue, vasa vasorum and nerves. A pronounced

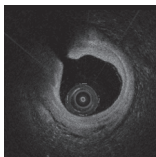

internal elastic membrane and external elastic membrane are distinguishing characteristics of muscular arteries. Elastic arteries also have an internal elastic membrane, however, their tunica media contains abundant layers of elastin interspersed by SMCs and are basically indistinguishable from the single internal elastic lamina.

Atherosclerotic changes

Atherosclerotic lesions represent a series of highly specific cellular and molecular responses and therefore atherosclerosis is proposed to be an inflammatory disease. In fact, the earliest type of lesion is a pure inflammatory lesion, consisting of macrophages and T lymphocytes, called the "fatty streak".[7]

The currently accepted classifications of coronary artery lesions are based on pathological findings.[8, 9] The classification of lesion types proposed by the American Heart Association consists of (I) Adaptive intimal thickening, constructed of isolated macrophage foam cells; (II) Fatty streak, consisting of multiple foam cell layers and lipid-laden SMCs; (III) An intermediate stage between type II and type IV that contains isolated extracellular lipid pools; (IV) Atheroma, which is potentially symptom-producing and includes a confluent extracellular lipid core; (V) A lipid core containing fibromuscular tissue layers; (VI) A lipid core containing a surface defect, hematoma and/ or thrombosis; (VII) A lesion where calcification predominates; and (VIII) A lesion where fibrous-tissue changes predominate.[9] The classification proposed by Virmani is similar and includes intimal thickening, intimal xanthoma or "fatty streak", pathological intimal thickening with or without erosion, fibrous cap atheroma with or without erosion, thin fibrous cap atheroma, calcified nodule and fibrocalcific plaque.[8]

The term intimal thickening describes the 7accumulation of SMCs in the intima without lipid or macrophage foam cell accumulation and is commonly observed in young individuals. Intimal xanthoma or "fatty streak" describes luminal (superficial) accumulation of foam cells without a necrotic core or fibrous cap. Pathological intimal thickening consists of the accumulation of SMCs in a proteoglycan-rich matrix with areas of extracellular lipid accumulation without necrosis. Endothelial erosion may occur in response to the existence of pathological intimal thickening. Typically, the endothelium is absent and the eroded site often (50% of cases) contains macrophages. Erosions are pro-thrombotic in nature and are a frequent cause of coronary thrombosis in sudden coronary death.[10] A fibrous cap atheroma is defined as a necrotic core with an overlying layer of connective tissue, the fibrous cap. A thin fibrous cap atheroma (TCFA) has a thin cap (≤ 65 µm thick) infiltrated by macrophages and lymphocytes with an underlying necrotic core. SMCs are rarely seen and the fibrous cap is thin, which

distinguishes a TCFA from the other lesions. Plaque rupture, often seen with fibroatheroma, is described as cap disruption with an overlying thrombus communicating with the underlying necrotic core. Other descriptive features of fibrous cap lesions include the extent of inflammation in the cap, fissuring, calcification, intraplaque vasa vasorum or intraplaque hemorrhage. A calcified nodule is defined as eruptive nodular calcification with underlying fibrocalcific plaque. A fibrocalcific plaque is defined as a collagen-rich plaque with significant stenosis and usually contains large areas of calcification with inflammatory cells. A necrotic core may also be present.[8]

Vulnerable plaque

The term "vulnerable" plaque has been coined to describe the phenomenon that a clinically silent atherosclerotic plaque suddenly and obviously unpredictably triggers sudden coronary thrombosis causing acute myocardial infarction (AMI).[11] Since the introduction of the term vulnerable plaque, series of histopathology studies in patients dying from acute sudden cardiac death have provided clinicians with a detailed description of morphological findings in culprit lesions associated with coronary thrombosis, myocardial infarction and death. These morphological findings include a thin fibrous cap (<65 μm), large lipid pool, large necrotic core, fissuring of the cap, calcification, intraplaque vasa vasorum, intraplaque hemorrhage and presence of activated macrophages and lymphocytes in or near the fibrous cap.

The most frequent event causing ACS and intracoronary thrombosis is the rupture of an inflamed, thin fibrous cap, exposing the highly thrombogenic necrotic core to the blood stream triggering thrombus formation and consecutive vessel occlusion.[12] Other postulated mechanisms are acute lumen narrowing by intraplaque bleeding in regions with dense neovascularization or thrombus formation in regions without intact endothelium as can be observed in plaques with erosion or calcified nodules. Vulnerable plaques are difficult to diagnose as they are often clinically silent and do not cause flow limiting stenosis. This can be explained by a mechanism first suggested by Glagov et al. in 1987.[13] Glagov described positive (also called expansive or outward) remodeling of the vessel wall as a compensatory mechanism of the vessel to preserve the lumen caliber despite atherosclerotic plaque accumulation. Only when the plaque burden reaches more than 40 percent of the total vessel area, plaque accumulation results in functionally important lumen narrowing. Subsequently, several studies showed an increase in inflammatory marker levels, larger lipid cores and pronounced medial thinning in positive remodeled vessels.[14-16] On the other hand, the inability for compensatory vessel enlargement and vessel shrinkage (also called constrictive or

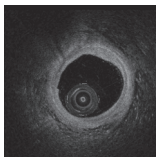

negative vessel wall remodeling) have been postulated as major contributors to the development of flow-limiting stenosis.[17]

While histopathology allows for the description of the morphology of atherosclerotic lesions in great detail, the natural history in disease progression of individual lesions, the capability and time needed for regression or progression, and the mechanisms of plaque rupture and healing are poorly understood, as by its very nature, histology represents a single time snap shot within the disease process. Today, a number of these specific features of atherosclerotic lesions can be diagnosed with intravascular imaging modalities, offering a unique potential to study the dynamic nature of coronary artery disease and the impact of therapeutic interventions longitudinally in patients. This might offer new insights for risk stratification, therapy and prevention.

Determining the presence of coronary atherosclerosis in patients

Coronary angiography

For more than 40 years, selective coronary angiography has represented the standard modality for visualisation of the coronary vasculature.[18] It is used for defining the presence or absence of coronary atherosclerosis and is most commonly used to assess the feasibility and appropriateness of therapies such as revascularization by percutaneous or surgical intervention. Also it is used when the diagnosis of CAD is uncertain and coronary disease cannot be reasonably excluded by noninvasive techniques.

Diagnostic catheters (diameter 4-6F) are sequentially positioned in the ostium of the right coronary artery and in the ostium of the left main stem, using either the femoral or the radial artery as access site. A radio-opaque contrast agent is injected through a diagnostic catheter into the coronary artery and visualized by X-ray. This results in a two-dimensional representation of the coronary lumen (also dubbed luminogram) representing a road map of the coronary artery tree with a spatial resolution of up to 100 µm.[19] The risk of major complications, including death, myocardial infarction, stroke, bleeding, vascular complications and contrast reactions, is <0.2%.[19]

Coronary angiography provides a unique overview of the coronary tree and can confirm the presence of atherosclerosis with high specificity. The presence or absence of coronary atherosclerosis is indirectly determined by lumen contour and caliber, as well as by contrast flow and distribution.[20] The extent of disease is defined as one, two or three-vessel disease, reflecting the number of coronaries showing lumen narrowing (>50% diameter stenosis). While coronary angiography is routinely used to confirm the

presence and extent of severe lumen narrowing and, thus, allows guiding treatment strategy, it is a poor predictor of acute coronary events in the absence of severe lumen narrowing. Moreover, the percentage diameter stenosis of a lesion does not provide reliable information concerning the risk of myocardial infarction and death.[21-25]

In a study determining whether coronary angiography could predict the site of a future coronary occlusion that would produce a myocardial infarction (MI), the coronary angiograms of 42 patients who had undergone angiography before and a month after acute MI were evaluated. Twenty-nine patients had a newly occluded artery. In 66% of the 29 patients, the artery that subsequently occluded had less than a 50% diameter stenosis on the first angiogram. In 97% of the 29 patients the diameter stenosis was less than 70%. No correlation was found between the severity of the coronary lesion at the time of the first catheterization until the myocardial infarction (R^2 = 0.0005, p=NS). These data suggest that the assessment of the angiographic severity of coronary stenosis may be inadequate to predict the time or location of a subsequent coronary occlusion that will produce MI.[23] An explanation for the low predictive value could be the inability to visualize the pathophysiologic substrate directly. Coronary angiography as luminogram technique is not able to provide information on vessel wall remodeling, the content of the plaque or on the functional information of lesion severity.

Acute coronary events are in the majority of cases caused by coronary lesions with the propensity of rupture or erosion resulting in acute thrombosis.[26, 27] These lesions do not necessarily present as hemodynamically significant prior to the acute clinical event.[22] Non-flow limiting lesions are ubiquitous but they are missed by non-invasive functional diagnostic approaches.

Intravascular, catheter-based imaging of coronary atherosclerotic plaque

IVUS

Intravascular ultrasound provides real-time high-resolution images of the vessel wall and lumen and is an established method for the analysis of the coronary vessel wall. An example of the principle of quantitative analysis by IVUS is depicted in **Figure 1**.

Ultrasound waves at frequencies between 20-50 MHz are emitted into the coronary tissue. The ultrasound waves are reflected by tissue interfaces that differ in ultrasound propagation properties. The time delay of reflected ultrasound waves is translated into spatial image information. The intensity of the reflected ultrasound waves is translated into an intensity map encoded by a gray scale. The angular position of the imaged

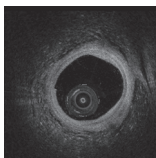

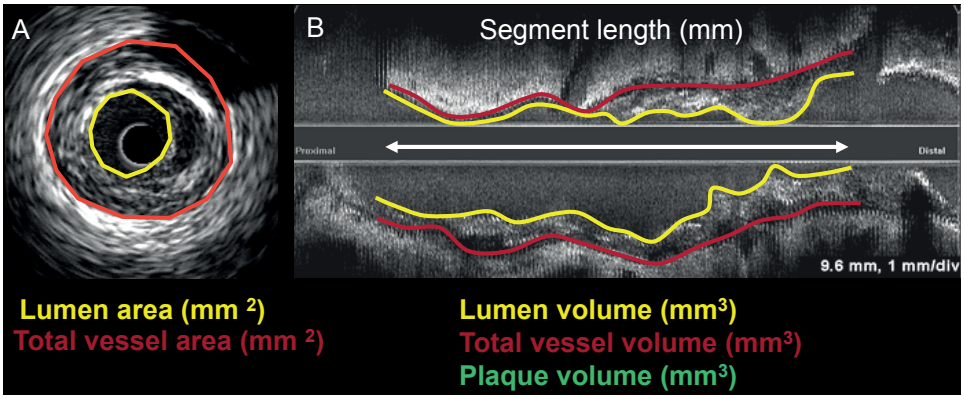

Figure 1 Gray Scale IVUS: Principle of quantitative analysis of plaque area and volume
A) Cross-sectional image. Planimetry of the lumen is performed by following the inner leading edge, planimetry of the total vessel area is performed by following the echodense adventitial border. The plaque area is calculated as difference between total vessel area and lumen area. B) Longitudinal display of the IVUS data. Planimetry of the lumen and vessel area can also be performed on the longitudinal display over the entire length of the segment of interest allowing to calculate lumen, vessel and plaque volume. Planimetry can be performed by manual tracing, or by using (semi-)automated analysis software.

line is varied over 360 degrees and converted into a two-dimensional spatial image. Electronic systems use multiple transducer elements, which are mounted around the circumference of the catheter tip. A variable number of crystals are activated sequentially, allowing for scanning of the complete vessel circumference (phased array system). In mechanical systems, sequential scanning of the vessel circumference is achieved by mechanical rotation of a single element transducer.

Features of the vessel can be detected based on the echogenicity and the thickness of the material. Depending on the distance from the catheter, the axial resolution is approximately 150 microns, the lateral 300 microns.

IVUS allows for determining the anatomical location of atherosclerotic lesions, which is in particular important when the interpretation of the angiogram is difficult because of side branch overlap, incomplete contrast filling or haziness.[28] Furthermore, IVUS can visualize vessel wall remodeling and identify morphological components of plaque.

Comparison to histology has shown that IVUS can detect three plaque types with high sensitivity and specificity (**Table 1**). The histological plaque types are classified based on their tissue echogenicity on IVUS. First, predominantly lipid-rich plaques have low echogenicity. Lesion echogenicity is higher than that of the lumen but lower than that of the surrounding adventitia. Second, predominantly fibrous plaques have intermediate echogenicity. The echogenicity is higher than that of echolucent atheromas or lipid-rich plaques but lower

than that of highly echogenic calcific plaques. Third, predominantly calcified plaques appear as bright echoes with acoustic shadowing. The echogenicity of these plaques is higher than that of the adventitia. However, since sound is backscattered because of calcium, the thickness of the calcified plaque cannot be determined with IVUS.[29-37]

In the catheterization laboratory IVUS can be used to diagnose the presence of coronary atherosclerosis, to guide the angioplasty procedure, to assess the long-term outcome of therapeutic procedures or to investigate treatment failures, such as restenosis or stent thrombosis.[32] An example of IVUS-guided stent implantation is shown in **Figure 2**. For research purposes IVUS has been successfully used to document the effect of pharmacological therapy on the extent and composition of atherosclerotic lesions.[31, 38, 39]

Several trials have been conducted to study the effect of statins on plaque volume. The ESTABLISH trial investigated the effect of early statin treatment on plaque volume of a non-culprit lesion by serial volumetric IVUS in patients with ACS. Following PCI, patients were randomized to lipid lowering with atorvastatin 20 mg/d or control. Serial volumetric intravascular ultrasound analyses at baseline and 6-month follow-up in 48 patients (atorvastatin, n=24; control, n=24) demonstrated a significant reduction in plaque volume in the atorvastatin group (13.1 +/- 12.8% decrease) compared to the control group (8.7 +/- 14.9% increase; P<0.001).[40] The REVERSAL (Reversal of Atherosclerosis with Aggressive Lipid Lowering) double blind, randomized active control multicenter trial compared the effects of pravastatin (40 mg) and atorvastatin (80 mg). At 18 months follow-up IVUS demonstrated a significant change in total atheroma volume (5.1 +/- 31.4 mm^3 increase vs 0.4 +/- 31.8 mm^3 decrease; P = 0.02), change in percentage atheroma volume (1.9 +/- 4.9% vs 0.6 +/- 5.1%; P< 0.001), and change in atheroma volume in the most severely diseased 10-mm vessel subsegment (1.7 +/- 12.4 mm^3 decrease vs 4.2 +/- 12.8 mm^3 decrease; P<0.01) in the pravastatin compared to the atorvastatin group.[41] The prospective, open-label ASTEROID (A Study to Evaluate the Effect of Rosuvastatin on Intravascular Ultrasound-Derived Coronary Atheroma Burden) trial was designed to assess whether statin therapy with rosuvastatin, 40 mg/d could regress coronary atherosclerosis after 24 months of treatment in 349 patients. Statin therapy achieved significant regression of atherosclerosis for pre-specified IVUS measures of disease burden, namely change in percent atheroma volume for the entire vessel (0.98% +/- 3.15%; P<0.001 vs baseline) and the change in nominal atheroma volume in the 10-mm sub-segment with the greatest disease severity at baseline (-6.1 +/- 10.1 mm^3; P<0.001 vs baseline).[42] The ongoing SATURN study (Study of Coronary Atheroma by InTravascular Ultrasound: Effect of Rosuvastatin versus AtorvastatiN) evaluates the effects of high-dose atorvastatin and rosuvastatin in order to understand if there are differences of statins on coronary plaque progression.[43]

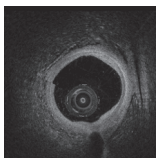

Table 1 Intravascular ultrasound (IVUS) tissue characterization sensitivity and specificity

Author	Study setting	N	IVUS frequency	Tissue characteristic	Sens	Spec	PPV	NPV
Potkin et al.[34]	Ex vivo; coronary	112	25 MHz					
				Lipid-rich	78%	97%	70%	98%
				Fibrous	96%	93%	98%	90%
				Calcified	100%	100%	100%	100%
DiMario et al.[31]	In vivo; muscular human vessels	120	30 and 40 MHz					
				Lipid	89%	-	-	-
				Fibrous intimal thickening	67%	-	-	-
				Calcium	97%	-	-	-
Hiro et al.[35]	Iliac	33	25 MHz					
				Lipid-rich	40%	-	-	-
				Fibrous	50%	-	-	-
				Calcified	91%	-	-	-
Palmer et al.[36]	In vitro; coronary human	44	30 MHz					
				Echodense (dense fibrous)	95%	78%	94%	-
				Echolucent (loose fibrous with lipid deposition)	96%	94%	90%	-
				Heterogeneous	94%	85%	92%	-
				Calcified	92%	100%	91%	-
Kostamaa et al.[33]	Ex vivo; 5 coronary, 5 iliac		25 MHz					
				Calcified lesions	89%	97%	-	-
Prati et al.[30]		122	40 MHz					
				Lipid pool	65%	95%	79%	89%

Table 1 Intravascular ultrasound (IVUS) tissue characterization sensitivity and specificity (continued)

Author	Study setting	N	IVUS frequency	Tissue characteristic	Sens	Spec	PPV	NPV
Kawasaki et al.[29]	Ex vivo; coronary	108	40 MHz					
				Caclification	100%	99%	88%	100%
				Fibrosis	93%	61%	87%	74%
				Lipid pool	67%	95%	67%	95%
Kume et al.[37]	Ex vivo; coronary	166	40 MHz					
				Fibrous	88%	86%	69%	95%
				Fibrocalcific	98%	96%	96%	97%
				Lipid rich	59%	97%	86%	88%

N = number of segments; IVUS = intravascular ultrasound; Sens = sensitivity; Spec = specificity; PPV = positive predictive value; NPV = negative predictive value.

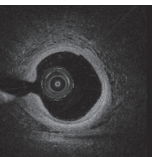

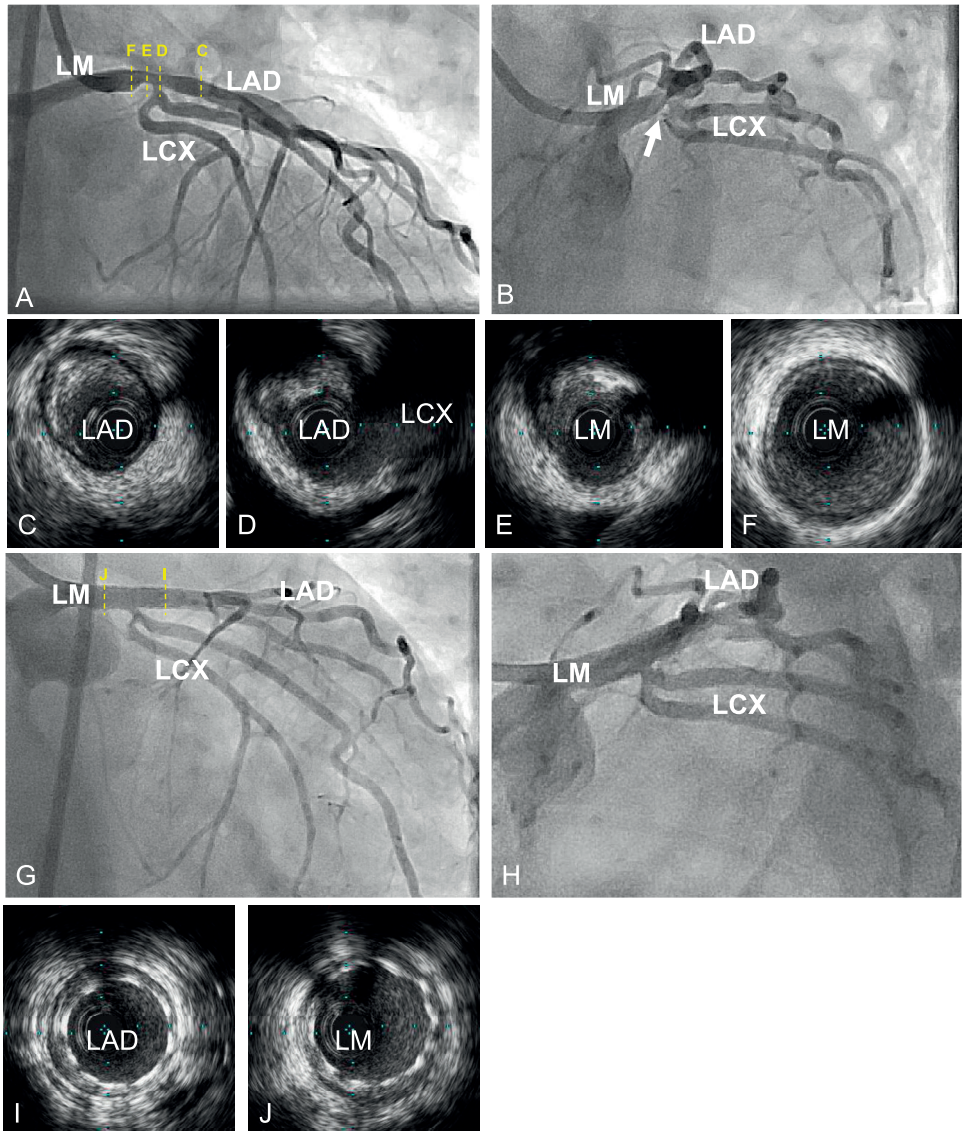

Figure 2 Clinical case example for IVUS guided PCI of the left main stem (LM)

A) and B) Pre-intervention coronary angiograms (right oblique caudal view (A), left oblique caudal view (B)) of the left coronary artery. A lumen narrowing of the left main (LM) stem can be recognized. It is difficult to assess whether the ostium of the left circumflex artery (LCX) is significantly narrowed or potentially jeopardized by plaque shift at the carina, and in consequence it is difficult to decide on the optimal PCI strategy (bifurcation stenting vs. single stent). C-F) Pre-intervention IVUS pullback from the left descendens anterior (LAD) artery through the LM. C) Eccentric, echodense plaque can be recognized in 9 to 12 o'clock position, despite angiographic normal vessel appearance. D) Bifurcation of the LAD with the left circumflex (LCX) artery. Eccentric, echodense plaque with dorsal shadowing can be recognized in 9 to 1 o'clock position, while the carina and the ostial portion of the LCX are plaque-free. E) Distal LM with eccentric, echodense plaque with dorsal shadowing in 9 to 4 o'clock position with a

minimal lumen area of 3.4mm². F) Proximal LM showing a normal, three layered appearance of the vessel wall. Pre-intervention IVUS demonstrated clearly significant plaque burden and lumen narrowing of the proximal LAD and the distal LM while the ostium of the LCX did not show atherosclerotic plaque with a wide open carina towards the LAD. Based on this information, a single stent strategy was chosen. G and H) Post-intervention coronary angiograms (right oblique caudal view (G), left oblique caudal view (H)) of the left coronary artery after implantation of a 3.5/15mm stent (Xience prime). The angiogram demonstrates a good result with an open carina of the LCX. J) and I) Post-intervention IVUS; IVUS of the distal stent portion (I) and the proximal stent portion (J) demonstrates good stent expansion and strut apposition.

The randomized, double blind, multicentre EUROPA/PERSPECTIVE trial evaluated the effect of perindopril 8 mg/day on coronary remodeling. After a median follow-up of 3 years, there was no significant difference in the change of plaque cross-sectional area (CSA) between perindopril (-0.15 +/- 1.7 mm^2) and placebo (-0.01 +/- 1.7 mm^2) groups, P=0.27. However, the change in vessel CSA was significantly different between groups (-0.18 +/- 2.4 mm^2 vs 0.19 +/- 2.4 mm^2 in the perindopril vs placebo group, respectively; P=0.04). These results show that in the perindopril group negative remodeling occurred more frequently.[44]

It has been hypothesized in the past that intravascular ultrasound plaque characterization and assessment of vascular remodelling might help to classify plaques with the highest probability of spontaneous rupture. However, IVUS has been disappointing and it became clear that visual assessment of the gray scale pattern lacks prognostic relevant information. The detection of vulnerable plaques by IVUS was mainly based on a series of case reports.[45-47] These reports described morphologic features of already ruptured plaques but not the prospective detection of plaques prone to rupture. Yamagishi et al. performed a prospective study with two years follow-up. Large eccentric plaques containing an echolucent zone by IVUS were found to be at increased risk of instability even though the lumen area was preserved at the time of initial study.[48] A retrospective study showed that ruptured plaques in culprit lesions of patients presenting with acute coronary syndrome tend to have a smaller lumen, greater plaque burden and area stenosis and more thrombus. In this study, plaque rupture itself did not cause symptoms. Symptoms were caused by the lumen narrowing and/or thrombus formation. [49]

The image resolution of IVUS is limited to approximately 200mm and it is thus likely to miss the thin fibrous cap that is covering the lipid/necrotic core. The interpretation of tissue characteristics is based on visual assessment of the gray scale image. The dynamic range of gray values can theoretically go up to 256 levels, however, the human eye can recognize only a maximum of 32 gray levels. Echogenicity and texture

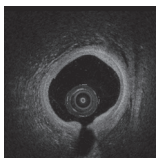

of different tissues may appear very similar. As a consequence, the sensitivity and specificity to detect lipid is relatively low.

IVUS backscattering image analysis

In order to improve the diagnostic accuracy of tissue characterization of IVUS, IVUS backscattering analysis methods have been developed, such as IVUS-VH (Volcano Corp., Rancho Cordoba, California, USA)[50, 51], iMAP (Boston Scientific Corp, Fremont, CA, USA)[52] and integrated backscatter IVUS (IB-IVUS).[53]

IVUS-VH

The IVUS-VH data acquisition in the catheterization laboratory is similar to standard IVUS, however, data analysis is performed on dedicated consoles. IVUS-VH was the first commercially available IVUS backscattering image analysis system and was built on the rotational mechanical 45 MHz IVUS platform. **Figure 3** shows a photograph and a schematic example of an IVUS catheter and shows an example of the cross-sectional images obtained using IVUS-VH. VH tissue characterization is based on constructing tissue maps that classify plaque into 4 major components labeled with a specific color. Calcium appears white, fibrous tissue green, fibrolipidic tissue greenish-yellow and necrotic core appears red.[51, 54]

Validation studies have been performed in ex-vivo and in-vivo human and animal vessel segments (**Table 2**).[50, 51, 55-58] In-vivo reproducibility has been documented in 16 patients who underwent IVUS-VH imaging prior to and following PCI. A total of 24 IVUS-VH frames were used for analysis. Spearman rank-order correlation coefficients between the two pullback measurements were 0.96 for vessel area, 0.96 for lumen area and 0.95 for plaque burden. For plaque components by VH, the coefficients ranged from 0.90 to 0.97 and 0.84 to 0.92 for segmental volumetric analysis. These findings show that discrete measurements of plaque compositional area and volume in the clinical setting appear to have reproducibility comparable to that of IVUS measurements. [59]

IVUS-VH was applied to study the incidence and spatial distribution of necrotic core in the epicardial artery tree and culprit lesions in different patient cohorts (ACS versus stable angina) and to study treatment effects of the lipoprotein (Lp) PLA^2 inhibitor darapladib. In the IBIS 2 study [60], after 12 months and despite high adherence to standard-of-care treatment, the necrotic core continued to expand among 330 patients with angiographically documented coronary disease. While lipoprotein (Lp) PLA^2 inhibition

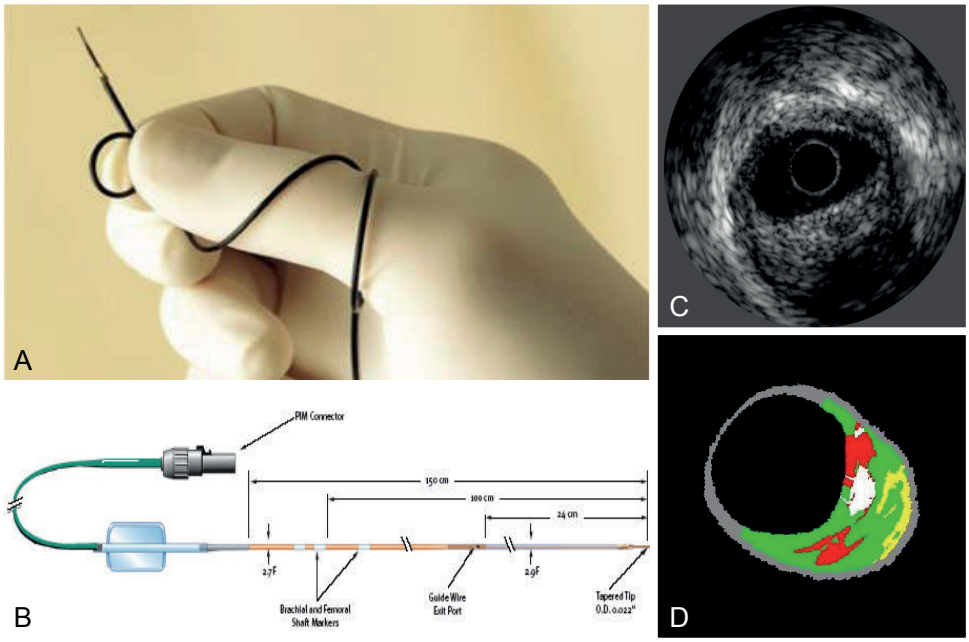

Figure 3 Example of an IVUS catheter (Volcano Eagle Eye Catheter)
A) Photography; B) Schematic; The catheter has an outer diameter of 2.9F and can be introduced into the coronary artery in rapid exchange technique over a standard 0.014" guide wire and a 6F guiding catheter. The ultrasound transducer at the distal catheter tip is a solid state transducer consisting of 64 piezo-electric elements and operates at 20 MHz. During a single IVUS catheter pullback through the artery C) IVUS gray scale data as well as D) IVUS VH data are registered. IVUS VH data are displayed as a color-coded representation of different plaque components.

with darapladib (160 mg/d) prevented necrotic core expansion resulting in a treatment difference of -5.2 mm^3 (P=0.012), no differences in plasma high-sensitive C-reactive protein or in plaque deformability were observed between the placebo and the treatment group. These findings might suggest that Lp-PLA^2 inhibition can represent a novel therapeutic approach.[60]

The potential value of IVUS-VH for predicting adverse coronary events was evaluated by the multicenter, prospective, international Providing Regional Observations to Study Predictors of Events in the Coronary Tree (PROSPECT) study [61] in patients undergoing PCI for ACS. Patients underwent 3-vessel IVUS and IVUS-VH imaging in the acute phase after treatment of their culprit lesions followed by clinical follow-up. Subsequent, non-culprit-lesion related cardiac events during 3-year follow-up were associated with the presence of a small lumen area, large plaque burden and large necrotic core by IVUS-VH at baseline.

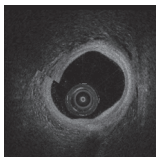

Table 2 Intravascular ultrasound-VH tissue characterization sensitivity and specificity

Author	Study setting	N	IVUS frequency	Tissue characteristic	Sens	Spec	PPV	NPV
Nasu et al.[50]	In vivo VH vs. in vitro histology; coronary	307	30 MHz					
				Fibrous tissue	86%	90.5%	-	-
				Fibrofatty	79.3%	100%	-	-
				Necrotic core	67.3%	92.9%	-	-
				Dense calcium	50%	98.9%	-	-
Nair et al.[56]	Ex vivo	889	20 MHz					
				Fibrous tissue	95.7%	90.9%	92.2%	95%
				Fibrofatty	72.3%	97.9%	85.4%	95.4%
				Necrotic core	91.7%	96.6%	82.3%	98.5%
				Dense calcium	86.5%	98.9%	94.4%	97.2%
Granada et al.[55]	In vivo; porcine coronary	60	20 MHz					
				Fibrous tissue	76.1%	-	-	-
				Fibrofatty	46%	80%	-	-
				Necrotic core	41.1%	50%	-	-
				Dense calcium	-	-	-	-
Thim et al.[58]	Porcine atherosclerotic coronary	18	20 MHz					
				Necrotic core	91.7%	17%	68.8%	50%

N = number of segments; IVUS = intravascular ultrasound; Sens = sensitivity; Spec = specificity; PPV = positive predictive value; NPV = negative predictive value.

Other studies applied IVUS-VH to investigate the relationship between plaque type and clinical outcome after PCI suggesting a role of necrotic core in peri-procedural distal embolization and delayed stent healing [62, 63].

iMAP-IVUS

Another radiofrequency-based processing method that is commercially available for coronary plaque characterization is iMAP-IVUS (Boston Scientific Corp, Fremont, CA, USA) [52], built on the rotating single element 40 MHz IVUS catheter. Similar to IVUS VH, iMAP-IVUS displays color-coded tissue maps. Fibrous tissue is coded in light green, lipidic tissue in yellow, necrotic core in pink and calcium in blue.

An ex vivo validation study demonstrates accuracy with the highest level of confidence of 97% for necrotic core, 98% for lipid, 95% for fibrous tissue and 98% for calcified regions (**Table 3**). [52]

Table 3 iMAP-IVUS tissue characterization accuracy

Author	Study setting	N	IVUS frequency	Tissue characteristic	Accuracy
Sathyanarayana et al.[52]	Ex vivo; human arteries		40 MHz		
				Necrotic	97%
				Lipidic	98%
				Fibrotic	95%
				Calcified	98%

N = number of segments; IVUS = intravascular ultrasound.

IB-IVUS

Integrated backscatter IVUS (IB-IVUS) uses the radiofrequency signals and is built on the mechanically rotating 40 MHz IVUS platform. IB-IVUS can identify three tissue components: calcified, fibrous and lipidic tissue.[29, 53, 64]

An ex vivo validation study showed a sensitivity of IB-IVUS for detecting calcification of 91% with a specificity of 98%. For detecting fibrosis sensitivity was 71% and specificity 97% and for lipid-rich plaque the sensitivity was 94% with a specificity of 85% (**Table 4**). [53]

However, backscatter analysis requires post-processing. The detection of vulnerable plaque is restricted to atheroma containing a large lipid/necrotic core as the resolution of IVUS is not high enough to detect thin (<100µm) fibrous caps.

The resolution is currently restricted by the used window for selection of regions of interest and VH tissue map reconstruction that is 480µm in radial direction. Validation data show a relatively low sensitivity for fibrolipidic tissue with some overlap in the fibrous and fibrolipidic regions that were determined by the classification schemes. However, validation data from different research groups are difficult to compare, as different histology definitions for plaque types were applied.

IV-OCT

The principle of OCT is analogous to pulse-echo ultrasound imaging, however, a near-infrared light source (approx. 1300nm wavelength) is used rather than sound to create the image. **Figure 4** shows an example of a commercially available intracoronary OCT system (St. Jude/Lightlab Imaging Inc, Westford, MA). Whereas ultrasound produces images from backscattered sound "echoes", OCT uses infrared-light waves that reflect the internal microstructure within the biological tissues. Both, the bandwidth of the infrared-light used and the wave velocity, are orders of magnitude higher than in medical ultrasound. The resulting resolution depends primarily on the ratio of these

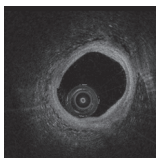

Table 4 Integrated backscatter intravascular ultrasound (IB-IVUS) tissue characterization sensitivity and specificity

Author	Study setting	N	IVUS frequency	Tissue characteristic	Sens	Spec	PPV	NPV
Kawasaki et al.[29]	Ex vivo; coronary	114	40 MHz					
				Calcification	100%	99%	88%	100%
				Fibrosis	94%	84%	94%	84%
				Lipid pool	84%	97%	84%	97%
				Intimal hyperplasia	67%	99%	80%	99%
Okubo et al.[53]	Ex vivo; human coronary	725	40 MHz					
				Calcification	95%	99%	99%	97%
				Fibrosis	94%	93%	93%	94%
				Lipid pool	90%	92%	85%	90%

N = number of segments; IVUS = intravascular ultrasound; Sens = sensitivity; Spec = specificity; PPV = positive predictive value; NPV = negative predictive value.

parameters, and is one order of magnitude larger than that of conventional IVUS, the axial resolution of OCT is about 15 mm.[65, 66]

Because of the high resolution of IV-OCT, the three layered structure of the healthy vessel wall can be imaged in detail as shown in **Figure 5**.[29, 67, 68] Likewise, the endoluminal layers of atherosclerotic plaque can be visualized in great detail.

Visual assessment of the OCT data, displayed in a color-coded or gray scale intensity map, allows for the identification of different plaque components. Fibrous plaques are defined as homogeneous, signal rich plaques. Fibrocalcific plaques are typically defined as low backscattering plaques with sharply delineated borders. Necrotic core is defined as a signal-poor region within an atherosclerotic plaque, with poorly delineated borders and little IV-OCT signal backscattering. The fibrous cap is typically defined as a signal rich layer overlying a signal poor region.[69]

Comparison to histology showed that visual assessment using these criteria allows to differentiate plaque components with high sensitivity and specificity (**Table 5 and 6**), confirming the findings of the first landmark study by Yabushita et al.[69]

Furthermore, OCT proved suitable to diagnose features of TCFA [70-73] and potentially vulnerable atherosclerotic plaques. **Figure 6** shows examples of atherosclerotic plaque features that can be visualized using OCT. Thrombi are identified as masses protruding into the vessel lumen discontinuous from the surface of the vessel wall. Red thrombi consist mainly of red blood cells; relevant OCT images are characterized as high-backscattering protrusions with signal-free shadowing. White thrombi con-

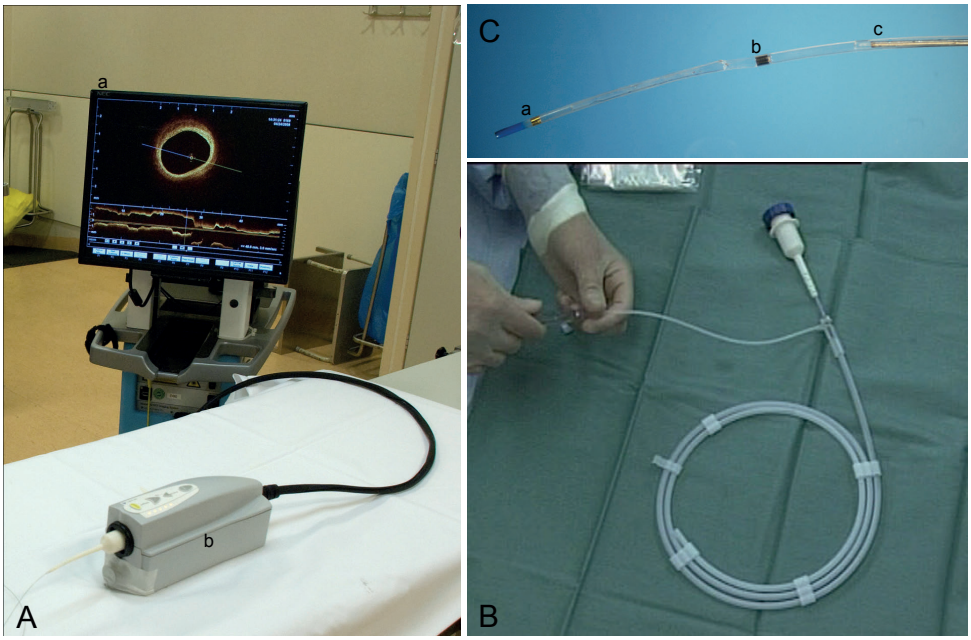

Figure 4 Commercially available intracoronary Fourier domain OCT system (St. Jude/Lightlab Imaging Inc, Westford, MA)

A) OCT system consisting of a) a console containing the light source, a computer and imaging display screen and b) the automated pullback device allowing for pullback speeds up to 20 mm/sec; B) OCT imaging catheter (Dragonfly™, Lightlab Imaging Inc, Westford, MA, USA); C) Magnification of the distal OCT catheter tip. The OCT imaging catheter is introduced into the coronary artery using a conventional guide wire in short monorail technique. The short monorail catheter segment is indicated by a) the radiopaque distal catheter tip marker and b) a more proximal radiopaque marker. c) The imaging core is located approximately 15mm proximal to the distal-tip marker and moderately radiopaque. During pullback, the imaging core is withdrawn within the transparent catheter sheath, while the OCT imaging catheter itself is stationary within the artery.

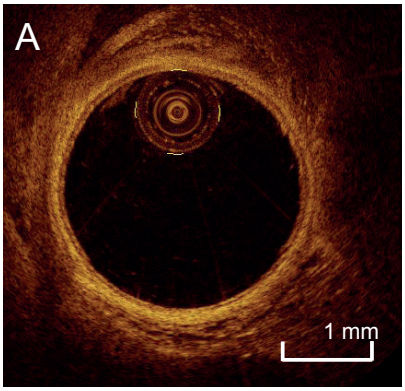

Figure 5 IV-OCT image visualizes all three layers of a healthy porcine coronary vessel wall

Table 5 Intravascular optical coherence tomography (IV-OCT) tissue characterization sensitivity and specificity

Author	Study setting	N	Tissue characteristic	Sens	Spec	PPV	NPV
Yabushita et al.[69]	Ex vivo; human (126 aortas, 105 carotid bulbs, 90 coronaries)	357					
			Fibrous	71-79%	97-98%	91-93%	91-93%
			Fibrocalcific	95-96%	97%	97%	95-96%
			Lipid rich	90-94%	90-92%	74-75%	97-98%
Kawasaki et al.[29]	Ex vivo; coronary	121					
			Caclification	100%	100%	100%	100%
			Fibrosis	98%	94%	98%	94%
			Lipid pool	95%	98%	90%	99%
			Intimal hyperplasia	86%	100%	100%	99%
Kume et al.[37]	Ex vivo; coronary	166					
			Fibrous	79%	99%	97%	93%
			Fibrocalcific	96%	88%	89%	96%
			Lipid rich	85%	94%	83%	95%

N = number of segments; Sens = sensitivity; Spec = specificity; PPV = positive predictive value; NPV = negative predictive value.

sist mainly of platelets and white blood cells and are characterized by a signal-rich, low-backscattering billowing projection protruding into the lumen.[74] Macrophages are seen by OCT as signal-rich, distinct or confluent punctate dots that exceed the intensity of background speckle noise.[75] Macrophages may often be seen at the boundary between the bottom of the cap and the top of a necrotic core. Vasa vasorum and neovascularization: (neo)vessels within the intima appear as signal poor voids that are sharply delineated and usually contiguous and seen on multiple frames.[76] OCT has been proven to allow the diagnosis of TCFA with a sensitivity of 90% and a specificity of 79% when compared to histopathology. [77]

Clinically, OCT is used similar to IVUS to assess the extent and distribution of coronary plaque and to guide therapeutic procedures. It's high resolution qualifies OCT as the new gold standard for the assessment of the acute and long-term result of coronary stents.[76, 78-91] Its unique ability to detect and characterize thin fibrous-cap atheroma's has enabled pathophysiologic studies on the prevalence, distribution and mechanism of rupture of thin-capped fibro-atheroma's in different clinical scenarios.[92, 93]

Table 6 IV-OCT tissue characterization. Correlation between histology and IV-OCT

Author	Study setting	N	Tissue characteristic	Correlation
Kume et al.[70]	Ex vivo; human coronary	102	Fibrous cap thickness	r =0.90; P<0.001
Cilingiroglu et al.[73]	In vivo and ex vivo; murine	7 and 12	Fibrous cap thickness	r = 0.97; P<0.0001
Tearney et al.[67]	Ex vivo		Fibrous cap macrophage density	r = 0.84; P<0.0001)

N = number of segments

Characteristics of the culprit lesion as assessed by IV-OCT were evaluated by Jang et al. in patients with AMI (n=20), ACS (n=20) and stable angina (n=17). Lipid-rich plaque was observed more frequently in patients with AMI (90%) and ACS (75%) than in patients with stable angina (59%; p=0.09). In patients with unstable syndromes, the fibrous cap thickness was also reported to be lower. Consistently, the frequency of TCFA was higher in the AMI (72%) and ACS group (50%) than in the stable angina group (20%).[94] Those results are in line with another study from Kubo et al.[95] showing a higher incidence of lipid-rich plaques (71% vs. 42% p=0.03), plaque rupture (42% vs. 3%, p<0.001), intracoronary thrombus (67% vs. 3%, p <0.001) and TCFA (46% vs. 3%, p=0.001) in patients with unstable angina compared to patients with stable angina.[95] Plaques with TCFA by OCT appear to be highly prevalent in patients with ACS. A study of the culprit lesion in AMI patients revealed an incidence of TCFA of 83% with a mean fibrous cap thickness of 49 ± 21μm.[96] The presence of lesions with thin cap fibro-atheroma was also investigated by Fuji et al.[97] where the investigators evaluated the geographic distribution of TCFAs in the coronaries. OCT examination of all three major epicardial arteries was performed in 34 patients with AMI and 20 patients with stable angina. OCT detected 94 TCFAs (defined as a lipid-rich plaque with a fibrous cap thickness < 65 micron) in 165 coronary arteries, of which 28 were located in the LAD, 18 in the LCX and 48 in the right coronary artery (RCA). Most LAD TCFAs were located within 0 and 30 mm from the ostium. LCX and RCA TCFAs were evenly distributed throughout the entire coronary. These results indicate that TCFAs tend to cluster in predictable spots within the proximal segment of the LAD and develop evenly in the LCX and RCA.

A recent study investigated changes in TCFA over time. Interestingly, the study demonstrated thickening of the thin fibrous cap because of statin therapy [98], offering exciting insights in mechanisms of action and potential plaque stabilization.

However, OCT cannot penetrate blood, and therefore requires flushing of the lumen during imaging for a couple of seconds. Limited tissue penetration (1.0-2.5 mm) does not always allow visualization of the media and adventitia in the presence of atherosclerotic wall thickening and thus hampers the evaluation of vessel wall remodeling.[99]

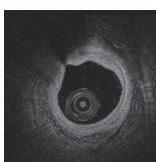

Differentiation of plaque components can be difficult in situations with limited penetration [100, 101] or eccentric OCT catheter position within the vessel.[102]

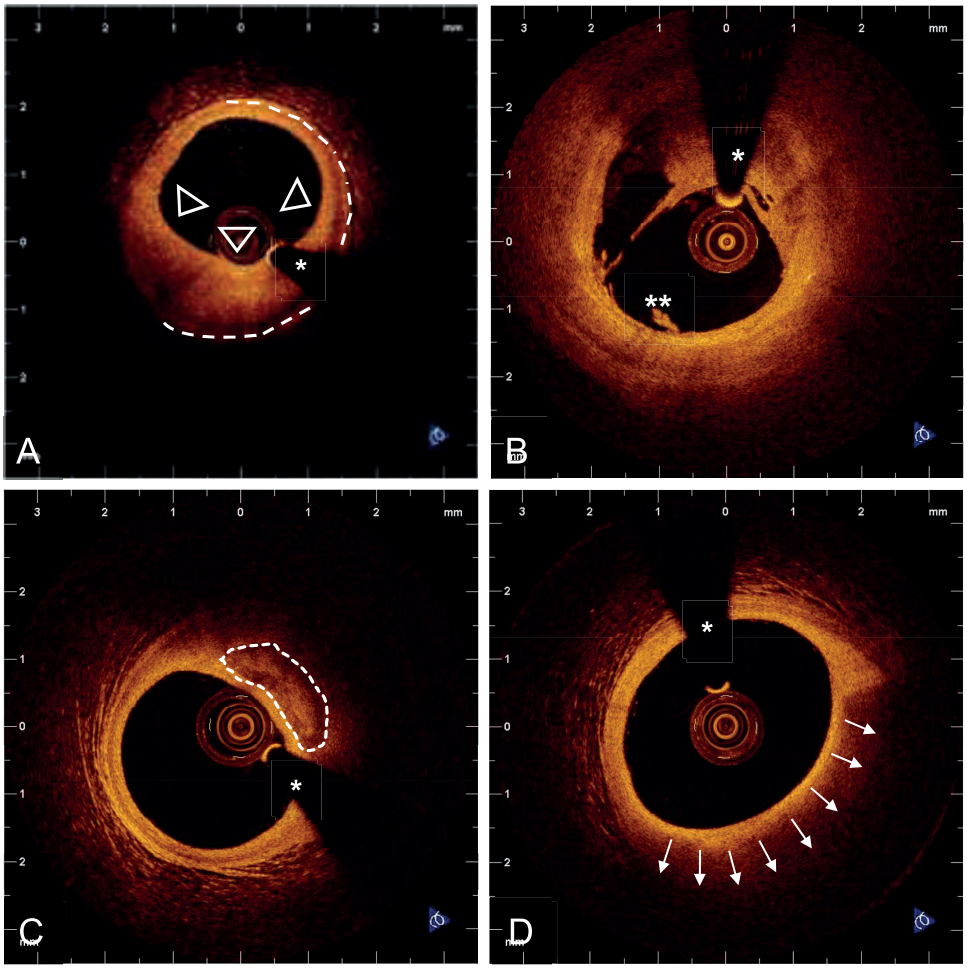

Figure 6 Intracoronary OCT plaque characterization

A) Eccentric fibro-atheroma with predominantly fibrous, homogenous signal-rich plaque in 2 to 9 o'clock position (arrow heads). The signal-poor media is visible as a dark band over the majority of the vessel circumference (dotted line). B) Ruptured thin cap fibro-atheroma. The thin fibrous cap (thickness 52 micron) has ruptured in the shoulder region of the eccentric plaque. Remnants of the necrotic core are in direct contact with the blood stream (**); C) Eccentric fibro-atheroma with focal calcification appearing as a signal poor, relatively dark structure with sharply delineated borders (dotted line); D) Eccentric fibro-atheroma with predominantly lipid-rich plaque in 2-8 o'clock position. Typically a fibrous cap can be recognized as signal rich, yellow structure towards the lumen with a rapid drop in signal intensity towards the abluminal plaque side, caused by the high attenuation of lipid-rich tissue (arrows). Asterix indicates guide wire artefact. OCT: St. Jude/Lightlab Imaging C7-XR.

NIRS

Near-infrared spectroscopy uses near-infrared light (wavelengths from 800 to 2500 nm) to identify specifically the presence of lipid core plaques (LCP).[103, 104]

Light of discrete wavelengths from a laser is directed onto the tissue sample via fiber glass. Light scattered from the samples is collected in fibers and launched into a spectrometer. The plot of signal intensity as a function of wavelength is then used to develop chemometric models to discriminate lipid-rich deposits from non-atherosclerotic tissue, and from atherosclerotic tissue that is predominantly fibrotic from blood elements. The primary presentation of the data is the chemogram, a plot of NIR spectroscopy values (yellow = high probability to red = low probability) obtained during a rotation and pullback of the imaging tip within the coronary artery. The lipid-core burden index (LCBI) score, summarizes the fraction of LCP in the imaged section of the coronary vessel on a scale of 0 to 1000.

The algorithm for the detection of lipid core plaques was validated in-vitro (**Table 7**). NIRS scanning through blood was performed in 212 coronary segments from 84 autopsy hearts. One histologic section was analyzed for every 2 mm of artery. LCP of interest was defined as a lipid core >60 degrees in circumferential extent, >200 micrometer thick, with a mean fibrous cap thickness <450 micrometer. To develop the algorithm, 4.2 meter of artery from 33 autopsy hearts were used. In addition, more than 5 meter of artery from 51 validation hearts were used in a prospective, double blind manner to evaluate the accuracy of NIRS in detecting LCP. The LCPs were present in 4.3% of the sections from the 51 validation hearts. The algorithm prospectively identified LCP with a receiver-operator characteristic (ROC) area of 0.80. The lipid core burden index (LCBI) detected the presence or absence of any fibro-atheroma with an area under the curve (AUC) of 0.86. These results show that the NIRS system can accurately identify LCP through blood in a prospective study in coronary autopsy specimens.[103]

The reproducibility of the NIRS system for the detection of LCP was evaluated in a study evaluating 36 vessels in 31 patients. The reproducibility of the LCBI and the presence and number of LCPs was assessed. LCBI of the first and second pullback was 64 ± 43 and 70 ± 62 respectively, with an intraclass correlation coefficient of 0.925. High correlation (intraclass coefficient ranged from 0.76 to 0.91) was found between the two pullbacks for total LCP length and for LCP number. These results show that the LCBI and LCP length NIRS measurements have high reproducibility.[105]

The SPECTroscopic Assessment of Coronary Lipid (SPECTACL) trial was a parallel first-in-human multicenter study designed to demonstrate the applicability of the LCP detection algorithm in living patients. NIRS was performed in patients undergoing PCI.

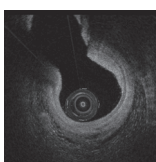

Table 7 Near-infrared spectroscopy (NIRS) tissue characterization sensitivity and specificity

Author	Study setting	N	Tissue characteristic	Sens	Spec	PPV	NPV
Gardner et al.[103]	Ex vivo; human coronary	2649	Lipid core plaque	49%	90%	19%	97%

N = number of segments; Sens = sensitivity; Spec = specificity; PPV = positive predictive value; NPV = negative predictive value.

Acquired spectra were blindly compared with autopsy NIRS signals with multivariate statistics. Spectral similarity was demonstrated in 40 of 48 spectrally adequate scans. The LCP was detected in 58% of 60 spectrally similar scans from both cohorts. These results demonstrate the feasibility of invasive detection of LCP with the NIRS system.[104]

Comparison of IVUS-VH with NIRS, however, showed a weak correlation (r=0.149) between the detection of LCP by NIRS and necrotic core by VH.[106]

Although NIR spectroscopy proved feasible in-vivo, it is limited by the lack of structural information. In order to overcome this shortcoming, a combined LipiScan IVUS system (LipiScan™ IVUS Coronary Imaging System; InfraReDx, Inc) was recently introduced. **Figure 7** shows an example of the commercially available IVUS Lipiscan system. This new multimodality imaging catheter combines the advantages of near-infrared spectroscopy and intravascular ultrasound and enables the interventional cardiologists to determine the structure of a plaque simultaneously with its chemical composition.[107-109]

An example of the clinical use of the Lipiscan IVUS system is depicted in **Figure 8**.

The first use of the combined NIRS and IVUS catheter to identify composition and structure of coronary plaque was demonstrated in a 70 year-old female with a history of hyperlipidaemia treated with statins that underwent coronary angioplasty of her right coronary artery (RCA). Post-procedure the RCA was assessed using the combined catheter, which indicated that the proximal end of the stent was located in an area of lipid core plaque. Strut penetration into an LCP is proposed to be a potential risk factor for stent thrombosis.[110, 111] Currently the ongoing CANARY registry is specifically evaluating the association of LCP and outcome of stent implantation.

The chemical analysis, however, is limited to the detection of lipid-core plaques, while other plaque components are being neglected. Larger scale clinical experience and prospective in-vivo evaluation of the prognostic relevance of LCP is not yet available.

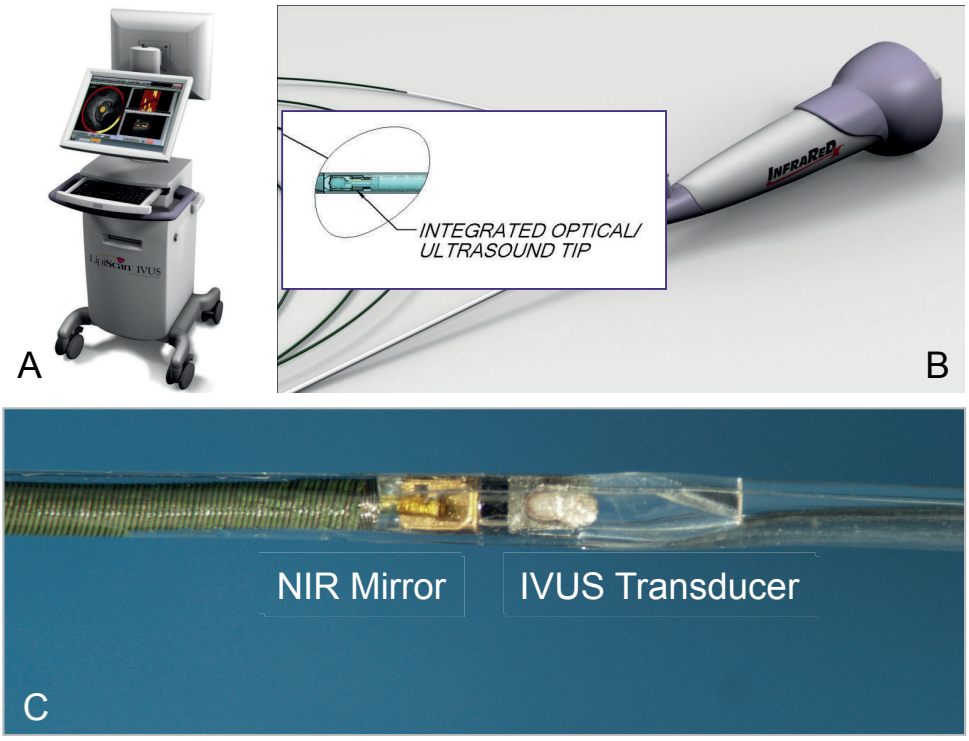

Figure 7 Commercially available intracoronary IVUS Lipiscan (Infraredx Inc,Boston, MA)
A) IVUS Lipiscan system console and automated pullback device allowing for pullback speeds up to 1mm/sec; B) Schematic of the IVUS Lipiscan imaging catheter; C) Magnification of the distal tip of the combined IVUS Lipiscan catheter. The catheter has an outer diameter of 3.2F and can be introduced into the coronary artery in rapid exchange technique over a standard 0.014" guide wire and a 6F guide catheter. NIR spectroscopy transducer is the same as LipiScan™, cleared by FDA Apr '08; ultrasound transducer: 40MHz, 16 fps.

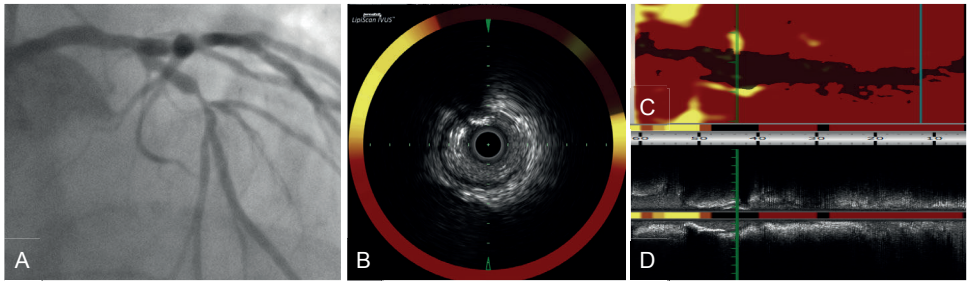

Figure 8 Clinical case example: Pre-interventional imaging of the left anterior descending artery with the combined NIR-spectroscopy/IVUS catheter
A) Coronary angiogram of the left anterior descending artery; B) Cross-sectional fusion image showing IVUS and NIR spectroscopy display of the minimal lumen area site. IVUS visualizes eccentric mixed plaque with sonolucent and echodense plaque components while NIR spectroscopy confirms the presence of lipid core plaque in 9-12 o'clock position as indicated by the yellow color coding on the outer circular chemogram display; C) and D) Longitudinal views of the simultaneously acquired chemogram (C) and IVUS data (D).

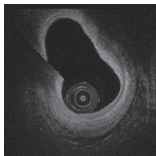

Coronary angioscopy

Angioscopy is an endoscopic imaging modality that allows direct visualization of the internal surface of a coronary artery.

The angioscope consists of a white light source and a flexible optical fiber bundle. The optic bundle consists of separate illumination and collection fibers and a distal lens at the tip of the catheter to form a field of view of 55° in air and an imaging depth of more than 0.5mm. The illumination fibers guide the light to the artery wall and the collection fibers collect the light reflected from the artery wall. Saline perfusion (1 ml/s) through the catheter is needed to visualize the coronary lumen.[112]

Comparison to histology has shown that angioscopy can detect the different colors of different plaque types. Fibrotic plaques are associated with a white color, plaques with lipid pools with a deep yellow color, and thin fibrous caps are associated with more intense shades of yellow (**Table 8**).[113]

Table 8 Coronary angioscopy tissue characterization sensitivity and specificity

Author	Study setting	N	Tissue characteristic	Sens	Spec	PPV	NPV
Thieme et al.[113]	Ex vivo; human coronary	44					
			Fibrous plaque	64%	88%	64%	88%
			Degenerated fibrous plaque	43%	78%	64%	60%
			Lipid pool	83%	72%	53%	92%
Uchida et al.[114]							
			Vulnerable plaque	90%	97%	84%	98%

N = number of segments; Sens = sensitivity; Spec = specificity; PPV = positive predictive value; NPV = negative predictive value.

In a study comparing findings of patients with different coronary syndromes, atherosclerotic material was retrieved by directional coronary atherectomy and angioscopic observations were validated. Angioscopy was compared with histologic findings in 44 patients with stable or unstable angina. Angioscopic findings were grouped into gray-white and yellow lesions. Patients with unstable angina showed predominantly yellow lesions (89%) whereas patients with stable angina showed a similar distribution (43% gray-white, 57% yellow) of lesions. Ruptured yellow plaques and red or pink thrombi were found in 11% of patients with stable and in 39% of patients with unstable angina. Histologically, gray-white lesions represented fibrous plaque without degeneration in 64% and with degeneration in 36% of patients. Gray-yellow lesions were associated with degenerated plaque (64%) and fibrous plaque (14%) or atheroma (14%). Deep

yellow and yellow-red lesions represented atheroma (53%) or degenerated plaque (42%). These findings show a basis for classification and interpretation of angioscopic findings.[113]

Clinically, angioscopy can be used for the assessment of coronary plaque, the evaluation of PCI or pharmacologic treatment.[115-117] Angioscopy has been intensely used to study patients with ACS because of its capability to detect plaque disruptions, thrombi and ulcerations.[118-122] A high incidence of thrombi in patients with AMI and unstable angina could be demonstrated (100% AMI, 90% unstable angina). Occlusive thrombi were more common in patients with AMI than in those with unstable angina (79% vs. 10%; P<0.001). Mural thrombi were more common in the unstable angina than in the AMI group (80% vs. 21%; P<0.001). Xanthomas were more common in patients with ACS (50%) than in those with stable angina (15%) or old MI (8%). These results suggested that the character of thrombus may differ between ACS and stable syndrome and that lipid-rich xanthomatous plaques may precede rupture.[118]

The effects of statin therapy on plaque color and morphology were assessed in 31 patients with CAD, assigned to atorvastatin or the control group. Serial angioscopy was performed and 145 plaques were characterized by color as 0 (white), 1 (light yellow), 2 (yellow), or 3 (dark yellow), and surface as 0 (smooth surface) or 1 (irregular surface). At 12 months follow-up it became apparent that statin therapy was associated with changes in plaque color and morphology. The mean yellow score decreased from 2.03 to 1.13 in the atorvastatin group and increased from 1.67 to 1.99 in the control group (P=0.002 vs. controls).[115]

However, angioscopy is restricted to the visualization of the endoluminal vessel surface. It cannot assess plaque burden, vessel remodeling or vessel and lumen dimensions and does not allow for quantitative measurement. The color classification is based on visual assessment and dependent on the experience of the operator and angioscopy is not widespread available for clinical use.

Challenges for invasive imaging

Over the last decade, advanced intracoronary imaging increased our understanding of coronary artery disease and the dynamic nature of atherosclerotic changes. Importantly, invasive imaging demonstrated therapeutic mechanisms of action in patients with coronary artery disease.

Despite the recent remarkable technology progresses, intracoronary imaging is principally limited by the physical boundaries affecting image resolution, applied en-

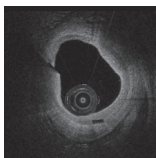

ergy, size of the sample volume, penetration depth into the tissue, spatial orientation and accuracy. Quantitative tissue analysis such as IVUS-VH, iMAP or NIR spectroscopy suffer from the fact that the histological definitions used to validate an imaging technology or to establish pre-specified diagnostic strata might differ between technologies. Comparison of data originating from different imaging technologies is therefore challenging. A possibility to overcome such problems might be the use of animal models for the validation of intracoronary imaging data.

The normal porcine model is often used for the evaluation of coronary devices.[123, 124] A porcine model offers the possibility to acquire invasive imaging data in-vivo under similar conditions as in patients, with respect to cardiac and respiratory motion, vascular tortuosity, susceptibility to ischemia, and instrumentation. Although such a model offers the advantage to allow validation with histology, it is of limited value for the validation of invasive imaging as healthy juvenile pigs lack atherosclerotic vessel wall alterations.

We therefore aimed to develop a porcine model that allows us to study early and late stages of atherosclerosis and to allow for validation of invasive imaging technologies. Our animals developed advanced atherosclerotic coronary lesions after induction of diabetes in combination with a saturated-fat-high-cholesterol diet.[125-128] Distinct morphologic features such as a large necrotic core, a thin fibrous cap, inflammation, angiogenesis and plaque hemorrhage can be observed. **Figure 9** shows an example of an advanced atherosclerotic lesion in a coronary of one of our pigs.[123, 128] Such a model could help to validate invasive imaging and to improve clinical diagnosis and decision making in the future. The progression of atherosclerotic lesions from an early to an advanced lesion can be studied and the sensitivity of invasive imaging technologies to detect distinct atherosclerotic lesions and their changes over time could be established. This information could help to integrate knowledge gained from clinical studies using different invasive imaging technologies and advance our understanding of atherosclerotic lesions, plaque vulnerability and ACS.

Outlook

Today intravascular imaging offers new levels of anatomical detail and new dimensions of information for the diagnosis of coronary artery disease, paving the way to an improved understanding and therapeutic targeting of atherosclerosis. However, the clinical and prognostic value needs to be determined and the indications for clinical application needs to be established.

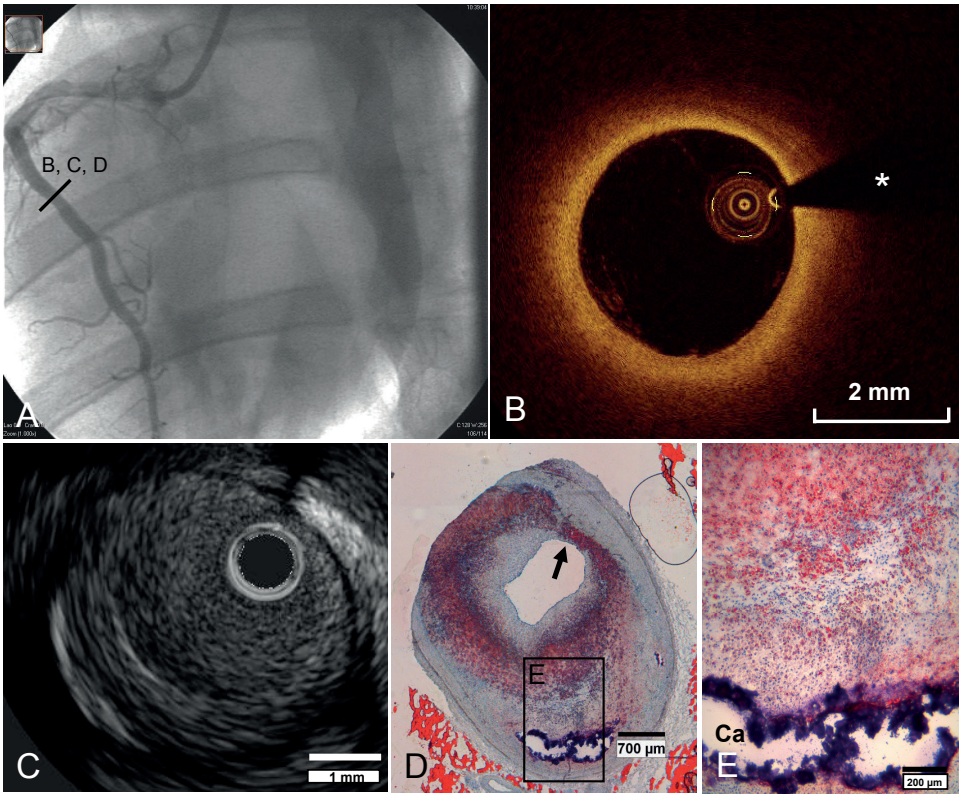

Figure 9 Coronary atherosclerosis in a porcine model with atherosclerosis and diabetes
A) Angiogram of the right coronary artery of a pig with the black line indicating the location of the atherosclerotic lesion; B) IV-OCT image of the atherosclerotic plaque. Asterix indicates the wire artifact. Bar in B is 2 mm; C) IVUS image of the same plaque as seen in B) and D). Bar in C is 1 mm; D) and E) show an overview and detail of the plaque with circumferential lipid accumulation (stained red) and deep calcification (CA, remaining rim stained blue). The black arrow indicates a thin fibrous cap with overlying superficial lipid-rich tissue, showing a likeness to a thin cap fibrous atheroma. Oil-red-O stain, bar in D is 700 µm, bar in E is 200 µm. Image is modified from van Ditzhuijzen and van den Heuvel et al. Neth Heart J 2011.[127]

New developments aim at more detailed and user-independent quantitative tissue characterization. OCT offers possibilities for quantitative tissue characterization by exploiting the optical attenuation coefficient for tissue identification.[129] Another possibility for tissue characterization consists in the measurement of tissue birefringence using polarization-sensitive OCT (PS-OCT) aimed at the assessment of collagen.[130, 131] Other options are dual-modality intra-arterial imaging tools, such as a combination of optical frequency domain imaging (OFDI) and near-infrared fluorescence (NIRF) imaging for simultaneous microstructural and molecular imaging.[132] Another interesting approach may consists of photoacoustic imaging. Photoacoustic tomography utilizes a short-

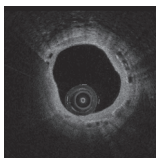

pulsed laser beam to diffusively penetrate into tissue. Upon absorption of the light by the target, photoacoustic waves are generated and used to reconstruct, at ultrasound resolution, the optical absorption distribution that reveals optical contrast [133, 134]

References

1. Roger VL, Go AS, Lloyd-Jones DM, Adams RJ, Berry JD, Brown TM, Carnethon MR, Dai S, de Simone G, Ford ES, Fox CS, Fullerton HJ, Gillespie C, Greenlund KJ, Hailpern SM, Heit JA, Ho PM, Howard VJ, Kissela BM, Kittner SJ, Lackland DT, Lichtman JH, Lisabeth LD, Makuc DM, Marcus GM, Marelli A, Matchar DB, McDermott MM, Meigs JB, Moy CS, Mozaffarian D, Mussolino ME, Nichol G, Paynter NP, Rosamond WD, Sorlie PD, Stafford RS, Turan TN, Turner MB, Wong ND, Wylie-Rosett J. Heart disease and stroke statistics--2011 update: a report from the American Heart Association. Circulation 2011;123(4):e18-e209.
2. Braunwald E, Antman EM, Beasley JW, Califf RM, Cheitlin MD, Hochman JS, Jones RH, Kereiakes D, Kupersmith J, Levin TN, Pepine CJ, Schaeffer JW, Smith EE, 3rd, Steward DE, Theroux P, Gibbons RJ, Alpert JS, Faxon DP, Fuster V, Gregoratos G, Hiratzka LF, Jacobs AK, Smith SC, Jr. ACC/AHA 2002 guideline update for the management of patients with unstable angina and non-ST-segment elevation myocardial infarction--summary article: a report of the American College of Cardiology/American Heart Association task force on practice guidelines (Committee on the Management of Patients With Unstable Angina). J Am Coll Cardiol 2002;40(7):1366-74.
3. Hamm CW, Bassand JP, Agewall S, Bax J, Boersma E, Bueno H, Caso P, Dudek D, Gielen S, Huber K, Ohman M, Petrie MC, Sonntag F, Uva MS, Storey RF, Wijns W, Zahger D, Bax JJ, Auricchio A, Baumgartner H, Ceconi C, Dean V, Deaton C, Fagard R, Funck-Brentano C, Hasdai D, Hoes A, Knuuti J, Kolh P, McDonagh T, Moulin C, Poldermans D, Popescu BA, Reiner Z, Sechtem U, Sirnes PA, Torbicki A, Vahanian A, Windecker S, Windecker S, Achenbach S, Badimon L, Bertrand M, Botker HE, Collet JP, Crea F, Danchin N, Falk E, Goudevenos J, Gulba D, Hambrecht R, Herrmann J, Kastrati A, Kjeldsen K, Kristensen SD, Lancellotti P, Mehilli J, Merkely B, Montalescot G, Neumann FJ, Neyses L, Perk J, Roffi M, Romeo F, Ruda M, Swahn E, Valgimigli M, Vrints CJ, Widimsky P. ESC Guidelines for the management of acute coronary syndromes in patients presenting without persistent ST-segment elevation: The Task Force for the management of acute coronary syndromes (ACS) in patients presenting without persistent ST-segment elevation of the European Society of Cardiology (ESC). Eur Heart J 2011.
4. Virchow. Thrombose und Embolie. Gefässentzündung und septische Infektion. 1956: 219–732.
5. Ross R. The pathogenesis of atherosclerosis--an update. N Engl J Med 1986;314(8):488-500.
6. Stary HC, Blankenhorn DH, Chandler AB, Glagov S, Insull W, Jr., Richardson M, Rosenfeld ME, Schaffer SA, Schwartz CJ, Wagner WD, et al. A definition of the intima of human arteries and of its atherosclerosis-prone regions. A report from the Committee on Vascular Lesions of the Council on Arteriosclerosis, American Heart Association. Circulation 1992;85(1):391-405.
7. Stary HC, Chandler AB, Glagov S, Guyton JR, Insull W, Jr., Rosenfeld ME, Schaffer SA, Schwartz CJ, Wagner WD, Wissler RW. A definition of initial, fatty streak, and intermediate lesions of atherosclerosis. A report from the Committee on Vascular Lesions of the Council on Arteriosclerosis, American Heart Association. Circulation 1994;89(5):2462-78.
8. Virmani R, Kolodgie FD, Burke AP, Farb A, Schwartz SM. Lessons from sudden coronary death: a comprehensive morphological classification scheme for atherosclerotic lesions. Arterioscler Thromb Vasc Biol 2000;20(5):1262-75.

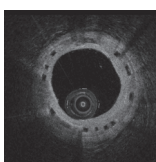

9. Stary HC, Chandler AB, Dinsmore RE, Fuster V, Glagov S, Insull W, Jr., Rosenfeld ME, Schwartz CJ, Wagner WD, Wissler RW. A definition of advanced types of atherosclerotic lesions and a histological classification of atherosclerosis. A report from the Committee on Vascular Lesions of the Council on Arteriosclerosis, American Heart Association. Circulation 1995;92(5):1355-74.
10. Farb A, Burke AP, Tang AL, Liang TY, Mannan P, Smialek J, Virmani R. Coronary plaque erosion without rupture into a lipid core. A frequent cause of coronary thrombosis in sudden coronary death. Circulation 1996;93(7):1354-63.
11. Muller JE, Abela GS, Nesto RW, Tofler GH. Triggers, acute risk factors and vulnerable plaques: the lexicon of a new frontier. J Am Coll Cardiol 1994;23(3):809-13.
12. Finn AV, Nakano M, Narula J, Kolodgie FD, Virmani R. Concept of vulnerable/unstable plaque. Arterioscler Thromb Vasc Biol 2010;30(7):1282-92.
13. Glagov S, Weisenberg E, Zarins CK, Stankunavicius R, Kolettis GJ. Compensatory enlargement of human atherosclerotic coronary arteries. N Engl J Med 1987;316(22):1371-5.
14. Pasterkamp G, Schoneveld AH, van der Wal AC, Haudenschild CC, Clarijs RJ, Becker AE, Hillen B, Borst C. Relation of arterial geometry to luminal narrowing and histologic markers for plaque vulnerability: the remodeling paradox. J Am Coll Cardiol 1998;32(3):655-62.
15. Varnava AM, Mills PG, Davies MJ. Relationship between coronary artery remodeling and plaque vulnerability. Circulation 2002;105(8):939-43.
16. Burke AP, Kolodgie FD, Farb A, Weber D, Virmani R. Morphological predictors of arterial remodeling in coronary atherosclerosis. Circulation 2002;105(3):297-303.
17. Pasterkamp G, Wensing PJ, Post MJ, Hillen B, Mali WP, Borst C. Paradoxical arterial wall shrinkage may contribute to luminal narrowing of human atherosclerotic femoral arteries. Circulation 1995;91(5):1444-9.
18. Sones FM, Jr., Shirey EK. Cine coronary arteriography. Mod Concepts Cardiovasc Dis 1962;31:735-8.
19. Scanlon PJ, Faxon DP, Audet AM, Carabello B, Dehmer GJ, Eagle KA, Legako RD, Leon DF, Murray JA, Nissen SE, Pepine CJ, Watson RM, Ritchie JL, Gibbons RJ, Cheitlin MD, Gardner TJ, Garson A, Jr., Russell RO, Jr., Ryan TJ, Smith SC, Jr. ACC/AHA guidelines for coronary angiography: executive summary and recommendations. A report of the American College of Cardiology/American Heart Association Task Force on Practice Guidelines (Committee on Coronary Angiography) developed in collaboration with the Society for Cardiac Angiography and Interventions. Circulation 1999;99(17):2345-57.
20. Ellis SG, Vandormael MG, Cowley MJ, DiSciascio G, Deligonul U, Topol EJ, Bulle TM. Coronary morphologic and clinical determinants of procedural outcome with angioplasty for multivessel coronary disease. Implications for patient selection. Multivessel Angioplasty Prognosis Study Group. Circulation 1990;82(4):1193-202.
21. Holmes DR, Jr., Topol EJ. Reperfusion momentum: lessons from the randomized trials of immediate coronary angioplasty for myocardial infarction. J Am Coll Cardiol 1989;14(6):1572-8.
22. Ambrose JA, Tannenbaum MA, Alexopoulos D, Hjemdahl-Monsen CE, Leavy J, Weiss M, Borrico S, Gorlin R, Fuster V. Angiographic progression of coronary artery disease and the development of myocardial infarction. J Am Coll Cardiol 1988;12(1):56-62.
23. Little WC, Constantinescu M, Applegate RJ, Kutcher MA, Burrows MT, Kahl FR, Santamore WP. Can coronary angiography predict the site of a subsequent myocardial infarction in

patients with mild-to-moderate coronary artery disease? Circulation 1988;78(5 Pt 1):1157-66.
24. Brensike JF, Levy RI, Kelsey SF, Passamani ER, Richardson JM, Loh IK, Stone NJ, Aldrich RF, Battaglini JW, Moriarty DJ, et al. Effects of therapy with cholestyramine on progression of coronary arteriosclerosis: results of the NHLBI Type II Coronary Intervention Study. Circulation 1984;69(2):313-24.
25. Brown G, Albers JJ, Fisher LD, Schaefer SM, Lin JT, Kaplan C, Zhao XQ, Bisson BD, Fitzpatrick VF, Dodge HT. Regression of coronary artery disease as a result of intensive lipid-lowering therapy in men with high levels of apolipoprotein B. N Engl J Med 1990;323(19):1289-98.
26. Virmani R, Burke AP, Farb A. Plaque rupture and plaque erosion. Thromb Haemost 1999;82 Suppl 1:1-3.
27. Lee RT, Libby P. The unstable atheroma. Arterioscler Thromb Vasc Biol 1997;17(10):1859-67.
28. Tenaglia AN, Buller CE, Kisslo KB, Phillips HR, Stack RS, Davidson CJ. Intracoronary ultrasound predictors of adverse outcomes after coronary artery interventions. J Am Coll Cardiol 1992;20(6):1385-90.
29. Kawasaki M, Bouma BE, Bressner J, Houser SL, Nadkarni SK, MacNeill BD, Jang IK, Fujiwara H, Tearney GJ. Diagnostic accuracy of optical coherence tomography and integrated backscatter intravascular ultrasound images for tissue characterization of human coronary plaques. J Am Coll Cardiol 2006;48(1):81-8.
30. Prati F, Arbustini E, Labellarte A, Dal Bello B, Sommariva L, Mallus MT, Pagano A, Boccanelli A. Correlation between high frequency intravascular ultrasound and histomorphology in human coronary arteries. Heart 2001;85(5):567-70.
31. Di Mario C, The SH, Madretsma S, van Suylen RJ, Wilson RA, Bom N, Serruys PW, Gussenhoven EJ, Roelandt JR. Detection and characterization of vascular lesions by intravascular ultrasound: an in vitro study correlated with histology. J Am Soc Echocardiogr 1992;5(2):135-46.
32. Mintz GS, Nissen SE, Anderson WD, Bailey SR, Erbel R, Fitzgerald PJ, Pinto FJ, Rosenfield K, Siegel RJ, Tuzcu EM, Yock PG. American College of Cardiology Clinical Expert Consensus Document on Standards for Acquisition, Measurement and Reporting of Intravascular Ultrasound Studies (IVUS). A report of the American College of Cardiology Task Force on Clinical Expert Consensus Documents. J Am Coll Cardiol 2001;37(5):1478-92.
33. Kostamaa H, Donovan J, Kasaoka S, Tobis J, Fitzpatrick L. Calcified plaque cross-sectional area in human arteries: correlation between intravascular ultrasound and undecalcified histology. Am Heart J 1999;137(3):482-8.
34. Potkin BN, Bartorelli AL, Gessert JM, Neville RF, Almagor Y, Roberts WC, Leon MB. Coronary artery imaging with intravascular high-frequency ultrasound. Circulation 1990;81(5):1575-85.
35. Hiro T, Leung CY, De Guzman S, Caiozzo VJ, Farvid AR, Karimi H, Helfant RH, Tobis JM. Are soft echoes really soft? Intravascular ultrasound assessment of mechanical properties in human atherosclerotic tissue. Am Heart J 1997;133(1):1-7.
36. Palmer ND, Northridge D, Lessells A, McDicken WN, Fox KA. In vitro analysis of coronary atheromatous lesions by intravascular ultrasound; reproducibility and histological correlation of lesion morphology. Eur Heart J 1999;20(23):1701-6.
37. Kume T, Akasaka T, Kawamoto T, Watanabe N, Toyota E, Neishi Y, Sukmawan R, Sadahira Y, Yoshida K. Assessment of coronary arterial plaque by optical coherence tomography. Am J Cardiol 2006;97(8):1172-5.

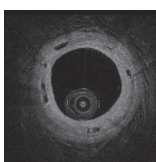

38. Tardif JC, Gregoire J, L'Allier PL, Ibrahim R, Lavoie MA, LeMay M, Cohen E, Levesque S, Keller PF, Heinonen T, Guertin MC. Effect of atherosclerotic regression on total luminal size of coronary arteries as determined by intravascular ultrasound. Am J Cardiol 2006;98(1):23-7.
39. Gussenhoven EJ, Essed CE, Frietman P, van Egmond F, Lancee CT, van Kappellen WH, Roelandt J, Serruys PW, Gerritsen GP, van Urk H, et al. Intravascular ultrasonic imaging: histologic and echographic correlation. Eur J Vasc Surg 1989;3(6):571-6.
40. Okazaki S, Yokoyama T, Miyauchi K, Shimada K, Kurata T, Sato H, Daida H. Early statin treatment in patients with acute coronary syndrome: demonstration of the beneficial effect on atherosclerotic lesions by serial volumetric intravascular ultrasound analysis during half a year after coronary event: the ESTABLISH Study. Circulation 2004;110(9):1061-8.
41. Nissen SE, Tuzcu EM, Schoenhagen P, Brown BG, Ganz P, Vogel RA, Crowe T, Howard G, Cooper CJ, Brodie B, Grines CL, DeMaria AN. Effect of intensive compared with moderate lipid-lowering therapy on progression of coronary atherosclerosis: a randomized controlled trial. Jama 2004;291(9):1071-80.
42. Nissen SE, Nicholls SJ, Sipahi I, Libby P, Raichlen JS, Ballantyne CM, Davignon J, Erbel R, Fruchart JC, Tardif JC, Schoenhagen P, Crowe T, Cain V, Wolski K, Goormastic M, Tuzcu EM. Effect of very high-intensity statin therapy on regression of coronary atherosclerosis: the ASTEROID trial. Jama 2006;295(13):1556-65.
43. Nicholls SJ, Borgman M, Nissen SE, Raichlen JS, Ballantyne C, Barter P, Chapman MJ, Erbel R, Libby P. Impact of statins on progression of atherosclerosis: rationale and design of SATURN (Study of Coronary Atheroma by InTravascular Ultrasound: effect of Rosuvastatin versus AtorvastatiN). Curr Med Res Opin 2011;27(6):1119-29.
44. Rodriguez-Granillo GA, de Winter S, Bruining N, Ligthart JM, Garcia-Garcia HM, Valgimigli M, de Feyter PJ. Effect of perindopril on coronary remodelling: insights from a multicentre, randomized study. Eur Heart J 2007;28(19):2326-31.
45. Ge J, Liu F, Gorge G, Haude M, Baumgart D, Erbel R. Angiographically 'silent' plaque in the left main coronary artery detected by intravascular ultrasound. Coron Artery Dis 1995;6(10):805-10.
46. Ge J, Baumgart D, Haude M, Gorge G, von Birgelen C, Sack S, Erbel R. Role of intravascular ultrasound imaging in identifying vulnerable plaques. Herz 1999;24(1):32-41.
47. Rioufol G, Finet G, Ginon I, Andre-Fouet X, Rossi R, Vialle E, Desjoyaux E, Convert G, Huret JF, Tabib A. Multiple atherosclerotic plaque rupture in acute coronary syndrome: a three-vessel intravascular ultrasound study. Circulation 2002;106(7):804-8.
48. Yamagishi M, Terashima M, Awano K, Kijima M, Nakatani S, Daikoku S, Ito K, Yasumura Y, Miyatake K. Morphology of vulnerable coronary plaque: insights from follow-up of patients examined by intravascular ultrasound before an acute coronary syndrome. J Am Coll Cardiol 2000;35(1):106-11.
49. Fujii K, Kobayashi Y, Mintz GS, Takebayashi H, Dangas G, Moussa I, Mehran R, Lansky AJ, Kreps E, Collins M, Colombo A, Stone GW, Leon MB, Moses JW. Intravascular ultrasound assessment of ulcerated ruptured plaques: a comparison of culprit and nonculprit lesions of patients with acute coronary syndromes and lesions in patients without acute coronary syndromes. Circulation 2003;108(20):2473-8.
50. Nasu K, Tsuchikane E, Katoh O, Vince DG, Virmani R, Surmely JF, Murata A, Takeda Y, Ito T, Ehara M, Matsubara T, Terashima M, Suzuki T. Accuracy of in vivo coronary plaque mor-

phology assessment: a validation study of in vivo virtual histology compared with in vitro histopathology. J Am Coll Cardiol 2006;47(12):2405-12.
51. Nair A, Kuban BD, Tuzcu EM, Schoenhagen P, Nissen SE, Vince DG. Coronary plaque classification with intravascular ultrasound radiofrequency data analysis. Circulation 2002;106(17):2200-6.
52. Sathyanarayana S, Carlier S, Li W, Thomas L. Characterisation of atherosclerotic plaque by spectral similarity of radiofrequency intravascular ultrasound signals. EuroIntervention 2009;5(1):133-9.
53. Okubo M, Kawasaki M, Ishihara Y, Takeyama U, Kubota T, Yamaki T, Ojio S, Nishigaki K, Takemura G, Saio M, Takami T, Minatoguchi S, Fujiwara H. Development of integrated backscatter intravascular ultrasound for tissue characterization of coronary plaques. Ultrasound Med Biol 2008;34(4):655-63.
54. Rodriguez-Granillo GA, Garcia-Garcia HM, Mc Fadden EP, Valgimigli M, Aoki J, de Feyter P, Serruys PW. In vivo intravascular ultrasound-derived thin-cap fibroatheroma detection using ultrasound radiofrequency data analysis. J Am Coll Cardiol 2005;46(11):2038-42.
55. Granada JF, Wallace-Bradley D, Win HK, Alviar CL, Builes A, Lev EI, Barrios R, Schulz DG, Raizner AE, Kaluza GL. In vivo plaque characterization using intravascular ultrasound-virtual histology in a porcine model of complex coronary lesions. Arterioscler Thromb Vasc Biol 2007;27(2):387-93.
56. Nair A, Margolis MP, Kuban BD, Vince DG. Automated coronary plaque characterisation with intravascular ultrasound backscatter: ex vivo validation. EuroIntervention 2007;3(1):113-20.
57. Van Herck J, De Meyer G, Ennekens G, Van Herck P, Herman A, Vrints C. Validation of in vivo plaque characterisation by virtual histology in a rabbit model of atherosclerosis. EuroIntervention 2009;5(1):149-56.
58. Thim T, Hagensen MK, Wallace-Bradley D, Granada JF, Kaluza GL, Drouet L, Paaske WP, Botker HE, Falk E. Unreliable assessment of necrotic core by virtual histology intravascular ultrasound in porcine coronary artery disease. Circ Cardiovasc Imaging 2010;3(4):384-91.
59. Prasad A, Cipher DJ, Prasad A, Mohandas A, Roesle M, Brilakis ES, Banerjee S. Reproducibility of intravascular ultrasound virtual histology analysis. Cardiovasc Revasc Med 2008;9(2):71-7.
60. Serruys PW, Garcia-Garcia HM, Buszman P, Erne P, Verheye S, Aschermann M, Duckers H, Bleie O, Dudek D, Botker HE, von Birgelen C, D'Amico D, Hutchinson T, Zambanini A, Mastik F, van Es GA, van der Steen AF, Vince DG, Ganz P, Hamm CW, Wijns W, Zalewski A. Effects of the direct lipoprotein-associated phospholipase A(2) inhibitor darapladib on human coronary atherosclerotic plaque. Circulation 2008;118(11):1172-82.
61. Stone GW, Maehara A, Lansky AJ, de Bruyne B, Cristea E, Mintz GS, Mehran R, McPherson J, Farhat N, Marso SP, Parise H, Templin B, White R, Zhang Z, Serruys PW. A prospective natural-history study of coronary atherosclerosis. N Engl J Med 2011;364(3):226-35.
62. Kubo T, Maehara A, Mintz GS, Garcia-Garcia HM, Serruys PW, Suzuki T, Klauss V, Sumitsuji S, Lerman A, Marso SP, Margolis MP, Margolis JR, Foster MC, De Bruyne B, Leon MB, Stone GW. Analysis of the long-term effects of drug-eluting stents on coronary arterial wall morphology as assessed by virtual histology intravascular ultrasound. Am Heart J 2010;159(2):271-7.
63. Hong YJ, Jeong MH, Choi YH, Ko JS, Lee MG, Kang WY, Lee SE, Kim SH, Park KH, Sim DS, Yoon NS, Youn HJ, Kim KH, Park HW, Kim JH, Ahn Y, Cho JG, Park JC, Kang JC. Impact of plaque components on no-reflow phenomenon after stent deployment in patients with

acute coronary syndrome: a virtual histology-intravascular ultrasound analysis. Eur Heart J 2009.

64. Kawasaki M, Takatsu H, Noda T, Sano K, Ito Y, Hayakawa K, Tsuchiya K, Arai M, Nishigaki K, Takemura G, Minatoguchi S, Fujiwara T, Fujiwara H. In vivo quantitative tissue characterization of human coronary arterial plaques by use of integrated backscatter intravascular ultrasound and comparison with angioscopic findings. Circulation 2002;105(21):2487-92.
65. Tearney GJ RE, Akasaka T, Adriaenssens T, Barlis P, Bezerra HG, Bouma B, Bruining N, Cho J, Chowdhary S, Costa MA, de Silva R, Dijkstra J, DiMario C, Dudeck D, Falk E, Feldman MD, Fitzgerald P, Garcia H, Gonzalo N, Granada JF, Guagliumi G, Holm NR, Honda Y, Ikeno F, Kawasaki M, Kochman J, Koltowski L, Kubo T,Kume T, Kyono H, Lam CCS, Lamouche G, Lee DP, Leon M, Maehara A, Manfrini O, Mintz GS, Mizuno K, Morel MA, Nadkarni S, Okura H, Otake H, Pietrasik A, Prati F, Räber L, Radu MD, Rieber J, Riga M, Rollins A, Rosenberg M, Sirbu V, Serruys PW, Shimada K, Shinke T, Shite J, Siegel E, Sonada S, Suter M, Takarada S, Tanaka A, Terashima M, Uemura S, Ughi GJ, van Beusekom HMM, van der Steen AFW, van Es GA, van Soest G, Virmani R, Waxman S, Weissman NJ, Weisz G. Standards for Acquisition, Measurement, and Reporting of Intravascular OCT (IVOCT) Studies. A Consensus Report from The International Working Group for Intravascular OCT Standardization and Validation. J Am Coll Cardiol 2011; Accepted for publication.
66. Prati F, Regar E, Mintz GS, Arbustini E, Di Mario C, Jang IK, Akasaka T, Costa M, Guagliumi G, Grube E, Ozaki Y, Pinto F, Serruys PW, Expert's OCTRD. Expert review document on methodology, terminology, and clinical applications of optical coherence tomography: physical principles, methodology of image acquisition, and clinical application for assessment of coronary arteries and atherosclerosis. Eur Heart J 2010;31(4):401-15.
67. Tearney GJ, Jang IK, Kang DH, Aretz HT, Houser SL, Brady TJ, Schlendorf K, Shishkov M, Bouma BE. Porcine coronary imaging in vivo by optical coherence tomography. Acta Cardiol 2000;55(4):233-7.
68. Kume T, Akasaka T, Kawamoto T, Watanabe N, Toyota E, Neishi Y, Sukmawan R, Sadahira Y, Yoshida K. Assessment of coronary intima--media thickness by optical coherence tomography: comparison with intravascular ultrasound. Circ J 2005;69(8):903-7.
69. Yabushita H, Bouma BE, Houser SL, Aretz HT, Jang IK, Schlendorf KH, Kauffman CR, Shishkov M, Kang DH, Halpern EF, Tearney GJ. Characterization of human atherosclerosis by optical coherence tomography. Circulation 2002;106(13):1640-5.
70. Kume T, Akasaka T, Kawamoto T, Okura H, Watanabe N, Toyota E, Neishi Y, Sukmawan R, Sadahira Y, Yoshida K. Measurement of the thickness of the fibrous cap by optical coherence tomography. Am Heart J 2006;152(4):755 e1-4.
71. Jang IK, Bouma BE, Kang DH, Park SJ, Park SW, Seung KB, Choi KB, Shishkov M, Schlendorf K, Pomerantsev E, Houser SL, Aretz HT, Tearney GJ. Visualization of coronary atherosclerotic plaques in patients using optical coherence tomography: comparison with intravascular ultrasound. J Am Coll Cardiol 2002;39(4):604-9.
72. Yamaguchi T, Terashima M, Akasaka T, Hayashi T, Mizuno K, Muramatsu T, Nakamura M, Nakamura S, Saito S, Takano M, Takayama T, Yoshikawa J, Suzuki T. Safety and feasibility of an intravascular optical coherence tomography image wire system in the clinical setting. Am J Cardiol 2008;101(5):562-7.
73. Cilingiroglu M, Oh JH, Sugunan B, Kemp NJ, Kim J, Lee S, Zaatari HN, Escobedo D, Thomsen S, Milner TE, Feldman MD. Detection of vulnerable plaque in a murine model of atherosclerosis with optical coherence tomography. Catheter Cardiovasc Interv 2006;67(6):915-23.

74. Kume T, Akasaka T, Kawamoto T, Ogasawara Y, Watanabe N, Toyota E, Neishi Y, Sukmawan R, Sadahira Y, Yoshida K. Assessment of coronary arterial thrombus by optical coherence tomography. Am J Cardiol 2006;97(12):1713-7.
75. Tearney GJ, Yabushita H, Houser SL, Aretz HT, Jang IK, Schlendorf KH, Kauffman CR, Shishkov M, Halpern EF, Bouma BE. Quantification of macrophage content in atherosclerotic plaques by optical coherence tomography. Circulation 2003;107(1):113-9.
76. Regar E, van Beusekom HM, van der Giessen WJ, Serruys PW. Images in cardiovascular medicine. Optical coherence tomography findings at 5-year follow-up after coronary stent implantation. Circulation 2005;112(23):e345-6.
77. Kume T, Okura H, Yamada R, Kawamoto T, Watanabe N, Neishi Y, Sadahira Y, Akasaka T, Yoshida K. Frequency and spatial distribution of thin-cap fibroatheroma assessed by 3-vessel intravascular ultrasound and optical coherence tomography: an ex vivo validation and an initial in vivo feasibility study. Circ J 2009;73(6):1086-91.
78. Barlis P, van Soest G, Serruys PW, Regar E. Intracoronary optical coherence tomography and the evaluation of stents. Expert Rev Med Devices 2009;6(2):157-67.
79. Barlis P, Serruys PW, Gonzalo N, van der Giessen WJ, de Jaegere PJ, Regar E. Assessment of culprit and remote coronary narrowings using optical coherence tomography with long-term outcomes. Am J Cardiol 2008;102(4):391-5.
80. Barlis P, Regar E, Serruys PW, Dimopoulos K, van der Giessen WJ, van Geuns RJ, Ferrante G, Wandel S, Windecker S, van Es GA, Eerdmans P, Juni P, di Mario C. An optical coherence tomography study of a biodegradable vs. durable polymer-coated limus-eluting stent: a LEADERS trial sub-study. Eur Heart J 2010;31(2):165-76.
81. Serruys PW, Ormiston JA, Onuma Y, Regar E, Gonzalo N, Garcia-Garcia HM, Nieman K, Bruining N, Dorange C, Miquel-Hebert K, Veldhof S, Webster M, Thuesen L, Dudek D. A bioabsorbable everolimus-eluting coronary stent system (ABSORB): 2-year outcomes and results from multiple imaging methods. Lancet 2009;373(9667):897-910.
82. Gonzalo N, Tearney GJ, van Soest G, Serruys P, Garcia-Garcia HM, Bouma BE, Regar E. Witnessed coronary plaque rupture during cardiac catheterization. JACC Cardiovasc Imaging 2011;4(4):437-8.
83. Gonzalo N, Tearney GJ, Serruys PW, van Soest G, Okamura T, Garcia-Garcia HM, Jan van Geuns R, van der Ent M, Ligthart J, Bouma BE, Regar E. Second-generation optical coherence tomography in clinical practice. High-speed data acquisition is highly reproducible in patients undergoing percutaneous coronary intervention. Rev Esp Cardiol 2010;63(8):893-903.
84. Gonzalo N, Serruys PW, Okamura T, Shen ZJ, Onuma Y, Garcia-Garcia HM, Sarno G, Schultz C, van Geuns RJ, Ligthart J, Regar E. Optical coherence tomography assessment of the acute effects of stent implantation on the vessel wall: a systematic quantitative approach. Heart 2009;95(23):1913-9.
85. Gutierrez-Chico JL, Serruys PW, Girasis C, Garg S, Onuma Y, Brugaletta S, Garcia-Garcia H, van Es GA, Regar E. Quantitative multi-modality imaging analysis of a fully bioresorbable stent: a head-to-head comparison between QCA, IVUS and OCT. Int J Cardiovasc Imaging 2011.
86. Gutierrez-Chico JL, Regar E, Nuesch E, Okamura T, Wykrzykowska J, di Mario C, Windecker S, van Es GA, Gobbens P, Juni P, Serruys PW. Delayed coverage in malapposed and side-branch struts with respect to well-apposed struts in drug-eluting stents: in vivo assessment with optical coherence tomography. Circulation 2011;124(5):612-23.

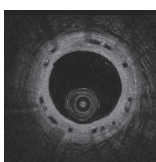

87. Gutierrez-Chico JL, van Geuns RJ, Regar E, van der Giessen WJ, Kelbaek H, Saunamaki K, Escaned J, Gonzalo N, di Mario C, Borgia F, Nuesch E, Garcia-Garcia HM, Silber S, Windecker S, Serruys PW. Tissue coverage of a hydrophilic polymer-coated zotarolimus-eluting stent vs. a fluoropolymer-coated everolimus-eluting stent at 13-month follow-up: an optical coherence tomography substudy from the RESOLUTE All Comers trial. Eur Heart J 2011;32(19):2454-63.
88. Gutierrez-Chico JL, Juni P, Garcia-Garcia HM, Regar E, Nuesch E, Borgia F, van der Giessen WJ, Davies S, van Geuns RJ, Secco GG, Meis S, Windecker S, Serruys PW, di Mario C. Long-term tissue coverage of a biodegradable polylactide polymer-coated biolimus-eluting stent: comparative sequential assessment with optical coherence tomography until complete resorption of the polymer. Am Heart J 2011;162(5):922-31.
89. Gonzalo N, Serruys PW, Okamura T, Shen ZJ, Garcia-Garcia HM, Onuma Y, van Geuns RJ, Ligthart J, Regar E. Relation between plaque type and dissections at the edges after stent implantation: an optical coherence tomography study. Int J Cardiol 2011;150(2):151-5.
90. Okamura T, Gonzalo N, Gutierrez-Chico JL, Serruys PW, Bruining N, de Winter S, Dijkstra J, Commossaris KH, van Geuns RJ, van Soest G, Ligthart J, Regar E. Reproducibility of coronary Fourier domain optical coherence tomography: quantitative analysis of in vivo stented coronary arteries using three different software packages. EuroIntervention 2010;6(3):371-9.
91. Schinkel AF, Barlis P, van Beusekom HM, Serruys PW, Regar E. Images in intervention. Optical coherence tomography findings in very late (4 years) paclitaxel-eluting stent thrombosis. JACC Cardiovasc Interv 2008;1(4):449-51.
92. Regar E vLA, Serruys PW *Optical coherence tomography in cardiovascular research*: London: Informa Healthcare; 2007.
93. Regar E, van Soest G, Bruining N, Constantinescu AA, van Geuns RJ, van der Giessen W, Serruys PW. Optical coherence tomography in patients with acute coronary syndrome. EuroIntervention 2010;6 Suppl G:G154-60.
94. Jang IK, Tearney GJ, MacNeill B, Takano M, Moselewski F, Iftima N, Shishkov M, Houser S, Aretz HT, Halpern EF, Bouma BE. In vivo characterization of coronary atherosclerotic plaque by use of optical coherence tomography. Circulation 2005;111(12):1551-5.
95. Kubo T IT, Kitabata H, Kuroi A, Ueno S, Yamano T, Tanimoto T, Matsuo Y, Masho T, Takarada S, Tanaka A, Nakamura N, Mizukoshi M, Tomobuchi Y, Akasaka T. Comparison of vascular response after sirolimus eluting stent implantation between patients with unstable and stable angina pectoris. A serial optical coherence tomography study. J Am Coll Cardiol Imaging 2008;1(4):475-484.
96. Kubo T, Imanishi T, Takarada S, Kuroi A, Ueno S, Yamano T, Tanimoto T, Matsuo Y, Masho T, Kitabata H, Tsuda K, Tomobuchi Y, Akasaka T. Assessment of culprit lesion morphology in acute myocardial infarction: ability of optical coherence tomography compared with intravascular ultrasound and coronary angioscopy. J Am Coll Cardiol 2007;50(10):933-9.
97. Fujii K, Kawasaki D, Masutani M, Okumura T, Akagami T, Sakoda T, Tsujino T, Ohyanagi M, Masuyama T. OCT assessment of thin-cap fibroatheroma distribution in native coronary arteries. JACC Cardiovasc Imaging 2010;3(2):168-75.
98. Takarada S, Imanishi T, Kubo T, Tanimoto T, Kitabata H, Nakamura N, Tanaka A, Mizukoshi M, Akasaka T. Effect of statin therapy on coronary fibrous-cap thickness in patients with acute coronary syndrome: assessment by optical coherence tomography study. Atherosclerosis 2009;202(2):491-7.

99. Regar E, Ligthart J, Bruining N, van Soest G. The diagnostic value of intracoronary optical coherence tomography. Herz 2011;36(5):417-29.
100. Manfrini O, Mont E, Leone O, Arbustini E, Eusebi V, Virmani R, Bugiardini R. Sources of error and interpretation of plaque morphology by optical coherence tomography. Am J Cardiol 2006;98(2):156-9.
101. Goderie TP, van Soest G, Garcia-Garcia HM, Gonzalo N, Koljenovic S, van Leenders GJ, Mastik F, Regar E, Oosterhuis JW, Serruys PW, van der Steen AF. Combined optical coherence tomography and intravascular ultrasound radio frequency data analysis for plaque characterization. Classification accuracy of human coronary plaques in vitro. Int J Cardiovasc Imaging 2010;26(8):843-50.
102. van Soest G, Regar E, Goderie TP, Gonzalo N, Koljenovic S, van Leenders GJ, Serruys PW, van der Steen AF. Pitfalls in plaque characterization by OCT: image artifacts in native coronary arteries. JACC Cardiovasc Imaging 2011;4(7):810-3.
103. Gardner CM, Tan H, Hull EL, Lisauskas JB, Sum ST, Meese TM, Jiang C, Madden SP, Caplan JD, Burke AP, Virmani R, Goldstein J, Muller JE. Detection of lipid core coronary plaques in autopsy specimens with a novel catheter-based near-infrared spectroscopy system. JACC Cardiovasc Imaging 2008;1(5):638-48.
104. Waxman S, Dixon SR, L'Allier P, Moses JW, Petersen JL, Cutlip D, Tardif JC, Nesto RW, Muller JE, Hendricks MJ, Sum ST, Gardner CM, Goldstein JA, Stone GW, Krucoff MW. In vivo validation of a catheter-based near-infrared spectroscopy system for detection of lipid core coronary plaques: initial results of the SPECTACL study. JACC Cardiovasc Imaging 2009;2(7):858-68.
105. Garcia BA, Wood F, Cipher D, Banerjee S, Brilakis ES. Reproducibility of near-infrared spectroscopy for the detection of lipid core coronary plaques and observed changes after coronary stent implantation. Catheter Cardiovasc Interv 2010;76(3):359-65.
106. Brugaletta S, Garcia-Garcia HM, Serruys PW, de Boer S, Ligthart J, Gomez-Lara J, Witberg K, Diletti R, Wykrzykowska J, van Geuns RJ, Schultz C, Regar E, Duckers HJ, van Mieghem N, de Jaegere P, Madden SP, Muller JE, van der Steen AF, van der Giessen WJ, Boersma E. NIRS and IVUS for characterization of atherosclerosis in patients undergoing coronary angiography. JACC Cardiovasc Imaging 2011;4(6):647-55.
107. Regar E. Invasive imaging technologies: can we reconcile light and sound? J Cardiovasc Med (Hagerstown) 2011;12(8):562-70.
108. Schultz CJ, Serruys PW, van der Ent M, Ligthart J, Mastik F, Garg S, Muller JE, Wilder MA, van de Steen AF, Regar E. First-in-man clinical use of combined near-infrared spectroscopy and intravascular ultrasound: a potential key to predict distal embolization and no-reflow? J Am Coll Cardiol 2010;56(4):314.
109. Wentzel JJ, van der Giessen AG, Garg S, Schultz C, Mastik F, Gijsen FJ, Serruys PW, van der Steen AF, Regar E. In vivo 3D distribution of lipid-core plaque in human coronary artery as assessed by fusion of near infrared spectroscopy-intravascular ultrasound and multislice computed tomography scan. Circ Cardiovasc Imaging 2010;3(6):e6-7.
110. Joner M, Finn AV, Farb A, Mont EK, Kolodgie FD, Ladich E, Kutys R, Skorija K, Gold HK, Virmani R. Pathology of drug-eluting stents in humans: delayed healing and late thrombotic risk. J Am Coll Cardiol 2006;48(1):193-202.
111. Garg S, Serruys PW, van der Ent M, Schultz C, Mastik F, van Soest G, van der Steen AF, Wilder MA, Muller JE, Regar E. First use in patients of a combined near infra-red spec-

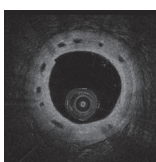

troscopy and intra-vascular ultrasound catheter to identify composition and structure of coronary plaque. EuroIntervention 2010;5(6):755-6.
112. Schuurbiers JC, Slager CJ, Serruys PW. Luminal volume reconstruction from angioscopic video images of casts from human coronary arteries. Am J Cardiol 1994;74(8):764-8.
113. Thieme T, Wernecke KD, Meyer R, Brandenstein E, Habedank D, Hinz A, Felix SB, Baumann G, Kleber FX. Angioscopic evaluation of atherosclerotic plaques: validation by histomorphologic analysis and association with stable and unstable coronary syndromes. J Am Coll Cardiol 1996;28(1):1-6.
114. Uchida Y, Uchida Y, Hiruta N. Histological characteristics of glistening yellow coronary plaques seen on angioscopy. -With special reference to vulnerable plaques. Circ J;75(8):1913-9.
115. Takano M, Mizuno K, Yokoyama S, Seimiya K, Ishibashi F, Okamatsu K, Uemura R. Changes in coronary plaque color and morphology by lipid-lowering therapy with atorvastatin: serial evaluation by coronary angioscopy. J Am Coll Cardiol 2003;42(4):680-6.
116. Yokoyama S, Takano M, Yamamoto M, Inami S, Sakai S, Okamatsu K, Okuni S, Seimiya K, Murakami D, Ohba T, Uemura R, Seino Y, Hata N, Mizuno K. Extended follow-up by serial angioscopic observation for bare-metal stents in native coronary arteries: from healing response to atherosclerotic transformation of neointima. Circ Cardiovasc Interv 2009;2(3):205-12.
117. Yamamoto M, Okamatsu K, Inami S, Takano M, Yokoyama S, Ohba T, Ibuki C, Hata N, Seino Y, Mizuno K. Relationship between neointimal coverage of sirolimus-eluting stents and lesion characteristics: a study with serial coronary angioscopy. Am Heart J 2009;158(1):99-104.
118. Mizuno K, Miyamoto A, Satomura K, Kurita A, Arai T, Sakurada M, Yanagida S, Nakamura H. Angioscopic coronary macromorphology in patients with acute coronary disorders. Lancet 1991;337(8745):809-12.
119. Kubo T, Imanishi T, Takarada S, Kuroi A, Ueno S, Yamano T, Tanimoto T, Matsuo Y, Masho T, Kitabata H, Tanaka A, Nakamura N, Mizukoshi M, Tomobuchi Y, Akasaka T. Implication of plaque color classification for assessing plaque vulnerability: a coronary angioscopy and optical coherence tomography investigation. JACC Cardiovasc Interv 2008;1(1):74-80.
120. Uchida Y, Nakamura F, Tomaru T, Morita T, Oshima T, Sasaki T, Morizuki S, Hirose J. Prediction of acute coronary syndromes by percutaneous coronary angioscopy in patients with stable angina. Am Heart J 1995;130(2):195-203.
121. Ueda Y, Ohtani T, Shimizu M, Hirayama A, Kodama K. Assessment of plaque vulnerability by angioscopic classification of plaque color. Am Heart J 2004;148(2):333-5.
122. Uchida Y, Uchida Y, Hiruta N. Histological characteristics of glistening yellow coronary plaques seen on angioscopy. -With special reference to vulnerable plaques. Circ J 2011;75(8):1913-9.
123. Granada JF, Kaluza GL, Wilensky RL, Biedermann BC, Schwartz RS, Falk E. Porcine models of coronary atherosclerosis and vulnerable plaque for imaging and interventional research. EuroIntervention 2009;5(1):140-8.
124. van den Heuvel M, Sorop O, Batenburg WW, Bakker CL, de Vries R, Koopmans SJ, van Beusekom HM, Duncker DJ, Danser AH, van der Giessen WJ. Specific coronary drug-eluting stents interfere with distal microvascular function after single stent implantation in pigs. JACC Cardiovasc Interv 2010;3(7):723-30.

125. Thim T. Human-like atherosclerosis in minipigs: a new model for detection and treatment of vulnerable plaques. Dan Med Bull 2010;57(7):B4161.
126. Thim T, Hagensen MK, Drouet L, Bal Dit Sollier C, Bonneau M, Granada JF, Nielsen LB, Paaske WP, Botker HE, Falk E. Familial hypercholesterolaemic downsized pig with human-like coronary atherosclerosis: a model for preclinical studies. EuroIntervention 2010;6(2):261-8.
127. van Ditzhuijzen NS, van den Heuvel M, Sorop O, van Duin RW, Krabbendam-Peters I, van Haeren R, Ligthart JM, Witberg KT, Duncker DJ, Regar E, van Beusekom HM, van der Giessen WJ. Invasive coronary imaging in animal models of atherosclerosis. Neth Heart J 2011;19(10):442-6.
128. Gerrity RG, Natarajan R, Nadler JL, Kimsey T. Diabetes-induced accelerated atherosclerosis in swine. Diabetes 2001;50(7):1654-65.
129. van Soest G, Goderie T, Regar E, Koljenovic S, van Leenders GL, Gonzalo N, van Noorden S, Okamura T, Bouma BE, Tearney GJ, Oosterhuis JW, Serruys PW, van der Steen AF. Atherosclerotic tissue characterization in vivo by optical coherence tomography attenuation imaging. J Biomed Opt 2010;15(1):011105.
130. Nadkarni SK, Pierce MC, Park BH, de Boer JF, Whittaker P, Bouma BE, Bressner JE, Halpern E, Houser SL, Tearney GJ. Measurement of collagen and smooth muscle cell content in atherosclerotic plaques using polarization-sensitive optical coherence tomography. J Am Coll Cardiol 2007;49(13):1474-81.
131. Giattina SD, Courtney BK, Herz PR, Harman M, Shortkroff S, Stamper DL, Liu B, Fujimoto JG, Brezinski ME. Assessment of coronary plaque collagen with polarization sensitive optical coherence tomography (PS-OCT). Int J Cardiol 2006;107(3):400-9.
132. Yoo H, Kim JW, Shishkov M, Namati E, Morse T, Shubochkin R, McCarthy JR, Ntziachristos V, Bouma BE, Jaffer FA, Tearney GJ. Intra-arterial catheter for simultaneous microstructural and molecular imaging in vivo. Nat Med 2011;17(12):1680-4.
133. Cai X, Kim C, Pramanik M, Wang LV. Photoacoustic tomography of foreign bodies in soft biological tissue. J Biomed Opt 2011;16(4):046017.
134. Kumavor PD, Xu C, Aguirre A, Gamelin J, Ardeshirpour Y, Tavakoli B, Zanganeh S, Alqasemi U, Yang Y, Zhu Q. Target detection and quantification using a hybrid hand-held diffuse optical tomography and photoacoustic tomography system. J Biomed Opt 2011;16(4):046010.

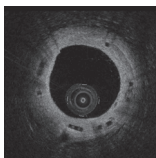

Safety of optical coherence tomography in daily practice: a comparison with intravascular ultrasound

JN van der Sijde, A Karanasos, NS van Ditzhuijzen, T Okamura, RJ van Geuns, M Valgimigli, JM Ligthart, KT Witberg, S Wemelsfelder, JM Fam, B Zhang, R Diletti, PP de Jaegere, NM van Mieghem, G van Soest, F Zijlstra, RT van Domburg, E Regar

Eur Heart J Cardiovasc Imaging. 2016 Mar 18

3

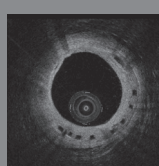

Abstract

Introduction Previous studies have reported the safety and feasibility of both time-domain optical coherence tomography (TD-OCT) and Fourier-domain OCT (FD-OCT) in highly selected patients and clinical settings. However, the generalizability of these data is limited, and data in unselected patient populations reflecting a routine cathlab practice are lacking. We compared the safety of intracoronary FD-OCT imaging to intravascular ultrasound (IVUS) imaging in a large real-world series of consecutive patients who underwent invasive imaging during coronary catheterization in our center.

Methods This is a prospective, single-center registry of patients scheduled for coronary angiography or intervention undergoing intracoronary imaging with FD-OCT or IVUS between April 2008 and December 2013. Intra-procedural and major in- hospital adverse events that could be possibly related to invasive imaging were registered routinely by the operator as part of our clinical report and prospectively recorded in our database. These events were retrospectively individually adjudicated by an independent safety committee.

Results Between April 2008 and December 2013, 13 418 diagnostic or interventional coronary catheterization procedures were performed. Of these, 1142 procedures used OCT and 2476 procedures used IVUS. Invasive imaging-related complications were rare, did not differ between the two imaging methods (OCT: n =7, 0.6%; IVUS: n =12, 0.5%; P =0.6), and were self-limiting after retrieval of the imaging catheter or easily treatable in the catheterization laboratory. No major adverse events, prolongation of hospital stay, or permanent patient harm was observed.

Conclusion FD-OCT is safe in an unselected and heterogeneous group of patients with varying clinical settings.

Introduction

Intracoronary optical coherence tomography (OCT) is increasingly used in the catheterization laboratory. Various clinical applications have been proposed, including assessment of plaque morphology in angiographic ambiguous lesions, guidance of stent placement during percutaneous coronary interventions (PCI) and follow-up stent assessment.[1, 2] In the early days of the first generation, time domain OCT (TD-OCT), intracoronary application was hampered by the need for proximal balloon occlusion to limit antegrade blood flow in combination with distal delivery of a translucent flush solution in order to create a blood-free environment during OCT data acquisition.[3] The currently commercially available and widespread used second-generation intracoronary Fourier domain OCT (FD-OCT) was developed to overcome these limitations, allowing for a simplification of the image acquisition procedure. Importantly, the imaging device was redesigned to a monorail OCT imaging catheter that could be introduced into the coronary artery over any PCI guide wire of choice, which substantially facilitated instrumentation. Further, the data acquisition speed was massively increased by using frequency domain ranging techniques that are capable of acquiring images at high speed (up to 180 frames/sec) and with fast pullback (up to 40mm/sec), alleviating the need for proximal balloon occlusion during imaging and the risk of creating ischemia during imaging.[4] Previous smaller studies [5-10] have reported the safety and feasibility of both TD-OCT and FD-OCT in highly selected patients and clinical settings. However, the generalizability of these data is limited and data in unselected patient populations reflecting a routine cathlab practice are lacking.

We report thesafety of intracoronary FD-OCT imaging in a large real world series of consecutive patients who underwent OCT imaging during coronary catheterization in our centre since the introduction of FD-OCT imaging in 2008 and compare the results to our intravascular ultrasound (IVUS) safety data from the same time period.

Methods

Study population

This is a single-centre study, prospectively evaluating the safety of FD-OCT. Consecutive patients who underwent FD-OCT examination during cardiac catheterization between April 2008 and December 2013 were included. These data were then compared with the cohort of patients who underwent IVUS within the same time period. All consecutive patients who underwent intracoronary OCT or IVUS during the study

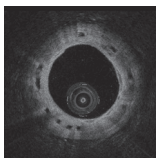

period were included. Additionally, to assess generalizability of our data, the indications for catheterization and patient baseline characteristics were also compared with the cohort that, at the discretion of the operators, did not undergo any form of invasive imaging during the same time period. Both OCT and IVUS were performed either as part of various clinical trial protocols or at the discretion of the operators. In the latter case, the exclusion criteria were acute, life-threatening hemodynamic instability and coronary anatomy not deemed suited for introduction of an imaging catheter, such as extensive tortuosity or calcification or a lumen diameter >5mm, beyond the penetration depth of OCT and lesions considered too tight to allow crossing of a device of ~3F. In acute settings, restoration of antegrade flow always was the main priority and had to be secured before introduction of an imaging catheter.

Invasive imaging procedure

Invasive imaging was performed via radial or femoral access according to routine clinical standard in our center using 6F (range 5-7F) guide catheters. Patients received weight-adjusted intravenous heparin in order to maintain the activated clotting time >300 seconds and intracoronary administration of 0.2mg nitroglycerine, as standard prior to invasive imaging. Imaging catheters were advanced distally to a region of interest over 0.014-inch conventional angioplasty guide wires, chosen at the discretion of the operators. All the imaging systems have dedicated pullback devices and consoles that allow data processing and storage.

IVUS image acquisition

IVUS images were acquired with different systems (Galaxy I, Galaxy II and iLab: Boston Scientific, Marlborough, MA, USA; In-Vision Gold and S5 imaging system: Volcano Corporation, San Diego, CA, USA). Different types of catheters (range 20-45MHz, 3.2-3.5F) were used with a default motorized pullback speed of 0.5 mm/sec.

OCT image acquisition

OCT imaging was performed with commercially available FD-OCT systems (Lightlab C7XR, Ilumien and Ilumien Optis: St Jude Medical, St Paul, MN, USA; Terumo Lunawave: Terumo, Tokyo, Japan) and in a limited number of patients with several different OCT prototypes (Lightlab M4: St Jude Medical, St Paul, MN, USA; MGH OCT system: The Wellman Center for Photomedicine, Boston, MA, USA; Volcano OCT system: Volcano Corporation, San Diego, CA, USA).

OCT imaging probes had a short monorail design with a fibre-optic imaging core integrated in a catheter. The catheter profile ranged from 2.4 to 2.7F. During OCT image acquisition the optic imaging core rotated at a rate of 100–180 revolutions per second. OCT pullbacks were performed automated at the pullback speed of generally 20mm/sec (range 10-40mm/sec) during simultaneous flushing of viscous iso-osmolar contrast (Iodixanol 320, Visipaque™, GE Health Care, Cork, Ireland at 37˚C) through the guiding catheter by use of an automated power injector (Medrad Inc., Warrendale, PA, USA) with a flow rate of 3ml/sec as standard setting, or in selected cases by manual injection.

Safety assessment

Both major in-hospital and intra-procedural adverse events were recorded and considered as potential imaging-related complications. Major in-hospital adverse events were defined as cerebrovascular event, emergency revascularization, and death. Intra-procedural events were defined as the occurrence of clinical symptoms (new or worsened chest pain or shortness of breath), adverse angiographic outcomes (dissection, perforation, vasospasm, thrombus formation, and no-reflow), or electrocardiographic changes (ST-segment elevation, severe bradycardia, and ventricular arrhythmias) requiring interruption of the imaging procedure during intracoronary imaging and were routinely registered by the operator as a standard item being part of our clinical PCI report and collected in our PCI database. In addition, all free text comments in the PCI database/reporting system were screened for 'OCT' or 'IVUS'. Comments containing these keywords were individually reviewed for any possible association with an adverse event. Major peri-procedural adverse events were also recorded and defined as cerebrovascular event, emergency revascularization, and death.

Adjudication

Complications were individually adjudicated by an independent safety committee by thorough review of the patient files, procedural notes, angiogram, and intracoronary images. A complication was considered related to the imaging procedure if it would not have occurred if the invasive imaging would not have been performed. 'Definitely related' was used for complications that were with great certainty caused by the invasive imaging. If the relation between invasive imaging procedure and registered event was less clear, but could not be completely ruled out, the event was defined as 'possibly related'. Possible and definite invasive imaging-related events were categorized as self-limiting after withdrawal of the imaging catheter, requiring action or major adverse events. The safety committee consisted of two teams that reviewed

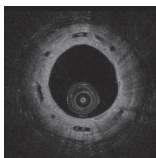

the events independently. In case of disagreement, the case was re- evaluated and discussed between both teams until consensus was reached. Each team consisted of a senior invasive cardiologist not directly involved in clinical or research coronary imaging projects and an invasive imaging expert (R.J.G. and J.M.R.L.; M.V. and K.T.W.).

Statistical analysis

Continuous data were expressed as mean values ± SD. An independent-samples *t*-test was used to analyze continuous data between two groups and ANOVA for more than two groups. Significance of associations of categorical variables were assessed using the chi-square test or Fisher's exact test, as appropriate. Univariate analyses to identify predictors of an adverse event during image acquisition were performed using a logistic regression model. A *P*-value of <0.05 was considered significant.

Results

Patient population

Between April 2008 and December 2013, 13418 diagnostic or interventional coronary catheterization procedures were performed in our center. During 1142 procedures (984 patients with 3045 pullbacks) FD-OCT was used, and during 2476 procedures (2054 patients with 5148 pullbacks) IVUS was used. A combination of OCT and IVUS images were acquired during 307 procedures. Invasive imaging was performed by 13 different senior operators, of whom 11 had >5 years of experience and the other two between 1 and 5 years of experience as senior operator in the catheterization laboratory. Baseline demographic characteristics of all patients who underwent OCT or IVUS are displayed in **Table 1**. Invasive imaging was used in a variety of clinical settings. Patients undergoing OCT had less renal failure (5.3 vs. 9.1%, *P*< 0.001) when compared with IVUS. OCT imaging was performed more often in patients with ST-elevation myocardial infarction (24.7 vs. 14.5%, *P* <0.001). Procedural characteristics are given in **Table 2**. The mean number of pullbacks per procedure was significantly higher in the OCT group compared with IVUS (2.66 vs. 2.07, *P* <0.001), which might be explained in part by the shorter artery segment, which can be visualized in one pullback (typically 50 mm OCT vs. 100 mm IVUS). Imaged vessels and lesion types were roughly equal. Clearing of the coronary from blood during OCT imaging was performed with a contrast flush rate of 3 mL/s in 78% and 4 mL/s in 21% of the pullbacks.

Table 1 Characteristics of all consecutive patients undergoing invasive imaging in our center between 2008-2013

	OCT*	IVUS*	P-value
N	1142	2476	
Age, years	61.9±11.1	62.6±11.2	0.112
Male	853 (74.7)	1852 (74.8)	0.967
Risk factors			
Hypertension	589 (53.9)	1465 (62.0)	<0.001
Diabetes	206 (18.1)	500 (20.5)	0.105
Dyslipidemia	600 (55.3)	1413 (60.4)	0.006
Current smokers	299 (26.3)	576 (23.5)	0.073
Family history	471 (44.0)	1025 (44.2)	0.911
History			
Prior myocardial infarction	344 (30.1)	776 (31.3)	0.462
Prior CABG	50 (4.4)	136 (5.5)	0.169
Prior PCI	529 (46.3)	1058 (42.7)	0.047
Renal Failure	60 (5.3)	224 (9.1)	<0.001
Indications for catheterization			
Stable angina	433 (37.9)	1114 (45.0)	<0.001
Unstable angina	180 (15.7)	466 (18.8)	0.028
Non-STEMI	97 (8.5)	233 (9.4)	0.385
STEMI	282 (24.7)	360 (14.5)	<0.001
Other	150 (13.1)	303 (12.2)	0.45

**A combination of OCT and IVUS images were acquired during 307 procedures. Age: mean ± standard deviation, other values: n (%).*

Generalizability of invasive imaging cohorts

Table 3 shows the comparison between baseline characteristics of the OCT and IVUS cohorts and the population that did not undergo invasive imaging within the same time window. The most pronounced differences were the higher incidence of renal failure (12.7 vs 5.3 vs 9.1%, p<0.001) in the non-imaging group, the lower incidence of patient with a prior PCI (26.9 vs. 46.4 vs. 42.7%), and the larger number of type C lesions (35.9 vs 25.2 vs 24.1%, p<0.001) when compared with OCT and IVUS, respectively. **Figure 1** illustrates three examples of clinical settings that are typically considered difficult for

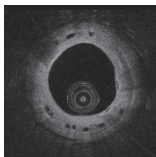

Table 2 Invasive imaging procedure details

Procedures	OCT	IVUS	P-value
N	1142	2476	
Mean number of pullbacks	2.66±1.54	2.07±1.32	<0.001
Mean number of imaged vessels	1.18±0.42	1.28±0.51	<0.001
Total pullbacks, n	3,042	5135	
Pullback distribution among vessels			
LAD	1484 (48.8)	2459 (47.9)	0.436
LCX	577 (19.0)	1136 (22.1)	0.001
RCA	846 (27.8)	1266 (24.7)	0.002
Other	135 (4.4)	274 (5.3)	0.074
Lesion type, n	946	1927	
A	115 (12.2)	214 (11.1)	0.418
B1	235 (24.8)	519 (26.9)	0.241
B2	358 (37.8)	729 (37.8)	1.000
C	238 (25.2)	465 (24.1)	0.549

Values in n (%) or mean (± standard deviation)

invasive imaging acquisition. OCT images were successfully acquired in all of these cases without complications.

Safety assessment

After adjudication, 7 (0.6%) complications that occurred during image acquisition were possibly or definitely related to OCT and twelve (0.5%) to IVUS imaging (P=0.6) (**Figure 2**). **Table 4** further specifies the complications as adjudicated. Transient ST-elevation requiring withdrawal of the imaging catheter was seen in 0.26 vs 0.08% (P=0.2), hypotension during image acquisition in 0.18 vs 0.04% (P=0.2), coronary spasm requiring infusion of additional intracoronary nitroglycerin in 0.09 vs 0.04% (P=0.6), thrombus formation in 0.09 vs 0.16% (P=0.6), dissection of the imaged vessel in 0.00 vs 0.12% (P=0.2), and stent deformation in 0.00 vs 0.04% (P=0.5) during OCT and IVUS imaging, respectively. The event rate per pullback was the same for both modalities (0.23%). **Figure 3** shows an example of a typical angiographic and OCT image of coronary spasm occurring during image acquisition. A more detailed description of the complications that were encountered can be found in the **Supplementary Material (Appendix A)**

Table 3 Comparison between invasive imaging cohorts and non-imaging population

	OCT	IVUS	Non-imaging	P-value
N	1142	2476	10107	
Age, years	61.9±11.1	62.6±11.2	63.7±12.8	<0.001
Male	853 (74.7)	1852 (74.8)	6992 (69.2)	<0.001
Risk factors				
Hypertension	589 (53.9)	1465 (62.0)	5037 (54.6)	<0.001
Diabetes	206 (18.1)	500 (20.5)	1981 (20.3)	0.210
Dyslipidemia	600 (55.3)	1413 (60.4)	4347 (48.0)	<0.001
Current smokers	299 (26.3)	576 (23.5)	2345 (24.1)	0.180
Family history	471 (44.0)	1025 (44.2)	3248 (36.6)	<0.001
History				
Prior myocardial infarction	344 (30.1)	776 (31.3)	2324 (23.4)	<0.001
Prior CABG	50 (4.4)	136 (5.5)	1002 (10.1)	<0.001
Prior PCI	529 (46.3)	1058 (42.7)	2682 (26.9)	<0.001
Renal Failure	60 (5.3)	224 (9.1)	1260 (12.7)	<0.001
Indications for catheterization				
Stable angina	433 (37.9)	1114 (45.0)	2768 (27.4)	<0.001
Unstable angina	180 (15.7)	466 (18.8)	1552 (15.4)	<0.001
Non-STEMI	97 (8.5)	233 (9.4)	1271 (12.6)	<0.001
STEMI	282 (24.7)	360 (14.5)	2787 (27.6)	<0.001
Other	150 (13.1)	303 (12.2)	1729 (17.1)	<0.001
Lesion type, n	946	1,927	7,263	
A	115 (12.2)	214 (11.1)	571 (7.9)	<0.001
B1	235 (24.8)	519 (26.9)	1690 (23.3)	0.003
B2	358 (37.8)	729 (37.8)	2398 (33.0)	<0.001
C	238 (25.2)	465 (24.1)	2604 (35.9)	<0.001

Risk factors for adverse event

All baseline characteristics and indications for catheterization were tested in univariate analyses for the risk of invasive imaging events (**Supplementary Table 1; Appendix B**). The use of both modalities, the total number of pullbacks and the total number

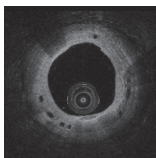

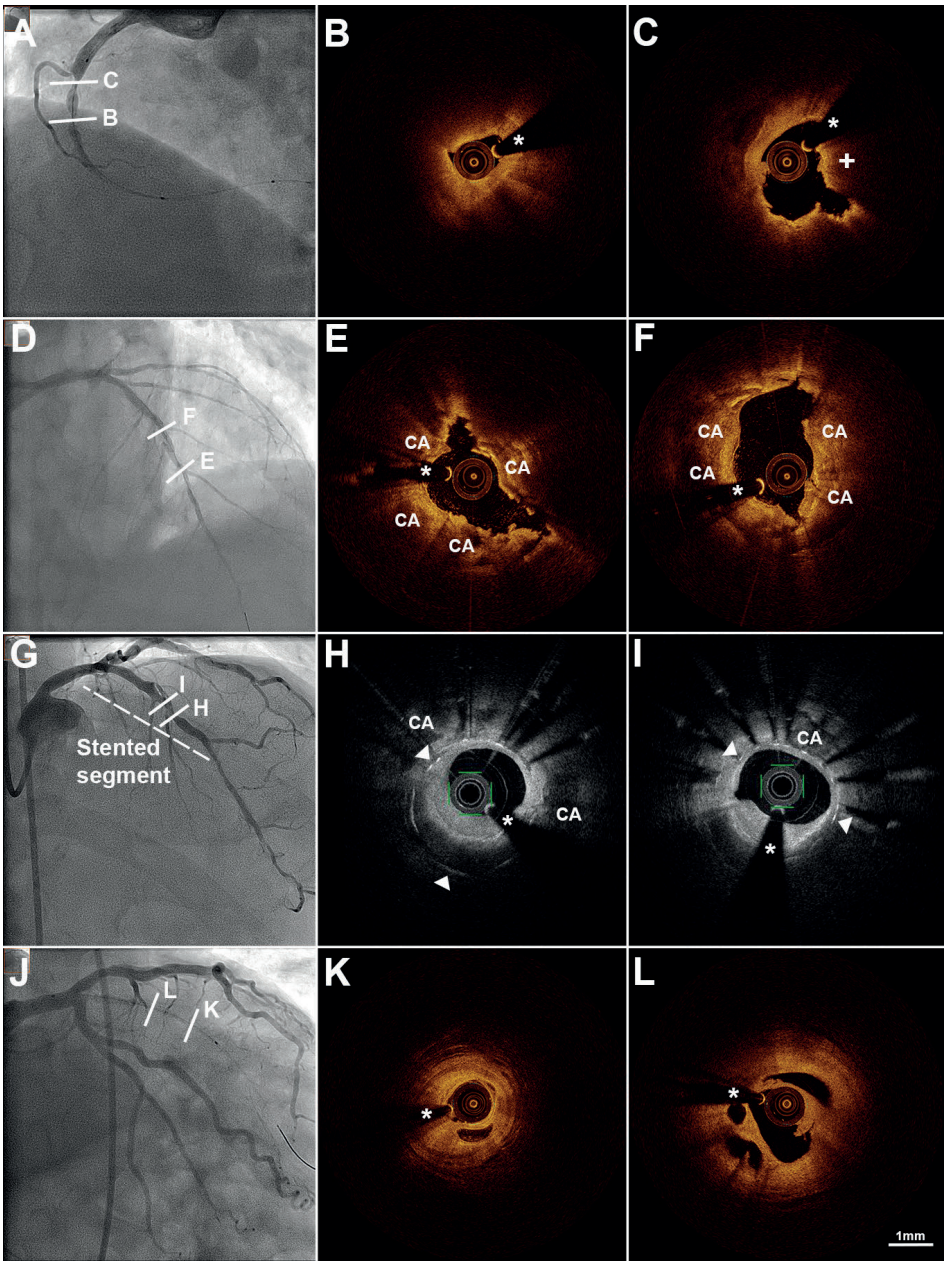

Figure 1 Examples of the use OCT in different clinical settings.
*Angiogram (A) of a STEMI patient with corresponding OCT cross-sectional images (B and C) with the presence of thrombus (+). Angiogram (D) of a severely calcified vessel, which is clearly appreciated (CA) on the OCT-images (E and F) after lesion preparation with a cutting balloon and rotablator. Angiogram (G) of a patient with in-stent restenosis. The OCT-images reveal a lesion with neoatherosclerosis within the stent (H and I) with underexpansion of the stent, probably related to the presence of calcium (CA) locally. Angiographic (J) and OCT image acquisition (K and L) in a recanalized chronic total occlusion. *Guide wire artifact*

of invasively imaged main vessels were also tested. No predictor of adverse events was identified in the individual OCT and IVUS cohorts, nor in the combined invasive imaging cohort. Additionally, the impact of the interventional cardiologist's experience with the use of invasive imaging on the risk of an adverse event was evaluated. When compared to the most experienced operator, there was no significant increase in risk for every individual senior operator.

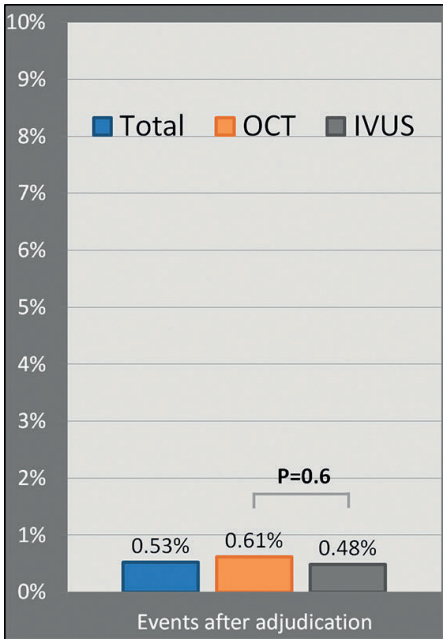

Figure 2 Event rates of IVUS and OCT after adjudication

Table 4 Invasive imaging complications after adjudication

	OCT	IVUS	P-value
Transient ST-elevation	3 (0.26)	2 (0.08)	0.2
Bradycardia	2 (0.18)	1 (0.04)	0.2
Coronary spasm	1 (0.09)	1 (0.04)	0.6
Thrombus formation	1 (0.09)	4 (0.16)	0.6
Dissection	0 (0.00)	3 (0.12)	0.2
Stent deformation	0 (0.00)	1 (0.04)	0.5
Major adverse events	0 (0.00)	0 (0.00)	NA

Values in n (%)

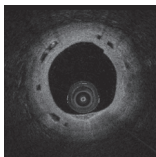

Discussion

The present study demonstrates that intracoronary OCT and IVUS imaging is comparably safe in an unselected and heterogeneous group of patients with varying clinical settings, reflecting daily routine catheterization laboratory practice in a tertiary care

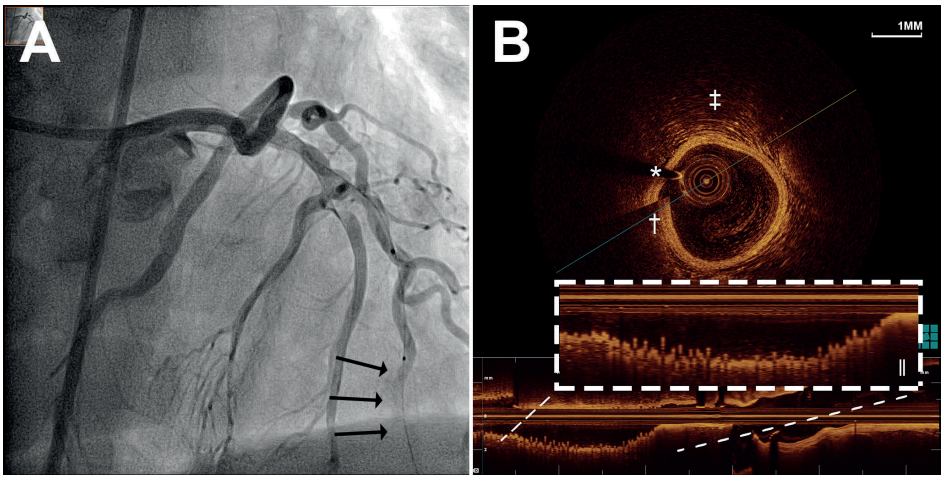

Figure 3 Coronary spams during OCT pullback.
*Angiogram (A) and OCT image (B) of a diagonal branch with coronary spasm. Vasospasm can potentially mimic streaming effect due to poor contrast injection or dissection on the coronary angiogram. The seam-line (†) and non-uniform rotational distortion artefact (‡) on the cross-sectional ad the 'saw-tooth' appearance (II) on the longitudinal image, together with poor clearing of the artery from blood (arrows) despite good guide catheter position, suggest that coronary spasm could be present. *Guide wire artefact.*

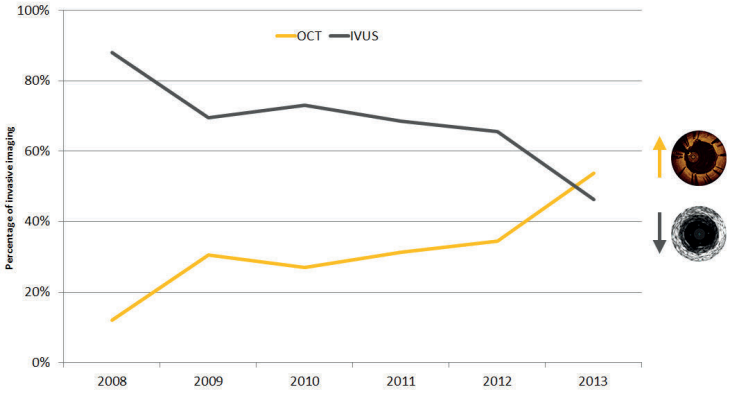

Figure 4 Change of invasive imaging policy during the study period
The use of VUS and OCT has balanced out over time

centre. Imaging-related events were scarce, with a similar incidence for OCT and IVUS imaging and most importantly, self-limiting after withdrawal of the imaging catheter or easily treatable in the catheterization laboratory. No major adverse events, prolongation of hospital stay, or permanent patient harm was observed.

Comparison between the OCT and IVUS cohorts

During the study period, the frequency in the use of OCT and IVUS has changed in our center. In 2008 OCT was not yet CE marked and, thus, infrequently used. In 2013, however, the use of OCT and IVUS has balanced out (**Figure 4**). While IVUS was more often performed in patients with stable angina, OCT was used more often in ST-segment elevation myocardial infarction (STEMI) patients. OCT has a higher sensitivity in visualizing thrombus and plaque ruptures, often present in STEMI patients.

OCT and IVUS were used in a heterogeneous population and in several clinical settings. Although most non-imaging variables in **Table 3** differ significantly from the OCT and IVUS cohorts, most differences can be explained by the features that are inextricably linked to both modalities. For example, in patients with renal failure, X-ray contrast exposure has to be kept to a minimum. This explains the smaller numbers of patients with renal impairment in the OCT and, in lesser extent, the IVUS group. In patients with a chronic total occlusion (lesion type C), operators are less inclined to use invasive imaging, while additional imaging can be of great help in complex lesions (type B2), such as bifurcations. We believe that our data reflect the diversity in the use of invasive imaging and its many possible applications.

Previous studies demonstrating the safety of OCT

OCT's need of clearance of blood from the vessel during image acquisition was perceived as the Achilles heel in the early days of intracoronary OCT imaging with time-domain technology, limiting its clinical application to a few expert centres. Today, this problem is largely solved by the introduction of FD-OCT technology. With FD-OCT, the need to clear the artery temporarily from blood does not appear as a major drawback anymore. The first studies that reported the safety of OCT[10, 11] used the currently abandoned TD-OCT systems. At that time, OCT image acquisition was relatively slow (frame rate 15 frames/s and pullback speed of 1 mm/s) and thus requiring longer pullback times with temporary occlusion of the proximal vessel segment using a dedicated occlusion balloon. Prati et al.[5] were the first to perform OCT with a pullback speed of 3mm/sec and a non-occlusive technique demonstrating improved feasibility and reduced complication risk. This was then confirmed in a larger multicenter registry[6]

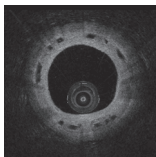

comparing the occlusive balloon technique (n=256) to the non-occlusive TD-OCT (n=212) technique. No major adverse cardiac events (MACE) were observed during or in the 24-hour period following OCT imaging.

The first study to report the safety and feasibility of FD-OCT was published by Imola et al.[7] in a group of 90 patients with unstable or stable coronary artery disease. In this population, one case of coronary spasm was recorded, but no MACE were observed. Likewise, two other studies [8, 9] reported FD-OCT safety in small, selected groups. Our study presents safety of OCT in a high volume center, over several years. The findings corroborate the results of the prior, smaller studies with complication rates of 0 – 2%. The few complications that were encountered were all resolved before the patient left the catheterization laboratory. These complications were also in line with individual case reports that described rare adverse events during OCT imaging.[12-15] Importantly, our large scale, systematic registry can demonstrate that these complications occur very rarely (all <0.2%) in a tertiary, high volume center and seem to happen randomly.

Comparison with IVUS

Although IVUS image acquisition shows many similarities to that of OCT, there are some distinct differences, most importantly IVUS's lack of need for a temporarily blood-free environment. Despite the differences, complications are seen very rarely for both modalities and do not significant differ. In our study, we report 12 (0.5%) adverse events during IVUS image acquisition.

Large IVUS safety trials have been performed,[16, 17] reporting 1 – 3% complications, a number that may be partially driven by a larger catheter size. The most recent large-scale study implementing IVUS, the PROSPECT[18] study, reported 11 patients (1.6%) with complications that were attributed to IVUS procedures. In contrast to our findings, all events were caused by mechanical damage (10 dissections and 1 perforation) to the vessel wall. The reason for this difference is unclear. The mean number of vessels that were imaged with IVUS in our cohort is 1.28 per procedure, in contrast to the three vessels that were imaged as part of the protocol in the PROSPECT study. Furthermore, in the PROSPECT study, images were acquired within a shorter time window and in multiple centres.

Risk factors for adverse event

We did not find any patient characteristics, nor any procedural related characteristics that increase the chance of occurrence of an imaging-related event in the light of our very low event rate. The absence of risk factors most likely demonstrates that adverse

events occur infrequently and randomly, implicating that OCT and IVUS can both be used in a large variety of patients and in different clinical settings. We additionally explored if the amount of adverse events declined with increasing experience, however an association between the operator's experience and the number of imaging procedures was not identified, tracking with previous reports.[9]

Limitations

A limitation of this study is its design. Collection of data that has been recorded over several years as part of our clinical routine catheterization database. This could possibly cause inconsistency and create bias. Furthermore, reproduction of the procedures associated with adverse events that occurred during coronary catheterizations that were performed years ago can be complex. However, the registration of events is done by experienced operators in a standardized way and for a long period of time. We included every patient undergoing FD-OCT and IVUS within the selected time window and used all available procedural data to reproduce the procedures with two independent adjudication committees. Therefore we feel that the reported results represent clinical practice. The fact that imaging was acquired at the discretion of very experienced operators could create selection bias. Moreover, the high level of experience in this single-centre study does not mean that reported results can be translated to less experienced centres. Furthermore, it is of note that it is possible that the differences in clinical characteristics between OCT, IVUS, and non-imaging groups as presented in **Table 3** were mainly driven by its use in predefined research protocols in specific clinical settings. However, we intentionally included all imaging procedures that have taken place within the specified time window to assure that the presented data represent a modern, real-world catheterization laboratory population. Success rates of individual pullbacks were not routinely recorded in our databases. Therefore, we were unable to report on the feasibility of OCT image acquisition in daily clinical practice.

Another limitation of this study is that we were not able to report the incidence of peri-procedural myocardial infarctions and contrast-induced nephropathy, as the majority of our patients are being transferred to the referring hospital within 6 h after the procedure or dismissed after an uneventful procedure.

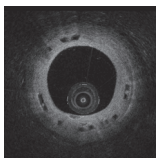

Conclusion

FD-OCT is safe in an unselected and heterogeneous group of patients with varying clinical settings. Adverse events that occur during image acquisition are rare, and similar to the event rates occurring during IVUS image acquisition.

References

1. Tearney GJ, Regar E, Akasaka T, Adriaenssens T, Barlis P, Bezerra HG, Bouma B, Bruining N, Cho JM, Chowdhary S, Costa MA, de Silva R, Dijkstra J, Di Mario C, Dudek D, Dudeck D, Falk E, Feldman MD, Fitzgerald P, Garcia-Garcia HM, Garcia H, Gonzalo N, Granada JF, Guagliumi G, Holm NR, Honda Y, Ikeno F, Kawasaki M, Kochman J, Koltowski L, Kubo T, Kume T, Kyono H, Lam CC, Lamouche G, Lee DP, Leon MB, Maehara A, Manfrini O, Mintz GS, Mizuno K, Morel MA, Nadkarni S, Okura H, Otake H, Pietrasik A, Prati F, Räber L, Radu MD, Rieber J, Riga M, Rollins A, Rosenberg M, Sirbu V, Serruys PW, Shimada K, Shinke T, Shite J, Siegel E, Sonoda S, Sonada S, Suter M, Takarada S, Tanaka A, Terashima M, Thim T, Troels T, Uemura S, Ughi GJ, van Beusekom HM, van der Steen AF, van Es GA, van Soest G, Virmani R, Waxman S, Weissman NJ, Weisz G, (IWG-IVOCT) IWGfIOCT. Consensus standards for acquisition, measurement, and reporting of intravascular optical coherence tomography studies: a report from the International Working Group for Intravascular Optical Coherence Tomography Standardization and Validation. *J Am Coll Cardiol* 2012;**59**:1058-72.
2. Karanasos A, Ligthart J, Witberg K, van Soest G, Bruining N, Regar E. Optical Coherence Tomography: Potential Clinical Applications. *Curr Cardiovasc Imaging Rep* 2012;**5**:206-220.
3. Prati F, Guagliumi G, Mintz GS, Costa M, Regar E, Akasaka T, Barlis P, Tearney GJ, Jang IK, Arbustini E, Bezerra HG, Ozaki Y, Bruining N, Dudek D, Radu M, Erglis A, Motreff P, Alfonso F, Toutouzas K, Gonzalo N, Tamburino C, Adriaenssens T, Pinto F, Serruys PW, Di Mario C, Document EsOR. Expert review document part 2: methodology, terminology and clinical applications of optical coherence tomography for the assessment of interventional procedures. *Eur Heart J* 2012;**33**:2513-20.
4. Yun SH, Tearney GJ, Vakoc BJ, Shishkov M, Oh WY, Desjardins AE, Suter MJ, Chan RC, Evans JA, Jang IK, Nishioka NS, de Boer JF, Bouma BE. Comprehensive volumetric optical microscopy in vivo. *Nat Med* 2006;**12**:1429-33.
5. Prati F, Cera M, Ramazzotti V, Imola F, Giudice R, Albertucci M. Safety and feasibility of a new non-occlusive technique for facilitated intracoronary optical coherence tomography (OCT) acquisition in various clinical and anatomical scenarios. *EuroIntervention* 2007;**3**:365-70.
6. Barlis P, Gonzalo N, Di Mario C, Prati F, Buellesfeld L, Rieber J, Dalby MC, Ferrante G, Cera M, Grube E, Serruys PW, Regar E. A multicentre evaluation of the safety of intracoronary optical coherence tomography. *EuroIntervention* 2009;**5**:90-5.
7. Imola F, Mallus MT, Ramazzotti V, Manzoli A, Pappalardo A, Di Giorgio A, Albertucci M, Prati F. Safety and feasibility of frequency domain optical coherence tomography to guide decision making in percutaneous coronary intervention. *EuroIntervention* 2010;**6**:575-81.
8. Yoon JH, Di Vito L, Moses JW, Fearon WF, Yeung AC, Zhang S, Bezerra HG, Costa MA, Jang IK. Feasibility and safety of the second-generation, frequency domain optical coherence tomography (FD-OCT): a multicenter study. *J Invasive Cardiol* 2012;**24**:206-9.
9. Lehtinen T, Nammas W, Airaksinen JK, Karjalainen PP. Feasibility and safety of frequency-domain optical coherence tomography for coronary artery evaluation: a single-center study. *Int J Cardiovasc Imaging* 2013;**29**:997-1005.
10. Yamaguchi T, Terashima M, Akasaka T, Hayashi T, Mizuno K, Muramatsu T, Nakamura M, Nakamura S, Saito S, Takano M, Takayama T, Yoshikawa J, Suzuki T. Safety and feasibility of an intravascular optical coherence tomography image wire system in the clinical setting. *Am J Cardiol* 2008;**101**:562-7.

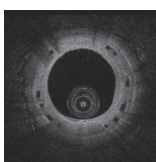

11. Tanigawa J, Barlis P, Di Mario C. Intravascular optical coherence tomography: optimisation of image acquisition and quantitative assessment of stent strut apposition. *EuroIntervention* 2007;**3**:128-36.
12. Koyama K, Yoneyama K, Mitarai T, Kobayashi Y, Saito M, Oono T, Kuwata S, Ishibashi Y, Kongoji K, Akashi YJ, Harada T. Periprocedural myocardial injury and right bundle branch block during coronary optical coherence tomography in an acute coronary syndrome patient with severe coronary ectasia. *Int J Cardiol* 2014;**177**:1113-5.
13. Dobarro D, Jiménez-Valero S, Moreno R. Severe coronary spasm induced by OCT wire. There are no innocuous procedures. *J Invasive Cardiol* 2010;**22**:385.
14. Sato K, Panoulas VF, Naganuma T, Miyazaki T, Latib A, Colombo A. Bioresorbable vascular scaffold strut disruption after crossing with an optical coherence tomography imaging catheter. *Int J Cardiol* 2014;**174**:e116-9.
15. Smith DK, Bourenane H, Strange JW, Baumbach A, Johnson TW. Catheter-induced coronary dissection during optical coherence tomography investigation. *EuroIntervention* 2012;**7**:1124-5.
16. Hausmann D, Erbel R, Alibelli-Chemarin MJ, Boksch W, Caracciolo E, Cohn JM, Culp SC, Daniel WG, De Scheerder I, DiMario C. The safety of intracoronary ultrasound. A multicenter survey of 2207 examinations. *Circulation* 1995;**91**:623-30.
17. Batkoff BW, Linker DT. Safety of intracoronary ultrasound: data from a Multicenter European Registry. *Cathet Cardiovasc Diagn* 1996;**38**:238-41.
18. Stone GW, Maehara A, Lansky AJ, de Bruyne B, Cristea E, Mintz GS, Mehran R, McPherson J, Farhat N, Marso SP, Parise H, Templin B, White R, Zhang Z, Serruys PW, Investigators P. A prospective natural-history study of coronary atherosclerosis. *N Engl J Med* 2011;**364**:226-35.

Appendix A - Supplementary material and methods

Complications that occurred during invasive imaging were witnessed very rarely (0.53%) in our center. The adverse events that did occur, however, are described below in more detail.

Transient ST-elevation

Vessel occlusion by the imaging catheter resulting in transient ST-elevation on electrocardiographic (ECG) monitoring requiring withdrawal of the imaging catheter occurred during three OCT and two IVUS image acquisitions. The ECG changes were transient and resolved promptly upon withdrawal of the imaging catheter. **Supplementary Figure 1** demonstrates an example of an IVUS imaging procedure of a narrow lesion. Antegrade flow in the coronary artery was occluded by the IVUS catheter, which resulted in angina with ST-segment elevations on ECG telemetry. After retrieval of the imaging catheter the electrocardiogram normalized.

Bradycardia

Bradycardia with hypotension was witnessed during two OCT procedures and one IVUS procedure. In two out of three cases, this was secondary to occlusion of flow in the artery by an imaging catheter, which resolved upon withdrawal of the catheter. The third case was caused by deep intubation of the guide catheter into the left main coronary artery, possibly to facilitate adequate flushing during OCT image acquisition and resulting in pressure dampening. This led to bradycardia and hypotension, which improved upon prompt adjustment of the position of the guide catheter and an intravenous admission of 0.5mg atropine with good response.

Coronary spasm

Severe vasospasm may occur due to the manipulation of the imaging equipment within the coronary vasculature. In severe cases, this may lead to flow reduction. In both reported cases, spasm was resolved by intracoronary infusion of nitrates. Severe cases may mimic dissection. Therefore, early recognition is important. OCT can help differentiate vasospasm from other differential causes. Pullbacks acquired during spasm showed poor blood clearing and a typical pattern of a fast, irregular, saw-tooth artefact (**Figure 3** main manuscript), which has previously been described as a "wavy configuration".[1]

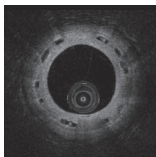

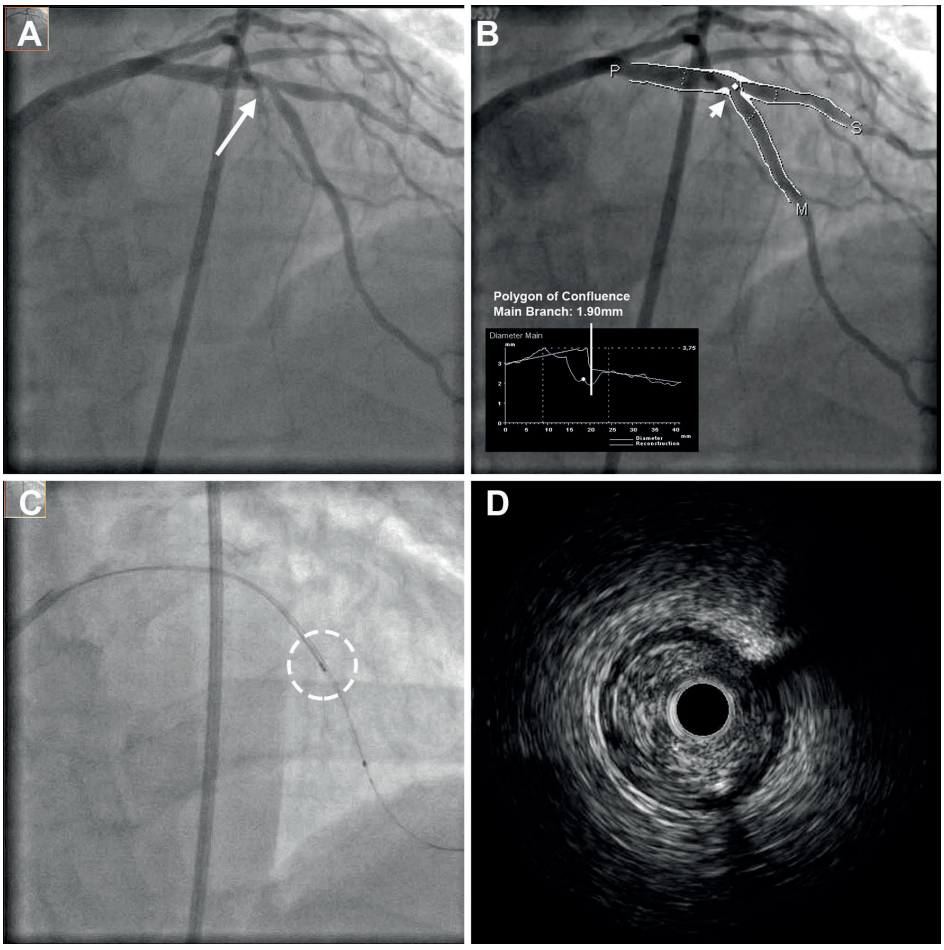

Supplementary Figure 1 Transient ST-elevation caused by occlusive IVUS-catheter
Lesion (arrow) in the bifurcation of the left descending artery and a diagonal branch (panel A and B). During the IVUS pullback (panel C) the patient develops ST-segment elevation and chest pain from blockage of antegrade flow in the LAD by the IVUS imaging catheter. Although the IVUS shows the 3.5F (= 1.16mm) IVUS-catheter is occlusive (panel D), this was not apparent on angiography (minimum lesion diameter in main branch 1.90mm)

Thrombus formation

Thrombus formation on the invasive imaging catheter occurred once during OCT imaging and four times during IVUS imaging. **Supplementary Figure 2** shows an example of thrombus formation during invasive imaging in a patient undergoing primary PCI for anterior STEMI. The patient was preloaded with prasugrel, acetylsalicylic acid and heparin according to current guidelines. An emergency coronary angiogram showed that the culprit lesion was in the left anterior descending artery (LAD). The patient subsequently received an extra bolus of 5,000 units of heparin before com-

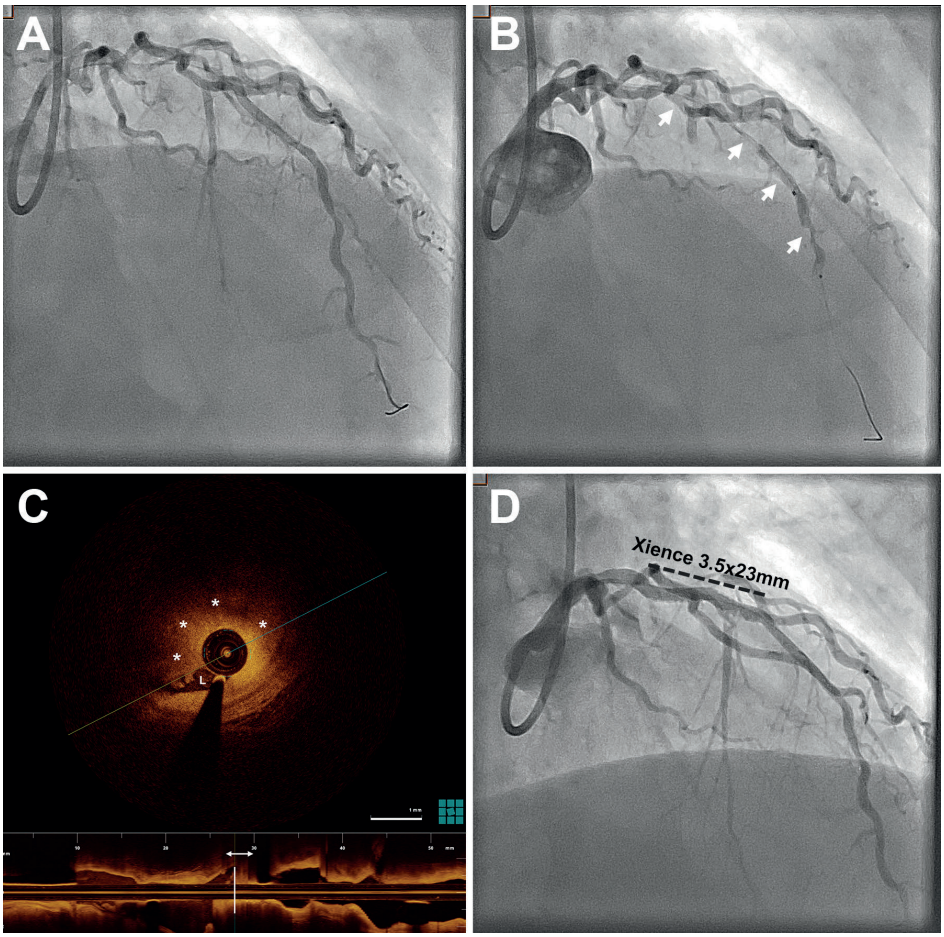

Supplementary Figure 2 Thrombus formation during OCT pullback
Angiographic image of the left descending artery with TIMI-II flow after successfully wiring and aspiration thrombectomy of the culprit lesion (panel A). During the OCT pullback, several hazy spots appeared (arrows, panel B). On the OCT images (panel C) there is a focal segment (arrow, longitudinal view) with a narrow lumen (L) due to thrombotic material (*). After pre-dilatation, a Xience™ 3.5x23mm stent was deployed with good angiographic result (panel D)

mencement of PCI. After successful wiring and aspiration thrombectomy of the culprit lesion, there was TIMI-II flow in the LAD. During the passage of the C7 Dragonfly™ OCT-catheter in the LAD, several filling defects with a hazy appearance could be seen on the angiogram, suggesting the presence of thrombus formation. This was confirmed by the appearance of thrombotic material on the OCT images. A Xience™ Xpedition 3.5x23 mm drug-eluting stent (DES) was deployed in the proximal LAD with good angiographic result. Two additional boluses of Grp IIb/IIIa-inhibitor were given.

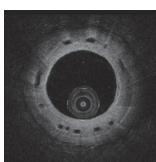

The mechanism of the thrombus formation is not entirely clear. Possibly causes for the new appearance of thrombus include the migration of thrombotic material during the passage of the imaging catheter within the culprit vessel or insufficient anticoagulation. We did not find any ACT of less than 300 seconds in the cases with thrombus formation during invasive imaging. Furthermore, the interval between admission of intravenous heparin and the introduction of the imaging catheter was a relatively short duration of fourteen minutes, which strengthens the idea that the etiology is related to the acute setting of the procedure rather than a problem with anticoagulation, although the latter cause cannot be ruled out.

Dissection

Three dissections were possibly caused by an IVUS imaging catheter, whereas we could not identify any dissections caused by an OCT catheter. Two of these three dissections were caused by wiring of a vessel to facilitate IVUS imaging. In one case, the dissection occurred at a proximal location, which suggested that it was guide catheter related rather than due to the imaging catheter itself. It is, however, possible that the IVUS pullback created additional traction on the guide catheter, thereby possibly damaging the vessel wall (**Supplementary Figure 3**). Therefore, this dissection was labeled as a possible complication. To treat the dissection, a 4.0x18mm Xience™ Prime drug-eluting DES was implanted to secure vessel patency.

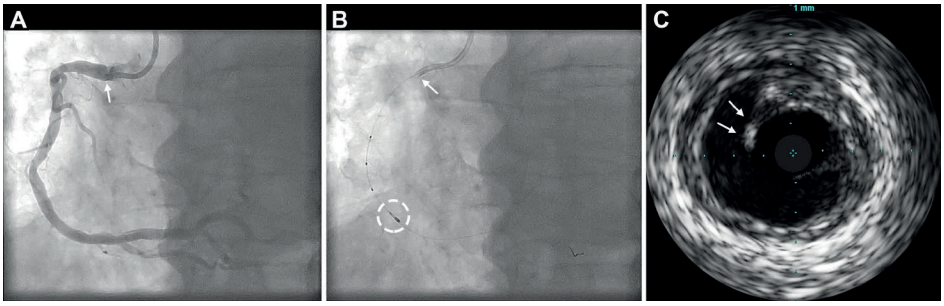

Supplementary Figure 3 Proximal dissection caused by the guide catheter
Pre-interventional angiographic image of the right coronary artery (panel A) with the arrow indicating the guide catheter position. During the IVUS pullback the guide catheter (arrow, panel B) is pulled distally, possibly creating a proximal dissection as seen on the IVUS cross-sectional image (arrows, panel C)

Stent deformation

One case of potential stent deformation involving the use of IVUS (3.5Fr Volcano™ 20Mhz EagleEye Platinum catheter) imaging to assess post deployment result of

Xience™ Prime (4.0x28mm) stent in the right coronary artery was recorded in our database. The post deployment IVUS images (**Supplementary Figure 4**) revealed a proximal stent edge that was circular, not apposed to the vessel wall, with a stent diameter of 2.60mm circularly. Possible explanations for this appearance include deformation of the stent by the IVUS catheter, deformation of the stent by the guide catheter or simply underexpansion of the stent in its proximal portion.

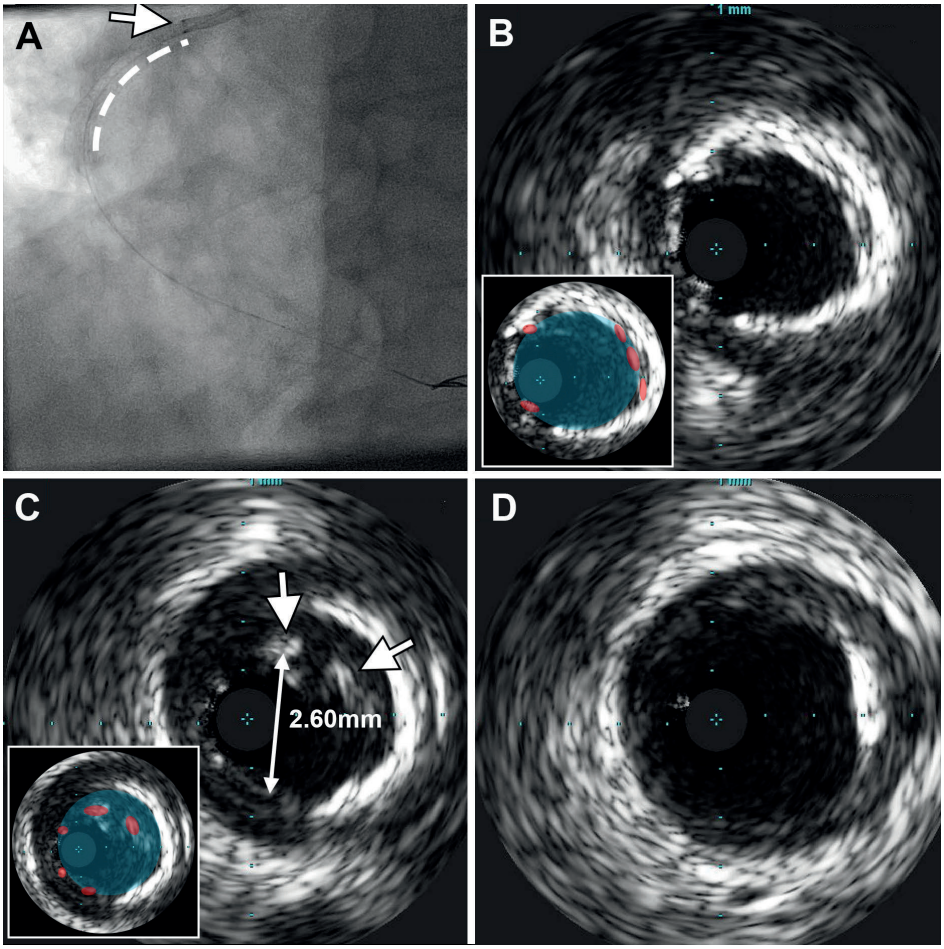

Supplementary Figure 4 Potential stent deformation

Angiographic image (panel A) of a Xience™ 4.0x28mm stent (dotted line) in the right coronary artery. The guide catheter is in close proximity of the proximal stent (arrow). After IVUS image acquisition, the distal part of the stent is well apposed to the vessel wall (panel B), but the proximal part is malapposed (arrows, panel C), which could either be related to underexpansion or deformation of the stent by the IVUS or guide catheter. The inlayed panels delineate the stent struts in red and the lumen in blue. Panel D shows an IVUS image of the proximal reference area

Further intervention was performed with additional balloon dilatation and implantation of another Xience™ Prime (4.0x8mm) DES, overlapping with the previous stent to assure an optimal mechanical result.

Lessons learned

When imaging a very tight lesion and the imaging catheter seems occlusive, do not start the pullback too distally because visualization is very poor and time of ischemia will be prolonged. A rather general measure, that is worth repeating, however, is that a guide catheter should be positioned coaxially, but wedging should be avoided at all times. Be aware that during invasive imaging, deep intubation of the guide catheter into the vessel may occur resulting in pressure dampening effect or damage to the vessel wall.

All witnessed events appeared isolated events and no systematic contributory cause was detected. Nevertheless, these events are a reminder of the need for caution particularly in view of the large number of intracoronary imaging procedures performed. If these rather general measures are applied, we believe that invasive imaging is a tool that can be of additional value in various clinical situations and can be used safely with low threshold.

References

1. Morikawa Y, Uemura S, Ishigami K, Soeda T, Okayama S, Takemoto Y, Onoue K, Somekawa S, Nishida T, Takeda Y, Kawata H, Horii M, Saito Y. Morphological features of coronary arteries in patients with coronary spastic angina: assessment with intracoronary optical coherence tomography. *Int J Cardiol* 2011;**146**:334-40.

Appendix B - Supplementary Tables

Supplementary Table 1 Univariate analysis for adverse events during invasive-image acquisition

	OCT	P-value	IVUS	P-value	OCT + IVUS	P-value
N	1142		2476		3311*	
Clinical risk factors						
Age	0.99 (0.93-1.06)	0.869	1.00 (0.95-1.06)	0.884	1.00 (0.96-1.04)	0.985
Male gender	NA (0.00-NA)	0.994	1.69 (0.37-7.73)	0.500	2.95 (0.68-12.8)	0.148
Hypertension	0.64 (0.14-2.87)	0.558	0.61 (0.20-1.90)	0.395	0.61 (0.25-1.50)	0.282
DM	0.75 (0.09-6.27)	0.792	0.35 (0.05-2.73)	0.352	0.48 (0.11-2.06)	0.321
Dyslipidaemia	2.03 (0.39-10.5)	0.399	0.47 (0.15-1.48)	0.195	0.80 (0.32-1.97)	0.625
Smoking	2.11 (0.47-9.50)	0.329	1.08 (0.29-4.02)	0.904	1.42 (0.54-3.75)	0.479
Family history	0.95 (0.21-4.28)	0.950	0.25 (0.06-1.15)	0.074	0.45 (0.16-1.26)	0.131
History						
Prior MI	1.74 (0.39-7.83)	0.469	0.73 (0.20-2.69)	0.631	0.95 (0.39-2.72)	0.952
Prior CABG	3.68 (0.23-31.2)	0.232	1.56 (0.20-12.2)	0.671	2.11 (0.48-9.22)	0.320
Prior PCI	2.90 (0.56-15.0)	0.204	1.34 (0.43-4.15)	0.617	1.79 (0.72-4.47)	0.211
Renal Failure	3.00 (0.36-25.3)	0.313	0.90 (0.12-7.03)	0.923	1.34 (0.31-5.83)	0.696
Indication						
Stable angina	1.00		1.00		1.00	
Unstable angina	0.00 (0.00-NA)	0.996	0.30 (0.04-2.38)	0.253	0.21 (0.03-1.63)	0.136
Non-STEMI	0.00 (0.00-NA)	0.997	1.20 (0.25-5.67)	0.821	0.82 (0.18-3.72)	0.798
STEMI	1.02 (0.17-6.17)	0.980	0.00 (0.00-NA)	0.994	0.41 (0.09-1.87)	0.250
Other	1.94 (0.32-11.7)	0.471	0.46 (0.06-3.67)	0.462	0.92 (0.26-3.32)	0.902
Imaging variables						
Use of both modalities	1.09 (0.21-5.64)	0.920	1.42 (0.31-6.49)	0.655	2.63 (0.87-7.98)	0.087
Total number of pullbacks	0.51 (0.22-1.16)	0.108	1.10 (0.75-1.61)	0.645	1.06 (0.82-1.36)	0.672
Total number of imaged vessels	0.79 (0.11-5.79)	0.820	1.19 (0.43-3.32)	0.737	1.57 (0.88-2.80)	0.130

**307 Patients underwent both OCT and IVUS during the same procedure. Risk values as Hazard Ratio (95% Confidence Interval). OCT: Optical coherence tomography; IVUS: Intravascular ultrasound; DM: Diabetes mellitus; MI: Myocardial infarction; CABG: Coronary artery bypass graft; PCI: Percutaneous coronary intervention*

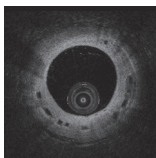

The impact of Fourier-Domain optical coherence tomography catheter induced motion artefacts on quantitative measurements of a PLLA-based bioresorbable scaffold

NS van Ditzhuijzen, A Karanasos, N Bruining, M van den Heuvel, O Sorop, J Ligthart, K Witberg, HM Garcia-Garcia, F Zijlstra, DJ Duncker, HM van Beusekom, E Regar

Int J Cardiovasc Imaging. 2014 May 16

Supplementary video's *can be retrieved online at Int J Cardiovasc Imaging*

4

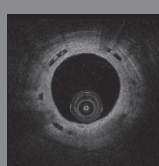

Abstract

Introduction Intracoronary Fourier-Domain optical coherence tomography (FD-OCT) enables imaging of the coronary artery within 2-4 seconds, a so far unparalleled speed. Despite such fast data acquisition, cardiac and respiratory motion can cause artefacts due to longitudinal displacement of the catheter within the artery. We studied the influence of longitudinal FD-OCT catheter displacement on serial global lumen and scaffold area measurements in coronary arteries of swine that received PLLA-based bioresorbable scaffolds.

Methods In 10 swine, 20 scaffolds (18x3.0mm) were randomly implanted in 2 epicardial coronary arteries. Serial FD-OCT imaging was performed immediately after implantation (T1) and at 3 (T2) and 6 months (T3) follow-up. Two methods for the selection of OCT cross-sections were compared. Method A did not take into account longitudinal displacement of the FD-OCT catheter. Method B accounted for longitudinal displacement of the FD-OCT catheter.

Results Fifty-one OCT pullbacks of 17 scaffolds were serially analyzed. The measured scaffold length differed between time points, up to one fourth of the total scaffold length, indicating the presence of longitudinal catheter displacement. Between method A and B, low error was demonstrated for mean area measurements. Correlations between measurements were high: R^2 ranged from 0.91 to 0.99 for all mean area measurements at all time points.

Conclusions Considerable longitudinal displacement of the FD-OCT catheter was observed, diminishing the number of truly anatomically matching cross-sections in serial investigations. Global OCT dimensions such as mean lumen and scaffold area were not significantly affected by this displacement. Accurate co-registration of cross-sections, however, is mandatory when specific regions, e.g. jailed side branch ostia, are analyzed.

Introduction

Optical coherence tomography (OCT) allows for detailed evaluation of the coronary vessel wall. One of the main advantages of OCT is the high resolution allowing for detailed evaluation of therapeutic devices used for the treatment of coronary artery disease, e.g. coronary stents and scaffolds.[1, 2] Recently, the second generation Fourier Domain (FD)-OCT has been introduced. FD-OCT enables unparalleled fast imaging of the coronary artery employing a wavelength-swept laser as a light source allowing for a high A-line and frame rate (typically ≥100 frames/sec) and fast automated catheter pullback speed (≥20mm/sec).[3-5] Despite the fast pullback speed of the FD-OCT catheter, the catheter can longitudinally move within the coronary artery during the cardiac cycle and can therefore cause distortions in the representation of the data. Little is known about the magnitude of longitudinal catheter displacement in vivo. To study the influence of longitudinal displacement of the FD-OCT catheter on serial mean lumen and scaffold area measurements, we performed serial FD-OCT imaging of PLLA-based bioresorbable scaffolds implanted in atherosclerotic swine, and compared two OCT data analysis methods. Method A did not account for longitudinal displacement of the FD-OCT catheter, method B accounted for longitudinal displacement of the FD-OCT catheter.

Materials and methods

Experimental design

This study was approved by the Erasmus MC Animal Care committee and was performed in accordance with the Guide for the Care and Use of Laboratory Animals (National Institutes of Health Publication 85-23, 1996).

Ten male crossbred (Yorkshire x Landrace) swine fed a high-cholesterol diet were included.[6] Following 2 mg isosorbide dinitrate, twenty 18x3.0mm bioresorbable scaffolds (Abbott Vascular, Santa Clara, CA) were implanted randomly in 2 of 3 epicardial coronary arteries of anesthetized swine.[7, 8] Serial FD-OCT (C7XR Fourier-Domain system, St. Jude Medical, Westford, MA, USA) was performed in the anesthetized swine immediately after implantation (T1), 3 months (T2) and 6 months (T3) after implantation of the scaffolds, while care was taken to keep the heart rate (average 106±27 bpm) and blood pressure (mean arterial pressure 87±17mmHg) stable at all time points. The influence of longitudinal catheter displacement on serial mean lumen, scaffold and coverage area measurements was evaluated by comparing two different approaches for the selection of OCT cross-sections (method A and method B).

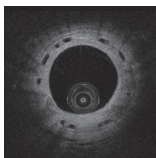

OCT image acquisition

The OCT catheter was advanced distally to the scaffold through an 8F guiding catheter. The OCT catheter was withdrawn automatically with a pullback speed of 20 mm/s and a frame rate of 100 frames/s during continuous flushing, using a power injector (Mark V ProVis, Medrad, Inc, Indianola, Pa), with 5 or 6 ml/s contrast agent preheated to 37°C (iodixanol 370; Visipaque, GE Health Care, Cork, Ireland). Since the maximum length of the pullback was 54mm, the total pullback consists of 270 frames (cross-sections). Moreover, the interval between two consecutive cross-sections corresponds to 0.2mm.

OCT image analysis

Selection of OCT cross-sections

Analysis method A is the most often employed method for the selection of OCT cross-sections and has been widely described in studies evaluating bioresorbable scaffolds.[7, 9] At each analysis time point, cross-sectional images were selected independently and manually at 1-mm intervals within the region of interest (ROI). Thus, per timepoint, every 5 cross-sections, 1 cross-section was selected independently.

Analysis method B employed a computerized matching method for the selection of serially corresponding cross-sections. OCT pullbacks were digitally saved in DICOM format to allow for matching of corresponding cross-sections by dedicated software (CURAD vessel analysis, CURAD BV, Wijk bij Duurstede, The Netherlands) (**Figure 1**).[10] OCT pullbacks acquired at different time points were tiled horizontally onto one single screen, allowing for accurate matching of the ROI. The pullbacks were divided into three sub-segments within the ROI: 1) the distal segment of the scaffold: starting at the most distal OCT cross-section containing any scaffold strut extending to the first OCT cross-section in which the opening of a distal side branch was clearly visible, 2) the mid segment of the scaffold: starting at the last OCT cross-section in which the opening of the distal side branch was clearly visible, extending to the first OCT cross-section in which the opening of a proximal side branch was clearly visible and 3) the proximal segment of the scaffold: starting at the last OCT cross-section in which the opening of the proximal side branch was clearly visible, extending to the most proximal OCT cross-section containing any scaffold strut. In order to allow for serial matching of corresponding segments irrespective to the uniformity of the pullback, the vessel analysis software provides synchronization of the sub-segments within the three time points (**Figure 1**). Within these synchronized segments, corresponding OCT cross-sections were manually selected in 1-mm intervals for quantitative OCT analysis.

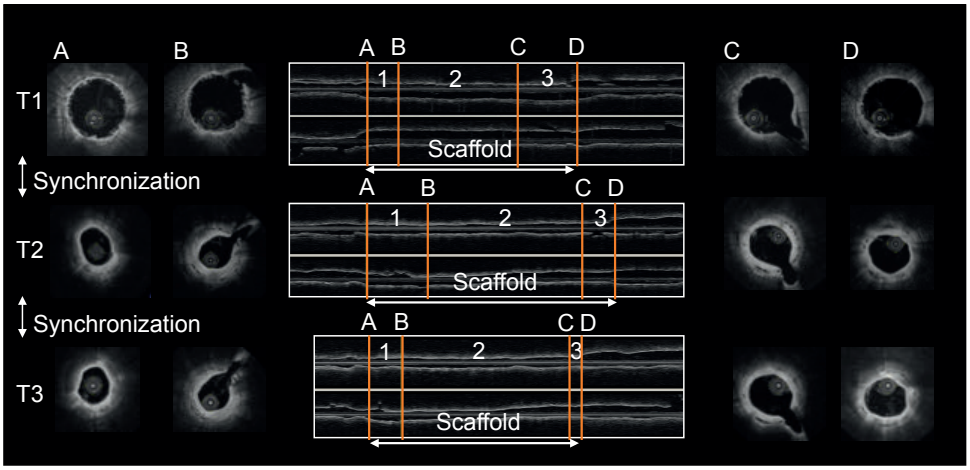

Figure 1 Matching of a scaffolded segment using dedicated analysis software (CURAD vessel analysis, CURAD BV, Wijk bij Duurstede, The Netherlands)

The OCT cross-sections A to D correspond to the letters A to D of the longitudinal view in the center of the figure (A to D = the ROI). The numbers 1 to 3 correspond to the distal (1), mid (2) and proximal (3) segment of the scaffold, which are matched within the different time points using side branches as landmarks. T1 = time-point 1: immediately after scaffold implantation, T2 = time-point 2: 3 months after scaffold implantation, T3 = time-point 3: 6 months after scaffold implantation

Quantitative OCT analysis

Quantitative OCT analysis was performed on the OCT cross-sections selected by method A or method B using proprietary software for off-line OCT analysis (St. Jude medical, Westford, MA, USA).

The Z-offset is a manually adjustable image calibration that is critical for accurate measurements. When the sheath of the OCT catheter is aligned with the 4 yellow fiducials in the OCT image, the Z-offset is correctly adjusted. During image acquisition the optical fibers can however stretch, resulting in possible changes in the size of the Z-offset. Therefore, before off-line OCT analysis, the Z-offset was checked and modified if necessary in all pullbacks, and OCT pullbacks with poor image quality were excluded from the analysis.

The ROI was defined as the region containing the scaffold, delineated by the most distal OCT cross-section containing any scaffold strut until the most proximal OCT cross-section containing any scaffold strut. The length of the ROI – the scaffold length – was measured at all time points using the longitudinal view (l-mode) of the proprietary software for off-line OCT analysis.

Quantitative OCT area measurements included lumen area (LA), scaffold area (SA) and coverage area (CA), according to previously described methodology.[11] Contour tracing of the lumen, scaffold and coverage area are depicted in **Figure 2**. Immedi-

ately after implantation (T1), lumen area can be imaged because of the translucency of the polymeric struts, and is delineated by the endoluminal contour of the vessel wall behind the struts. At T2 and T3, contours of the lumen area can be drawn by following the endoluminal contour of the coverage between and on top of the struts. The contours for lumen area were obtained by a semi-automated detection algorithm and additional manual corrections were performed if necessary. At all time points the contour of the scaffold area is measured by joining the middle point of the abluminal side of the black core of the struts.[7-9] Coverage area was determined at follow-up (T2 and T3) and defined as scaffold area minus lumen area [CA = SA-LA].[11]

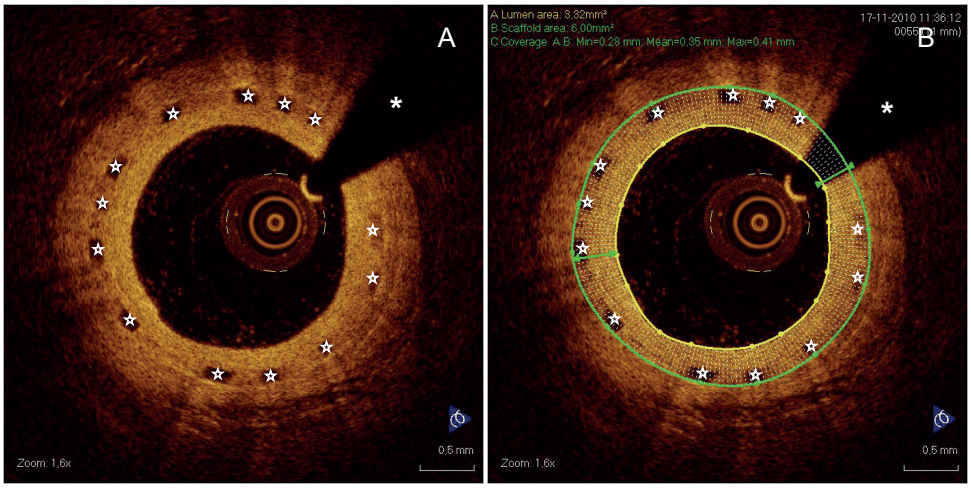

Figure 2 Lumen, scaffold and coverage area measurements at T2
OCT cross-sections of the scaffold at T2 A) without and B) with the lumen area (LA), scaffold area (SA), and coverage area (CA) measurement contours. The 'open' stars indicate the scaffold struts, the asterix (*) indicates the guide wire artefact. The yellow line in (B) indicates the contour of the LA, the green line the contour of the SA and the area between LA and SA is the CA (white dotted area)

Longitudinal catheter displacement

To evaluate the extent of longitudinal displacement of the FD-OCT catheter, we compared the scaffold length, as measured in the l-mode of the off-line OCT analysis software, between the various time points. Furthermore, we compared the amount of cross-sections selected according to method A between the various time points.

To determine the effect of longitudinal catheter displacement on serial mean lumen, scaffold and coverage area measurements, we performed inter-method reproducibility analysis for the measurements per time point (T1, T2 and T3) and for the measurements between time points (ΔT1-T2 and ΔT2-T3). Moreover, we compared the mean

area measurements obtained by method A – employing no co-registration of the OCT cross-sections between time points and therefore not taking into account longitudinal displacement of the OCT catheter – with the mean area measurements obtained by method B – employing co-registration of OCT cross-sections within time points and therefore taking into account longitudinal displacement of the OCT catheter.

To evaluate the effect of longitudinal catheter displacement on the analysis of specific scaffold regions, the amount of OCT cross-sections containing a side branch selected according to method A were compared between the various time points. This analysis was only performed for method A because cross-sections were selected independently at the various time points. By method B corresponding cross-sections were, per protocol, carefully selected and therefore no difference in the amount of selected cross-sections containing a side branch is present between the various time points.

Inter- and intra-observer reproducibility

Two experienced observers independently analyzed 5 scaffolds at T1, T2 and T3 to assess the inter-observer reproducibility for the quantitative OCT area measurements. To assess the intra-observer reproducibility of the quantitative area measurements, one experienced observer repeated the analysis in all 5 scaffolds with ≥3 months between the first and second analysis. For both the inter- and intra-observer reproducibility analysis, the selection of OCT cross-sections was performed according to method B.

Statistical analysis

GraphPad Prism version 5.00 for Windows (GraphPad Software, San Diego, CA, USA) and SPSS version 20.0 (SPSS Inc., Chicago, IL) were used for statistical analysis. To analyze the difference between time points, repeated measures analysis was performed by GEE modeling using a linear response model with an autoregressive (AR(1)) structure for the within-cluster correlation matrix. GEE is a statistical method that accounts for the clustered nature of >1 scaffold analyzed from one swine, which might result in unknown correlations among measurements within these scaffold clusters. The agreement between method A and B for the analysis of quantitative OCT parameters was determined by Bland-Altman analysis, setting the limits of agreement to 1.96 standard deviations of the mean difference. The Bland-Altman plots show the absolute difference between method A and B ([A-B]; y-axis) versus the average of method A and B ([(A+B)/2]; x-axis).[12] Linear regression analysis was performed to show the correlation between the two methods.

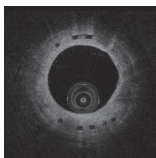

The inter- and intra-observer reproducibility for quantitative area measurements were assessed using the intra-class correlation coëfficient (ICC) for absolute agreement. An ICC <0.4 indicates poor agreement, an ICC between 0.4 and 0.75 indicates moderate agreement, and ICC values >0.75 indicate excellent agreement.[13] Bland-Altman plots were used to illustrate the agreement between inter- and intra-observer reproducibility measurements at cross-sectional level.[12] A p-value of <0.05 indicates statistical significance.

Results

The presence of longitudinal catheter displacement

Fifty-one OCT pullbacks of 17 scaffolds were included in the analysis. Six scaffolds were implanted in the LAD, six in the LCX and five in the RCA. Mean measured scaffold length was similar between LAD, LCX and RCA at all time points (P=NS), indicating that the extent of longitudinal catheter displacement was similar in the various coronary arteries. Moreover, mean scaffold length as measured in the LAD was 17±2mm at T1, 15±1mm at T2 and 17±2mm at T3, in LCX 18±2mm at T1, 16±2mm at T2, 16±1mm at T3 and in the RCA 18±2mm at T1, 17±1mm at T2 and 17±1mm at T3. All scaffolds demonstrated

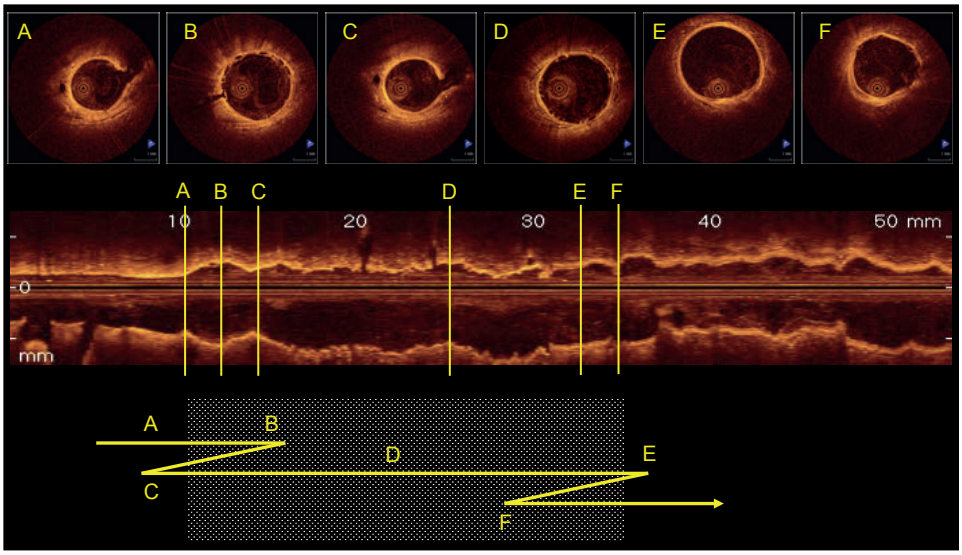

Figure 3 Representation of longitudinal displacement of the OCT catheter

The middle panel demonstrates the l-mode view of the OCT pullback. The letters A to F indicate the OCT cross-sections that are visualized in the upper panel of the figure. In the lower panel of the figure the displacement of the OCT catheter is schematically depicted, with the letters (A to F) corresponding to the letters in the OCT cross-sections and the longitudinal view of the pullback

some difference between measured and nominal scaffold length (18mm), indicating the presence of longitudinal FD-OCT catheter displacement. Moreover, the greatest difference between measured and nominal scaffold length was 5.2mm, whereas the smallest difference between measured and nominal scaffold length was 0.1mm. A schematic representation of longitudinal displacement of the OCT catheter is demonstrated in **Figure 3**.

As expected from the scaffold length measurements documented above, the number of OCT cross-sections selected by method A differed between the three time points, with the greatest difference between T1 and T2 (median (IQR) was 19 (18;21) at T1, 17 (16;19) at T2 and 18 (17;19) at T3; P<0.01). **Figure 4** demonstrates a 3D reconstruction of the scaffold in which repetition of the same struts (indicated in yellow) can be observed, as has been described previously.[14]

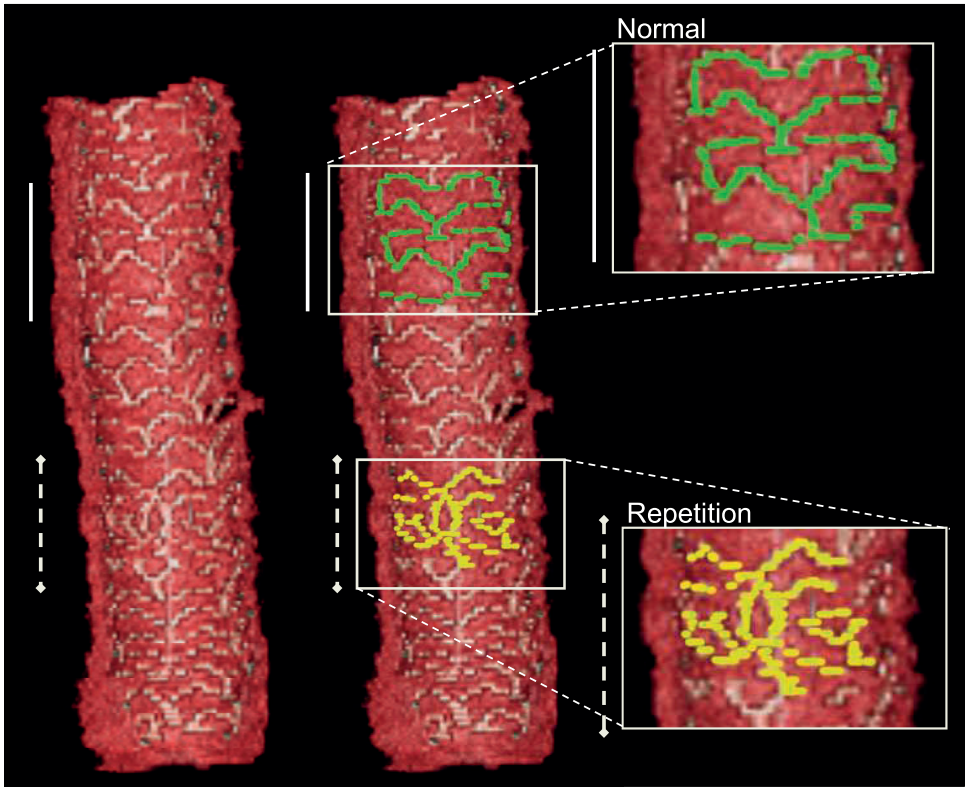

Figure 4 Three dimensional reconstruction of one of the PLLA-based bioresorbable scaffolds
Because of forward and backward displacement of the FD-OCT catheter, repetition of the same struts (indicated in yellow) can be observed, as has been described previously.[14] In the upper right a magnification of a normal appearance of the scaffold struts can be observed (indicated in green), in the lower right a magnification of the repetition can be observed (indicated in yellow)

The effect of longitudinal catheter displacement

The results of the quantitative OCT global area measurements are summarized in **Table 1**. The greatest difference between method A and B was small and observed for the mean coverage area measurement at T3 (absolute difference 0.29±0.15mm^2). The smallest difference was observed for the mean lumen area measurement at T2 (0.02±0.08mm^2). The Bland-Altman analyses demonstrate high agreement between both methods for all mean area measurements at and between all time points (**Figures 5 to 10**). Linear regression analysis demonstrated excellent correlations with small overall differences between the two methods per time point: R^2 ranged from 0.91 to 0.99 for all mean area measurements (**Table 1; Figure 5, 7 and 9**). For the measurements between T1 and T2, also excellent correlations were observed: R^2 was 0.96 and 0.93 for mean lumen and scaffold area respectively. For the change in mean lumen area and mean coverage area between T2 and T3, good correlations were observed (R^2 0.95 and 0.70) and for the change in mean scaffold area between T2 and T3 a moderate correlation was observed (R^2 0.45) (**Figure 6, 8 and 10**).

The amount of selected cross-sections containing a side branch differed between the three time points, however, not statistically significant (median (IQR) was 2 (2;3) at T1, 2 (1;3) at T2 and 2 (1;3) at T3; P=0.48).

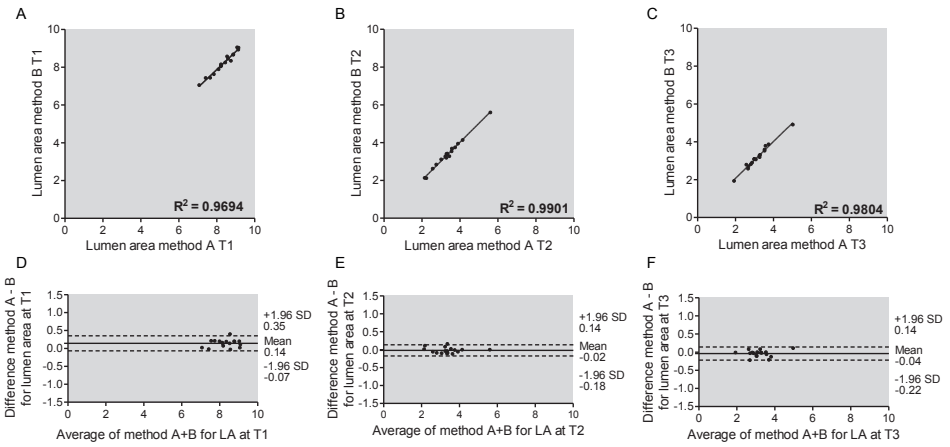

Figure 5 Inter-method variability for lumen area (mm^2) measurements

The linear regression analysis demonstrates very high correlation between method A and B for mean lumen area (mm^2) at T1 (A), T2 (B), T3 (C). The Bland-Altman plots demonstrate the inter-method variability for mean lumen area (LA; mm^2) at T1 (D), T2 (E) and T3 (F)

Table 1. Inter-method reproducibility at scaffold level

	Method A	Method B	Difference (A-B)	Relative difference	Limits of agreement*	Linear regression analysis				
	Mean ± SD (mm^2)	Mean ± SD (mm^2)	Mean ± SD (mm^2)	(Method A/ Method B)	Lower	Upper	Slope	Intercept	R^2	P
Mean lumen area										
T1	8.36 ± 0.61	8.22 ± 0.59	0.14 ± 0.11	1.02	-0.07	0.35	0.95	0.2	0.97	<0.01
T2	3.36 ± 0.79	3.38 ± 0.80	-0.02 ± 0.08	1.00	-0.18	0.14	1	0.01	0.99	<0.01
T3	3.16 ± 0.66	3.20 ± 0.64	-0.04 ± 0.09	0.99	-0.22	0.14	0.97	0.1	0.98	<0.01
ΔT1-T2	5.00 ± 0.65	4.84 ± 0.69	0.16 ± 0.13	1.04	-0.10	0.42	1.04	-0.4	0.96	<0.01
ΔT2-T3	0.20 ± 0.47	0.17 ± 0.52	0.02 ± 0.12	0.64	-0.22	0.25	1.08	-0.03	0.95	<0.01
Mean scaffold area										
T1	8.53 ± 0.62	8.25 ± 0.58	0.28 ± 0.11	1.03	0.07	0.48	0.93	0.3	0.97	<0.01
T2	7.54 ± 0.60	7.40 ± 0.61	0.14 ± 0.11	1.02	-0.07	0.35	0.99	-0.1	0.97	<0.01
T3	7.55 ± 0.71	7.38 ± 0.72	0.27 ± 0.21	1.04	-0.14	0.68	1	-0.3	0.92	<0.01
ΔT1-T2	0.98 ± 0.40	0.85 ± 0.46	0.13 ± 0.13	1.27	-0.12	0.38	1.11	-0.2	0.93	<0.01
ΔT2-T3	-0.12 ± 0.31	0.02 ± 0.28	-0.13 ± 0.23	2.76	-0.59	0.32	0.58	-0.1	0.45	<0.01
Mean coverage area										
T2	4.15 ± 0.55	4.00 ± 0.61	0.15 ± 0.17	1.04	-0.18	0.48	1.07	-0.5	0.93	<0.01
T3	4.30 ± 0.51	4.09 ± 0.48	0.29 ± 0.15	1.07	-0.01	0.58	0.88	0.2	0.91	<0.01
ΔT2-T3	-0.16 ± 0.39	-0.05 ± 0.47	-0.12 ± 0.26	0.49	-0.62	0.39	1.00	-0.1	0.97	<0.01

**Bland-Altman limits of agreement defined as mean ± 1.96 SD of absolute difference. T1 = time point 1: immediately after scaffold implantation, T2 = time point 2: 3 months after scaffold implantation, T3 = time point 3: 6 months after scaffold implantation. SD = standard deviation*

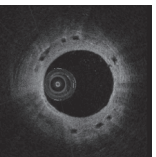

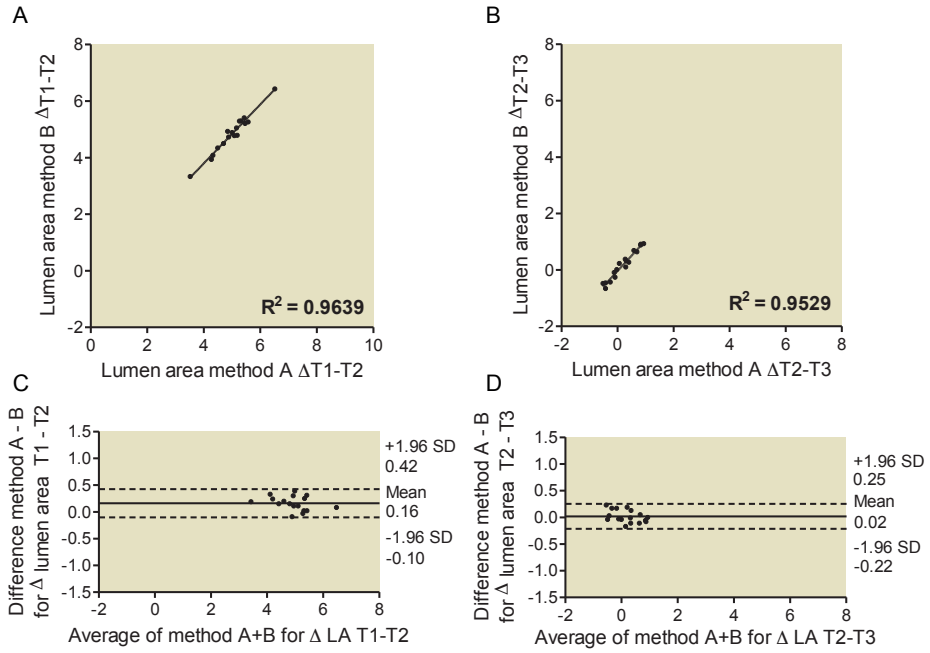

Figure 6 Inter-method variability for the difference in mean lumen area measurements between T1 and T2 and T2 and T3

The linear regression analysis demonstrates high correlation between method A and B for the difference in mean lumen area measurement between T1 and T2 (ΔT1-T2) (A), and between T2 and T3 (ΔT2-T3) (B). The Bland-Altman plots demonstrate the inter-method variability for the difference in mean lumen area between T1 and T2 (ΔT1-T2) (C) and T2 and T3 (ΔT2-T3) (D)

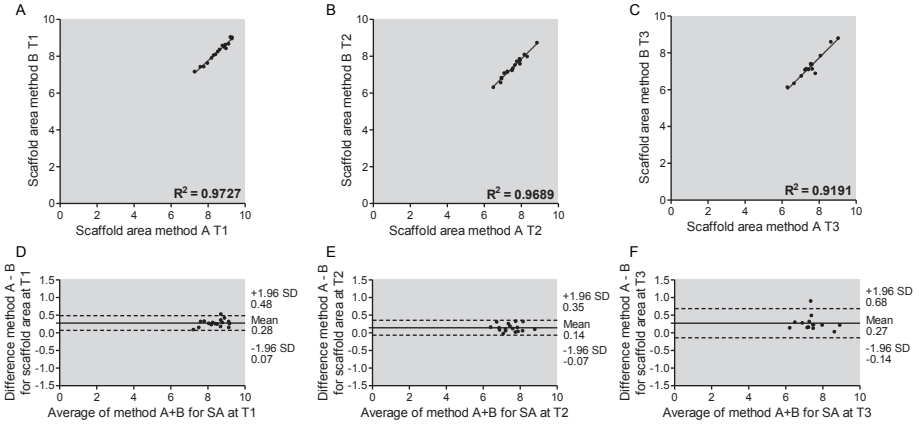

Figure 7 Inter-method variability for scaffold area (mm²) measurements

The linear regression analysis demonstrates very high correlation between method A and B for mean scaffold area (mm²) at T1 (A), T2 (B), T3 (C). The Bland-Altman plots demonstrate the inter-method variability for mean scaffold area (SA; mm²) at T1 (D), T2 (E) and T3 (F)

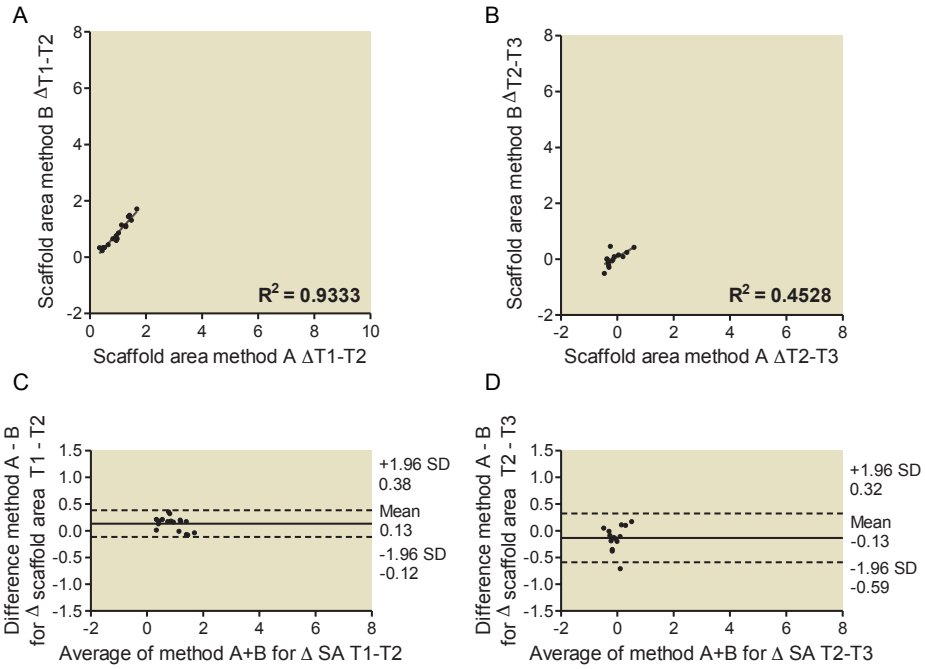

Figure 8 Inter-method variability for the difference in mean scaffold area measurements between T1 and T2 and T2 and T3

The linear regression analysis demonstrates high correlation between method A and B for the difference in mean scaffold area measurement between T1 and T2 (ΔT1-T2) (A), and between T2 and T3 (ΔT2-T3) (B). The Bland-Altman plots demonstrate the inter-method variability for the difference in scaffold lumen area between T1 and T2 (ΔT1-T2) (C) and T2 and T3 (ΔT2-T3) (D)

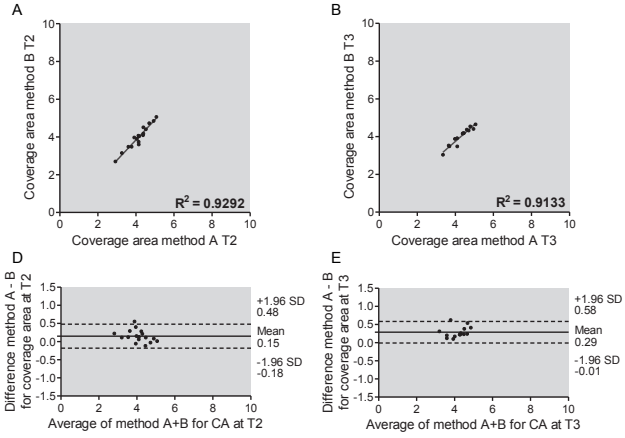

Figure 9 Inter-method variability for coverage area (mm²) measurements

The linear regression analysis demonstrates high correlation between method A and B for mean coverage area (mm²) at T2 (A) and T3 (B). The Bland-Altman plots demonstrate the inter-method variability for mean coverage area (CA; mm²) at T2 (C) and T3 (D)

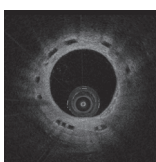

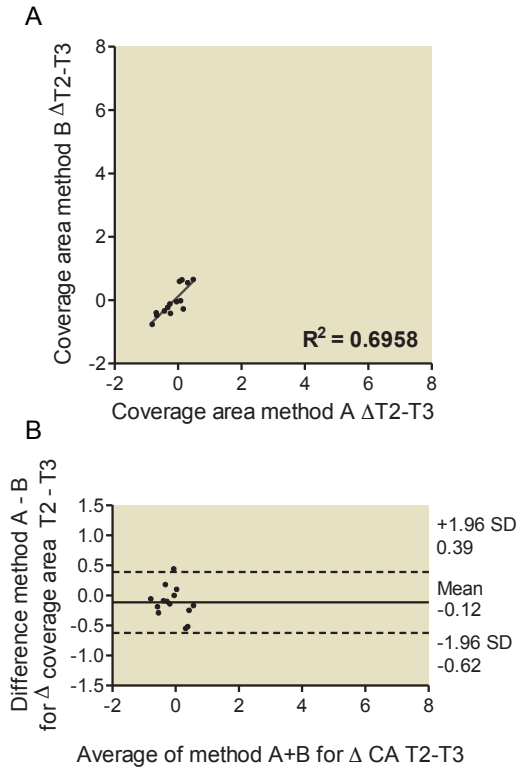

Figure 10 Inter-method variability for the difference in mean coverage area measurements between T1 and T2 and T2 and T3

The linear regression analysis demonstrates high correlation between method A and B for the difference in mean coverage area measurement between T2 and T3 (ΔT2-T3) (A). The Bland-Altman plots demonstrate the inter-method variability for the difference in mean coverage area between T2 and T3 (ΔT2-T3) (B)

Inter-and intra-observer reproducibility

A total of 92 OCT cross-sections per time point were included in the inter- and intra-observer analysis (**Tables 2 to 5**). Bland-Altman analyses for inter-observer reproducibility demonstrated excellent agreement between both observers for all area measurements at all time points (**Figure 11**). Intra-class correlation coefficients ranged from 0.89 to 1.00 at cross-sectional level and from 0.90 to 1.00 at scaffold level (**Tables 2 and 3**). For the intra-observer reproducibility, Bland-Altman analyses demonstrated excellent agreement between the 2 observations for all mean area measurements at all time points (**Figure 12**). Intra-class correlation coefficients ranged from 0.96 to 1.00 at cross-sectional level and from 0.95 to 1.00 at scaffold level (**Tables 4 and 5**).

Table 2 Inter-observer reproducibility at cross-sectional level

	Observer 1	Observer 2	Difference (Obs 1 – Obs 2)	Relative difference	ICC
	Mean ± SD (mm²)	Mean ± SD (mm²)	Mean ± SD (mm²)	(Obs1/Obs2)	
Mean lumen area					
T1	8.15 ± 0.95	8.08 ± 0.93	0.07 ± 0.10	1.01	1.00
T2	3.70 ± 1.27	3.70 ± 1.27	0.00 ± 0.04	1.00	0.99
T3	3.66 ± 0.99	3.66 ± 1.00	0.00 ± 0.05	1.00	1.00
Mean scaffold area					
T1	8.18 ± 0.92	8.16 ± 0.90	0.08 ± 0.11	1.01	0.99
T2	7.45 ± 0.85	7.27 ± 0.87	0.19 ± 0.13	1.03	0.97
T3	7.53 ± 0.90	7.41 ± 0.95	0.18 ± 0.17	1.03	0.96
Mean coverage area					
T2	3.75 ± 0.61	3.52 ± 0.60	0.19 ± 0.13	1.06	0.93
T3	3.90 ± 0.52	3.72 ± 0.55	0.18 ± 0.17	1.05	0.89

ICC = intra-class correlation coefficient for absolute agreement. T1 = time point 1: immediately after scaffold implantation, T2 = time point 2: 3 months after scaffold implantation, T3 = time point 3: 6 months after scaffold implantation. Obs = observer, SD = standard deviation

Table 3 Inter-observer reproducibility at scaffold level

	Observer 1	Observer 2	Difference (Obs 1 – Obs 2)	Relative difference	ICC
	Mean ± SD (mm²)	Mean ± SD (mm²)	Mean ± SD (mm²)	(Obs1/Obs2)	
Mean lumen area					
T1	8.14 ± 0.88	8.07 ± 0.87	0.07 ± 0.04	1.01	1.00
T2	3.68 ± 1.29	3.68 ± 1.29	-0.00 ± 0.02	1.00	1.00
T3	3.65 ± 0.88	3.65 ± 0.89	-0.00 ± 0.02	1.00	1.00
Mean scaffold area					
T1	8.17 ± 0.85	8.13 ± 0.84	0.04 ± 0.08	1.01	1.00
T2	7.43 ± 0.80	7.24 ± 0.78	0.19 ± 0.06	1.03	0.97
T3	7.48 ± 0.78	7.35 ± 0.83	0.13 ± 0.09	1.02	0.98
Mean coverage area					
T2	3.76 ± 0.61	3.55 ± 0.61	0.21 ± 0.02	1.06	0.94
T3	3.90 ± 0.39	3.71 ± 0.42	0.19 ± 0.05	1.05	0.90

ICC = intra-class correlation coefficient for absolute agreement. T1 = time point 1: immediately after scaffold implantation, T2 = time point 2: 3 months after scaffold implantation, T3 = time point 3: 6 months after scaffold implantation. Obs = observer, SD = standard deviation

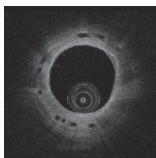

Table 4 Intra-observer reproducibility at cross-sectional level

	Analysis 1	Analysis 2	Difference (An1 – An2)	Relative difference	
	Mean ± SD (mm²)	Mean ± SD (mm²)	Mean ± SD (mm²)	(An1/An2)	ICC
Mean lumen area					
T1	8.15 ± 0.95	8.17 ± 0.93	-0.02 ± 0.10	1.00	0.99
T2	3.70 ± 1.27	3.70 ± 1.27	0.00 ± 0.02	1.00	1.00
T3	3.66 ± 0.99	3.66 ± 1.00	-0.01 ± 0.04	1.00	1.00
Mean scaffold area					
T1	8.18 ± 0.92	8.17 ± 0.93	0,02 ± 0.09	1.00	1.00
T2	7.45 ± 0.85	7.49 ± 0.87	-0.03 ± 0.12	1.00	0.99
T3	7.53 ± 0.90	7.62 ± 0.99	-0.09 ± 0.12	0.99	0.99
Mean coverage area					
T2	3.75 ± 0.61	3.77 ± 0.61	-0.03 ± 0.12	0.99	0.98
T3	3.90 ± 0.52	3.99 ± 0.56	-0.09 ± 0.12	0.98	0.96

ICC = intra-class correlation coefficient for absolute agreement. T1 = time point 1: immediately after scaffold implantation, T2 = time point 2: 3 months after scaffold implantation, T3 = time point 3: 6 months after scaffold implantation. An = analysis, SD = standard deviation

Table 5 Intra-observer reproducibility at scaffold level

	Analysis 1	Analysis 2	Difference (An1 – An2)	Relative difference	
	Mean ± SD (mm²)	Mean ± SD (mm²)	Mean ± SD (mm²)	(An1/An2)	ICC
Mean lumen area					
T1	8.14 ± 0.88	8.16 ± 0.86	-0.02 ± 0.02	1.00	1.00
T2	3.68 ± 1.29	3.69 ± 1.29	-0.00 ± 0.01	1.00	1.00
T3	3.65 ± 0.88	3.66 ± 0.89	-0.01 ± 0.01	1.00	1.00
Mean scaffold area					
T1	8.17 ± 0.85	8.16 ± 0.86	0.02 ± 0.03	1.00	1.00
T2	7.43 ± 0.80	7.47 ± 0.82	-0.04 ± 0.04	0.99	1.00
T3	7.48 ± 0.78	7.59 ± 0.89	-0.11 ± 0.11	0.99	0.99
Mean coverage area					
T2	3.76 ± 0.61	3.79 ± 0.61	-0.03 ± 0.05	0.99	1.00
T3	3.90 ± 0.39	3.99 ± 0.43	0.09 ± 0.12	0.98	0.95

ICC = intra-class correlation coefficient for absolute agreement. T1 = time point 1: immediately after scaffold implantation, T2 = time point 2: 3 months after scaffold implantation, T3 = time point 3: 6 months after scaffold implantation. An = analysis, SD = standard deviation

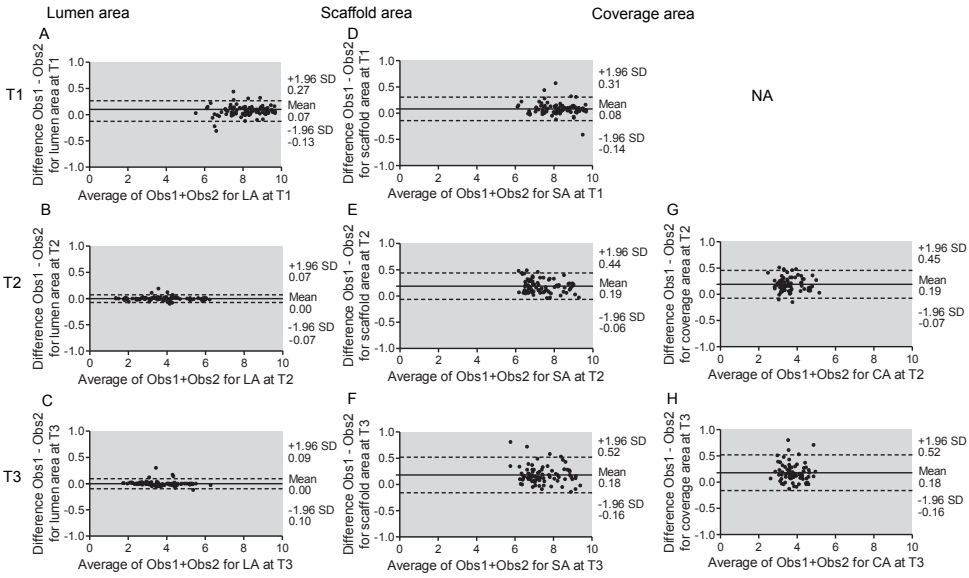

Figure 11 Inter-observer reproducibility

Bland-Altman plots for the inter-observer variability for mean lumen (A to C), mean scaffold (D to F) and mean coverage area (G and H) at the various time points. T = time point, Obs = observer, LA = lumen area (mm²), SA = scaffold area (mm²), CA = coverage area (mm²), SD = standard deviation

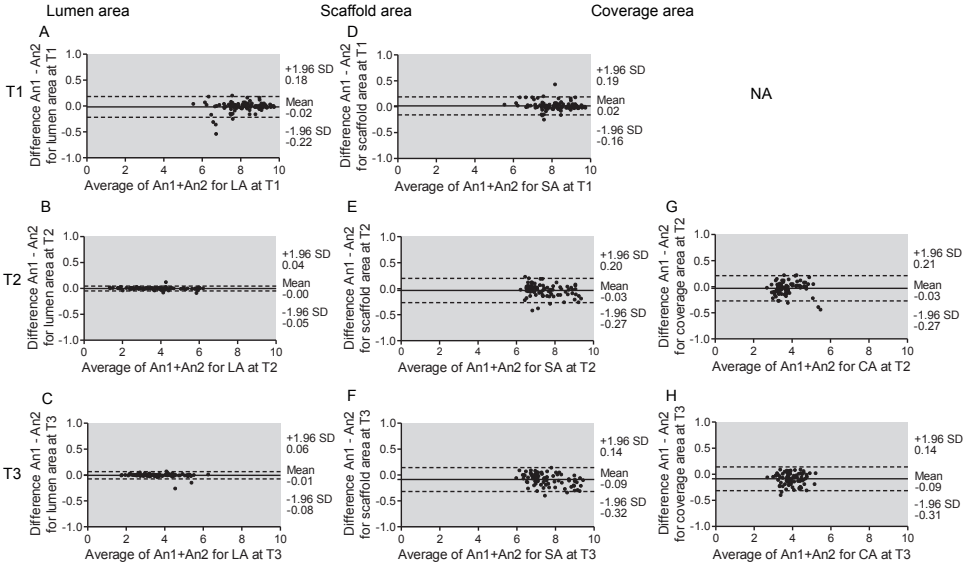

Figure 12 Intra-observer reproducibility

Bland-Altman plots for the intra-observer variability for mean lumen (A to C), mean scaffold (D to F) and mean coverage area (G and H) at the various time points. T = time point, An = analysis, LA = lumen area (mm²), SA = scaffold area (mm²), CA = coverage area (mm²), SD = standard deviation

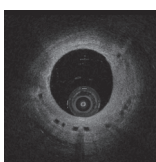

Discussion

In the present study we observed considerable variation in the imaged length of the scaffolded segment, indicating longitudinal displacement of the OCT catheter during pullback acquisition in swine treated with PLLA-based bioresorbable scaffolds. The observed catheter displacement did not affect the reliability of global quantitative OCT area measurements such as mean lumen, mean scaffold and mean coverage area. When not accounted for by the analysis method, however, imaging catheter displacement can cause considerable variation in scaffold length measurements and in the measurements of specific scaffold regions such as side branch take offs.

The presence of longitudinal displacement of the imaging catheter is a long-known pitfall of intravascular imaging and can be attributed to the pullback speed and the catheter's frame acquisition rate. In studies evaluating intravascular ultrasound (IVUS) – that typically uses automated catheter pullback speeds of 0.5-1.0mm/sec and a frame rate of 10-30 frames/sec.[15] – the longitudinal catheter displacement has been described as a consequence of the relative slow pullback speed.[16] When there is a slow pullback speed, the catheter can be displaced during pullback acquisition due to the dynamic movement of the coronary arteries within the cardiac and respiratory cycle. Likewise, longitudinal displacement of the imaging catheter has been observed for the first generation, Time Domain (TD)-OCT catheter. TD-OCT applies higher pullback speeds (1.0-3.0mm/sec) but lower frame rates (5-20 frames/sec) than IVUS. Despite the higher pullback speed compared to IVUS, longitudinal catheter displacement is not alleviated. Consequently, longitudinal catheter displacement during pullback acquisition can cause difficulties interpreting serial stent or scaffold analysis data.[17] FD-OCT, evaluated in the present study, applies a faster pullback speed (20 mm/sec) and frame rate (100 frames/sec) than both IVUS and TD-OCT. Despite the fast data acquisition, we demonstrated the presence of considerable longitudinal catheter displacement. Scaffold length measurements differed between the various time points, with the greatest length difference between two time points corresponding to 29% of the total scaffold length (5.2 of 18mm total scaffold length).

Serial global lumen and scaffold area measurements were however not significantly affected by the longitudinal displacement of the FD-OCT catheter. By comparing two methods for the selection of OCT cross-sections – one commonly used method employing random selection of OCT cross-sections at the consecutive time points (method A), not taking into account the effect of longitudinal catheter displacement, and one method employing accurate co-registration of the cross-sections within the

consecutive time points (method B), taking into account longitudinal displacement of the catheter – we demonstrated that there was high agreement between the methods for global in-vivo quantitative area measurements. Okamura et al. examined the agreement between two consecutively acquired FD-OCT pullbacks from patients treated with elective coronary stent implantation. The ROI was determined in the two FD-OCT pullbacks, and in the corresponding ROI OCT cross-sections were selected at 1-mm longitudinal intervals, not taking into account longitudinal displacement of the FD-OCT catheter. The agreement for mean lumen and scaffold area measurements between the two consecutively acquired pullbacks was high.[18] Jamil et al. [19] evaluated the inter-study variability of FD-OCT by independently analyzing every single cross-section of two repeated pullbacks acquired from patients immediately after stent placement. Per-stent analysis demonstrated small differences between measurements for mean lumen area (relative difference 0.81%) and mean stent area (relative difference 0.93%), demonstrating high reproducibility of two consecutively acquired FD-OCT pullbacks. We observed a comparable high agreement between the two methods for the selection of OCT cross-sections, suggesting minor influence of longitudinal catheter displacement on serial global dimension measurements. The differences between measurements for mean lumen and mean stent area assessed by Jamil et al. were however slightly smaller than what we observed, suggesting that a smaller interval of analysis may reduce the effect of longitudinal catheter displacement.

We furthermore examined the impact of longitudinal catheter displacement on the analysis of specific scaffold regions. The PLLA-based bioresorbable scaffolds are increasingly used in clinical practice outside of controlled studies, resulting in the treatment of patients with more complex lesions, including treatment of longer lesions and treatment with overlapping scaffolds.[20] The accurate evaluation of specific scaffold regions is therefore becoming increasingly important. In the present study, the amount of OCT cross-sections containing a side-branch selected by method A differed, however not statistically significant, between the time points: from T1 to T2, the number of selected OCT cross-sections containing a side branch decreased, whereas from T2 to T3, the number of selected OCT cross-sections increased. Important to note is that the reduction in OCT cross-sections containing a side branch from T1 to T2 could be attributed to neointimal growth at T2, possibly resulting in a diameter reduction of the side branch opening.[21] From T2 to T3, however, the number of OCT cross-sections containing a side branch increased, suggesting that longitudinal catheter displacement can truly affect the assessment of specific scaffold regions when accurate matching of corresponding cross-sections is not performed. More importantly, the fact that the

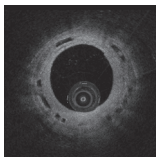

number of selected OCT cross-sections containing a side branch differed between the several time points suggests that for the analysis of specific scaffold regions either a smaller interval of analysis may be beneficial, as has been eluted to by Mehanna et al., who suggested that analysis of specific stent regions should be performed by analyzing all frames,[22] or an analysis method such as method B should be considered.

Important to note is the shortcoming to reconstruct three-dimensional (3D) images when longitudinal catheter displacement is present. The accurate reconstruction of the 3D vessel structure including the scaffold, could enable a more comprehensive assessment of scaffold strut coverage, apposition and side-branch jailing.[23, 24] A study assessing the impact of cardiac motion artefacts on 3D reconstructions of FD-OCT pullbacks demonstrated that faster pullback acquisition with higher frame rates reduces the amount of artefacts caused by cardiac motion.[14] The development of high-speed OCT imaging with faster pullback speeds and higher frame rates might therefore improve the understanding of scaffold strut coverage, apposition and side-branch jailing because of the ability to accurately reconstruct the volumetric 3D vessel including the scaffold.[25]

Inter- and intra-observer reproducibility of quantitative OCT area measurements

The present study demonstrates that FD-OCT allows for the serial analysis of PLLA-based bioresorbable scaffolds in a highly reproducible way. The inter- and intra-observer differences on cross-sectional and scaffold level were low (**Tables 2 to 5**). Likewise, Gomez-Lara et al.[26] reported excellent inter- and intra-observer reproducibility of OCT in assessing bioresorbable vascular scaffolds (ICC for quantitative OCT measurements >0.97). Gonzalo et al.[27] reported on inter- and intra-observer differences in patients undergoing intracoronary OCT after treatment with sirolimus and biolimus-eluting stents. They, similar to what we observed, demonstrated low inter- and intra-observer differences for lumen area measurements and slightly greater for stent area measurements. Okamura et al. evaluated inter- and intra-observer correlation coefficients for lumen area measurements in non-stented coronary arteries of swine. They demonstrated excellent (>0.75) intra-class correlation coefficients, similar to the intra-class correlation coefficients documented in the present study (**Tables 2 to 5**).[14] Concerning scaffold area, the inter-observer analysis of the present study demonstrated low differences for scaffold area at T1, and slightly greater differences at T2 and T3. The intra-observer analysis demonstrated similar results for scaffold area, with the lowest intra-observer variability at T1 and slightly greater variability at T2 and

T3. This finding is not surprising as the use of a semi-automatic contour detection for lumen area helped diminish inter- and intra-observer reproducibility, whereas for scaffold area measurements at follow-up, the manual tracing of the contours and the relatively high amount of coverage could be associated with higher variability. Notably, the coverage observed in the present study was relatively high (coverage area >2mm^2), potentially leading to the inability to segment the scaffold area because of the limited penetration depth of OCT.

Limitations

Swine typically have a higher heart rate compared to humans [28] – the average heart rate of the anesthetized swine in the present study was 109±28 beats/min – resulting in a possibly greater longitudinal displacement of the OCT catheter during pullback acquisition. A previously published study that evaluated the three-dimensional motion of coronary arteries by cine-magnetic resonance imaging (MRI), however, demonstrated that the swine RCA, LAD and LCX displacements appear qualitatively similar to those seen in humans, despite differing heart rates.[29] Furthermore, the presence of longitudinal displacement of the OCT catheter has also been described in humans (**Figure 13**), limiting the accurate reconstruction of the 3D vessel structure.[30] In the **electronic supplementary material** an angiogram and OCT pullback of longitudinal displacement of the FD-OCT catheter in a patient is demonstrated (**Supplementary videos 1 and 2**).

Off-line, manual tracing of scaffold areas after coronary scaffolding is feasible for experienced observers with acceptable reproducibility. It is however time consuming. In the present study, semi-automatic contour detection of the lumen area demonstrated advantages for reproducibility of the data. For scaffold contour and coverage area measurements we demonstrated a slightly higher inter- and intra-observer variability, possibly due to the lack of algorithms for the automatic detection of polymeric scaffold struts. For the automatic detection of metallic stent struts, algorithms have been developed that show high accuracy and high inter-observer agreement.[31, 32] Further development of contour detection algorithms for the detection of polymeric scaffold struts by OCT might help eliminating the remaining small observer-related variability observed in the present study.

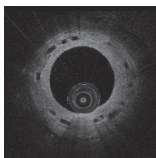

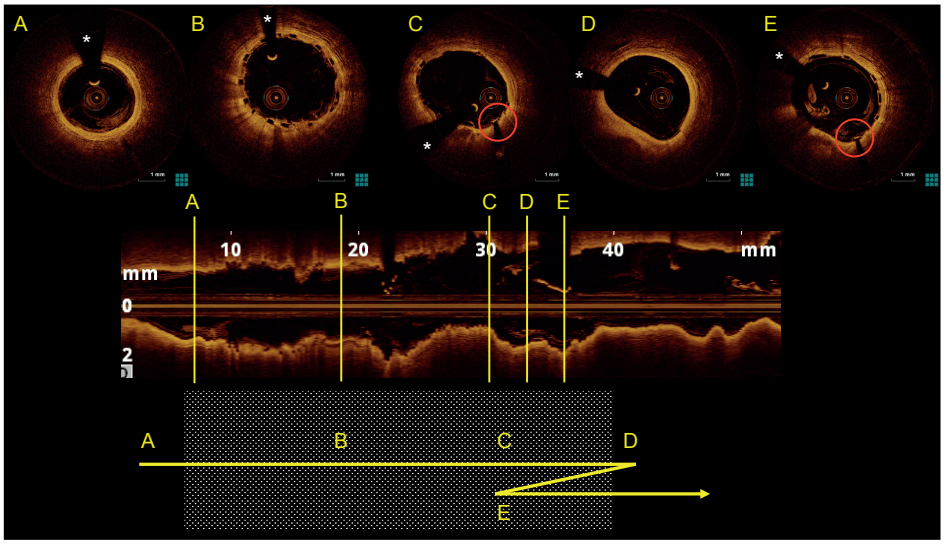

Figure 13 Representation of longitudinal FD-OCT catheter displacement in a patient
The middle panel demonstrates the l-mode of the OCT pullback. The letters A to E indicate the OCT cross-sections that are visualized in the upper panel of the figure. In the lower panel of the figure the displacement of the OCT catheter is schematically depicted, with the letters (A to E) corresponding to the letters in the OCT cross-sections and the longitudinal view of the pullback. In OCT cross-sections C and E the proximal marker of the scaffold is visible (red circle). The asterix (*) indicates the shadow artefact caused by the guide wire

Conclusion

Considerable longitudinal displacement of the FD-OCT catheter was observed, diminishing the number of truly anatomically matching cross-sections in serial investigations. The longitudinal catheter displacement, however, did not affect global dimension measurements such as mean lumen area and mean scaffold area.

References

1. Huang D, Swanson EA, Lin CP, Schuman JS, Stinson WG, Chang W, Hee MR, Flotte T, Gregory K, Puliafito CA, et al. Optical coherence tomography. Science 1991;**254**(5035):1178-81.
2. Regar E, Schaar JA, Mont E, Virmani R, Serruys PW. Optical coherence tomography. Cardiovasc Radiat Med 2003;**4**(4):198-204.
3. Choma M, Sarunic M, Yang C, Izatt J. Sensitivity advantage of swept source and Fourier domain optical coherence tomography. Opt Express 2003;**11**(18):2183-9.
4. Yun SH, Tearney GJ, Vakoc BJ, Shishkov M, Oh WY, Desjardins AE, Suter MJ, Chan RC, Evans JA, Jang IK, Nishioka NS, de Boer JF, Bouma BE. Comprehensive volumetric optical microscopy in vivo. Nat Med 2006;**12**(12):1429-33.
5. Liu B, Brezinski ME. Theoretical and practical considerations on detection performance of time domain, Fourier domain, and swept source optical coherence tomography. J Biomed Opt 2007;**12**(4):044007.
6. van Ditzhuijzen NS, van den Heuvel M, Sorop O, van Duin RW, Krabbendam-Peters I, van Haeren R, Ligthart JM, Witberg KT, Duncker DJ, Regar E, van Beusekom HM, van der Giessen WJ. Invasive coronary imaging in animal models of atherosclerosis. Neth Heart J 2011;**19**(10):442-6.
7. Ormiston JA, Serruys PW, Regar E, Dudek D, Thuesen L, Webster MW, Onuma Y, Garcia-Garcia HM, McGreevy R, Veldhof S. A bioabsorbable everolimus-eluting coronary stent system for patients with single de-novo coronary artery lesions (ABSORB): a prospective open-label trial. Lancet 2008;**371**(9616):899-907.
8. Serruys PW, Ormiston JA, Onuma Y, Regar E, Gonzalo N, Garcia-Garcia HM, Nieman K, Bruining N, Dorange C, Miquel-Hebert K, Veldhof S, Webster M, Thuesen L, Dudek D. A bioabsorbable everolimus-eluting coronary stent system (ABSORB): 2-year outcomes and results from multiple imaging methods. Lancet 2009;**373**(9667):897-910.
9. Serruys PW, Onuma Y, Ormiston JA, de Bruyne B, Regar E, Dudek D, Thuesen L, Smits PC, Chevalier B, McClean D, Koolen J, Windecker S, Whitbourn R, Meredith I, Dorange C, Veldhof S, Miquel-Hebert K, Rapoza R, Garcia-Garcia HM. Evaluation of the second generation of a bioresorbable everolimus drug-eluting vascular scaffold for treatment of de novo coronary artery stenosis: six-month clinical and imaging outcomes. Circulation 2010;**122**(22):2301-12.
10. Hamers R, Bruining N, Knook M, Sabate M, Roelandt JRTC. A novel approach to quantitative analysis of intravascular ultrasound images. Computers In Cardiology 2001:589-92.
11. Brugaletta S, Radu MD, Garcia-Garcia HM, Heo JH, Farooq V, Girasis C, van Geuns RJ, Thuesen L, McClean D, Chevalier B, Windecker S, Koolen J, Rapoza R, Miquel-Hebert K, Ormiston J, Serruys PW. Circumferential evaluation of the neointima by optical coherence tomography after ABSORB bioresorbable vascular scaffold implantation: can the scaffold cap the plaque? Atherosclerosis 2012;**221**(1):106-12.
12. Bland JM, Altman DG. Statistical methods for assessing agreement between two methods of clinical measurement. Lancet 1986;**1**(8476):307-10.
13. Haber M, Barnhart HX. Coefficients of agreement for fixed observers. Stat Methods Med Res 2006;**15**(3):255-71.

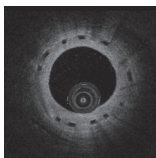

14. Okamura T, Onuma Y, Garcia-Garcia HM, Bruining N, Serruys PW. High-speed intracoronary optical frequency domain imaging: implications for three-dimensional reconstruction and quantitative analysis. EuroIntervention 2012;**7**(10):1216-26.
15. Regar E. Invasive imaging technologies: can we reconcile light and sound? J Cardiovasc Med (Hagerstown) 2011;**12**(8):562-70.
16. Arbab-Zadeh A, DeMaria AN, Penny WF, Russo RJ, Kimura BJ, Bhargava V. Axial movement of the intravascular ultrasound probe during the cardiac cycle: implications for three-dimensional reconstruction and measurements of coronary dimensions. Am Heart J 1999;**138**(5 Pt 1):865-72.
17. Sihan K, Botha C, Post F, de Winter S, Gonzalo N, Regar E, Serruys PW, Hamers R, Bruining N. Retrospective image-based gating of intracoronary optical coherence tomography: implications for quantitative analysis. EuroIntervention 2011;**6**(9):1098-103.
18. Okamura T, Garg S, Gutierrez-Chico JL, Shin ES, Onuma Y, Garcia-Garcia HM, Rapoza RJ, Sudhir K, Regar E, Serruys PW. In vivo evaluation of stent strut distribution patterns in the bioabsorbable everolimus-eluting device: an OCT ad hoc analysis of the revision 1.0 and revision 1.1 stent design in the ABSORB clinical trial. EuroIntervention 2010;**5**(8):932-8.
19. Jamil Z, Tearney G, Bruining N, Sihan K, van Soest G, Ligthart J, van Domburg R, Bouma B, Regar E. Interstudy reproducibility of the second generation, Fourier domain optical coherence tomography in patients with coronary artery disease and comparison with intravascular ultrasound: a study applying automated contour detection. Int J Cardiovasc Imaging 2013;**29**(1):39-51.
20. Farooq V, Gogas BD, Okamura T, Heo JH, Magro M, Gomez-Lara J, Onuma Y, Radu MD, Brugaletta S, van Bochove G, van Geuns RJ, Garcia-Garcia HM, Serruys PW. Three-dimensional optical frequency domain imaging in conventional percutaneous coronary intervention: the potential for clinical application. Eur Heart J 2013;**34**(12):875-85.
21. Kyono H, Guagliumi G, Sirbu V, Rosenthal N, Tahara S, Musumeci G, Trivisonno A, Bezerra HG, Costa MA. Optical coherence tomography (OCT) strut-level analysis of drug-eluting stents (DES) in human coronary bifurcations. EuroIntervention 2010;**6**(1):69-77.
22. Mehanna EA, Attizzani GF, Kyono H, Hake M, Bezerra HG. Assessment of coronary stent by optical coherence tomography, methodology and definitions. Int J Cardiovasc Imaging 2011;**27**(2):259-69.
23. Farooq V, Serruys PW, Heo JH, Gogas BD, Onuma Y, Perkins LE, Diletti R, Radu MD, Raber L, Bourantas CV, Zhang Y, van Remortel E, Pawar R, Rapoza RJ, Powers JC, van Beusekom HM, Garcia-Garcia HM, Virmani R. Intracoronary optical coherence tomography and histology of overlapping everolimus-eluting bioresorbable vascular scaffolds in a porcine coronary artery model: the potential implications for clinical practice. JACC Cardiovasc Interv 2013;**6**(5):523-32.
24. Karanasos A, Tu S, van der Linden M, van Weenen S, Ligthart J, Regar E. Online 3-dimensional rendering of optical coherence tomography images for the assessment of bifurcation intervention. Can J Cardiol 2012;**28**(6):759 e1-3.
25. Wang T, Wieser W, Springeling G, Beurskens R, Lancee CT, Pfeiffer T, van der Steen AF, Huber R, van Soest G. Intravascular optical coherence tomography imaging at 3200 frames per second. Opt Lett 2013;**38**(10):1715-7.
26. Gomez-Lara J, Brugaletta S, Diletti R, Gogas BD, Farooq V, Onuma Y, Gobbens P, Van Es GA, Garcia-Garcia HM, Serruys PW. Agreement and reproducibility of gray-scale intravas-

cular ultrasound and optical coherence tomography for the analysis of the bioresorbable vascular scaffold. Catheter Cardiovasc Interv 2011;**79**(6):890-902.
27. Gonzalo N, Garcia-Garcia HM, Serruys PW, Commissaris KH, Bezerra H, Gobbens P, Costa M, Regar E. Reproducibility of quantitative optical coherence tomography for stent analysis. EuroIntervention 2009;**5**(2):224-32.
28. van den Heuvel M, Sorop O, Koopmans SJ, Dekker R, de Vries R, van Beusekom HM, Eringa EC, Duncker DJ, Danser AH, van der Giessen WJ. Coronary microvascular dysfunction in a porcine model of early atherosclerosis and diabetes. Am J Physiol Heart Circ Physiol 2012;**302**(1):H85-94.
29. Schmidt EJ, Yoneyama R, Dumoulin CL, Darrow RD, Klein E, Kiruluta AJ, Hayase M. 3D coronary motion tracking in swine models with MR tracking catheters. J Magn Reson Imaging 2009;**29**(1):86-98.
30. Ha J, Yoo H, Tearney GJ, Bouma BE. Compensation of motion artifacts in intracoronary optical frequency domain imaging and optical coherence tomography. Int J Cardiovasc Imaging 2012;**28**(6):1299-304.
31. Wang A, Eggermont J, Dekker N, Garcia-Garcia HM, Pawar R, Reiber JH, Dijkstra J. Automatic stent strut detection in intravascular optical coherence tomographic pullback runs. Int J Cardiovasc Imaging 2013;**29**(1):29-38.
32. Xu C, Schmitt JM, Akasaka T, Kubo T, Huang K. Automatic detection of stent struts with thick neointimal growth in intravascular optical coherence tomography image sequences. Phys Med Biol 2011;**56**(20):6665-75.

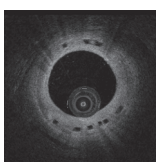

Part II

Preclinical coronary atherosclerosis development

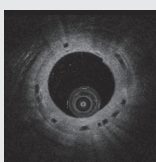

Invasive coronary imaging in animal models of atherosclerosis

NS van Ditzhuijzen*, M van den Heuvel*, O Sorop, RW van Duin, I Krabbendam-Peters, R van Haeren, JM Ligthart, KT Witberg, DJ Duncker, E Regar, HM van Beusekom, WJ van der Giessen

Neth Heart J. 2011 Oct;19(10):442-6

**Equal contribution*

5

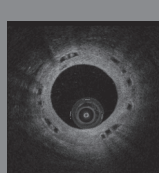

Abstract

Atherosclerosis is a complex disease that is influenced by a multitude of environmental factors. Animal models have enhanced our understanding of the pathogenesis of atherosclerosis development but the need for an experimental disease model that mimics human atherosclerosis remains. Since pigs have a highly similar anatomy and physiology of the coronary system to that of humans, it is an excellent model to use for the study of coronary artery disease (CAD), also with respect to the development of new diagnostic and therapeutic interventions. Invasive coronary imaging modalities such as optical coherence tomography and grey-scale intravascular ultrasound are designed to gain more information about the size and composition of a coronary lesion. Therefore, we describe the most relevant animal models of atherosclerosis, while focusing on CAD development and the use of coronary diagnostic and therapeutic interventions. In addition, we present preliminary data of a swine model that may be used for the investigation of experimental atherosclerosis using intracoronary imaging techniques.

Experimental disease models have enhanced our understanding of the pathogenesis of atherosclerosis development. For example, insight has been gained into the role of the endothelium, lipids, platelets and inflammation, as well as into potential diagnostic and therapeutic interventions. Moreover, transgenic and knock-out technologies have become a widespread approach and this is a growing field to assess the role of individual genes in vascular biology and pathology. However, atherosclerosis is most of all a multifactorial disease, influenced by a multitude of environmental factors. Therefore, it is important to also study non-transgenic animal models that closely resemble the human situation with atherosclerotic lesions at anatomical locations that mimic the clinical manifestation of the disease, e.g. coronary artery disease (CAD). Although no model completely mimics human atherosclerosis, much can be learned from existing models in the study of this disease, also with respect to the development of new interventions. Here, we describe the most relevant animal models of atherosclerosis, while focusing on CAD development and the use of coronary diagnostic and therapeutic interventions. Here, we describe the most relevant animal models of atherosclerosis, while focusing on CAD development and the use of coronary diagnostic and therapeutic interventions. In addition, we show examples of features of a large diseased animal model including pictures of invasive coronary imaging.

Small versus large animal models

Small animal models, primarily small rodents and rabbits, have been used extensively in atherosclerosis research. Some of the reasons include low costs, availability, and easy usability (**Table 1**). However, mice do not spontaneously develop atherosclerosis without genetic manipulation since they have a lipid profile that is different from the human. Yet, due to genetic modification and cross-breeding specific strains can be generated and used to unravel molecular mechanisms involved in the atherosclerosis process.[1] However, transgenic mouse models do not typically develop advanced lesions, including plaque rupture and thrombosis [2], which is typical in patients presenting with symptomatic disease. When size becomes more important, small animal models need to be complemented by larger animal models in which vessel characteristics are more similar to human arteries. The rabbit model on a high cholesterol diet has been widely used in the study of experimental atherosclerosis (**Table 1**). Combined with arterial wall injury, lesions at least partly resembling human plaque will develop in the aorta or iliac arteries of this model.[3] However, when coronary atherosclerosis is the study object, pigs seem to be the most representative model (**Table 1**). Pigs

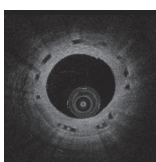

have a highly similar anatomy and physiology of the coronary system as compared to humans.[4] In addition, with use of toxin-mediated pancreatic damage and a high fat diet, human diabetes mellitus (DM)-like metabolic alterations will develop, [5] followed by coronary lesions resembling the human condition closely with even some characteristics of vulnerable plaque.[6, 7] Historically monkeys have also been considered to be a good model of human atherosclerosis (**Table 1**); in particular the effects of hormones and the role of behaviour can be studied with this model.[8, 9] However, nowadays monkeys are not widely used due to obvious species-specific ethical concerns and costs.[2]

In the validation process of coronary interventional devices and therapies for diagnosis and treatment of human CAD, both healthy rabbit [10] and pig models [11] have been used extensively, although the rat model has also been used occasionally [12] (**Table 1**). In these models, arterial overstretch injury with stenting will result in a restenosis process with re-endothelialisation, inflammation and neointima formation.

Table 1 Animal models of atherosclerosis

Animal model	Advantages	Limitations
Mouse	1 Rapid development of atherosclerotic plaque 2 Short reproductive cycle + large litters 3 Well-known genome + genome manipulation possible 4 Cheap	1 Limited resemblance to humans 2 Limited complex atherosclerotic lesion formation 3 Very high levels of blood lipids + different lipid profile
Rat	1 Useful as restenosis model 2 Cheap	1 No development of atherosclerotic lesions
Rabbit	1 Fibroatheroma lesions 2 Useful as restenosis model 3 Affordable	1 Need for high plasma cholesterol levels to develop atherosclerosis 2 No plaque rupture model 3 Model for neointima formation + re-endothelialisation rather than atherosclerosis 4 Coronary evaluation difficult
Pig	1 Atherosclerotic lesions more similar to human disease 2 Blood lipids more in human range 3 Invasive coronary imaging possible Post-intervention: 4 Useful as restenosis model 5 Useful for detailed coronary endothelial function studies	1 Expensive 2 Difficult to handle due to size 3 Limited genomic tools
Monkey	1 Atherosclerotic lesions more similar to human disease 2 Influence of behavioural factors including psychosocial stress 3 Influence of hormonal status	1 Ethical concerns 2 Very expensive 3 Difficult to handle

However, these are healthy animal models in which the vascular healing response occurs faster than in diseased humans.[10, 11] Therefore, the USA Food and Drug Administration proposed a guidance (2008) that new coronary diagnostic and therapeutic interventional devices need to be tested in more clinically relevant animal models of disease. Since the porcine model is the only model in which CAD can be truly studied and catheters and coronary interventional devices can be applied to the vascular bed they are designed for, this model might be the most suitable.[13] New types of invasive coronary imaging techniques have already been applied in the pig model, e.g. optical coherence tomography (OCT) in healthy porcine coronaries [14] and intravascular ultrasound (IVUS) in diseased porcine coronaries.[7]

Present Animal Model

In light of the considerations outlined above, the present study was undertaken to investigate coronary atherosclerosis development over time with the use of a diseased porcine model. The study was performed in accordance with the Guide for Care and Use of Laboratory Animals (NIH Publication No. 85-23, revised 1996), and with approval of the Erasmus MC Animal Care committee. For this purpose, diabetes was induced in a subgroup of male crossbred (Yorkshire x Landrace) pigs by single dose injection of streptozotocin (140 mg/kg) to give a subtotal destruction of pancreatic beta-cells, as described previously.[5] After two weeks of stable DM induction, a high fat atherogenic diet was introduced to all pigs. The pigs (diabetic: n=8; non-diabetic: n=7) were adjusted to this diet and followed up to study atherosclerosis development over time up to 15 months. Similar growth patterns were maintained in all pigs via adjustment of individual caloric intake. Moreover, blood glucose levels were monitored in diabetic pigs and insulin therapy was started only when plasma ketones appeared to prevent severe DM-related complications. Anaesthetised pigs were imaged at 9, 12 and 15 months of study duration by two invasive coronary imaging modalities. Moreover, arterial blood samples were taken at these time points. A subgroup of pigs (n=5) was sacrificed at 12 months, the remaining animals (n=10) at 15 months to obtain coronary tissue for histology. Afterwards, plasma concentrations of glucose, total cholesterol, and low and high density lipoprotein (LDL and HDL) cholesterol were measured at the clinical chemical laboratory of the Erasmus MC using standard protocols.

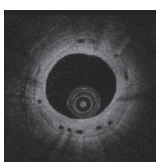

Imaging Modalities

Two invasive coronary imaging modalities were used in the present study: OCT and gray-scale IVUS. OCT, using an infrared light source, has an imaging depth of approximately 1.5 mm into tissue, an axial resolution of 10-15 µm and a lateral resolution of 25-40 µm. This image resolution of OCT offers the potential to assess coronary atherosclerosis in detail.[15, 16] Evaluation of atherosclerosis by OCT was performed in vivo in all pigs at 9, 12 and 15 months using the C7 XR Fourier-Domain OCT system (St. Jude Medical, Westford, MA, USA). Cross-sectional images were acquired at 100 frames per second with an automatic pullback speed of 20 mm/s.

The limited penetration depth of OCT is a shortcoming for the assessment of the total vessel wall, particularly in case of a diseased vessel. Therefore, in case of a plaque thickness >1.5 mm, evaluation of the plaque was done by gray-scale IVUS using an automated pullback speed of 0.5 mm/s (Atlantis SR Pro, Boston Scientific Corp., Natick, MA, USA). During pullback acquisition, images were obtained at a rate of 30 frames/s. This technique, using sound instead of light, has an axial resolution of 80-200 µm and a lateral resolution of 200-400 µm. The penetration depth is 4–8 mm, which permits visualisation of the total vessel wall and therefore precise assessment of the extent of atherosclerosis within a segment of a coronary artery.[17]

Preliminary Results

In diabetic pigs, plasma glucose levels were elevated at every measured time point as compared with the non-diabetic pigs (**Table 2**, $P<0.05$). Moreover in this group of pigs, plasma triglycerides were increased over time (**Table 2**, $P<0.05$) as well. Since both groups were fed an atherogenic diet, both showed elevated total cholesterol, LDL and HDL levels, which were not different over time (**Table 2**). In summary, diabetic pigs showed human-like DM characteristics of hyperglycaemia and triglyceridaemia, whereas all pigs showed evidence of hypercholesterolaemia.

These metabolic alterations were accompanied by coronary atherosclerosis development. Indeed, at 9 months small early lesions could be detected in the coronary arteries of most pigs, specifically seen with OCT imaging (**Figure 1A**). With IVUS this early stage of atherosclerosis was not visible (**Figure 1B**). Over time (12 and 15 months), these lesions showed progression, both in size and in quantity as exemplified with OCT and IVUS (**Figure 1C to F**). Histology at 12 months confirmed the formation of more complex coronary atherosclerosis at this time point, consisting of lipid accumulation and calcification also seen on IVUS (**Figure 2**). All pigs were sacrificed at 15 months

because of the attained body weight and related handling difficulties (diabetic vs. non-diabetic: 97±3 vs. 96±1 kg).

Table 2 Plasma characteristics

Plasma markers	Diabetic pigs	Non-diabetic pigs	Two-way ANOVA
Glucose (mmol/l)			
9 months	15 ± 2.9*	4.1 ± 0.27	P<0.01†
12 months	13 ± 2.3*	4.5 ± 0.47	
15 months	18 ± 4.5*	5.1 ± 0.42	
Triglycerides (mmol/l)			
9 months	1.15 ± 0.26	0.64 ± 0.27	P=0.02†
12 months	0.95 ± 0.25	0.44 ± 0.08	
15 months	1.26 ± 0.50	0.64 ± 0.19	
Cholesterol (mmol/l)			
9 months	20 ± 2.0	20 ± 2.6	P=0.86
12 months	18 ± 1.8	19 ± 2.0	
15 months	17 ± 1.7	18 ± 2.7	
LDL cholesterol (mmol/l)			
9 months	17 ± 1.9	16 ± 2.2	P=0.75
12 months	15 ± 1.6	15 ± 1.9	
15 months	14 ± 1.7	15 ± 2.5	
HDL cholesterol (mmol/l)			
9 months	5.2 ± 0.22	5.8 ± 0.21	P=0.13
12 months	5.7 ± 0.31	5.7 ± 0.31	
15 months	5.1 ± 0.40	5.7 ± 0.35	

*Values are mean ± SEM, *P<0.05 diabetic vs. non-diabetic pigs at corresponding time points, † diabetic vs. non-diabetic pigs over time. LDL = low density lipoprotein; HDL = high density lipoprotein*

Conclusion

Different animal models are useful to study different aspects in the process of atherosclerosis development (**Table 1**). However, for the study of CAD and related diagnostic and therapeutic interventions, a porcine disease model seems most suitable. In the presence of several metabolic alterations, lesions develop within 9 to 12 months, closely resembling human coronary atherosclerotic plaques upon examination by histology.

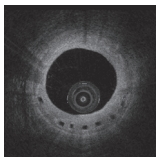

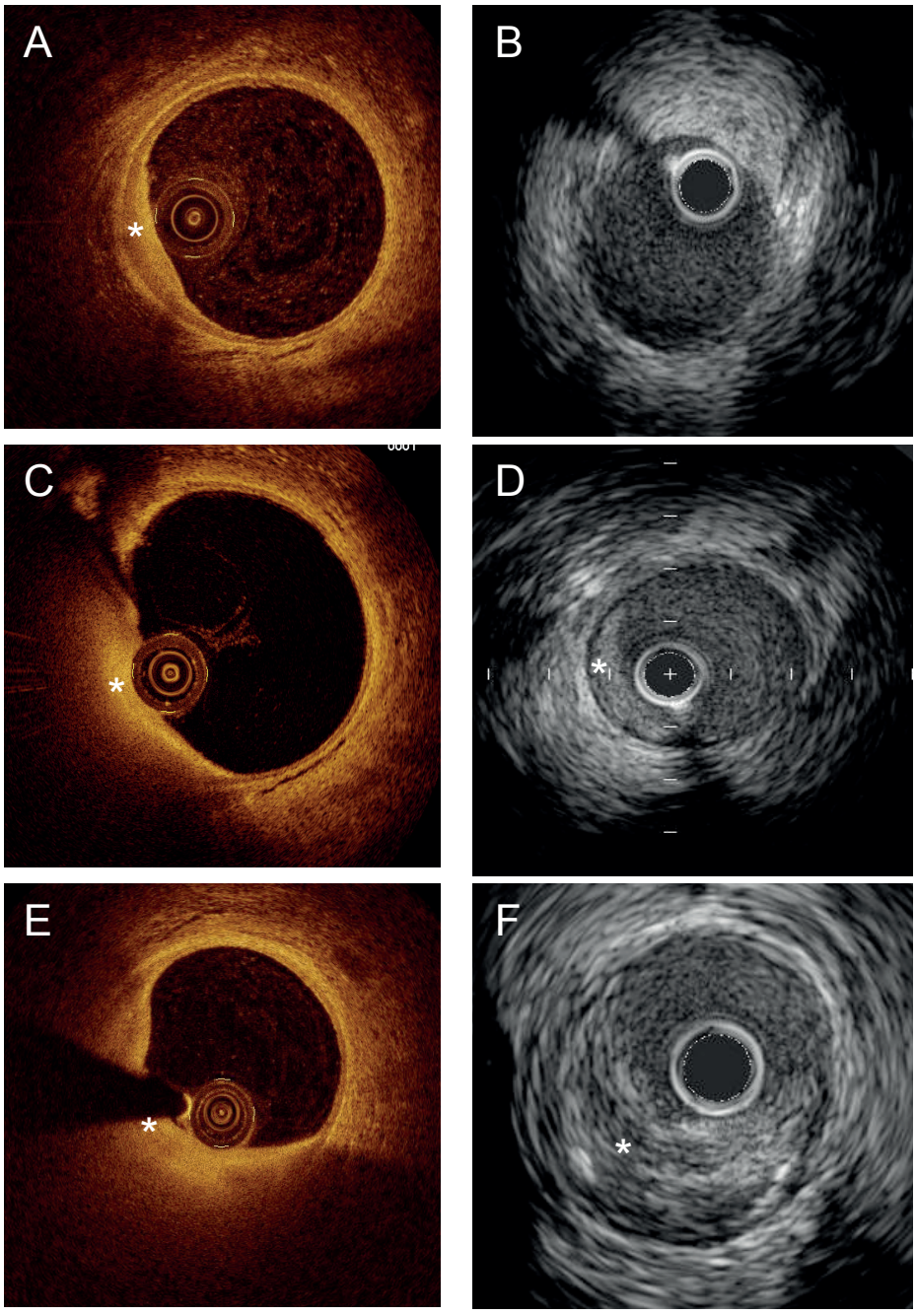

Figure 1 Typical example of the development of an atherosclerotic plaque over time on OCT and IVUS in a diabetic pig

A) OCT of intimal hyperplasie at 9 months (*); B) IVUS of the same cross-section as shown in (A) fails to clearly detect the early lesion; C and D) OCT and IVUS of the growing plaque at 12 months (*); E and F) OCT and IVUS of the same growing plaque at 15 months (*)

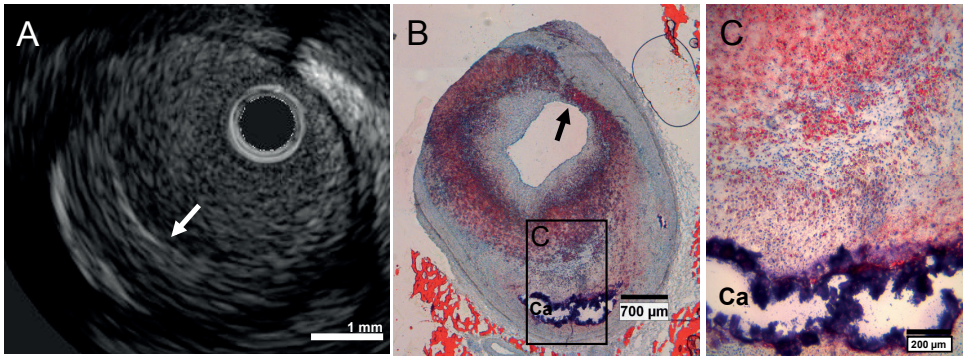

Figure 2 Typical example of IVUS (A) and histology (B and C) of a coronary atherosclerotic plaque in a diabetic pig

A) IVUS of the same plaque as seen in B) and C) with deep calcium (white arrow). B) and C) show an overview and detail of the plaque with circumferential lipid accumulation (stained red) and deep calcification (Ca, remaining rim stained blue). The coronary plaque even shows the presence of a thin fibrous cap (black arrow) overlying the superficial lipid rich tissue, showing a likeness to a thin cap fibrous atheroma. [18] *Oil-red-O stain, bar in B) is 700 µm, bar in C) is 200 µm*

In addition, examples from this model show that OCT and gray-scale IVUS appear to be highly complementary imaging modalities for the evaluation of the development of coronary atherosclerotic plaque over time. The present preliminary results indicate that these modalities can be used for plaque characterisation in vivo, making this large diseased animal model ideal for studying new coronary diagnostic and therapeutic interventions.

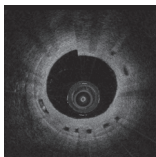

References

1. Bentzon JF, Falk E. Atherosclerotic lesions in mouse and man: is it the same disease? Curr Opin Lipidol 2010;21(5):434-40.
2. Badimon L. Atherosclerosis and thrombosis: lessons from animal models. Thromb Haemost 2001;86(1):356-65.
3. Aikawa M, Sugiyama S, Hill CC, Voglic SJ, Rabkin E, Fukumoto Y, Schoen FJ, Witztum JL, Libby P. Lipid lowering reduces oxidative stress and endothelial cell activation in rabbit atheroma. Circulation 2002;106(11):1390-6.
4. Duncker DJ, Bache RJ. Regulation of coronary blood flow during exercise. Physiol Rev 2008;88(3):1009-86.
5. Koopmans SJ, Mroz Z, Dekker R, Corbijn H, Ackermans M, Sauerwein H. Association of insulin resistance with hyperglycemia in streptozotocin-diabetic pigs: effects of metformin at isoenergetic feeding in a type 2-like diabetic pig model. Metabolism 2006;55(7):960-71.
6. Gerrity RG, Natarajan R, Nadler JL, Kimsey T. Diabetes-induced accelerated atherosclerosis in swine. Diabetes 2001;50(7):1654-65.
7. Chatzizisis YS, Jonas M, Coskun AU, Beigel R, Stone BV, Maynard C, Gerrity RG, Daley W, Rogers C, Edelman ER, Feldman CL, Stone PH. Prediction of the localization of high-risk coronary atherosclerotic plaques on the basis of low endothelial shear stress: an intravascular ultrasound and histopathology natural history study. Circulation 2008;117(8):993-1002.
8. Clarkson TB, Mehaffey MH. Coronary heart disease of females: lessons learned from nonhuman primates. Am J Primatol 2009;71(9):785-93.
9. Shively CA, Musselman DL, Willard SL. Stress, depression, and coronary artery disease: modeling comorbidity in female primates. Neurosci Biobehav Rev 2009;33(2):133-44.
10. Nakazawa G, Finn AV, Ladich E, Ribichini F, Coleman L, Kolodgie FD, Virmani R. Drug-eluting stent safety: findings from preclinical studies. Expert Rev Cardiovasc Ther 2008;6(10):1379-91.
11. van den Heuvel M, Sorop O, Batenburg WW, Bakker CL, de Vries R, Koopmans SJ, van Beusekom HM, Duncker DJ, Danser AH, van der Giessen WJ. Specific coronary drug-eluting stents interfere with distal microvascular function after single stent implantation in pigs. JACC Cardiovasc Interv 2010;3(7):723-30.
12. Langeveld B, Roks AJ, Tio RA, van Boven AJ, van der Want JJ, Henning RH, van Beusekom HM, van der Giessen WJ, Zijlstra F, van Gilst WH. Rat abdominal aorta stenting: a new and reliable small animal model for in-stent restenosis. J Vasc Res 2004;41(5):377-86.
13. Granada JF, Kaluza GL, Wilensky RL, Biedermann BC, Schwartz RS, Falk E. Porcine models of coronary atherosclerosis and vulnerable plaque for imaging and interventional research. EuroIntervention 2009;5(1):140-8.
14. Tearney GJ, Jang IK, Kang DH, Aretz HT, Houser SL, Brady TJ, Schlendorf K, Shishkov M, Bouma BE. Porcine coronary imaging in vivo by optical coherence tomography. Acta Cardiol 2000;55(4):233-7.
15. Yabushita H, Bouma BE, Houser SL, Aretz HT, Jang IK, Schlendorf KH, Kauffman CR, Shishkov M, Kang DH, Halpern EF, Tearney GJ. Characterization of human atherosclerosis by optical coherence tomography. Circulation 2002;106(13):1640-5.

16. Regar E, van Soest G, Bruining N, Constantinescu AA, van Geuns RJ, van der Giessen W, Serruys PW. Optical coherence tomography in patients with acute coronary syndrome. EuroIntervention 2010;6 Suppl G:G154-60.
17. Mintz GS, Nissen SE, Anderson WD, Bailey SR, Erbel R, Fitzgerald PJ, Pinto FJ, Rosenfield K, Siegel RJ, Tuzcu EM, Yock PG. American College of Cardiology Clinical Expert Consensus Document on Standards for Acquisition, Measurement and Reporting of Intravascular Ultrasound Studies (IVUS). A report of the American College of Cardiology Task Force on Clinical Expert Consensus Documents. J Am Coll Cardiol 2001;37(5):1478-92.
18. Virmani R, Burke AP, Farb A, Kolodgie FD. Pathology of the vulnerable plaque. J Am Coll Cardiol 2006;47(8 Suppl):C13-8.

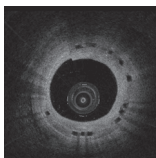

Serial coronary imaging of early atherosclerosis development in fast-food fed diabetic and non-diabetic swine

N.S. van Ditzhuijzen, M. van den Heuvel, O. Sorop, A. Rossi, N. Bruining, S. Roest, J. Ligthart, K. Witberg, F. Zijlstra, D.J. Duncker, H.M.M. van Beusekom, E. Regar

JACC Basic to Translational Science. 2016 Oct;449-6

6

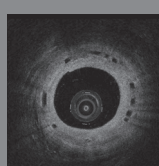

Abstract

Patients with diabetes mellitus (DM) are at increased risk of atherosclerosis-related events compared to non-DM (NDM) patients. With an expected worldwide epidemic of DM, early detection of anatomic and functional coronary atherosclerotic changes is gaining attention. To improve our understanding of early atherosclerosis development, we studied a swine model that gradually developed coronary atherosclerosis. Interestingly, optical coherence tomography (OCT), near-infrared spectroscopy (NIRS), vascular function testing, and histology demonstrated no differences between development of early atherosclerosis in fast-food-fed (FF) DM swine and that in FF-NDM swine. Coronary computed tomography angiography did not detect early atherosclerosis, but OCT and NIRS demonstrated coronary atherosclerosis development in FF-DM and FF-NDM swine.

Introduction

Patients with diabetes mellitus (DM) have a 2- to 6-fold increased risk to encounter atherosclerosis-related events compared to their non-DM (NDM) counterparts.[1] With a worldwide DM epidemic expected, early detection of anatomical and functional atherosclerotic changes in the coronary vasculature is gaining attention. However, patients typically present to the clinician with advanced atherosclerotic disease, thus complicating the study of early atherosclerosis development.

Animal models may provide a solution. Several small animal models, such as a rodent model, have been used to unravel disease mechanisms of coronary artery disease, but their ability to mimic human coronary artery disease is limited.[2] The swine coronary artery model can be especially suitable for evaluation of human-like coronary artery disease development. First, the anatomy and physiology of swine hearts are similar to those of human hearts. Second, swine can be rendered diabetic by injection of streptozotocin. Third, patient-like spontaneous coronary atherosclerosis development can be mimicked by additionally feeding the swine a high-cholesterol, high-sugar diet[3] and fourth, in vivo longitudinal invasive and noninvasive imaging can be performed using imaging techniques such as optical coherence tomography (OCT), near-infrared spectroscopy (NIRS), and coronary computed tomography angiography (CCTA).[4] Ex-vivo coronary endothelial function can be tested to compare functional to morphological coronary changes and histology can be performed to assess the magnitude of coronary and aortic atherosclerosis at different time-points.[4, 5]

Because there is little understanding about whether DM affects atherosclerosis development at the onset of coronary artery disease, the aim of our observational study was to assess whether DM affects early atherosclerosis development as assessed by OCT, NIRS and CCTA in swine fed a high-cholesterol, high sugar ('fast-food') diet.

Methods

This experimental study was approved by the Erasmus MC Animal Ethics committee and performed in accordance with the Guide for Care and Use of Laboratory Animals.[6]

See **Supplementary Material (Appendix A)** for a detailed description of all anaesthesia procedures. Thirteen male crossbred [Yorkshire x Landrace] swine aged ~11 weeks, with an average weight of ~30kg were included. DM was induced in 8 randomly selected anesthetized swine by streptozotocin (STZ, single-dose intravenous injection, 140 mg/kg).[4] All swine were given a fast-food (FF) diet, containing 10% sucrose, 15%

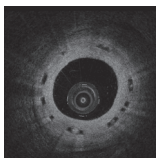

fructose, 25% (swine) lard, 1% cholesterol and 0.7% sodium cholate (bile salts). Follow-up duration was 12 months (n=8 FF-DM swine; n=5 FF-NDM swine) or 15 months (n=5 FF-DM swine; n=3 FF-NDM swine), during which similar growth patterns were achieved by adjusting individual caloric intake. See **Figure 1A** for the study flow chart.

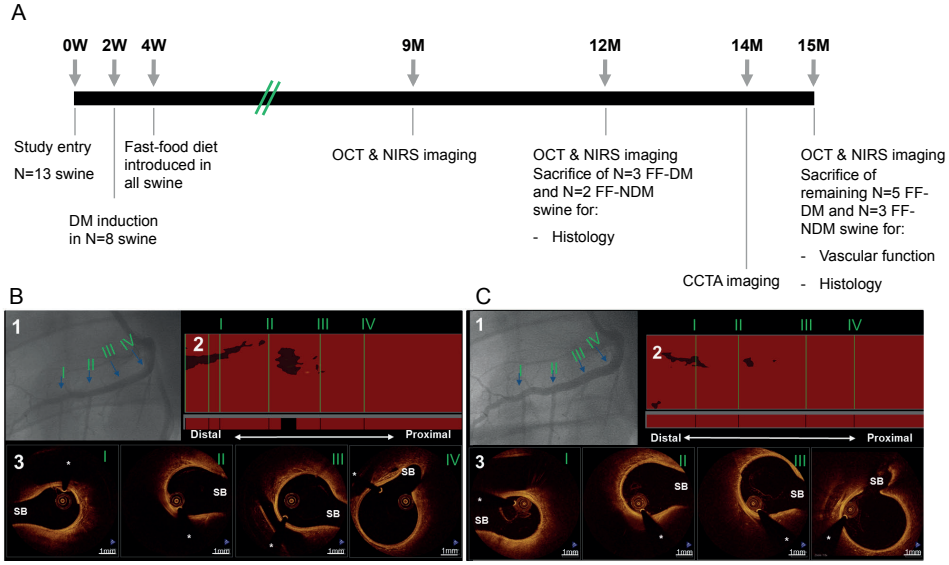

Figure 1 Study flow chart (A) and matching of invasive imaging (B and C)

The coronary angiograms (B1 and C1) were used to match the OCT (B2 and C2) and NIRS pullbacks (B3 and C3) within and at the various time points. Large side branches on the coronary angiogram (I to IV) were indicated on the NIRS chemogram (B3 and C3, green lines, I to IV) and matched to the OCT cross-sections (B2 and C2, I to IV). The asterisk (*) indicates the guide wire. M=month, SB=side branch, OCT=optical coherence tomography, NIRS=near-infrared spectroscopy

Arterial access was obtained by introducing a 9F sheath in the carotid artery to monitor blood pressure and obtain fasting blood samples to assess plasma insulin, glucose, triglyceride, total cholesterol (TC), low-density lipoprotein (LDL) and high-density lipoprotein (HDL) cholesterol levels and lipoprotein profiles. As control, fasting blood samples were taken from 5 weight-, age- and sex-matched crossbred swine fed standard chow. In FF-DM swine, blood glucose and ketone levels were monitored weekly by 24-hour urine samples and insulin was administered when needed to prevent ketoacidosis. To obtain lipoprotein profiles, we used density gradient ultra-centrifugation and measured cholesterol and triglyceride concentrations spectrophotometrically in the fractions in FF-DM (N=7), FF-NDM (N=3) and 1 age-, weight- and

sex-matched control swine (please see **Supplementary Material (Appendix A)** for detailed methodology).

To evaluate insulin sensitivity, we calculated the quantitative insulin sensitivity check index, QUICKI, calculated as $1/[(\log(I_0) + \log(G_0)]$, I_0 being the fasting plasma insulin level in μU/ml and G_0 the fasting blood glucose level in mg/dl), at 9, 12 and 15 months.

In-vivo OCT, NIRS and CCTA

Serial OCT (C7XR FD system, St Jude Medical, St. Paul, Minnesota) and NIRS (InfraReDx; Nipro, Osaka, Japan) were performed to assess the coronary arteries at 9, 12 and 15 months. The region of interest was defined as the region in which both the OCT and NIRS were available at all 2 time points (9 and 12 months) or all 3 time-points (9, 12 and 15 months) and divided into 5-mm sub-segments. On the NIRS chemogram, side-branches were marked during image acquisition, based on the location of the catheter in the coronary angiogram. Afterwards, NIRS and angiographically determined side-branches were matched to side-branches visible in the OCT pullback (**Figures 1B and C**).

See **Supplementary Material (Appendix A)** for the OCT acquisition methods. Mean lumen area and diameter and minimum lumen diameter were documented every frame within the region of interest using CURAD vessel analysis software (Curad, Maastricht, The Netherlands).

OCT tissue classification

The incidence of lesion-positive sub-segments was noted, with lesions classified as fibrous intimal thickening (FIT), lipid-laden (LL), calcified or mixed (**Figure 2A**), as published previously [7, 8] (see **Supplementary Material (Appendix A)** for lesion definitions). According to the lesion, lesion burden was calculated as the average number of lesion-positive quadrants (see **Supplementary Material (Appendix A)** for lesion definitions).

For NIRS, the catheter was withdrawn automatically with 0.5mm/sec pullback speed. Within the region of interest, NIRS documents the probability that lipid core plaque (LCP) was present. The data are displayed in a 2-dimensional arterial map, the chemogram. A summary of the results for each 2-mm of artery is computed (block chemogram) and mapped to a color scale with 4 discrete colors (**Figure 4**). The colors correspond to the probability that LCP is present, with red indicating low probability and yellow high probability (red $P \leq 0.57$, orange $0.57 \leq P < 0.84$, tan $0.84 \leq P < 0.98$, yellow $P \geq 0.98$).[9] In the current analysis, yellow, tan or orange blocks were considered NIRS-positive.

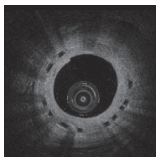

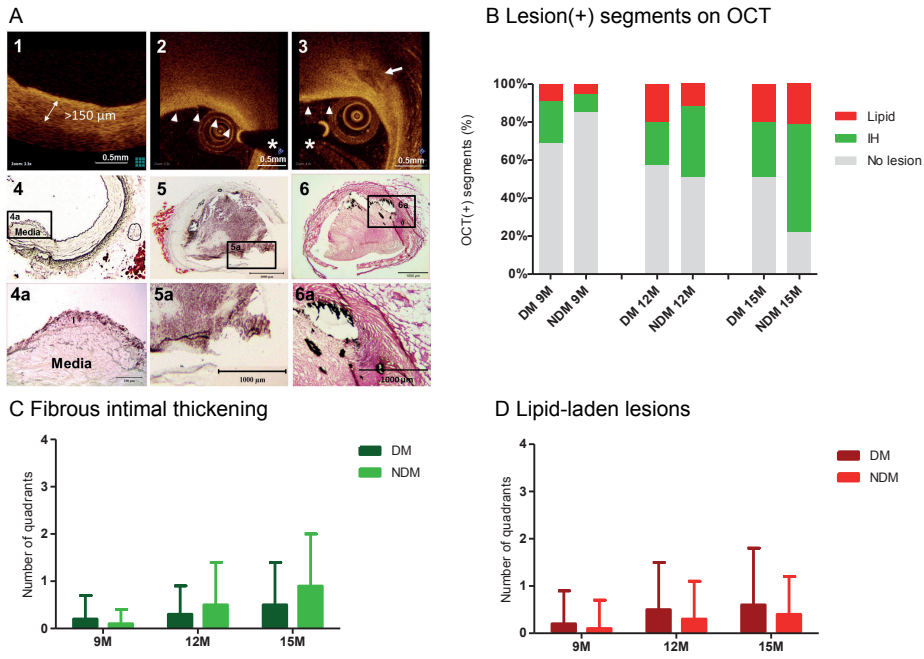

Figure 2 Early atherosclerosis development in FF-DM and FF-NDM swine

Several lesion types were assessed by OCT (A1 to A3) and matched with histology (Oil-red-O stain, (A4 and A5) and von Kossa stain (A6)). Intimal hyperplasia was defined as a fibrous lesion >150µm thickness on OCT (A1), a lipid-laden lesion (A2 and A5) as diffusely delineated signal poor region (arrowheads in A2) and a mixed lesion (A3 and 6) as a lesion containing both lipid (arrowheads in A3) and calcium, which was defined as a sharply delineated signal poor region (arrow in A3). In histology red stain denotes lipid (A5 and 6) and black denotes calcium deposits (A6). The prevalence (B) and burden (C and D) of disease increased from 9 to 15 months, without any significant difference between FF-DM and FF-NDM. DM = diabetic, NDM = non-diabetic, IH = intimal hyperplasia, M=month, OCT=optical coherence tomography. The asterix (*) indicates the guide wire artifact

See the **Supplementary Material (Appendix A)** for a description of the CCTA acquisition methods. CCTA was performed using the electrocardiography (ECG)-gated spiral scan mode. Data sets with optimal image quality were reconstructed mainly in the mid- to end-diastolic phase with a slice thickness of 0.75mm at an increment of 0.4mm. Coronary lesions were classified as high-density or low-density as described previously.[10] High-density was recognized as > 220 HU, low density as <220 HU.

Ex-vivo assessment

Sacrifice was scheduled after imaging at 12 months (n=3 FF-DM swine, n=2 FF-NDM swine) or 15 months (n=5 FF-DM swine, n=3 FF-NDM swine). The hearts were removed

and the coronary tree was dissected free and placed in cold, oxygenated Krebs bicarbonate buffer solution or fixed in formalin.

Vascular function

To assess coronary endothelial function at 15 months, segments of coronary arteries (~4mm length) were suspended in organ baths. Vascular responses were measured as changes in isometric force to different concentrations of vasoactive substances, as described previously using pEC50 values.[11-13] Endothelium-dependent relaxation to bradykinin (BK, 10^{-10} to 10^{-6} mol/L) was recorded upon pre-constriction with the thromboxane analogue U46619 (10^{-6} mol/L). Similarly, endothelium-independent vasodilation to S-nitroso-N-acetylpenicillamine (SNAP, 10^{-9} to 10^{-5} mol/L) and endothelium-dependent vasoconstriction to endothelin-1 (ET1, 10^{-10} to 10^{-7} mol/L) were assessed.

Histology

The remaining coronary artery segments were used for histological analysis. Two-millimeter segments taken from areas that demonstrated vascular wall changes by coronary angiography or OCT were embedded in optimal cutting temperature compound and then frozen. Tissue sections were cut and stained with Hematoxylin-Eosin as an overview stain, with Oil-red-O (Abcam, Cambridge, United Kingdom) for lipid and von Kossa for calcium. The sections were matched with OCT and NIRS images by using angiographic images, pullback length and arterial landmarks. Abdominal aortae were harvested and stained en face by Oil-red-O to assess atherosclerotic burden, expressed as a percentage of stained area to total area.

Statistical analysis

SPSS version 20.0 (SPSS Inc., Chicago, IL) was used for statistical analysis. Normally distributed data were expressed as mean ± standard deviation. For swine-level analysis, an independent samples Student *t*-test was used, and for segment-level analysis generalized estimating equations modeling was used. For swine-level repeated measures, repeated measures analysis of variance and for segment-level generalized estimating equations modeling were performed using a linear response model with an autoregressive (AR(1)) structure for the within-cluster correlation matrix. A P-value of <0.05 was considered statistically significant.

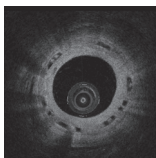

Results

In all 13 swine plasma measurements were obtained. In **Figure 3A**, average plasma insulin, glucose and cholesterol levels at the time of anesthesia, thus at 9, 12 and 15 months, are documented. TC, LDL, HDL and triglyceride levels were higher in FF-DM and FF-NDM swine than in age-, weight- and sex-matched control swine (TC 2.14 ± 0.6mmol/L, HDL 0.94 ± 0.2mmol/L, LDL 1.22 ± 0.6mmol/L, triglycerides 0.20 ± 0.1mmol/L). DM was successfully induced, as indicated by higher glucose levels in FF-DM than FF-NDM swine ($P<0.05$) and glucose levels remained fairly stable over time (**Figure 3B**). Mean arterial pressure was similar between FF-DM and FF-NDM swine at 15 months (89 ± 10mmHg, 85 ± 5mmHg, respectively; $P>0.10$) and, because similar growth patterns were maintained by monitoring individual caloric intake (**Figure 3C**), mean final weights were comparable (FF-DM swine 97.3 ± 7.3kg, FF-NDM swine 96.5 ± 3.3kg; $P=0.87$). Moreover, we created hyperglycaemic levels in FF-DM swine without evidence of hypoglycaemia.

Because lipoprotein profiles were comparable between 9, 12 and 15 months, all lipid profiles for respectively FF-DM and FF-NDM swine were combined. LDL and triglycerides were higher and HDL lower in FF-DM and FF-NDM swine compared with an age-, weight- and sex-matched control. Furthermore, the LDL-peak was dramatically increased and shifted to the right in FF-DM and FF-NDM swine compared with control, indicating a lower density of LDL (**Supplementary Figure 1; Appendix C**). QUICKI results were slightly lower in FF-DM swine (0.56 ± 0.10 at 9 months, 0.69 ± 0.14 at 12 months and 0.53 ± 0.03 at 15 months) than FF-NDM swine at 9 and 15 months (0.68 ± 0.11 at 9 months, 0.72 ± 0.14 at 12 months and 0.60 ± 0.04 at 15 months) ($P=0.04$ at 9 months, $P=0.69$ at 12 months and $P=0.02$ at 15 months). Compared with age-, weight- and sex-matched control swine, QUICKI results were reduced in both FF-DM and FF-NDM swine at 9 months ($P=0.02$) and 15 months ($P<0.01$), suggesting that insulin resistance occurred due to experimentally induced islet dysfunction as well as the FF diet.

OCT, NIRS and CCTA findings

Serial 9- and 12-month OCT and NIRS were performed in 12 of 13 swine and additional 15-month evaluations were performed in 7 of 8 swine. Due to technical difficulties, NIRS could not be performed in one swine at 9 months that was excluded from analysis. Additionally, one swine died during imaging at 15 months due to a technical complication that caused myocardial ischemia. CCTA was performed in all 8 swine at 14 months ($n=5$ FF-DM swine, $n=3$ FF-NDM swine).

A

	9M			12M			15M		
	FF-DM (n=8)	FF-NDM (n=5)	P-value *	FF-DM (n=8)	FF-NDM (n=5)	P-value *	FF-DM (n=5)	FF-NDM (n=3)	P-value*
Plasma measurements									
Glucose, mmol/L	15.31±8.08	4.38±0.66	0.01	12.96±6.43	4.7±1.44	0.01	17.64±10.15	5.37±1.22	0.09
Insulin, µu/mL	0.28±0.07	0.44±0.18	0.04	0.19±0.15	0.36±0.20	0.12	0.35±0.26	0.52±0.07	0.33
Total cholesterol, mmol/L	20.30±5.75	17.84±5.10	0.45	18.23±4.97	15.84±2.38	0.34	16.82±3.83	14.33±4.16	0.42
LDL, mmol/L	16.57±5.41	14.63±4.56	0.52	14.63±0.57	12.67±1.95	0.39	13.63±3.82	11.30±3.54	0.43
HDL, mmol/L	5.22±0.63	5.64±0.55	0.26	5.68±0.87	5.33±0.60	0.46	5.12±0.90	5.27±0.68	0.81
Triglycerides, mmol/L	1.15±0.73	0.43±0.22	0.03	0.95±0.71	0.37±0.20	0.06	1.26±1.12	0.35±0.07	0.14

B

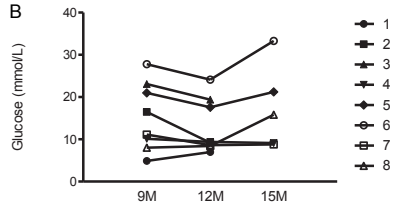

C

Animal	**1**	**2**	**3**	**4**	**5**	**6**	**7**	**8**	**9**	**10**	**11**	**12**	**13**
Sacrifice moment	12M	12M	12M	15M	15M	15M	15M	15M	12M	12M	15M	15M	15M
Frequency of insulin given	8	8	47	12	9	56	8	8	-	-	-	-	-
Total insulin given (U)	70	70	357	120	85	489	70	70	-	-	-	-	-
Average diet (gram/week)	661± 84	738± 83	873± 79	793± 80	786 ± 97	1295± 316	690± 99	725± 86	634± 63	589± 69	661± 73	661± 92	673± 86

Figure 3 Plasma measurement results (A and B) and individual insulin and food administration (C)

*Data are mean ± SD. Animals 1 to 8 are FF-DM swine, 9 to 13 are FF-NDM swine. FF-DM = fast-food fed diabetic, FF-NDM = fast-food fed non-diabetic, OCT = optical coherence tomography, 9M = 9 months follow-up, 12M = 12 months follow-up, 15M = 15 months follow-up. *P-value for the comparison between FF-DM and FF-NDM swine*

Mean and minimal lumen diameters decreased slightly from 9 to 15 months in all swine (P>0.10), without a significant difference between FF-DM and FF-NDM swine (P>0.10) (**Supplementary Table 1; Appendix B**).

OCT demonstrated focal lesions that were highly variable in presence, location and morphology. Between FF-DM and FF-NDM swine, there were no differences regarding lesion type (P=0.42 for FIT, P=0.77 for LL) or burden (P=0.17 for intimal hyperplasia, P=0.49 for LL), except for 1 mixed lesion that developed in an FF-DM swine with a calcified burden that increased from 2 lesion-positive quadrants at 9 months to 3 lesion-positive quadrants at 15 months. Of the 115 segments analyzed at 9 months (n=74 FF-DM swine, n=41 FF-NDM swine), 17% demonstrated FIT and 8% LL. From 9 to 15 months the prevalence of disease increased in FF-DM and FF-NDM swine (**Figure 2B to D**). At 12 months, 28% of sub-segments displayed FIT and 18% LL. At 15 months, 40% demonstrated FIT and 21% LL. Similarly, lesion burden increased, indicated by the

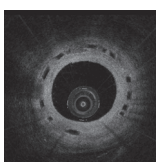

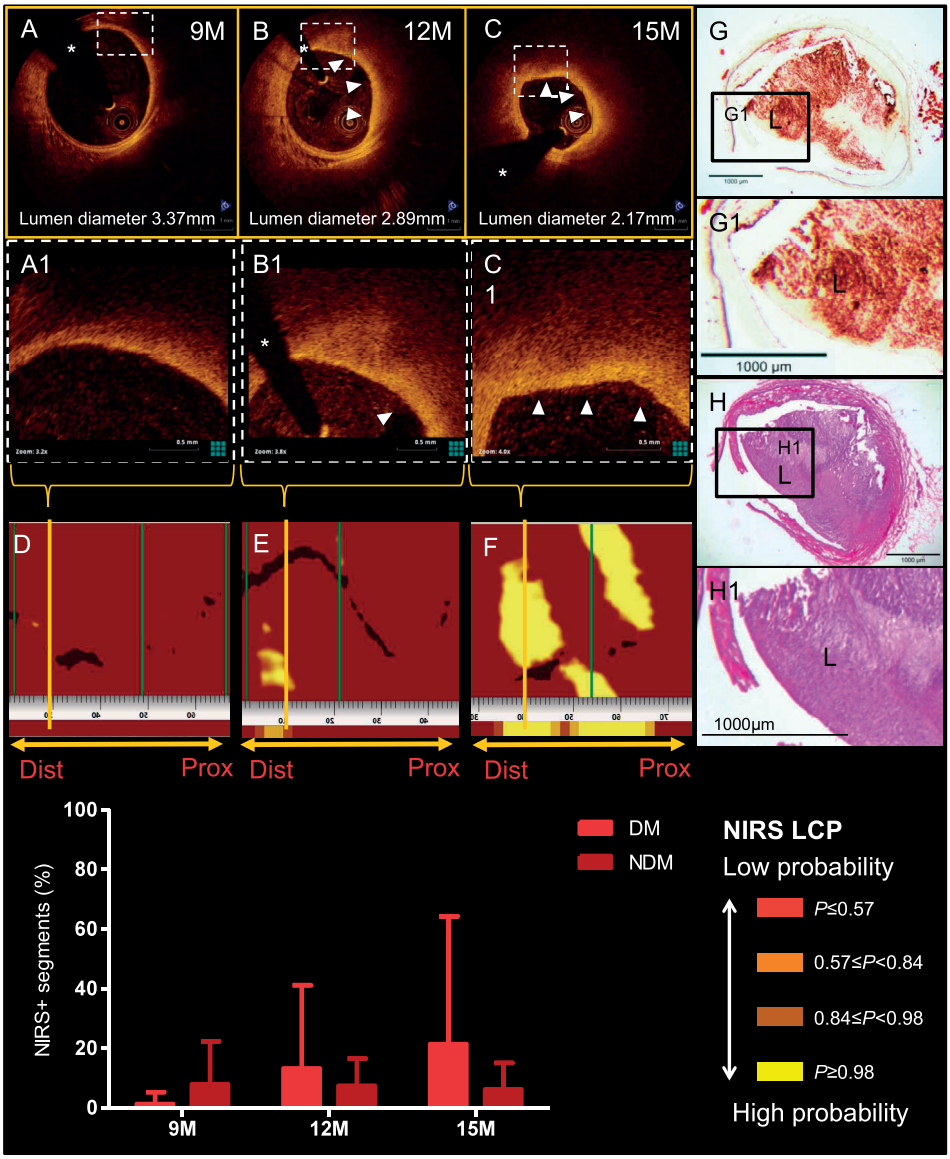

Figure 4 Lipid-containing lesion development observed by OCT, NIRS and histology

The development of an eccentric LL lesion can be observed by OCT (A to C, arrowheads) and NIRS (D to F, yellow) from 9 (9M) to 12 (12M) and 15 months (15M). The OCT cross-sections (A to C) correspond to the region in the NIRS chemograms (D to F) depicted by the orange lines. At 15 months, a high lipid burden was detected by both OCT (arrowheads in C) and NIRS (yellow in F). Histological analysis (G and H) of sequential sections stained with Oil red-O (G) and hematoxylin eosin (H) confirmed the development of an eccentric atheromatous plaque with a large lipid pool (G and H; L). The percentage (%) of NIRS-positive segments increased over time in both DM and NDM swine fed a fast-food diet (I). The graph indicates the mean percentage (%) of NIRS-positive segments per swine. Abbreviations as in **Figure 1 and 2**

increased number of lesion-positive quadrants (**Figure 2B to D**). Hence, lipid burden increased, but no OCT-derived thin-cap fibroatheroma developed in any swine (mean cap thickness 0.21 ± 0mm in FF-DM swine; 0.18 ± 0mm in FF-NDM swine; P>0.10; minimal cap thickness 0.07mm in FF-DM swine; 0.10mm in FF-NDM swine at 15 months).

Similar to the OCT results that demonstrated an increase in LL appearance (7% to 21%) and lipid burden, NIRS demonstrated an increase in the probability that LCP was present from 9 to 15 months (3% to 12% NIRS-positive sub-segments) (**Figure 4**). Agreement between OCT and NIRS for the presence of lipid-containing lesions was moderate (κ 0.56).

CCTA documented a single low-density lesion (186 +/- 38.3 Hounsfield units) in the swine that died during the intracoronary imaging procedure at 15 months (**Supplementary Figure 2; Appendix C**). In the remaining swine, CCTA was unable to detect any coronary lesion, despite the fact that OCT and NIRS showed the development of calcified lesions or lipid-containing lesions, respectively.

Ex-vivo findings

Vascular function

The contractile response to the endothelium independent vasoconstrictor (U46619) was not different between FF-DM and FF-NDM swine at 12 months (91±47 vs. 98±45mm; p>0.10). Coronary segments dilated to endothelium-dependent and -independent vasodilators (BK and SNAP) in a concentration-dependent manner. FF-DM swine demonstrated a reduced response to the endothelium-dependent vasodilator BK similar to that of FF-NDM swine (pEC50 FF-DM 7.6±0.5 vs. FF-NDM 7.7±0.3; p>0.10). The response to the endothelium-independent vasodilator SNAP remained unaltered in FF-DM and FF-NDM swine (P>0.10) and the response to the endothelium-dependent vasoconstriction ET-1 was increased (Emax FF-DM 102±18 vs. FF-NDM: 102±22, p>0.10) (**Figure 5**).

Histology

Of the swine that died during the imaging procedure, histological analysis demonstrated an eccentric atherosclerotic lesion with necrotic core in the distal left circumflex coronary artery (**Supplementary Figure 3; Appendix C**). In the remaining swine, coronary atherosclerosis was heterogeneously divided between and within swine, ranging from early (**Figure 2A4**) to more advanced atherosclerosis (**Figure 2A5 and A6**), as was also documented by OCT (**Figure 2A to D**).

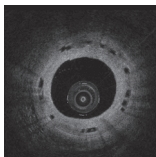

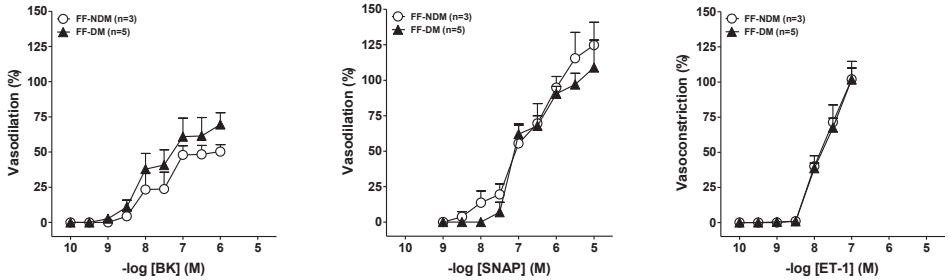

Figure 5 Concentration response curves to BK, SNAP and ET-1
Concentration response curves to BK (A), SNAP (B) and ET-1 (C) of coronary segments of FF-DM and FF-NDM swine. No significant differences in vasodilatory or vasoconstrictor response were noted. BK = Bradykinin, SNAP = S-nitroso-N-acetylpenicillamine, ET-1 = endothelin-1. Remaining abbreviations as in **Figure 1**

Substantial aortic atherosclerosis developed in all swine at 12 months (72 ± 6% surface area covered by plaque in FF-DM swine and 58 ± 12% in FF-NDM swine) and at 15 months (67 ± 9% FF-DM swine and 46 ± 31% FF-NDM swine) (P>0.10) (**Supplementary Figure 4; Appendix C**). There was no correlation between the percentage of aortic atherosclerosis and triglyceride (R^2 0.12; P=0.24), TC (R^2 0.26; P=0.08), LDL (R^2 0.22; P=0.11) or HDL levels (R^2 0.25; P=0.09). Furthermore, there was no relation between abdominal aortic atherosclerosis and coronary atherosclerosis. The R^2 value was 0.01 (P=0.73) for aortic atherosclerosis compared to any lesion observed by OCT and the R^2 value was 0.10 (P=0.34) for aortic atherosclerosis compared to that for NIRS-positive lesions.

Discussion

We present a longitudinal, multi-modality imaging study assessing early atherosclerosis development in FF-DM and FF-NDM swine. OCT, NIRS, vascular function and histology demonstrated no differences in early atherosclerosis development between FF-DM and FF-NDM swine. OCT and NIRS enabled the detailed assessment of early coronary atherosclerosis, demonstrating focal lesions that were highly variable in presence, location and morphology in all swine while CCTA was not able to detect these discrete early atherosclerotic changes.

Atherosclerosis development in FF-DM versus FF-NDM swine

As expected, coronary and aortic atherosclerosis progressed in all swine over time. In line with findings by Fernandez-Friera et al., [14] who demonstrated variable distribution

of subclinical atherosclerosis in coronary arteries and aortae of middle-aged patients, we observed no correlation between aortic and coronary atherosclerosis within swine. Furthermore, a gene expression study demonstrated that inflammatory genes were markedly upregulated in coronary arteries compared to aorta from the same animal, potentially explaining the different atherosclerosis development in the different vascular beds.[15]

Between FF-DM and FF-NDM swine, there were no significant differences in extent or morphology of atherosclerosis as assessed by intracoronary imaging, and there were no differences in endothelium-dependent and independent vasodilation. This might indicate a final common pathway in the atherosclerotic disease process, as has also recently been described in a minipig model, with a similar atherosclerosis development in DM and NDM swine.[16] However, Duff et al.[17] was one of the first to assess experimental atherosclerosis and suggested hyperglycemia served as a protective factor against the development of experimental atherosclerosis in rabbits. The differences between our study findings and those by Duff et al. [17] regarding the effect of hyperglycemia on the development of atherosclerosis, may be explained by several factors, including species differences, duration of DM, the toxins used to induce DM and the type and amount of diet given to the swine.[18]

First, rabbits are highly responsive to cholesterol manipulation and develop lesions in a fairly short time. Lesions are generally fattier and morenmacrophage rich than human lesions.[19] Swine, on the other hand, develop spontaneous coronary atherosclerosis similar to humans.[4] Second, follow-up by Duff et al. [17] reached up to 4 months, whereas we followed the FF-DM and FF-NDM swine from 9 months to either 12 or 15 months. The protective effect of hyperglycemia may only be apparent in the early stages of the disease. This observation of protection against atherosclerosis development is in line with observations by Niccoli et al., [20] who demonstrated that diabetic patients experience their first event at a later stage of the atherosclerotic disease than non-diabetic patients. Third, Duff et al. [17] used Alloxan to render the rabbits diabetic, whereas we used a single-dose injection of streptozotocin. Differences in the toxin used to induce DM might have resulted in non-comparable atherosclerosis development. Fourth, we fed our swine twice daily but monitored individual caloric intake to maintain similar growth patterns, whereas Duff et al. [17] fed their rabbits ad libitum. Monitoring individual caloric intake may have accounted for similar atherosclerosis development in FF-DM and FF-NDM swine.

Interestingly, DM was associated with accelerated atherogenesis under comparable conditions of hyperlipidemia in other swine models. Moreover, Dixon et al. and Gerrity

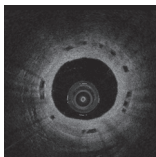

et al. demonstrated enhanced lesion development in diabetic hyperlipemic swine.[21, 22] The differences between our findings of a similar atherosclerosis development between FF-DM and FF-NDM swine and the findings by Dixon et al. and Gerrity et al. may also be explained by differences in species, the duration of diabetic disease, the toxins used to induce diabetes mellitus and the type and amount of diet given to the swine.[18] Dixon et al. used male Sinclair miniature swine and induced diabetes mellitus by Alloxan, whereas Gerrity et al. used Yorkshire swine and induced diabetes by 50mg/kg streptozotocin each day for 3 days; we used crossbred Yorkshire x Landrace swine and induced diabetes by a single-dose injection of 140mg/kg streptozotocin. Furthermore, Gerrity et al. fed the swine ad libitum in the beginning of the study, whereas we fed our swine twice daily, and monitored individual caloric intake to achieve similar growth patterns. This may have resulted in similar atherosclerosis development in the FF-DM and FF-NDM swine in our study.

As our swine demonstrated similar lipid profiles as the swine studied by Gerrity et al. and Dixon et al., but demonstrated different patterns of atherosclerosis development, we believe that hypercholesterolemia, with or without hyperglycemia, is not the only factor contributing to the development of atherosclerosis in these animal models. Factors such as duration of DM and hypertension may attribute to the severity of atherosclerotic disease. Moreover, hypertension, not present in the current study, has been associated with adverse atherosclerosis-related events in DM patients.[23] Future studies in atherosclerotic swine should consider using older-aged swine, and include risk factors such as hypertension to accurately evaluate development of advanced coronary atherosclerosis.

Comparison of imaging techniques

Over time, the prevalence and extent of disease increased in FF-DM and FF-NDM swine as detected by OCT and NIRS. OCT demonstrated increasing LL appearance and lipid burden (**Figure 2**) and NIRS demonstrated an increase in the probability that LCP was present from 9 to 15 months (**Figure 4**). Interestingly, a moderate agreement was observed between OCT and NIRS for the detection of lipid. This finding is in line with a previously published study that demonstrated a moderate correlation between OCT and NIRS for detection of lipid and measurement of lipid contents.[24] In contrast to OCT, which visualizes vessel structure and thus lipid morphology directly, NIRS provides calculated values of the probability of lipid in each pixel on the vessel surface.[9] This difference in data acquisition may contribute to the moderate correlation between the 2 modalities.

CCTA did not detect any of the lesions documented by OCT or NIRS. Subtle differences in tissue contrast were not noted because most of the lesions were small, non-obstructive and non-calcified, with a lesion burden of 1 to 2 lesion-positive quadrants. Moreover, the small non-obstructive coronary plaques observed in our swine appeared to be beyond the resolution of the technology.[25] In previous studies, CT emerged as a noninvasive technique to exclude coronary artery disease and demonstrated good accuracy for detection of coronary artery stenosis and assessment of high-density and low-density lesions.[10, 26] However, CCTA is limited by the fact that the image contrast between plaque and other soft tissues (e.g. FIT) is small.[27] This may affect identification and sizing of coronary plaque and most likely explains the inability of CCTA to detect the mainly non-calcified lesions in the present study.

OCT, NIRS and CCTA acquire data differently and thereby provide different types of information, which can be complementary and highly valuable for evaluating atherosclerosis development.[28]

Study limitations

Sample size was relatively small, especially at 15 months. To study differences in vascular function and histology over several time points, sacrifice of a small number of swine was mandatory. Furthermore, differences remain between swine and human. Although swine, like humans, develop spontaneous coronary atherosclerosis, in the present study swine were relatively young and thus did not develop advanced atherosclerosis as can be observed in older patients that suffer from hypercholesterolemia and/ or DM for a longer time period. However, the aim of our study was to assess the effect of DM on early atherosclerosis development.

Conclusion

Our swine model allows assessment of early coronary atherosclerosis development using intracoronary OCT and NIRS. CCTA could not detect the early atherosclerotic lesions, but OCT and NIRS demonstrated a similar gradual development of early atherosclerosis in FF-DM and FF-NDM swine. Moreover, OCT, NIRS, vascular function and histology demonstrated no differences in early atherosclerosis development between FF-DM and FF-NDM swine up to 15 months.

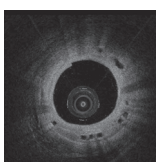

References

1. Norhammar A, Malmberg K, Diderholm E, Lagerqvist B, Lindahl B, Ryden L, Wallentin L. Diabetes mellitus: the major risk factor in unstable coronary artery disease even after consideration of the extent of coronary artery disease and benefits of revascularization. J Am Coll Cardiol 2004;43(4):585-91.
2. Wu KK, Huan Y. Diabetic atherosclerosis mouse models. Atherosclerosis 2007;191(2):241-9.
3. Skold BH, Getty R, Ramsey FK. Spontaneous atherosclerosis in the arterial system of aging swine. Am J Vet Res 1966;27(116):257-73.
4. van Ditzhuijzen NS, van den Heuvel M, Sorop O, van Duin RW, Krabbendam-Peters I, van Haeren R, Ligthart JM, Witberg KT, Duncker DJ, Regar E, van Beusekom HM, van der Giessen WJ. Invasive coronary imaging in animal models of atherosclerosis. Neth Heart J 2011;19(10):442-6.
5. van den Heuvel M, Sorop O, Koopmans SJ, Dekker R, de Vries R, van Beusekom HM, Eringa EC, Duncker DJ, Danser AH, van der Giessen WJ. Coronary microvascular dysfunction in a porcine model of early atherosclerosis and diabetes. Am J Physiol Heart Circ Physiol 2012;302(1):H85-94.
6. *Guide for the Care and Use of Laboratory Animals, 8th edition*. Washington, DC: National Academies Press (US); 2011.
7. Tearney GJ, Regar E, Akasaka T, Adriaenssens T, Barlis P, Bezerra HG, Bouma B, Bruining N, Cho JM, Chowdhary S, Costa MA, de Silva R, Dijkstra J, Di Mario C, Dudek D, Falk E, Feldman MD, Fitzgerald P, Garcia-Garcia HM, Gonzalo N, Granada JF, Guagliumi G, Holm NR, Honda Y, Ikeno F, Kawasaki M, Kochman J, Koltowski L, Kubo T, Kume T, Kyono H, Lam CC, Lamouche G, Lee DP, Leon MB, Maehara A, Manfrini O, Mintz GS, Mizuno K, Morel MA, Nadkarni S, Okura H, Otake H, Pietrasik A, Prati F, Raber L, Radu MD, Rieber J, Riga M, Rollins A, Rosenberg M, Sirbu V, Serruys PW, Shimada K, Shinke T, Shite J, Siegel E, Sonoda S, Suter M, Takarada S, Tanaka A, Terashima M, Thim T, Uemura S, Ughi GJ, van Beusekom HM, van der Steen AF, van Es GA, van Soest G, Virmani R, Waxman S, Weissman NJ, Weisz G. Consensus standards for acquisition, measurement, and reporting of intravascular optical coherence tomography studies: a report from the International Working Group for Intravascular Optical Coherence Tomography Standardization and Validation. J Am Coll Cardiol;59(12):1058-72.
8. Prati F, Regar E, Mintz GS, Arbustini E, Di Mario C, Jang IK, Akasaka T, Costa M, Guagliumi G, Grube E, Ozaki Y, Pinto F, Serruys PW, Expert's OCTRD. Expert review document on methodology, terminology, and clinical applications of optical coherence tomography: physical principles, methodology of image acquisition, and clinical application for assessment of coronary arteries and atherosclerosis. Eur Heart J 2010;31(4):401-15.
9. Gardner CM, Tan H, Hull EL, Lisauskas JB, Sum ST, Meese TM, Jiang C, Madden SP, Caplan JD, Burke AP, Virmani R, Goldstein J, Muller JE. Detection of lipid core coronary plaques in autopsy specimens with a novel catheter-based near-infrared spectroscopy system. JACC Cardiovasc Imaging 2008;1(5):638-48.
10. Motoyama S, Kondo T, Sarai M, Sugiura A, Harigaya H, Sato T, Inoue K, Okumura M, Ishii J, Anno H, Virmani R, Ozaki Y, Hishida H, Narula J. Multislice computed tomographic characteristics of coronary lesions in acute coronary syndromes. J Am Coll Cardiol 2007;50(4):319-26.

11. van den Heuvel M, Sorop O, Batenburg WW, Bakker CL, de Vries R, Koopmans SJ, van Beusekom HM, Duncker DJ, Danser AH, van der Giessen WJ. Specific coronary drug-eluting stents interfere with distal microvascular function after single stent implantation in pigs. JACC Cardiovasc Interv 2010;3(7):723-30.
12. Batenburg WW, de Vries R, Saxena PR, Danser AH. L-S-nitrosothiols: endothelium-derived hyperpolarizing factors in porcine coronary arteries? J Hypertens 2004;22(10):1927-36.
13. Batenburg WW, Popp R, Fleming I, de Vries R, Garrelds IM, Saxena PR, Danser AH. Bradykinin-induced relaxation of coronary microarteries: S-nitrosothiols as EDHF? Br J Pharmacol 2004;142(1):125-35.
14. Fernandez-Friera L, Penalvo JL, Fernandez-Ortiz A, Ibanez B, Lopez-Melgar B, Laclaustra M, Oliva B, Mocoroa A, Mendiguren J, Martinez de Vega V, Garcia L, Molina J, Sanchez-Gonzalez J, Guzman G, Alonso-Farto JC, Guallar E, Civeira F, Sillesen H, Pocock S, Ordovas JM, Sanz G, Jimenez-Borreguero LJ, Fuster V. Prevalence, Vascular Distribution, and Multiterritorial Extent of Subclinical Atherosclerosis in a Middle-Aged Cohort: The PESA (Progression of Early Subclinical Atherosclerosis) Study. Circulation 2015;131(24):2104-13.
15. Mohler ER, 3rd, Sarov-Blat L, Shi Y, Hamamdzic D, Zalewski A, Macphee C, Llano R, Pelchovitz D, Mainigi SK, Osman H, Hallman T, Steplewski K, Gertz Z, Lu MM, Wilensky RL. Site-specific atherogenic gene expression correlates with subsequent variable lesion development in coronary and peripheral vasculature. Arterioscler Thromb Vasc Biol 2008;28(5):850-5.
16. Ludvigsen TP, Kirk RK, Christoffersen BO, Pedersen HD, Martinussen T, Kildegaard J, Heegaard PM, Lykkesfeldt J, Olsen LH. Gottingen minipig model of diet-induced atherosclerosis: influence of mild streptozotocin-induced diabetes on lesion severity and markers of inflammation evaluated in obese, obese and diabetic, and lean control animals. J Transl Med 2015;13:312.
17. Duff GL, Mc MG. The effect of alloxan diabetes on experimental cholesterol atherosclerosis in the rabbit. J Exp Med 1949;89(6):611-30.
18. Granada JF, Kaluza GL, Wilensky RL, Biedermann BC, Schwartz RS, Falk E. Porcine models of coronary atherosclerosis and vulnerable plaque for imaging and interventional research. EuroIntervention 2009;5(1):140-8.
19. Badimon L. Atherosclerosis and thrombosis: lessons from animal models. Thromb Haemost 2001;86(1):356-65.
20. Niccoli G, Giubilato S, Di Vito L, Leo A, Cosentino N, Pitocco D, Marco V, Ghirlanda G, Prati F, Crea F. Severity of coronary atherosclerosis in patients with a first acute coronary event: a diabetes paradox. Eur Heart J 2013;34(10):729-41.
21. Dixon JL, Stoops JD, Parker JL, Laughlin MH, Weisman GA, Sturek M. Dyslipidemia and vascular dysfunction in diabetic pigs fed an atherogenic diet. Arterioscler Thromb Vasc Biol 1999;19(12):2981-92.
22. Gerrity RG, Natarajan R, Nadler JL, Kimsey T. Diabetes-induced accelerated atherosclerosis in swine. Diabetes 2001;50(7):1654-65.
23. Raggi P, Shaw LJ, Berman DS, Callister TQ. Prognostic value of coronary artery calcium screening in subjects with and without diabetes. J Am Coll Cardiol 2004;43(9):1663-9.
24. Yonetsu T, Suh W, Abtahian F, Kato K, Vergallo R, Kim SJ, Jia H, McNulty I, Lee H, Jang IK. Comparison of near-infrared spectroscopy and optical coherence tomography for detection of lipid. Catheter Cardiovasc Interv 2014;84(5):710-7.

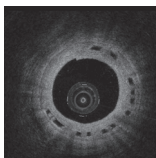

25. van der Giessen AG, Toepker MH, Donelly PM, Bamberg F, Schlett CL, Raffle C, Irlbeck T, Lee H, van Walsum T, Maurovich-Horvat P, Gijsen FJ, Wentzel JJ, Hoffmann U. Reproducibility, accuracy, and predictors of accuracy for the detection of coronary atherosclerotic plaque composition by computed tomography: an ex vivo comparison to intravascular ultrasound. Invest Radiol 2010;45(11):693-701.
26. Miller JM, Rochitte CE, Dewey M, Arbab-Zadeh A, Niinuma H, Gottlieb I, Paul N, Clouse ME, Shapiro EP, Hoe J, Lardo AC, Bush DE, de Roos A, Cox C, Brinker J, Lima JA. Diagnostic performance of coronary angiography by 64-row CT. N Engl J Med 2008;359(22):2324-36.
27. Halliburton SS, Schoenhagen P, Nair A, Stillman A, Lieber M, Murat Tuzcu E, Geoffrey Vince D, White RD. Contrast enhancement of coronary atherosclerotic plaque: a high-resolution, multidetector-row computed tomography study of pressure-perfused, human ex-vivo coronary arteries. Coron Artery Dis 2006;17(6):553-60.
28. Koskinas KC, Ughi GJ, Windecker S, Tearney GJ, Raber L. Intracoronary imaging of coronary atherosclerosis: validation for diagnosis, prognosis and treatment. Eur Heart J 2016;37(6):524-35.

Appendix A - Supplementary Methods

Anesthesia during diabetes induction, OCT and NIRS acquisition, and CCTA acquisition

During streptozotocin injection, the swine were anesthetized with intramuscular azaperone 2 mg/kg (Stressnil, Janssen, Tilburg, The Netherlands), followed by intravenous thiopental 15 mg/kg (Nesdonal, Rhone Merieux, Lyon, France).

One day prior to the imaging procedure the swine received 300 mg acetylsalicylic acid and a loading dose of 300 mg clopidogrel (Plavix, Sanofi). After an overnight fast, the swine were sedated using intramuscular ketamine/ midazolam (20 mg/kg/1 mg/kg) and atropine (1mg/30kg i.m.). After induction of anesthesia with intravenous thiopental (15 mg/kg; Nesdonal, Aventis), the swine were connected to a ventilator that administered a mixture of oxygen and nitrous oxide (1:2 [vol/vol]). Vascular access was obtained with an 8F vascular sheath in the carotid artery, 10.000IU heparin was administered initially and thereafter 5000IU of heparin was administered every hour.

For the CCTA acquisition all swine were anesthetized with Ketamine (20mg/kg), midazolam (1mg/kg) and intramuscular atropine (1mg/30kg). A catheter was placed in the ear vein, through which intravenous thiopental (15 mg/kg; Nesdonal, Aventis) was administered to induce anaesthesia. The swine were connected to a ventilator that administered a mixture of oxygen and nitrous oxide (1:2 [vol/vol]) and fentanyl (20µg/kg/h) was infused to maintain anaesthesia. Contrast infusion (5-8ml/sec) was performed via an abdominal vein, cannulated using a Vasocan braunule 17G with a balloon pump (100 ml saline + 5000 U heparine, 10ml/h).

Plasma measurements

When glucose appeared in undiluted urine samples, venous glucose and ketone levels were checked via ear vein puncture and a handheld reader. When glucose levels were high (>20 mmol/L), in combination with ketone production, subcutaneous insulin (approx. 5-15 units once daily) was given to eliminate detectable ketone production while maintaining hyperglycemic state. Moreover, we created hyperglycaemic levels, without evidence of hypoglycaemia.

Lipoprotein profiles were obtained using density gradient ultracentrifugation as described previously.[1] To obtain a density of 1.26 g/ml, potassium bromide (KBr) (in 0.35g/ml EDTA-plasma) was added to plasma of FF-DM swine (N=7), FF-NDM swine (N=5) and of an age-, weight- and sex-matched control swine. Of this plasma, 1 ml was

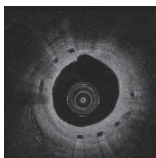

placed in an ultracentrifuge tube. On top, 1.9 ml of 1.21, 1.10, 1.063, 1.04 and 1.02g/ml in physiological salt solutions of KBr were layered, followed by 1 ml of water. Samples were centrifuged at 40,000 RPM for 18 hours at 4°C using a SW41 rotor in a L-70 Beckman ultracentrifuge (Beckman Instruments, USA). Thereafter, the density gradient was fractionated from the bottom into 250 µl fractions. Fractions with densities ranging from 1.125-1.21 g/ml and 1.062-1.125 g/ml were considered to constitute HDL3 and HDL2, respectively.[2] Cholesterol and triglyceride in the fractions were measured using a Selectra E (DDS Diagnostic system).

OCT acquisition

For OCT, the catheter was withdrawn automatically with a 20 mm/s pullback speed and 100 frames/s frame rate. A power injector was used for continuous flushing with preheated (37˚C) contrast agent (5-6 ml/s; iodixanol 370; Visipaque, GE Health Care). OCT pullback matching over time was performed according to previously published methodology.[3]

OCT tissue classification

Fibrous intimal thickening (FIT) was defined as homogeneous, signal-rich intimal thickening >150 µm, a lipid-laden (LL) lesion as a diffusely bordered signal-poor region with overlying signal-rich layer (the fibrous cap). Fibrous cap thickness was measured at the thinnest part and at 3 randomly selected parts of the cross-section. A LL lesion containing a lipid-pool ≥2 quadrants with a cap thickness <65 µm was considered a thin-cap fibroatheroma (TCFA). Calcium was defined as a sharply delineated signal-poor region and a mixed lesion as containing both lipid and calcium.

CCTA acquisition

CCTA was performed using a 128-slice dual-source CT scanner (Somatom Definition Flash, Siemens, Germany). Detector collimation was 2x64x0.6mm with z-flying focal spot (2x128 sections) and gantry rotation time was 285ms. First, a non-contrast scan for the calculation of the calcium score according to the Agatston method was performed.[4] A bolus of iodinated contrast agent (80mL; Ultravist 370 (Iopromide), Bayer) was injected intravenously at a flow rate of 5mL/sec, with a iodine delivery rate of 2g/sec, followed by a 40mL bolus chaser (saline) at the same injection rate. A bolus tracking technique was used to synchronize image acquisition with the arrival of the contrast bolus in the coronary arteries.

References

1. Versmissen J, Vongpromek R, Yahya R et al. Familial hypercholesterolemia: cholesterol efflux and coronary disease. Eur J Clin Invest 2016.
2. Superko HR, Pendyala L, Williams PT, Momary KM, King SB, 3rd, Garrett BC. High-density lipoprotein subclasses and their relationship to cardiovascular disease. J Clin Lipidol 2012;6:496-523.
3. van Ditzhuijzen NS, Karanasos A, Bruining N et al. The impact of Fourier-Domain optical coherence tomography catheter induced motion artefacts on quantitative measurements of a PLLA-based bioresorbable scaffold. The international journal of cardiovascular imaging 2014.
4. Agatston AS, Janowitz WR, Hildner FJ, Zusmer NR, Viamonte M, Jr., Detrano R. Quantification of coronary artery calcium using ultrafast computed tomography. Journal of the American College of Cardiology 1990;15:827-32.

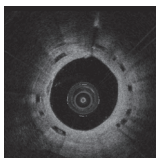

Appendix B - Supplementary Tables

Supplementary Table 1 OCT lumen dimensions

	9M			12M			15M			P-value**	
	FF-DM (n=7)	FF-NDM (n=5)	P-value*	FF-DM (n=7)	FF-NDM (n=5)	P-value*	FF-DM (n=4)	FF-NDM (n=3)	P-value*	FF-DM	FF-NDM
Optical Coherence Tomography											
Mean lumen area, mm^2;	10.20±2.05	10.82±3.86	0.72	10.14±1.93	10.21±2.54	0.95	8.52±4.11	10.33±4.45	0.63	0.57	0.96
Mean lumen diameter, mm	3.55±0.37	3.63±0.64	0.78	3.54±0.35	3.54±0.45	0.97	3.22±0.69	3.53±0.77	0.60	0.45	0.96
Minimal lumen diameter, mm	2.60±0.55	2.70±0.35	0.72	2.51±0.50	2.66±1.04	0.52	2.32±0.60	2.77±0.44	0.35	0.55	0.84

*Normally distributed data are presented as mean±SD. FF-DM = fast-food fed diabetic swine, FF-NDM = fast-food fed non-diabetic swine, OCT = optical coherence tomography, 9M = 9 months follow-up, 12M = 12 months follow-up, 15M = 15 months follow-up. *P-value for the comparison between FF-DM and FF-NDM swine, **P-value for the difference between 9M, 12M and 15M*

Appendix C - Supplementary Figures

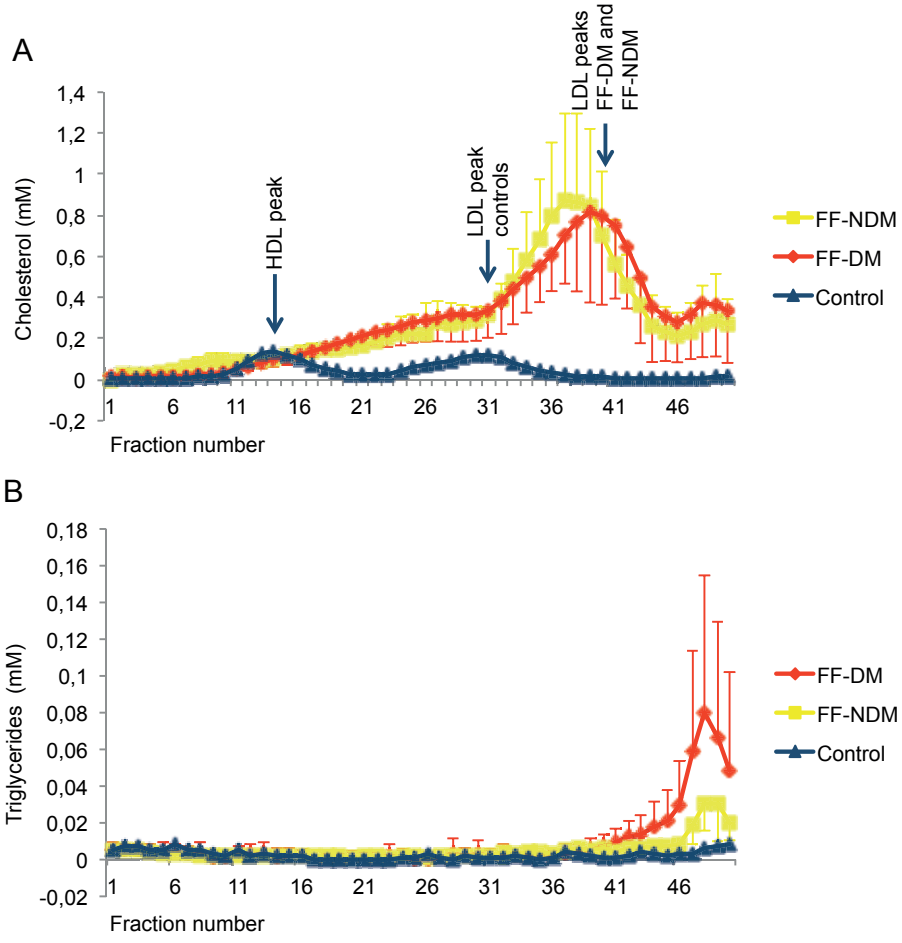

Supplementary Figure 1 Cholesterol (A) and Triglyceride (B) profiles

HDL and LDL peaks are indicated in the graph and show a decreased HDL and increased LDL (A). LDL shows a surprising shift to the left, indicating a change in density (A). FPLC analysis (data not shown) shows the appearance of VLDL and IDL species and a leftward shift of LDL indicating smaller size of the LDL particle

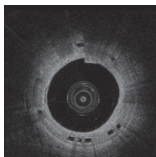

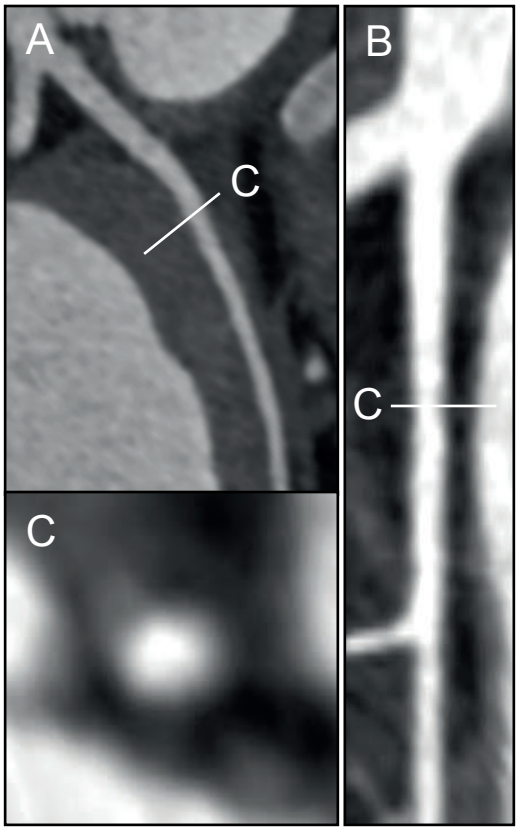

Supplementary Figure 2 CCTA detected a fibrous lesion at 14 months

In the left anterior descending artery (A and B) of one of the swine, CCTA detected a fibrous lesion (C). CCTA = coronary computed tomography angiography

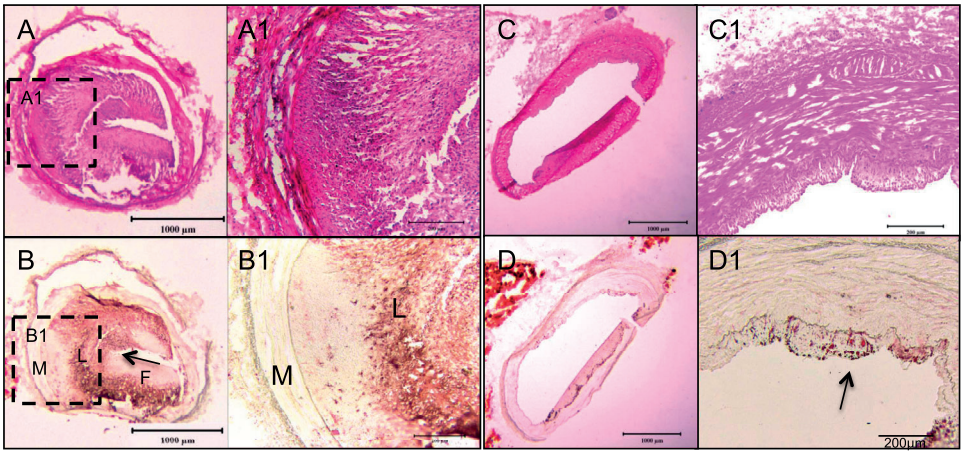

Supplementary Figure 3 Histological example of a large lipid-rich plaque (A and B) and a minimally diseased artery (C and D)

Eccentric lipid-rich lesion and a minimally diseased artery (hematoxilin eosin-staining (A and C), Oil-red-O staining (B and D)). The lipid-rich lesion shows a thick fibrous cap (B;F) with underlying lipid accumulation (B1; L). Details show an intact media (B1;M). The detail shows that whereas most of the cap was thick (F), part of the cap was lipid-rich (arrow in B). The minimally diseased artery shows a beginning intimal thickening with minimal accumulation of lipid-rich cells (arrow in D1)

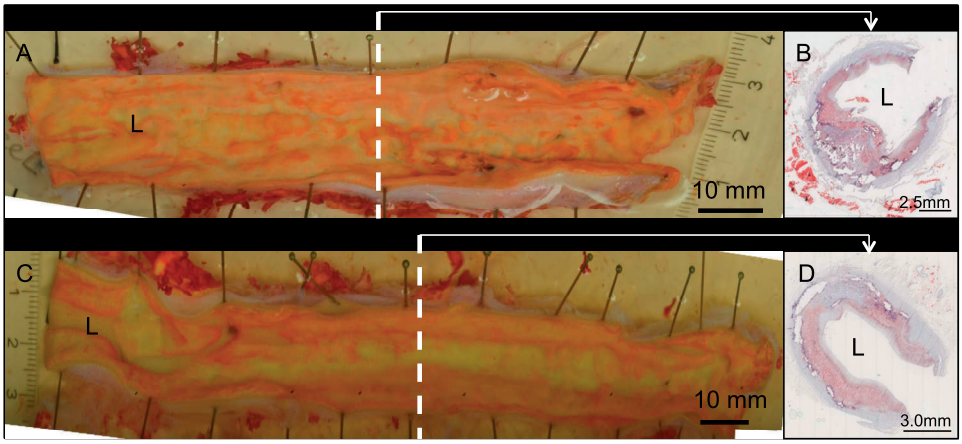

Supplementary Figure 4 Representative 'en-face' and cross-sectional images of Oil-red-O (ORO) stained infrarenal aorta of FF-DM (A) and FF-NDM (C)

Substantial aortic atherosclerosis was observed in both FF-DM (72% ORO-positive surface, red color) (A and C) and FF-NDM swine (60% ORO-positive surface, red color) (C and D). Note that the luminal surface of the media is calcified along 50-75% of the circumference. L= Lumen. Remaining abbreviations as in **Figure 1**

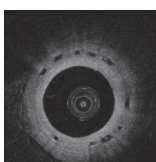

Coronary microvascular dysfunction after long-term diabetes and hypercholesterolemia

Oana Sorop*, Mieke van den Heuvel*, Nienke van Ditzhuijzen, Vincent de Beer, Ilkka Heinonen, Richard van Duin, Zhichao Zhou, Sietse Koopmans, Daphne Merkus, Wim van der Giessen, A.H. Jan Danser, Dirk J. Duncker

Am J Physiol Heart Circ Physiol. 2016 Sep 2

**Equal contribution*

Abstract

Introduction Coronary microvascular dysfunction (CMD) has been proposed as an important component of diabetes mellitus (DM) and hypercholesterolemia-associated coronary artery disease (CAD). Previously we observed that 2.5 months of DM and high fat diet (HFD) in swine blunted bradykinin (BK)-induced vasodilation and attenuated endothelin-1 (ET-1)- mediated vasoconstriction. Here, we studied the progression of CMD after 15 months in the same animal model of CAD.

Methods Ten male swine received HFD in the absence (HFD n=5) or presence of streptozotocin-induced DM (DM+HFD n=5). Coronary small arteries (~300μm) responses to BK, ET-1 and nitric oxide (NO) donor S-nitroso-N-acetylpenicillamine (SNAP) were examined *in vitro*, and compared to healthy control swine (n=12).

Results DM+HFD had elevated blood glucose (17.6±4.5mmol/l) versus HFD (5.1±0.4mmol/l) and control swine (5.8±0.6mmol/l), while both DM+HFD (16.8±1.7mmol/l) and HFD (18.1±2.6mmol/l), had markedly elevated cholesterol compared to control swine (2.1±0.2mmol/l, all $P<0.05$). Coronary small arteries showed early atherosclerotic plaques, in both HFD and DM+HFD groups. Surprisingly, both DM+HFD and HFD showed maintained BK-responsiveness compared to Control swine, due to an increase in NO availability relative to endothelium-derived hyperpolarizing factors (EDHF). However, ET-1 responsiveness was greater in HFD and DM+HFD versus Control swine (both $P<0.05$), resulting mainly from ET_B-mediated vasoconstriction. Moreover, calculated vascular stiffness coefficient was higher in DM+HFD and HFD versus Control swine (both $P<0.05$).

Conclusion 15-months of DM+HFD but also HFD alone resulted in CMD. Although the overall vasodilation to BK was unperturbed, the relative contributions of NO and EDHF pathways were altered. Moreover, the vasoconstrictor response to ET-1 was enhanced, involving the ET_B receptors. In conjunction with our previous study, these findings highlight the time-dependency of the phenotype of coronary microvascular dysfunction.

Introduction

Diabetes mellitus (DM) and hypercholesterolemia are widespread risk factors for ischemic heart disease and their prevalence continues to increase worldwide.[1-4] A large contribution to morbidity and mortality of diabetic patients can be attributed to the accelerated development of obstructive proximal coronary artery disease (CAD).[5] However, it is also becoming increasingly recognized that coronary microvascular dysfunction is an early feature of DM and hypercholesterolemia that may precede macrovascular disease and constitutes a major component of DM associated CAD.[6-10] Although the pathogenesis of coronary microvascular dysfunction is incompletely understood, DM-induced progressive endothelial dysfunction is thought to be a key player in this process. This endothelial dysfunction encompasses a shift in the secretion of endothelium-derived relaxing factors from nitric oxide (NO) to endothelium-derived hyperpolarizing factor (EDHF), as well as an imbalance between these relaxing factors and endothelium-derived constricting factors such as endothelin-1 (ET-1).[8, 11, 12]

In a recent study, we demonstrated impaired coronary microvascular NO bioavailability and reduced ET-1 responsiveness in diabetic swine on a high fat diet (HFD) during 2.5 months of follow-up.[12] The present study was undertaken to characterize the progression of coronary microvascular dysfunction in this model. Specifically, we tested the hypothesis that prolonged exposure to hyperglycemia and hypercholesterolemia leads to further impairment of the NO-availability and increased ET-1-mediated vasoconstriction. For this purpose, vascular function of coronary small arteries was studied *in vitro* at 15 months follow-up in DM+HFD swine and compared to vascular function in HFD swine as well as healthy animals.

Materials and Methods

The study was performed in a total of sixteen swine and an additional twelve slaughterhouse swine hearts, in accordance with the "Guiding Principles in the Care and Use of Laboratory Animals" as approved by the Council of the American Physiological Society, and with approval of the Animal Care Committee at Erasmus University Medical Center Rotterdam, Rotterdam, the Netherlands.

Animals

Ten castrated male Yorkshire x Landrace swine (18.2±0.4 kg) were studied. In five animals DM was induced by streptozotocin injection (140-180 mg/kg i.v.), to destroy

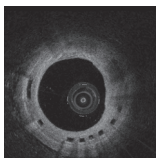

approximately 80% of the pancreatic βcell islets.[12, 13] Four weeks after DM induction, a high fat diet (HFD) consisting of 10% sucrose, 15% fructose, 25% saturated fats, 1% cholesterol and 0.7% sodiumcholate (bile salts) was gradually introduced to DM (DM+HFD group) and non-DM (HFD group) animals.[12] Swine were housed in metabolic cages and were fed two meals a day during each of which they had access to food for one hour. The food intake was monitored for each animal separately and titrated to maintain growth at ~1.5 kg/week. All ten animals completed the 15-months study duration. The diabetic status of the DM+HFD swine was regularly monitored by measurements of urinary and venous blood glucose and ketone levels.

Six weight-matched Yorkshire x Landrace control swine, were studied for comparison of heart rate, blood pressure and plasma characteristics, while three of these animals were used for vascular function experiments. In addition, twelve fresh healthy normal hearts were obtained from slaughterhouse swine of similar body weight (~100 kg at sacrifice) to compare vascular function characteristics. Since in a separate study no differences in the small artery functional responses to BK, ET and SNAP were observed between male (n=8) and female (n=9) swine of this size (**Figure 1**), data from normal, control animals of both genders were included.

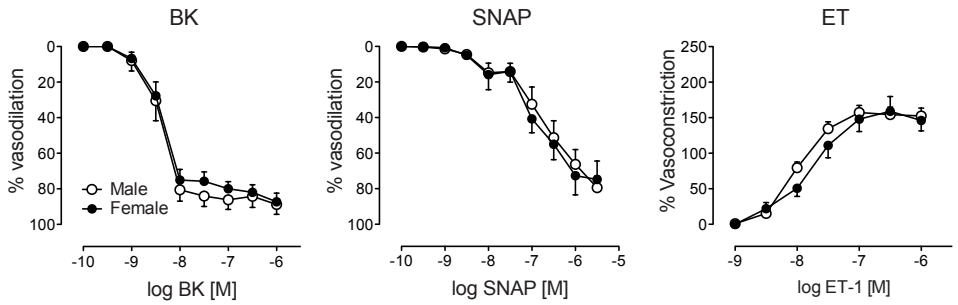

Figure 1 Concentration-response curves for BK, SNAP and ET-1 in small coronary arteries isolated from male (n=8) versus female (n=9), slaughterhouse pigs
No sex-differences were observed for any of the vasoactive factors used

Plasma characteristics

At sacrifice, animals were sedated with Zoletil (Tiletamine/Zolazepam; 5 mg/kg), Rompun (Xylazine; 2.25 mg/kg) and atropine (2 ml i.m.), anesthetized with pentobarbital (20 mg/kg/h i.v.) and artificially ventilated. Arterial access was obtained by introducing a 9F sheath in the carotid artery in order to monitor blood pressure and heart rate and to collect fasting arterial blood samples. Plasma levels of glucose, triglycerides, total

cholesterol, low density lipoprotein (LDL), high density lipoprotein (HDL), aspartate aminotransferase (ASAT), alanine aminotransferase (ALAT), and creatinine were measured at the clinical chemical laboratory of the Erasmus Medical Center using standardized protocols. Arterial plasma concentrations of insulin, (Mercodia AB, Uppsala, Sweden), ET-1, (ELISA, Enzo Life Sciences, Lausan, Switzerland) and tumor necrosis factor alpha (TNFα, R&D Systems Europe Ltd., Abingdon, UK), were determined using ELISA kits.

Vascular function in vitro

After all blood samples had been obtained and following thoracotomy, hearts were arrested and immediately excised and placed in cold, oxygenated Krebs bicarbonate buffer solution. For the HFD and DM+HFD groups epicardial coronary small arteries (~300 µm diameter) were isolated from the perfusion areas of either LAD, LCX or RCA, in such a design that in both groups vessels from all three perfusion areas were evenly distributed. From the Control animals, vessels have been isolated from the apical part of the heart such as vessels from all perfusion areas were used and included in the analysis. The isolated segments were studied *in vitro* in a Mulvany wire myograph (DMT, Aarhus, Denmark), as previously described.[12] Briefly, during the vascular function experiments, vessel segments (~2 mm length) were maintained at 37˚C, in Krebs buffer (10^{-3} M: NaCl 118, KCl 4.7, $CaCl_2$ 2.5, $MgSO_4$ 1.2, KH_2PO_4 1.2, $NaHFDO_3$ 25 and glucose 8.3; ph 7.4). After a 30 minute stabilization period, the normalization procedure was started; during this procedure, the internal diameter was set to a tension equivalent to 90% of the estimated diameter at 100 mmHg effective transmural pressure.[14] Thereafter the vascular segments were depolarized by 100 mM potassium chloride (KCl; Sigma-Aldrich, Zwijndrecht, The Netherlands) in order to achieve the maximal contractile response of the small artery segments. Subsequently, concentration-response curves (CRC) for various substances (all from Sigma- Aldrich) were acquired, using separate, but *in vivo* adjacently positioned, segments. Endothelium-dependent vasodilation was studied by constructing the CRC for BK (10^{-10} to 10^{-6} M) upon preconstriction by 10^{-6}M thromboxane-A_2 analogue U46619.[15] The contribution of NO and EDHF to BK-induced vasodilation was assessed by performing the same BK experiment in separate small artery segments upon 30 minutes of pre-incubation with the NO-synthase inhibitor N-nitro-L-arginine methyl ester (L-NAME, 10^{-4} M), the small- and intermediate-conductance Ca^{2+}-activated K+-channel inhibitors apamin (10^{-7}M) and TRAM34 (10^{-5} M), or their combination. It was previously shown that prostaglandins are not involved in BK-induced responses in healthy porcine coronary small arteries.[15] Endothelium-independent vasodilation was studied in separate small artery segments by constructing CRCs

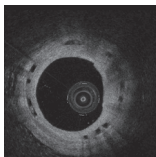

to the exogenous NO-donor, S-nitroso-N-acetylpenicillamine (SNAP, 10^{-10} to $3x10^{-5}$ M). In additional small artery segments, CRCs to ET-1 (10^{-10} to 10^{-6} M) were constructed. The specific contributions of the ET_A and ET_B receptors to this response were tested by performing the same experiment upon 30 minutes of incubation with either ET_A receptor antagonist BQ123 (10^{-6}M), the ET_B receptor antagonist BQ788 (10^{-7}M), or their combination.

To examine whether coronary small arteries had undergone changes in passive tension characteristics, the values of the relaxed steady state diameters at each wall tension of the normalization procedure were fitted by an exponential equation according to Halpern and Mulvany [14] and the stiffness coefficient was calculated.

Histology

After completion of the vascular function studies, each vascular segment was fixed in 4% buffered formaldehyde, embedded in paraffin, and stained with resorcin-fuchsin stain to assess atherosclerosis development. Atherosclerotic plaques of different complexity were described according to the AHA classification.[16]

Quantitative real-time PCR analysis

Small arteries, dissected simultaneously with vessels isolated for the vascular function studies, were used for detection of endothelial nitric oxide synthase (eNOS), ET_A and ET_B receptors, small, intermediate and big conductance K channels mRNA. RNA was extracted from frozen vessel samples using a Qiagen RNA kit. cDNA was synthesized from 100ng of total RNA with iScript Reverse Transcriptase (Bio-Rad Laboratories B.V. Veenendaal, The Netherlands). Quantitative real-time PCR (MyIQ, Bio-Rad Laboratories B.V.) was performed with SYBR Green (Bio-Rad Laboratories B.V.). Target gene mRNA levels were expressed relative to the housekeeping genes glyceraldehyde-3-phosphate dehydrogenase (GAPDH) and cyclophillin as endogenous controls.[17] Primer sequences are shown in **Table 1**.

Microvascular NO production

Microvascular NO production was evaluated in homogenized segments of microvessels of the same size and from the same animals used for the functional studies, which were snap frozen directly after excision from the hearts. The production of NO metabolites NO_2^- and NO_3^- was measured using the Griess reaction colorimetric assay (Cayman Chemical, Michigan, USA).

Table 1 Primer sequences

Primer	Sense	Antisense
eNOS	CTCTCCTGTTGGCCTGACCA	CCGGTTACTCAGACCCAAGG
ET_A receptor	TTTATCCTGGCCATCCCTGA	GCTCTTCGCCCTTGTATTCAA
ET_B receptor	CCCCTTCATCTCAGCAGGATT	GCACCAGCAGCATAAGCATG
Small-conductance K channels	TGGTGAAGAAGCCAGACCAC	CCGGAGCTTCTGAGCTTGAT
Intermediate-conductance K channels	CCATCAACACGTTCCGCCAG	AGCTGCAGGTCACACAGGAT
Big-conductance K channels	ATTGCTGAGGAGAATGCGCT	TAACAACCACCATCCCCCAG
GAPDH	TCGGAGTGAACGGATTTG	CCTGGAAGATGGTGATGG
Cyclophillin	GTCTCCTTCGAGCTGTTTGC	AATCCTTTCTCCCCAGTGCT

eNOS = endothelial nitric oxide synthase, ET = endothelin, GAPDH = glyceraldehyde-3-phosphate dehydrogenase

Data analysis

Data are presented as mean ± SEM. Comparison of normally distributed model characteristics was performed by one-way analysis of variance followed by Scheffe post-hoc test, (ANOVA, StatView 5.0 SAS Institute Inc.). Vasodilator responses to BK and SNAP were expressed as percentage of the preconstriction to U46619. Vasoconstrictor responses to U46619, L-NAME and ET-1 were normalized to 100 mM KCl. Statistical analysis of CRCs was performed using two-way ANOVA (with the increasing agonist concentrations and antagonists as independent variables), followed by Fisher's PLSD post-hoc correction. Two-tailed $P<0.05$ was considered statistically significant.

Results

Hemodynamic parameters and plasma characteristics

At sacrifice, all groups had similar body weights (DM+HFD: 93±3kg, HFD: 109±5kg and Control swine: 103±19kg). Furthermore, all groups had similar heart rates (DM+HFD: 114±3 bpm, HFD: 111±3 bpm and Control swine: 87±7 bpm; $P>0.05$) and mean arterial pressure values (DM+HFD: 103±4, mmHg HFD: 105±6 mmHg and Control swine: 121±7 mmHg; $P>0.10$), as measured under anesthesia.

The plasma levels of glucose, insulin, lipids and inflammation markers are summarized in **Figure 2**. The DM+HFD group showed significantly increased plasma glucose values as compared to HFD and Control groups. Plasma insulin values tended to be increased in DM+HFD (14.5±4.4 pg/ml) and particularly in HFD (18.2±1.4 pg/ml)

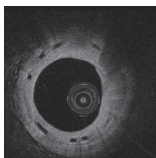

swine as compared to Control (10.1±1.6 pg/ml) animals, but failed to reach statistical significance. However, calculation of the quantitative insulin sensitivity check index (QUICKI; calculated as 1/[(log(I0) + log(G0)], with I0 being the fasting plasma insulin level in μU/ml and G0 the fasting blood glucose level in mg/dl)[18] showed significantly lower values in both DM+HFD and HFD animals, as compared to Control animals, indicative of insulin resistance in both groups. The high fat diet resulted in increased plasma total cholesterol and LDL cholesterol in both DM+HFD and HFD groups, as compared to Control animals. Plasma triglycerides were higher in both groups on high fat diet, reaching statistical significance only in the DM+HFD group, ($P<0.05$ vs Control). DM+HFD animals trended towards increased levels of TNF-α as compared to both HFD and Control groups, without reaching statistical significance. No significant differences between the three groups were observed in plasma markers of liver and kidney function (quantitative data not shown). Plasma ET-1 levels were elevated only in the DM+HFD group (**Figure 2**).

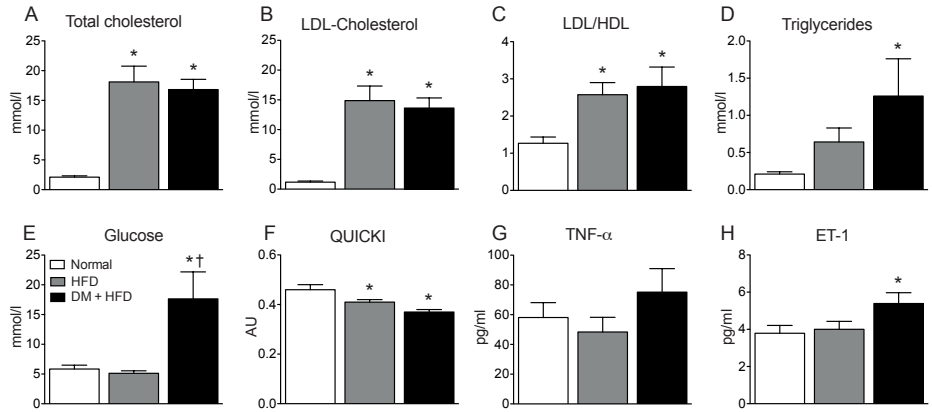

Figure 2 Plasma measurements

*Increased levels of total cholesterol (A), LDL-cholesterol (B), LDL/HDL-cholesterol ratio (C) were measured in both HFD (n=5) and DM+HFD (n=5) groups as compared to Control animals (n=6). Triglycerides (D), glucose (E) and endothelin-1 were only significantly increased in the DM+ HFD group. The QUICKI index (F), was significantly reduced in both HFD and DM+ HFD groups as compared to Control animals, suggestive of insulin resistance. *P<0.05 vs. ǂP<0.05 DM+HFD vs. HFD*

Coronary small artery structure and function

Figure 3 shows representative examples of resorcin-fuchsin stained coronary small arteries from all three groups. Plaques with different degrees of complexity, (from fatty streaks to more complex plaques), were observed in small arteries from both HFD (**Figure 3C and 3D**) and DM+HFD **(Figure 3E and 3F)** swine, to a similar extent, but not in the

Control group (**Figure 3A and 3B)**. The constrictor responses to 10^{-6} M U46619 (used for preconstriction) were similar among the three groups (DM+HFD: 74±5%, HFD: 66±4%, and Control: 67±6% of the response to 100 mM KCl; P=NS), indicating equal preconstriction levels. Coronary microvascular responses to BK, SNAP and ET-1 are summarized in **Figure 4**. Surprisingly, endothelium-dependent vasodilation to bradykinin was similar among the three groups, (**Figure 4A**). The response to the exogenous NO-donor SNAP was also similar among all groups indicating preserved vascular smooth muscle responsiveness to NO (**Figure 4B**). Vasoconstriction to ET-1 was significantly increased in both DM+HFD and HFD groups as compared to Control swine (**Figure 4C**).

Mechanisms of bradykinin-induced vasodilation: The specific contributions of NO and EDHF to the endothelium-dependent BK-mediated vasodilation were studied by blockade of eNOS and of small- and intermediate-conductance Ca^{2+}-activated K+ channels, respectively (**Figure 5**). In all groups, eNOS blockade with L-NAME resulted in a significant reduction in the vasodilator response to BK (**Figure 5**, all $P<0.05$). However, while EDHF blockade blunted the vasodilation to BK in the Control group (**Figure 5A**), no effect was observed in the HFD or DM+HFD groups (**Figure 5B and 5C**). Yet combined eNOS and EDHF blockade resulted in larger reductions in vasodilator response to BK, than eNOS alone in all three groups (**Figure 5**), suggesting that small arteries from HFD and DM+HFD swine were able to produce EDHF during inhibition of NO production.

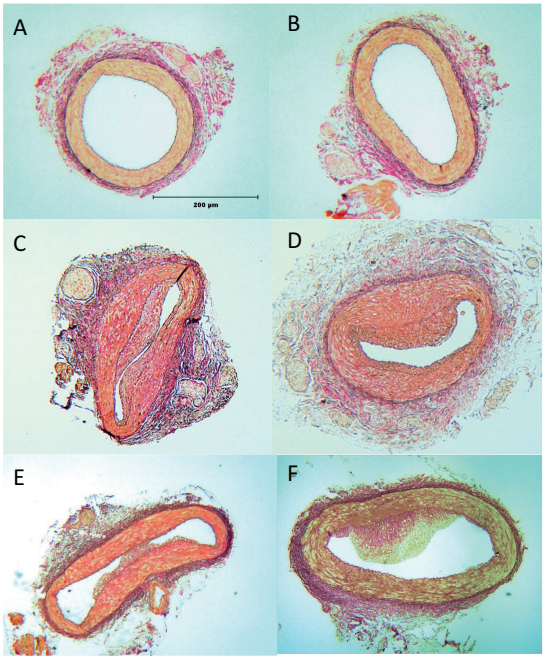

Figure 3 Examples of resorcin-fuchsin stained small coronary arteries.
Plaques with different degrees of complexity were seen in vessels from both the HFD (C and D) and DM+HFD (E and F) but not in the Control group (A and B)

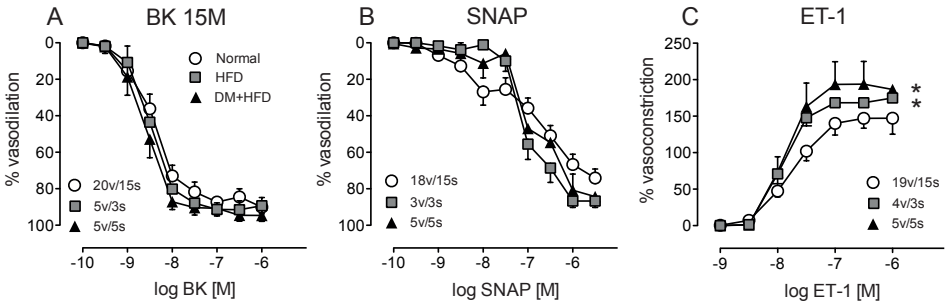

Figure 4 Concentration-response curves performed for bradykinin (BK, A), S-nitroso-N- acetyl-penicillamine (SNAP, B) and endothelin-1 (ET-1, C)

*No differences were seen in the endothelial-dependent and -independent responses to either BK or SNAP between groups. However, both HFD and DM+HFD animal groups showed increased responsiveness to ET-1 as compared to Control animals. *P<0.05 vs Control*

Mechanisms of ET-1-induced vasoconstriction: The specific contributions of ET_A and ET_B receptors to exogenous ET-1 induced vasoconstriction are shown in **Figure 6**. ET_A receptor blockade blunted ET-1 induced vasoconstriction in all three groups (all $P<0.05$) and was similar in magnitude between groups ($P=0.54$). In contrast, while ET_B blockade significantly enhanced the vasoconstrictor response to ET-1 in Control swine ($P<0.001$; **Figure 6A**), it had no effect in DM+HFD swine (**Figure 6C**), and significantly blunted vasoconstriction in the HFD group ($P<0.05$; **Figure 6B**). Similarly, compared to ET_A blockade alone, combined ET_AB blockade produced further blunting of the ET-1 induced vasoconstriction in HFD ($P<0.05$) and showed a trend towards further blunting in DM+HFD animals ($P=0.15$ at $3x10^{-9}$-10^{-7} M), but not in Control swine.

Quantitative real-time PCR analysis and microvascular NO production

eNOS expression was similar in the DM+HFD and Control groups and tended to be lower in the HFD group ($P=0.13$ HFD vs. DM+HFD, Control, **Figure 7A**). Interestingly, consistent with eNOS expression, similar levels of the NO metabolites, NO2- and NO3-, in small arteries indicated similar basal NO production in the DM+HFD and Control animals, while a significant reduction in the microvascular NO production was observed in the HFD animals as compared to the healthy controls (**Figure 7B**).

Expression of big-conductance K channels was similar between the three groups (**Figure 8C**). The expression of intermediate-conductance K channels was significantly lower in the HFD group as compared to the DM+HFD ($P<0.05$, **Figure 8B**) and tended

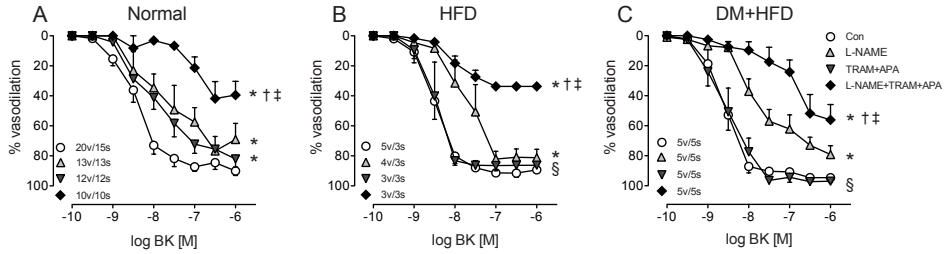

Figure 5 Concentration-response curves performed for BK upon blockade of the NO system (L-NAME), EDHF (TRAM+APA) system and their combination (L-NAME+TRAM+APA)

*Significant reduction in the BK -induced vasodilation was seen in the Control group, after the individual blockade of the NO and EDHF- dependent mechanisms, the combined blockade response being the sum of the individual mechanisms, (A). However in either HFD and DM+HFD groups (B and C), no effect of the EDHF blockade was observed, suggesting this system is becoming important only in conditions of reduced NO bioavailability (L-NAME), since in both groups, combined blockade resulted in a larger response than eNOS blockade alone. *P<0.05 vs Control; ǂP<0.05 L-NAME+TRAM+APA vs L-NAME; ǂP<0.05 L-NAME+TRAM+APA vs TRAM+APA; §P<0.05 TRAM+APA effect is different in HFD and DM+HFD vs Control*

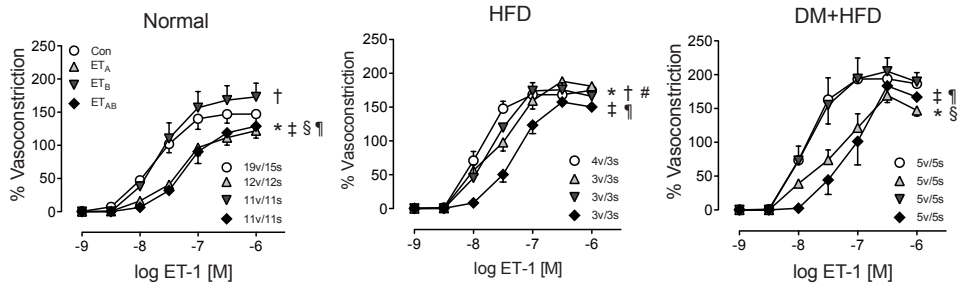

Figure 6 Concentration-response curves for ET-1 upon blockade of the ETA, (BQ123), ETB (BQ788) receptors or their combination (BQ123+BQ788)

*In the Control animals (Left), ET_B receptor blockade resulted in enhanced vasoconstriction, indicating the involvement of ET_B receptors in ET-1 dependent vasodilation. ET_A receptor blockade resulted in blunted vasoconstriction. The combined ET_AB blockade was not different from the ET_A blockade, suggesting that the ET-1 mediated vasoconstriction is mainly mediated via the ET_A receptor. The ET_B mediated vasodilation was abolished in both HFD (Middle panel) and DM+ HFD (Right) groups. In the HFD group, (Middle panel), the individual ET_A and ET_B receptor blockade resulted in blunted vasoconstriction, their contribution to the total response being additive, since the combined blockade equaled the sum of the individual blockades. In the DM+ HFD group (Right), ET_B blockade had no effect on the response to ET-1, however after ET_A receptor blockade, combined ET_AB blockade resulted in greater inhibition of ET-1 mediated vasoconstriction than ET_A receptor blockade alone. *P≤0.05 ET_A blockade vs Control; ǂP<0.05 ET_B blockade vs Control; ǂP<0.05 ET_AB blockade vs Control; §P<0.05 ET_A vs ET_B blockade; ¶P<0.05 ET_AB vs ET_B blockade; #P<0.05 ET_AB vs ET_A blockade*

to be lower when compared to the Control group (P=0.11). The expression of small-conductance K channels in the DM+HFD group was significantly decreased, (P<0.05, **Figure 8A**) and a trend towards a decrease in the HFD group (P=0.07) was measured as compared to Control.

Expression profiles of the ET receptors indicated a significantly increased mRNA expression of both ET_A (two-fold) and ET_B receptors (five-fold) in DM+HFD compared to Control swine (**Figure 9**). In contrast, only ET_B receptor mRNA expression was significantly increased (two-fold) in HFD compared to Control swine.

Vascular stiffness and wall/lumen ratio

The stiffness coefficient, as calculated from the relaxed wall tension-strain relations, was significantly increased in both DM+HFD, (6.45±0.14, n=93v/5s), and HFD (6.65±0.15, n=48v/5s) groups compared to Control (5.48±0.17, n=70v/15s) swine (both P<0.05). These findings indicate an increased stiffness in HFD and DM+HFD, which occurred in the absence of media hypertrophy, as the wall/lumen ratios measured on histological images were similar among groups, (0.36±0.03 in DM+HFD, 0.27±0.02 in HFD, and 0.37±0.03 in Control animals, P=NS).

Discussion

We previously showed that 2.5 months of exposure to DM and high fat diet resulted in an impaired BK-induced endothelium-dependent vasodilation due to loss of NO availability, accompanied by a reduced ET-1 mediated vasoconstriction resulting from a decreased ET_A receptor contribution.[12] The present study was undertaken to characterize the progression of coronary microvascular dysfunction at a later stage of the disease (i.e. 15 months) in the same swine model of DM and high fat diet.[19] The main findings of the present study were: (*i*) coronary microvessels from HFD and DM+HFD swine showed plaques with different degrees of complexity; (*ii*) the vasodilator response to BK was not further decreased but rather was maintained in both DM+HFD and HFD groups, due to ability of the NO/EDHF-mediated mechanisms to interact in synergy; (*iii*) an increased ET-1 responsiveness was present in DM+HFD and HFD groups, that appeared to be principally due to loss of ET_B-mediated vasodilation and increased ET_B-mediated constriction, in particular in the HFD group; (*iv*) coronary microvessels from HFD and DM+HFD demonstrated increased stiffness, which occurred in the absence of medial hypertrophy. The implications of these findings are discussed below.

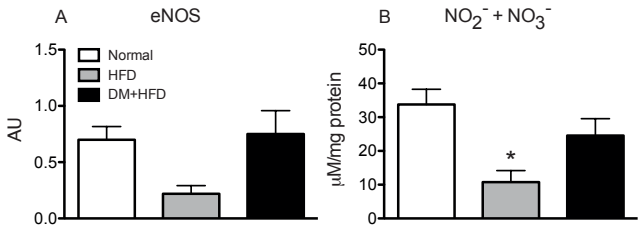

Figure 7 A) Expression of eNOS measured by qPCR in the small arteries of Control (n=4), HFD (n=3) and DM+HFD (n=5) animals; B) The production of NO metabolites NO2- and NO3- measured in small arteries isolated from all three groups (n=6 Control, n=3 HFD and n=5 DM+HFD). Similar levels of basal NO production were measured in the DM+HFD and Control animals, while a significant reduction in the microvascular NO production could be noted in the HFD animals as compared to the healthy controls. **P*<0.05 vs Control

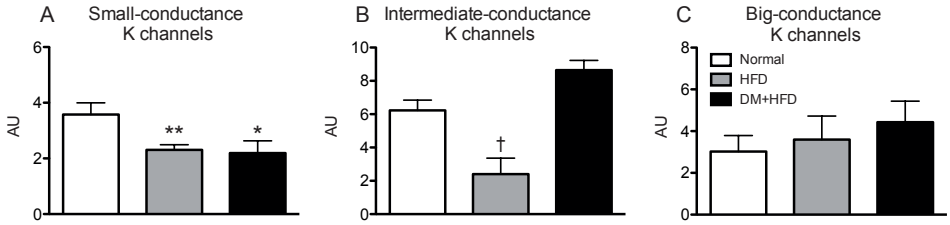

Figure 8 Expression of the small-, intermediate- and big-conductance K channel receptors measured by qPCR in the small arteries of Control (n=6), HFD (N=3) and DM+HFD (n=5) animals
*The expression of small-conductance K channels in the DM+HFD group was significantly decreased, (P=0.03) and a trend towards a decrease in the HFD group (P=0.07) was measured as compared to the Control. The expression of the intermediate-conductance K channels was significantly lower in the HFD group as compared to the DM+HFD (P=0.02), and tended to be lower when compared to the Control group (P=0.1). No difference in expression of the big-conductance K channels were recorded between the three groups. * P<0.05, **P = 0.07 vs Control, ǂP<0.05 DM+HFD vs HFD*

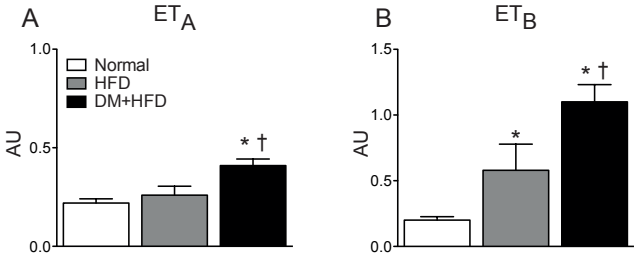

Figure 9 Expression of the ETA and ETB receptors measured by qPCR in the small arteries of Control (n=6), HFD (n=3) and DM+HFD (n=5) animals
*Increased expression of both ET_A and ET_B receptors was seen in the DM+HFD group as compared to the other groups. ET_B expression was also increased in the HFD animals as compared to Control. *P<0.05 vs Control, ǂP<0.05 DM+HFD vs HFD*

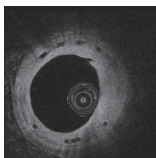

Model Characteristics

In the present study, DM induction, through partial pancreatic beta-cell destruction, combined with high fat diet, resulted in markedly elevated plasma glucose and cholesterol levels after 15 months of follow-up. Previously we performed similar experiments using the same experimental model followed for only 2.5 months of HFD with or without DM.[12] The DM+HFD group demonstrated increased insulin resistance (reflected in the QUICKI index), both at 2.5,[12] and 15 months (present study), while increased insulin resistance was only observed in the HFD group at 15 months (present study) but not at 2.5 months.[12] Furthermore, in the HFD group total cholesterol levels were slightly further elevated at 15 months compared to 2.5 months.[12] Importantly, only prolonged exposure to the *combination* of hypercholesterolemia and hyperglycemia resulted in hypertriglyceridemia, a form of dyslipidemia commonly present in diabetic patients and associated with the onset of CAD.[20] In our swine model, atherosclerotic plaques were observed in the large coronary arteries of DM+HFD and HFD animals after 15 months, which did not appear to produce flow limiting obstructions.[21] In the present study we also observed plaques of different complexities in small coronary arteries (second and third order vessels) of both groups. Unfortunately our focus on functional studies (requiring freshly isolated small arteries) precluded perfusion fixation of hearts under physiological pressures, which is a pre-requisite for accurate plaque burden quantification. Consequently, we limited the description of coronary atherosclerosis to the presence of plaques of heterogeneous complexity (from small fatty streaks to more complex fibro-atheromatous plaques), which appeared similar in both groups. Plaques were neither observed in Control swine nor in HFD or DM+HFD swine studied previously at 2.5 months,[12] underscoring the importance of long-term exposure of the coronary vasculature to pathological stimuli when developing a large animal model of coronary atherosclerosis.

Although coronary plaque formation required a longer follow-up time, functional and structural abnormalities of the small arteries were already observed in DM+HFD swine at 2.5 months of follow-up.[12] These findings are in accordance with clinical observations reporting microvascular alterations to precede obstructive CAD in patients without DM,[22] as well as in patients with DM and increased insulin resistance.[8, 10, 23, 24] Furthermore, there is evidence that coronary flow reserve is impaired not only in DM patients without CAD, but also in pre-diabetic subjects when compared to healthy individuals, indicating the early presence of coronary microvascular dysfunction.[25, 26] Microvascular dysfunction is associated with factors such as oxidative stress, poor glycemic control, insulin resistance and hypercholesterolemia,[27] which were present in our DM+HFD swine model. Since endothelial dysfunction is considered a key factor

in DM-associated coronary vascular disease development,[27] we investigated coronary endothelial function in more detail.

Endothelium-Dependent Vasodilation

In patients with DM, the severity of peripheral endothelial dysfunction correlates with duration of the disease.[28] Although coronary microvascular endothelial dysfunction is also likely related to the duration of DM, most animal studies (see **Table 2**) have investigated coronary microvascular dysfunction at a single time point only, usually rather early in the disease.[12, 29-31] One study in Zucker obese rats assessed multiple time points and showed that acetylcholine-induced coronary microvascular dilation was preserved up to 24 weeks of age, but was almost completely abolished in older animals as a result of increased oxidative stress,[32] while another study in DM type 2 Goto-Kakizaki rats showed impaired BK-induced vasodilation from 10 to 20 weeks of age.[33] However, while overall coronary endothelium-dependent vasodilation may be preserved early in the disease, the signaling pathways contributing to this vasodilation may already be altered. Thus, acetylcholine-mediated endothelium-dependent vasodilation in coronary arterioles of obese rats after 10 weeks of HFD, was maintained due to enhanced sGC-activity that increased coronary vascular sensitivity to NO.[34] Similarly, in aortic rings of female rats 4 weeks after induction of streptozotocin-induced diabetes, the overall vasodilator response to acetylcholine was preserved, as a reduction in NO bioavailability appeared to be compensated by a down regulation of phosphodiesterase (PDE) activity in combination with an increased vasodilator contribution of prostanoids.[35] In contrast, 4 weeks of high fructose diet, which resulted in increased insulin resistance, did not alter the NO-dependent coronary small artery vasodilator response to acetylcholine but rather reduced the contribution of EDHF,[30] while in the coronary arterioles of db/db mice with advanced DM type 2, EDHF compensated for diminished NO-dependent vasodilation to acetylcholine.[36] These findings suggest that compensatory mechanisms may vary, depending on species, DM model and possibly the duration of exposure to risk factors.

In the human coronary circulation (see **Table 2**), DM and CAD have been proposed to be associated with microvascular dysfunction[37, 38] and a shift in mediators of endothelium-dependent vasodilation from NO to EDHF [39] and PGI2,[40] although it is unclear when this shift occurs. In the present study we did not test the contribution of COX-2 to BK-induced dilation in animals with HFD or DM+HFD. However, data in healthy swine indicate no effect of COX-2 inhibition on BK-induced dilation.[15] In our swine model, vasodilation to BK was impaired early in the disease process (after 2.5

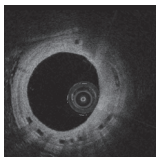

months), but only in DM+HFD, which was due to a reduction in NO bioavailability, while the contribution of EDHF was still preserved.[12]In contrast, after 15 months of exposure to DM+HFD, the overall response to BK was restored to control levels. This restoration of NO-mediated dilation was consistent with the preserved basal NO-production and eNOS expression in coronary small arteries of DM+HFD compared to Control swine. Surprisingly, basal NO production was significantly reduced in HFD swine, which was paralleled by a similar trend towards a reduction in eNOS expression. NO and EDHF may influence each other via intracellular and intercellular mechanisms,[41] as eNOS is capable of producing both NO and superoxide which in the presence of adequate anti-oxidant defense can be converted to H_2O_2 which could potentially contribute to BK-induced vasodilation by acting as an EDHF.[42] In the present study we observed a reduced expression as well as a reduced contribution of KCa channels to the BK-induced vasodilation in both HFD and DM+HFD swine, suggesting that NO remains the predominant eNOS metabolite contributing to bradykinin-induced vasodilation and that the interaction between NO and putative EDHF(s) is altered. Furthermore, the observation that vasodilation in response to the NO-donor SNAP was similar in all groups, implies that NO-responsiveness was maintained and hence that PDE activity was unaltered. Taken together, the results from the present study show that even after prolonged exposure to HFD and DM and despite the presence of CAD, the vasodilator response to BK is preserved and is largely mediated by NO. In addition, despite a reduction in small conductance K-channels expression, EDHF was still able to contribute to BK-induced vasodilation, but only when NO bioavailability was reduced.

In the present study we did not unravel the molecular mechanisms through which factors like hyperglycemia, hypercholesterolemia and inflammation result in endothelial dysfunction. However, it has been shown that high glucose levels can produce endothelial dysfunction by altering EDHF-dependent mechanisms,[43] and can also cause the formation of extracellular advanced-glycation end products (AGEs), which may result in altered cellular signaling, release of pro-inflammatory molecules and oxidative stress.[44] Furthermore, inflammatory cytokines released from perivascular fat in hypercholesterolemia may also contribute to increased superoxide production and eNOS uncoupling, thereby limiting basal NO bioavailability.[45-47] This is in agreement with the reduced microvascular NO production and eNOS expression seen in the HFD animals, but not with the data obtained in the DM+HFD group, where both eNOS expression and NO production were essentially maintained. Furthermore, inflammation and hyperglycemia have also been suggested to result in inactivation of small and intermediate-conductance K channels leading to an impaired EDHF-mediated

Table 2 Studies investigating the effects of bradykinin on coronary microvascular function in hypercholesterolemia and/or metabolic derangement

Author (Ref)	Species	Model	Tissue	FU time	Administration	Vasorelaxation	Mechanism
Mishra 2014[33]	Rat	Goto-Kaakizaki (non-obese, type 2 DM)	Isolated full heart (coronary flow)	10-12 & 18-20 weeks of age	Acute administration	↓	K_{ca} ↔, NO
Given 2001[29]	Rat	STZ (DM type 1)	Coronary microvasc.	12 weeks	Acute administration	↔	KCa ↔, cGMP ↔
Obrosova 2007[31]	Rat	STZ (DM type 1)	Isolated coronary arterioles	6 weeks	Incubation BK	↓	Peroxynitrite ↑
Tsai 2011 [43]	Pig	Glucose incubation	Isolated healthy coronary arterioles	1 h	Incubation BK	↓	EDHF↓
Van den Heuvel Sorop 2012 [12]	Pig	DM type 2 + HFD	Isolated coronary arterioles	2.5 months	Incubation BK	↓	NO↓ EDHF↔
Sorop 2016 (present study)	Pig	DM type 2 + HFD	Isolated coronary arterioles	15 months	Incubation BK	↔	NO & EDHF interact in synergy
Yoshino 2011[38]	Human	DM type 1 & 2 + dyslipidemia	In vivo CBF	-	IC administration	↓	-
Szerafin 2006[40]	Human	Type 1 and 2 (2/10)	Isolated coronary arterioles	-	Incubation BK	↑	COX-2 ↑
Matsumoto 2004[37]	Human	DM (type not specified)	In vivo CBF (LAD)	-	IC administration	↓CBF with ↑oxLDL	-

DM=diabetes mellitus, STZ=streptozotocin, HFD=high fat diet, CBF=coronary blood flow, LAD=left anterior descending coronary artery, IC=intracoronary, KCa=calcium-activated potassium channels, cGMP=cyclic guanosine monophosphate, COX-2=Cyclooxygenase 2, oxLDL=Oxidized low-density lipoprotein

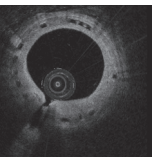

vasodilation.[48, 49]Our results confirm such reduction in the expression of the small and intermediate-conductance K channels, that can also partially explain the impaired basal EDHF mediated response to BK.

Endothelin-1 mediated vascular responses

Proper vascular tone control requires an optimal balance between vasodilator and vasoconstrictor influences.[7] Diabetes and insulin resistance are known to alter the production of, and the response to, endothelium-derived vasoconstrictors.[27] For example, the ET-1 system is activated in diabetes, resulting in increased ET-1 plasma levels,[50, 51] which correlates well with diabetic microangiopathy.[52] However, conflicting data have been reported regarding ET-1 reactivity, with reduced responsiveness to exogenous ET-1 in the peripheral circulation of obese [53] and DM type 2 patients [23, 54, 55] versus increased ET-1 vasoconstriction in animal models of DM.[56-58] Although this discrepancy is not readily explained, the present study in conjunction with our previous observations [12] demonstrates that disease progression might be an explanation. Thus, a reduced responsiveness to ET-1 was observed in DM+HFD swine at 2.5 months follow-up, in the absence of atherosclerotic plaques, while plasma ET-1 levels were still unchanged.[12] This is in accordance with reports in DM patients without evidence of atherosclerotic disease.[23, 54, 55] In addition, short-term exposure to HFD in a dog model did not alter plasma ET-1 levels and ET-1 responsiveness,[59] which was also observed in obese Zucker rats at 16-18 weeks of age,[60] similar to our results in HFD swine at 2.5 months.[12] In contrast, in the present study, 15 months of exposure to DM+HFD, but not HFD alone, resulted in increased plasma ET-1 levels, in accordance with observations in patients,[51, 52] as well as the presence of coronary atherosclerotic plaques. At this later time point, both HFD and DM+HFD groups showed an increased responsiveness to exogenous ET-1. These results are in agreement with rat models of long term DM type 1 showing exaggerated coronary ET-1 responsiveness combined with increased ET-1 plasma levels, although the presence of CAD was not verified.[56, 61]

Comparison of ET-1 responsiveness of the coronary circulation in animal models with results obtained in patients with CAD is difficult, since no data are available regarding the response to exogenous ET-1 in the coronary circulation of patients. However, endogenous ET-1 activity has been studied in the coronary vasculature of patients by using ET-1 receptor antagonists or agonists. The limited data on coronary circulation available from clinical studies yield conflicting results (**Table 3**). The coronary vasoconstrictor influence of ET-1 was increased in obese as compared to healthy humans, which correlated with the cholesterol levels.[62] Furthermore, Kyriakides et al reported

a reduced effect of endogenous ET-1 on coronary compliance in patients with type 2 DM,[63] improved coronary arterial compliance by acute ET_A receptor antagonism in patients with CAD,[64] while in hypertensive subjects the effect was not different than in controls.[65] In the coronary microcirculation of stable CAD patients with or without DM, endogenous ET_A receptor activity exerts a vasoconstrictor influence, while endogenous ET_B receptor activity exerts a vasodilator influence.[66-68] In contrast, Feng et al reported, besides ET_A-mediated vasoconstriction, absence of an ET_B-mediated vasodilating response in coronary small arteries of hypertensive, diabetic patients undergoing coronary bypass grafting, possibly a more advanced disease group.[69] Therefore, increased coronary ET-1 activity seems to be present in both obese, insulin-resistant individuals, as well as in overt DM patients. In our swine model, we previously showed that at 2.5 months the responsiveness to exogenous ET-1 was maintained in the HFD group and actually decreased in the DM+HFD animals due to reduced ET_A-mediated constriction.[12] ET_A receptor expression was not significantly altered, suggesting that ET_A receptor signaling was reduced at this early disease state. In contrast, at 15 months, both DM+HFD and HFD groups showed increased ET-1 responsiveness that was accompanied by increased expression of ET_B receptors in both groups, and, only in DM+HFD swine, by a small increase in ET_A receptors expression. Accordingly, the enhanced ET-1 vasoconstrictor responses appeared to be principally ET_B receptor mediated. Thus, the vasodilator influence of the ET_B receptors in Control swine was lost in DM+HFD swine and was reversed to a vasoconstrictor influence in HFD swine. Consequently, we hypothesize that the increased ET_B receptor expression occurred predominantly in coronary vascular smooth muscle cells, similar to observations in the cerebral vasculature of diabetic rats.[70] Importantly, these results suggest that with disease progression not only signaling of ET_A receptors is restored between 2.5 and 15 months of exposure to DM+HFD, but also that at 15 months, ET_B-receptor signaling has shifted from ET_B- mediated vasodilation to ET_B-mediated vasoconstriction. Finally, in all three groups, dual ET_AB receptor blockade appeared to be slightly greater than the sum of the individual effects of ET_A and ET_B receptor blockade, suggesting an interaction between the two receptors. Indeed, the formation of ET_A-ET_B receptor dimers has been shown to enhance the vasoconstrictor response to ET-1.[71-73] Whether this ET-1 receptor dimerization plays a role in the in vivo responsiveness of the coronary microcirculation should be the subject of future investigations.

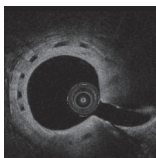

Table 3 Studies investigating the effects of ET-1 on coronary microvascular function in hypercholesterolemia and/or metabolic derangement

Author (Ref)	Species	Model	Tissue	FU Time	Administration	Vasoconstriction	Mechanism
Kamata 2008[56]	Rat	STZ-diabetic (Type 1)	Isolated heart	9 months	Heart perfusion	↑	-
Verma 2002[58]	Rat	STZ-diabetic (Type 1)	Isolated heart	8 weeks	Heart perfusion	↑	Reversed by Bosentan
Tickerhoof 2003[57]	Rat	STZ-diabetic (Type 1)	Isolated coronary arterioles	6 weeks	Incubation ET-1	↑	
Prakash 2006[60]	Rat	Obese Zucker (pre-DM)	Isolated coronary arterioles	16-18 weeks	Incubation ET-1	↓	
Van den Heuvel, Sorop 2012 [12]	Pig	DM type 2 + HFD	Isolated coronary arterioles	2.5 months	Incubation ET-1	↓	↓ ET_A
Sorop 2016 (present study)	Pig	DM type 2 + HFD	Isolated coronary arterioles	15 months	Incubation ET-1	↑	↑ET_A, ↑ET_B
Knudson 2006[59]	Dog	Metabolic syndrome	Isolated coronary arterioles	6 weeks	Incubation ET-1	↔	
Feng 2010[69]	Human	Hypertension and DM (type not specified)	Isolated coronary arterioles	-	Incubation ET-1	↔	↓ ET_B
Altieri 2015[50]	Human	DM type 2 and CAD	Intracoronary levels of circulating ET-1	-		↑	
Kyriakides 2004[65]	Human	Hypertension	Coronary compliance	-	IC infusion of BQ123	↔	
Kyriakides 2006[63]	Human	DM type 2	Coronary compliance	-	Intracoronary infusion of BQ123	↓	↓ effect of endogenous ET-1
Kyriakides 2002	Human	Hypercholesterolemia and CAD	Coronary compliance	-	Intracoronary infusion of BQ123	↑	↑ effect of ET_A antagonism
Bohm 2008[66]	Human	hypercholesterolemia and CAD	Coronary flow	-	Intracoronary infusion of BQ123, BQ788	↑	

Table 3 Studies investigating the effects of ET-1 on coronary microvascular function in hypercholesterolemia and/or metabolic derangement (continued)

Author (Ref)	Species	Model	Tissue	FU Time	Administration	Vasoconstriction	Mechanism
Halcox 2007[67]	Human	hypercholesterolemia and CAD	Coronary microvasc. vasomotion	-	Intracoronary infusion of BQ123, BQ788	↑ET_B	↓ET-1 clearance and NO bioavailability
Papadogeorgos 2009[68]	Human	DM type 2 and CAD	Coronary flow	-	Intracoronary infusion of BQ123, bosentan	↑	
Mather 2010[62]	Human	Obesity	Myocardial perfusion (PET)	-	Intracoronary infusion of BQ123	↔	↑ effect with increased BMI and Cholesterol

DM=diabetes mellitus, STZ=streptozotocin, HFD=high fat diet, CAD=coronary artery disease, IC=intracoronary, BQ123=ET_A receptor antagonist, BQ788=ET_B receptor antagonist, BMI=body mass index

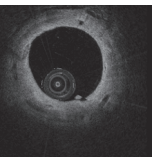

Vascular stiffness

A chronic increase in vascular tone is capable of inducing inward remodeling due to extracellular matrix restructuring.[71] Hence, the increased circulating levels of ET-1 in the DM+HFD swine, together with the increased responsiveness of the coronary small arteries to exogenous ET-1 observed in vitro, may have led to a chronic increase in coronary microvascular tone and thus extracellular matrix remodeling. Although we did not find evidence for microvascular inward remodeling, we did observe an increase in vascular stiffness, particularly in DM+HFD swine. These observations contrast with a study by Katz et al who reported reduced coronary arteriolar stiffness in type 2 diabetic mice, associated with inward hypertrophic remodeling and increased elastin-to-collagen ratio in the vascular wall.[74] Studying Ossabaw swine with metabolic syndrome, Trask et al also reported a reduced microvascular coronary stiffness that was associated with inward remodeling, capillary rarefaction, augmented myogenic tone, and reduced coronary blood flow reserve.[75] The divergent observations are not readily explained, but could be due to differences in disease severity. Indeed, an increased resistance artery stiffness due to hyperglycemia was observed in DM type 1 patients, particularly in the small and not in the large arteries.[76]

Conclusions

In summary, the present study, in conjunction with our previous study,[12] demonstrates that the balance of vasodilator and vasoconstrictor mechanisms contributing to coronary microvascular dysfunction changes markedly during disease progression. Thus, whereas at 2.5 months after induction of hyperglycemia and hypercholesterolemia, impaired endothelium-dependent vasodilation was accompanied by a reduced ET-1 mediated vasoconstriction,[12] the present study demonstrates that at 15 months follow-up, microvascular dysfunction was principally characterized by an increased vasoconstrictor response to ET-1, but with a normal endothelium-dependent vasodilator response to BK. In hypercholesterolemia only, the progression of microvascular dysfunction is more subtle, no significant alterations could be observed at 2.5 months.[12] In contrast, at 15 months in the present study, responses were characterized by a normal vasodilator response to BK and increased vasoconstriction to ET-1, that was principally due to ET_B-mediated vasoconstrictor influence. These findings indicate that the nature of coronary microvascular dysfunction early on in the disease process can be very different from, and is not necessarily predictive of, the nature of coronary microvascular dysfunction during later stages of the disease process. Furthermore, these findings

highlight the importance of performing longitudinal studies of microvascular function in experimental studies of DM and CAD.

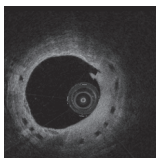

References

1. Almdal T, Scharling H, Jensen JS, Vestergaard H. The independent effect of type 2 diabetes mellitus on ischemic heart disease, stroke, and death: a population-based study of 13,000 men and women with 20 years of follow-up. Arch Intern Med 2004;**164**(13):1422-6.
2. Almdal T, Scharling H, Jensen JS, Vestergaard H. Higher prevalence of risk factors for type 2 diabetes mellitus and subsequent higher incidence in men. Eur J Intern Med 2008;**19**(1):40-5.
3. Ather S, Chan W, Bozkurt B, Aguilar D, Ramasubbu K, Zachariah AA, Wehrens XH, Deswal A. Impact of noncardiac comorbidities on morbidity and mortality in a predominantly male population with heart failure and preserved versus reduced ejection fraction. J Am Coll Cardiol 2012;**59**(11):998-1005.
4. Mokdad AH, Ford ES, Bowman BA, Dietz WH, Vinicor F, Bales VS, Marks JS. Prevalence of obesity, diabetes, and obesity-related health risk factors, 2001. JAMA 2003;**289**(1):76-9.
5. Bittencourt C, Piveta VM, Oliveira CS, Crispim F, Meira D, Saddi-Rosa P, Giuffrida FM, Reis AF. Association of classical risk factors and coronary artery disease in type 2 diabetic patients submitted to coronary angiography. Diabetol Metab Syndr 2014;**6**(1):46.
6. Crea F, Camici PG, Bairey Merz CN. Coronary microvascular dysfunction: an update. Eur Heart J 2014;**35**(17):1101-11.
7. Duncker DJ, Koller A, Merkus D, Canty JM, Jr. Regulation of coronary blood flow in health and ischemic heart disease. Prog Cardiovasc Dis 2015;**57**(5):409-22.
8. Paneni F, Beckman JA, Creager MA, Cosentino F. Diabetes and vascular disease: pathophysiology, clinical consequences, and medical therapy: part I. Eur Heart J 2013;**34**(31):2436-43.
9. Pries AR, Badimon L, Bugiardini R, Camici PG, Dorobantu M, Duncker DJ, Escaned J, Koller A, Piek JJ, de Wit C. Coronary vascular regulation, remodelling, and collateralization: mechanisms and clinical implications on behalf of the working group on coronary pathophysiology and microcirculation. Eur Heart J 2015;**36**(45):3134-46.
10. Task Force M, Montalescot G, Sechtem U, Achenbach S, Andreotti F, Arden C, Budaj A, Bugiardini R, Crea F, Cuisset T, Di Mario C, Ferreira JR, Gersh BJ, Gitt AK, Hulot JS, Marx N, Opie LH, Pfisterer M, Prescott E, Ruschitzka F, Sabate M, Senior R, Taggart DP, van der Wall EE, Vrints CJ, Guidelines ESCCfP, Zamorano JL, Achenbach S, Baumgartner H, Bax JJ, Bueno H, Dean V, Deaton C, Erol C, Fagard R, Ferrari R, Hasdai D, Hoes AW, Kirchhof P, Knuuti J, Kolh P, Lancellotti P, Linhart A, Nihoyannopoulos P, Piepoli MF, Ponikowski P, Sirnes PA, Tamargo JL, Tendera M, Torbicki A, Wijns W, Windecker S, Document R, Knuuti J, Valgimigli M, Bueno H, Claeys MJ, Donner-Banzhoff N, Erol C, Frank H, Funck-Brentano C, Gaemperli O, Gonzalez-Juanatey JR, Hamilos M, Hasdai D, Husted S, James SK, Kervinen K, Kolh P, Kristensen SD, Lancellotti P, Maggioni AP, Piepoli MF, Pries AR, Romeo F, Ryden L, Simoons ML, Sirnes PA, Steg PG, Timmis A, Wijns W, Windecker S, Yildirir A, Zamorano JL. 2013 ESC guidelines on the management of stable coronary artery disease: the Task Force on the management of stable coronary artery disease of the European Society of Cardiology. Eur Heart J 2013;**34**(38):2949-3003.
11. Koller A, Balasko M, Bagi Z. Endothelial regulation of coronary microcirculation in health and cardiometabolic diseases. Intern Emerg Med 2013;**8 Suppl 1**:S51-4.
12. van den Heuvel M, Sorop O, Koopmans SJ, Dekker R, de Vries R, van Beusekom HM, Eringa EC, Duncker DJ, Danser AH, van der Giessen WJ. Coronary microvascular dysfunction in

a porcine model of early atherosclerosis and diabetes. Am J Physiol Heart Circ Physiol 2012;**302**(1):H85-94.
13. Koopmans SJ, Dekker R, Ackermans MT, Sauerwein HP, Serlie MJ, van Beusekom HM, van den Heuvel M, van der Giessen WJ. Dietary saturated fat/cholesterol, but not unsaturated fat or starch, induces C-reactive protein associated early atherosclerosis and ectopic fat deposition in diabetic pigs. Cardiovasc Diabetol 2011;**10**:64.
14. Halpern W, Mulvany MJ, Warshaw DM. Mechanical properties of smooth muscle cells in the walls of arterial resistance vessels. J Physiol 1978;**275**:85-101.
15. Batenburg WW, Popp R, Fleming I, de Vries R, Garrelds IM, Saxena PR, Danser AH. Bradykinin-induced relaxation of coronary microarteries: S-nitrosothiols as EDHF? Br J Pharmacol 2004;**142**(1):125-35.
16. Stary HC, Chandler AB, Glagov S, Guyton JR, Insull W, Jr., Rosenfeld ME, Schaffer SA, Schwartz CJ, Wagner WD, Wissler RW. A definition of initial, fatty streak, and intermediate lesions of atherosclerosis. A report from the Committee on Vascular Lesions of the Council on Arteriosclerosis, American Heart Association. Circulation 1994;**89**(5):2462-78.
17. Zhou Z, Merkus D, Cheng C, Duckers HJ, Jan Danser AH, Duncker DJ. Uridine adenosine tetraphosphate is a novel vasodilator in the coronary microcirculation which acts through purinergic P1 but not P2 receptors. Pharmacol Res 2013;**67**(1):10-7.
18. Katz A, Nambi SS, Mather K, Baron AD, Follmann DA, Sullivan G, Quon MJ. Quantitative insulin sensitivity check index: a simple, accurate method for assessing insulin sensitivity in humans. J Clin Endocrinol Metab 2000;**85**(7):2402-10.
19. van Ditzhuijzen NS, Karanasos A, Bruining N, van den Heuvel M, Sorop O, Ligthart J, Witberg K, Garcia-Garcia HM, Zijlstra F, Duncker DJ, van Beusekom HM, Regar E. The impact of Fourier-Domain optical coherence tomography catheter induced motion artefacts on quantitative measurements of a PLLA-based bioresorbable scaffold. Int J Cardiovasc Imaging 2014;**30**(6):1013-26.
20. Tseng KH. Standards of medical care in diabetes--2006: response to the American Diabetes Association. Diabetes Care 2006;**29**(11):2563-4; author reply 2564-5.
21. van Ditzhuijzen NS, van den Heuvel M, Sorop O, van Duin RW, Krabbendam-Peters I, van Haeren R, Ligthart JM, Witberg KT, Duncker DJ, Regar E, van Beusekom HM, van der Giessen WJ. Invasive coronary imaging in animal models of atherosclerosis. Neth Heart J 2011;**19**(10):442-6.
22. Sara JD, Widmer RJ, Matsuzawa Y, Lennon RJ, Lerman LO, Lerman A. Prevalence of Coronary Microvascular Dysfunction Among Patients With Chest Pain and Nonobstructive Coronary Artery Disease. JACC Cardiovasc Interv 2015;**8**(11):1445-53.
23. Rizzoni D, Porteri E, Guelfi D, Muiesan ML, Piccoli A, Valentini U, Cimino A, Girelli A, Salvetti M, De Ciuceis C, Tiberio GA, Giulini SM, Sleiman I, Monteduro C, Rosei EA. Endothelial dysfunction in small resistance arteries of patients with non-insulin-dependent diabetes mellitus. J Hypertens 2001;**19**(5):913-9.
24. Rizzoni D, Porteri E, Guelfi D, Muiesan ML, Valentini U, Cimino A, Girelli A, Rodella L, Bianchi R, Sleiman I, Rosei EA. Structural alterations in subcutaneous small arteries of normotensive and hypertensive patients with non-insulin-dependent diabetes mellitus. Circulation 2001;**103**(9):1238-44.
25. Erdogan D, Yucel H, Uysal BA, Ersoy IH, Icli A, Akcay S, Arslan A, Aksoy F, Ozaydin M, Tamer MN. Effects of prediabetes and diabetes on left ventricular and coronary microvascular functions. Metabolism 2013;**62**(8):1123-30.

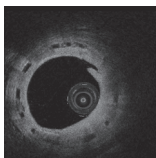

26. Pitkanen OP, Nuutila P, Raitakari OT, Ronnemaa T, Koskinen PJ, Iida H, Lehtimaki TJ, Laine HK, Takala T, Viikari JS, Knuuti J. Coronary flow reserve is reduced in young men with IDDM. Diabetes 1998;**47**(2):248-54.
27. Sena CM, Pereira AM, Seica R. Endothelial dysfunction - a major mediator of diabetic vascular disease. Biochim Biophys Acta 2013;**1832**(12):2216-31.
28. Naka KK, Papathanassiou K, Bechlioulis A, Kazakos N, Pappas K, Tigas S, Makriyiannis D, Tsatsoulis A, Michalis LK. Determinants of vascular function in patients with type 2 diabetes. Cardiovasc Diabetol 2012;**11**:127.
29. Given MB, Greenberg SS, Giles TD. Coronary vasodilator responses to bradykinin in euglycemic and diabetic rats. Am J Hypertens 2001;**14**(5 Pt 1):446-54.
30. Miller AW, Katakam PV, Ujhelyi MR. Impaired endothelium-mediated relaxation in coronary arteries from insulin-resistant rats. J Vasc Res 1999;**36**(5):385-92.
31. Obrosova IG, Drel VR, Oltman CL, Mashtalir N, Tibrewala J, Groves JT, Yorek MA. Role of nitrosative stress in early neuropathy and vascular dysfunction in streptozotocin-diabetic rats. Am J Physiol Endocrinol Metab 2007;**293**(6):E1645-55.
32. Oltman CL, Richou LL, Davidson EP, Coppey LJ, Lund DD, Yorek MA. Progression of coronary and mesenteric vascular dysfunction in Zucker obese and Zucker diabetic fatty rats. Am J Physiol Heart Circ Physiol 2006;**291**(4):H1780-7.
33. Mishra RC, Wulff H, Cole WC, Braun AP. A pharmacologic activator of endothelial KCa channels enhances coronary flow in the hearts of type 2 diabetic rats. J Mol Cell Cardiol 2014;**72**:364-73.
34. Jebelovszki E, Kiraly C, Erdei N, Feher A, Pasztor ET, Rutkai I, Forster T, Edes I, Koller A, Bagi Z. High-fat diet-induced obesity leads to increased NO sensitivity of rat coronary arterioles: role of soluble guanylate cyclase activation. Am J Physiol Heart Circ Physiol 2008;**294**(6):H2558-64.
35. Abboud K, Bassila JC, Ghali-Ghoul R, Sabra R. Temporal changes in vascular reactivity in early diabetes mellitus in rats: role of changes in endothelial factors and in phosphodiesterase activity. Am J Physiol Heart Circ Physiol 2009;**297**(2):H836-45.
36. Park Y, Capobianco S, Gao X, Falck JR, Dellsperger KC, Zhang C. Role of EDHF in type 2 diabetes-induced endothelial dysfunction. Am J Physiol Heart Circ Physiol 2008;**295**(5):H1982-8.
37. Matsumoto T, Takashima H, Ohira N, Tarutani Y, Yasuda Y, Yamane T, Matsuo S, Horie M. Plasma level of oxidized low-density lipoprotein is an independent determinant of coronary macrovasomotor and microvasomotor responses induced by bradykinin. J Am Coll Cardiol 2004;**44**(2):451-7.
38. Yoshino T, Nakae I, Matsumoto T, Mitsunami K, Horie M. Association between brachial-ankle pulse wave velocity and endothelium-dependent and -independent coronary vasomotor function. Clin Exp Pharmacol Physiol 2011;**38**(1):34-41.
39. Miura H, Wachtel RE, Liu Y, Loberiza FR, Jr., Saito T, Miura M, Gutterman DD. Flow-induced dilation of human coronary arterioles: important role of Ca(2+)-activated K(+) channels. Circulation 2001;**103**(15):1992-8.
40. Szerafin T, Erdei N, Fulop T, Pasztor ET, Edes I, Koller A, Bagi Z. Increased cyclooxygenase-2 expression and prostaglandin-mediated dilation in coronary arterioles of patients with diabetes mellitus. Circ Res 2006;**99**(5):e12-7.

41. Rath G, Dessy C, Feron O. Caveolae, caveolin and control of vascular tone: nitric oxide (NO) and endothelium derived hyperpolarizing factor (EDHF) regulation. J Physiol Pharmacol 2009;**60 Suppl 4**:105-9.
42. Chuaiphichai S, McNeill E, Douglas G, Crabtree MJ, Bendall JK, Hale AB, Alp NJ, Channon KM. Cell-autonomous role of endothelial GTP cyclohydrolase 1 and tetrahydrobiopterin in blood pressure regulation. Hypertension 2014;**64**(3):530-40.
43. Tsai SH, Hein TW, Kuo L, Yang VC. High glucose impairs EDHF-mediated dilation of coronary arterioles via reduced cytochrome P450 activity. Microvasc Res 2011;**82**(3):356-63.
44. Barlovic DP, Soro-Paavonen A, Jandeleit-Dahm KA. RAGE biology, atherosclerosis and diabetes. Clin Sci (Lond) 2011;**121**(2):43-55.
45. Bakker W, Eringa EC, Sipkema P, van Hinsbergh VW. Endothelial dysfunction and diabetes: roles of hyperglycemia, impaired insulin signaling and obesity. Cell Tissue Res 2009;**335**(1):165-89.
46. Eringa EC, Bakker W, van Hinsbergh VW. Paracrine regulation of vascular tone, inflammation and insulin sensitivity by perivascular adipose tissue. Vascul Pharmacol 2012;**56**(5-6):204-9.
47. Kougias P, Chai H, Lin PH, Lumsden AB, Yao Q, Chen C. Adipocyte-derived cytokine resistin causes endothelial dysfunction of porcine coronary arteries. J Vasc Surg 2005;**41**(4):691-8.
48. Cotter MA, Gibson TM, Nangle MR, Cameron NE. Effects of interleukin-6 treatment on neurovascular function, nerve perfusion and vascular endothelium in diabetic rats. Diabetes Obes Metab 2010;**12**(8):689-99.
49. Liu Y, Xie A, Singh AK, Ehsan A, Choudhary G, Dudley S, Sellke FW, Feng J. Inactivation of Endothelial Small/Intermediate Conductance of Calcium-Activated Potassium Channels Contributes to Coronary Arteriolar Dysfunction in Diabetic Patients. J Am Heart Assoc 2015;**4**(8):e002062.
50. Altieri PI, Marcial JM, Banchs HL, Escobales N, Crespo M, Gonzalez W. Coronary levels of angiotensin-II and endothelin-I in diabetic patients with and without coronary artery disease. Bol Asoc Med P R 2015;**107**(1):5-7.
51. Ferri C, Bellini C, Desideri G, Baldoncini R, Properzi G, Santucci A, De Mattia G. Circulating endothelin-1 levels in obese patients with the metabolic syndrome. Exp Clin Endocrinol Diabetes 1997;**105 Suppl 2**:38-40.
52. Ak G, Buyukberber S, Sevinc A, Turk HM, Ates M, Sari R, Savli H, Cigli A. The relation between plasma endothelin-1 levels and metabolic control, risk factors, treatment modalities, and diabetic microangiopathy in patients with Type 2 diabetes mellitus. J Diabetes Complications 2001;**15**(3):150-7.
53. Weil BR, Westby CM, Van Guilder GP, Greiner JJ, Stauffer BL, DeSouza CA. Enhanced endothelin-1 system activity with overweight and obesity. Am J Physiol Heart Circ Physiol 2011;**301**(3):H689-95.
54. Cardillo C, Campia U, Bryant MB, Panza JA. Increased activity of endogenous endothelin in patients with type II diabetes mellitus. Circulation 2002;**106**(14):1783-7.
55. McAuley DF, McGurk C, Nugent AG, Hanratty C, Hayes JR, Johnston GD. Vasoconstriction to endothelin-1 is blunted in non-insulin-dependent diabetes: a dose-response study. J Cardiovasc Pharmacol 2000;**36**(2):203-8.
56. Kamata K, Ozawa Y, Kobayashi T, Matsumoto T. Effect of long-term streptozotocin-induced diabetes on coronary vasoconstriction in isolated perfused rat heart. J Smooth Muscle Res 2008;**44**(5):177-88.

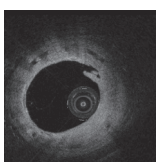

57. Tickerhoof MM, Farrell PA, Korzick DH. Alterations in rat coronary vasoreactivity and vascular protein kinase C isoforms in Type 1 diabetes. Am J Physiol Heart Circ Physiol 2003;**285**(6):H2694-703.
58. Verma S, Arikawa E, Lee S, Dumont AS, Yao L, McNeill JH. Exaggerated coronary reactivity to endothelin-1 in diabetes: reversal with bosentan. Can J Physiol Pharmacol 2002;**80**(10):980-6.
59. Knudson JD, Rogers PA, Dincer UD, Bratz IN, Araiza AG, Dick GM, Tune JD. Coronary vasomotor reactivity to endothelin-1 in the prediabetic metabolic syndrome. Microcirculation 2006;**13**(3):209-18.
60. Prakash R, Mintz JD, Stepp DW. Impact of obesity on coronary microvascular function in the Zucker rat. Microcirculation 2006;**13**(5):389-96.
61. Hopfner RL, McNeill JR, Gopalakrishnan V. Plasma endothelin levels and vascular responses at different temporal stages of streptozotocin diabetes. Eur J Pharmacol 1999;**374**(2):221-7.
62. Mather KJ, Lteif AA, Veeneman E, Fain R, Giger S, Perry K, Hutchins GD. Role of endogenous ET-1 in the regulation of myocardial blood flow in lean and obese humans. Obesity (Silver Spring) 2010;**18**(1):63-70.
63. Kyriakides ZS, Kremastinos DT, Raptis AE, Johnston N, Raptis SA, Webb DJ, Kyrzopoulos S, Sbarouni E. Impaired effect of endothelin-1 on coronary artery stiffness in type 2 diabetes. Int J Cardiol 2006;**112**(2):207-12.
64. Kyriakides ZS, Kremastinos DT, Kolokathis F, Kostopoulou A, Georgiadis M, Webb DJ. Acute endothelin(A) receptor antagonism improves coronary artery compliance in coronary artery disease patients. Clin Sci (Lond) 2002;**103 Suppl 48**:179S-183S.
65. Kyriakides Z, Kyrzopoulos S, Paraskevaidis I, Kolokathis F, Tsopotos I, Lyras T, Kremastinos D. Endothelin-A receptor antagonism promotes decreased vasodilation but has no differential effect on coronary artery compliance in hypertensive patients. J Cardiovasc Pharmacol 2004;**44 Suppl 1**:S85-8.
66. Bohm F, Jensen J, Svane B, Settergren M, Pernow J. Intracoronary endothelin receptor blockade improves endothelial function in patients with coronary artery disease. Can J Physiol Pharmacol 2008;**86**(11):745-51.
67. Halcox JP, Nour KR, Zalos G, Quyyumi AA. Endogenous endothelin in human coronary vascular function: differential contribution of endothelin receptor types A and B. Hypertension 2007;**49**(5):1134-41.
68. Papadogeorgos NO, Bengtsson M, Kalani M. Selective endothelin A-receptor blockade attenuates coronary microvascular dysfunction after coronary stenting in patients with type 2 diabetes. Vasc Health Risk Manag 2009;**5**:893-9.
69. Feng J, Liu Y, Khabbaz KR, Hagberg R, Sodha NR, Osipov RM, Sellke FW. Endothelin-1-induced contractile responses of human coronary arterioles via endothelin-A receptors and PKC-alpha signaling pathways. Surgery 2010;**147**(6):798-804.
70. Sundell J, Knuuti J. Insulin and myocardial blood flow. Cardiovasc Res 2003;**57**(2):312-9.
71. Bakker EN, Sorop O, Spaan JA, VanBavel E. Remodeling of resistance arteries in organoid culture is modulated by pressure and pressure pulsation and depends on vasomotion. Am J Physiol Heart Circ Physiol 2004;**286**(6):H2052-6.
72. Boesen EI. Endothelin ET_B receptor heterodimerization: beyond the ET_A receptor. Kidney Int 2008;**74**(6):693-4.

73. Hasselblatt M, Kamrowski-Kruck H, Jensen N, Schilling L, Kratzin H, Siren AL, Ehrenreich H. ET_A and ET_B receptor antagonists synergistically increase extracellular endothelin-1 levels in primary rat astrocyte cultures. Brain Res 1998;**785**(2):253-61.
74. Katz PS, Trask AJ, Souza-Smith FM, Hutchinson KR, Galantowicz ML, Lord KC, Stewart JA, Jr., Cismowski MJ, Varner KJ, Lucchesi PA. Coronary arterioles in type 2 diabetic (db/db) mice undergo a distinct pattern of remodeling associated with decreased vessel stiffness. Basic Res Cardiol 2011;**106**(6):1123-34.
75. Trask AJ, Katz PS, Kelly AP, Galantowicz ML, Cismowski MJ, West TA, Neeb ZP, Berwick ZC, Goodwill AG, Alloosh M, Tune JD, Sturek M, Lucchesi PA. Dynamic micro- and macrovascular remodeling in coronary circulation of obese Ossabaw pigs with metabolic syndrome. J Appl Physiol (1985) 2012;**113**(7):1128-40.
76. Gordin D, Ronnback M, Forsblom C, Heikkila O, Saraheimo M, Groop PH. Acute hyperglycaemia rapidly increases arterial stiffness in young patients with type 1 diabetes. Diabetologia 2007;**50**(9):1808-14.

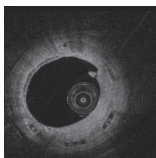

Part III

Bioresorbable scaffolds for the treatment of coronary artery disease

Bioabsorbable stent

Nienke Simone van Ditzhuijzen, Antonios Karanasos, Jors van der Sijde, Gijs van Soest, Evelyn Regar

Book chapter in: Jang IK. Cardiovascular OCT Imaging 2015

8

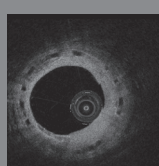

Abstract

Fully bioresorbable scaffolds are a promising approach to the treatment of coronary artery disease. The absence of residual foreign material and subsequent restoration of endothelial coverage may address the safety concerns associated with metallic drug-eluting stents such as permanent caging of the artery with or without malapposition, jailing of side branches and late stent thrombosis.

Currently, numerous bioresorbable scaffolds – the majority composed of bioresorbable polymers, and some of absorbable metals – are being developed. Coronary angiography is limited in its ability to visualize the scaffold, because of its low spatial resolution and the radiolucence of the scaffold's polymer backbone. Angiography alone cannot diagnose scaffold expansion, its interaction with the vessel wall or scaffold degradation over time.

Intracoronary imaging techniques such as intravascular ultrasound (IVUS) or optical coherence tomography (OCT) can overcome these limitations and allow for the evaluation of coronary arteries and scaffolds in great detail. OCT is particularly well suited for the assessment of atherosclerotic plaque, the scaffold and tissue coverage, and allows for detailed evaluation on the individual strut level.

Introduction and Rationale for the Use of Bioresorbable Scaffolds

In the past decades, the applications of percutaneous coronary intervention (PCI) have expanded steadily from balloon angioplasty, the use of bare metal stents, their refinement to drug-eluting stents, and currently fully bioresorbable (drug-eluting) stents are being developed. Fully bioresorbable scaffolds potentially allow for late luminal enlargement, late expansive remodelling and the return of vasomotion. The absence of residual foreign material and the subsequent restoration of endothelial coverage may address currently used stents' limitations including permanent caging with or without malapposition, jailing of side branches and late stent thrombosis.[1]

Today, numerous bioresorbable polymer or metal scaffolds are undergoing preclinical and clinical testing (**Table 1**). The most frequently used polymer is Poly-l-Lactide Acid (PLLA), which is widely used in clinical applications such as surgical sutures for wound closure, orthopaedic implants and dialysis media. The application of polymers as scaffolds in coronary arteries, however, still faces several challenges.

Challenges for the Evaluation of Bioresorbable Scaffolds

Bioresorbable scaffolds should possess a variety of key characteristics that are set by metallic stents, such as widespread availability, storage under standard conditions in the catheterization laboratory, fast preparation of the device, wide ranges of available sizes and lengths, a low crossing profile, good visibility under X-ray and a controlled and predictable expansion range. Polymeric scaffolds have however different material characteristics than metallic stents. The first polymeric scaffolds had to be stored under special conditions and had a shorter shelf-life than metallic stents. Today's bioresorbable scaffolds have similar storage conditions and shelf-lives to metallic stents.

Compared to metallic stents, bioresorbable materials are relatively rigid and non-elastic, resulting in the weakening of the polymeric scaffold by expansion and deformation, thus requiring careful sizing to the coronary artery dimensions. The majority of scaffolds have a balloon-expandable design, but there are also scaffolds with a self-expanding design (Igaki-Tamai) [2] or a slide-and-lock design (REVA), that is deployed by sliding open and is locked into place.[3]

Another important difference between the stent types lies in the fact that polymers are invisible under X-ray and thus suffer from poor visualization by coronary angiography. Most of the scaffolds are equipped with radio-opaque markers on both ends of

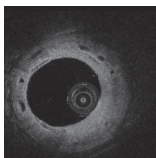

the scaffold or on both ends of the delivery balloon [2, 4, 5], whereas in the REVA bioresorbable scaffold a proprietary iodinated material is added to the polymer that allows visualization of the entire scaffold under X-ray.[3]

Table 1 Bioresorbable scaffolds under clinical evaluation

Scaffold	Manufacturer	Design	Drug-elution	Strut thickness (µm)	Resorption time (months)
Polymeric					
Igaki-Tamai	Kyoto Medical	Zigzag hoops	No	170	24-36
BVS1.0	Abbott Vascular	Circumferential hoops	Everolimus	150	24-48
BVS1.1	Abbott Vascular	In-phase zigzag hoops linked by bridges	Everolimus	150	36-60
DESolve gen 1	Elixir Medical	In-phase zigzag hoops linked by bridges	Myolimus	150	12-25
DESolve gen 2	Elixir Medical	In-phase zigzag hoops linked by bridges	Novolimus	150	12-25
REVA	Reva Medical	Slide-and-lock	No	114-228	4-6
ReZolve	Reva Medical	Slide-and-lock	Sirolimus	114-228	4-6
ReZolve2	Reva Medical	Slide-and-lock	Sirolimus	114-228	4-6
ART	Arterial remodeling technologies	Zigzag hoops	No	170	18-24
IDEAL	Xenogenics	In-phase zigzag hoops linked by bridges	Sirolimus	200	Unknown
Xinsorb	Huaan Biotech	Zigzag hoops	Sirolimus	160	12-24
ON-ABS	OrbusNeich	Zigzag hoops	Abluminal Sirolimus and luminal +CD34	150	Unknown
FORTITUDE	Amaranth	In-phase zigzag hoops linked by bridges	No	120	12-24
FORTITUDE gen 2	Amaranth	In-phase zigzag hoops linked by bridges	Sirolimus	120	12-24
Metallic					
AMS	Biotronik	Tubular slotted	No	Unknown	4-6
DREAMS gen 1	Biotronik	Zigzag hoops	Paclitaxel	120	12
DREAMS gen 2	Biotronik	In-phase zigzag hoops	Sirolimus	140	12

Coronary angiography is limited to assess scaffold expansion or scaffold degradation over time due to the poor spatial resolution and the radiolucence of the scaffold's polymer backbone. Furthermore, coronary angiography tends to underestimate the vessel dimensions (**Figure 1**).[6, 7] Intracoronary imaging techniques such as intravascular ultrasound (IVUS) or optical coherence tomography (OCT) can overcome these limitations.[8, 9] IVUS can provide real-time high-resolution cross-sectional images of the vessel wall and scaffold. IVUS, however, has a tendency to slightly overestimate vessel dimensions (**Figure 1**) and is hampered by the echogenic blooming effect caused by the polymeric struts (**Figure 2**). Additionally, the limited resolution of IVUS (80-150µm) compared to OCT (10-15µm) and the speckled echo signal from blood – that decreases the contrast between the lumen and vessel wall – make the assessment of scaffold expansion and especially the diagnosis of malapposition difficult by IVUS.

The high resolution of intracoronary OCT and the high contrast between lumen and vessel wall (**Figure 2**) offers advantages for the assessment of atherosclerotic plaque,[10] scaffold apposition (**Figure 3**) and tissue coverage [11, 12] and demonstrated consistently high accuracy and reproducibility in the assessment of coronary stents and scaffolds, irrespective of the analysis method or software used.[13-18]

	QCA	IVUS	OCT
		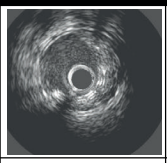	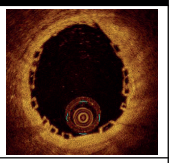
Dimension measurement	Underestimation	Overestimation	Correct
Detection of scaffold expansion and apposition	Not possible	Poor	Optimal
Detection of scaffold strut distribution	Not possible	Poor	Optimal
Detection of scaffold coverage	Poor	Poor	Optimal
Detection of scaffold strut degradation	Not possible	Poor	Optimal
Extra costs	No	Yes	Yes
Extra procedure time	No	Yes	Yes

Figure 1 Advantages of optical coherence tomography (OCT)

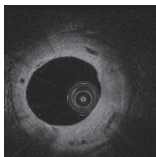

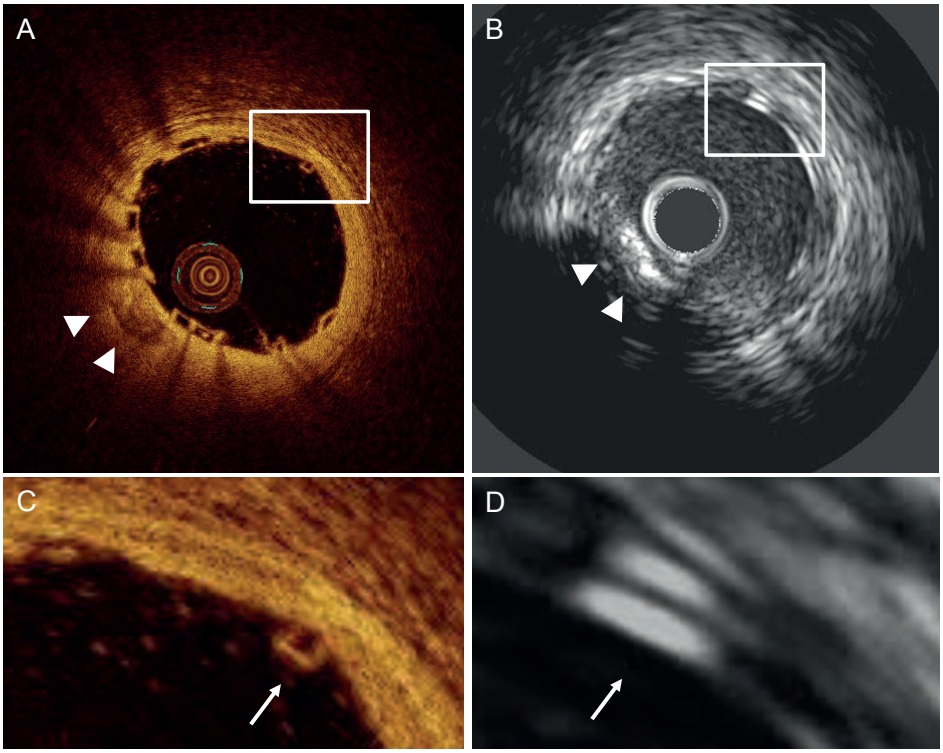

Figure 2 OCT and IVUS immediately after Absorb BVS-implantation in a patient with stable angina

The OCT cross-section (A) and magnification (C) demonstrate a box-shaped appearance of the scaffold struts (arrow), while in the IVUS cross-section (B) and magnification (D) the scaffold struts have a double-strut appearance due to the echogenic blooming effect of the polymeric struts of the Absorb bioresorbable vascular scaffold (Abbott Vascular, Santa Clara, USA). The arrowheads indicate a calcified region visible in both the OCT (A) and IVUS (B) cross-section

Intracoronary OCT Imaging of Bioresorbable Scaffolds

Intracoronary OCT enables high-resolution, *in-vivo*, serial imaging of the scaffold and has proven beneficial for the straight-forward detailed evaluation of atherosclerotic lesions and their composition, the vascular injury caused by the implantation procedure, the expansion, the apposition (**Figure 3**) and mechanical integrity of the scaffold over time, the effect of the underlying plaque on the performance of the scaffold, and the position of the scaffold relative to the side branches.[19-23]

OCT can reliably guide treatment strategy

Currently available bioresorbable scaffolds have relatively thick struts (114 – 228µm) resulting in a relatively high crossing profile. This means that adequate lesion prepa-

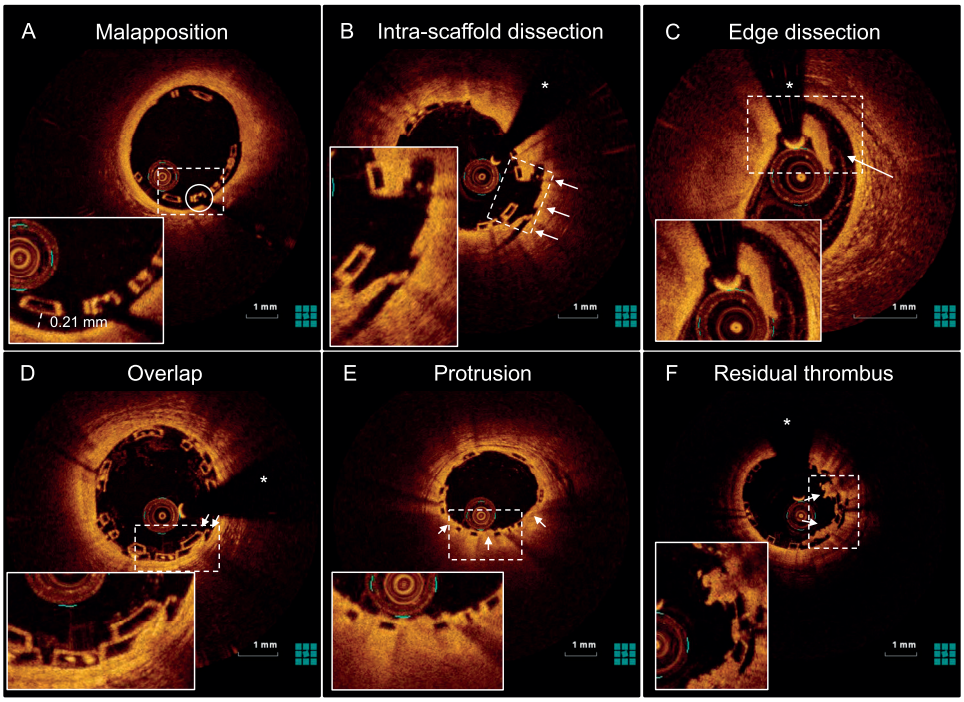

Figure 3 OCT can accurately detect scaffold apposition and peri-procedural vessel injury
OCT cross-sections of Absorb BVS demonstrate mild malapposition (A; circle and magnification), intra-scaffold dissection (B; arrows and magnification), edge dissection (C; arrow and magnification), scaffold overlap (D; arrows and magnification), tissue protrusion between the scaffold struts (E; arrows and magnification) and residual thrombus on top of the struts (F; arrows and magnification) after implantation of an Absorb BVS for ST-elevation myocardial infarction. The asterisk (*) indicates the guidewire artefact, the circle indicates the platinum marker of the scaffold strut, the dotted rectangles indicate the magnification

ration, e.g. by pre-dilatation, or another appropriate technique, is crucial to pass the device for implantation. Accurate determination of the lumen size and lesion characteristics prior to bioresorbable scaffold implantation is important to ensure appropriate sizing of the device. For instance, the Absorb bioresorbable vascular scaffold (BVS) (Abbott Vascular, Santa Clara, CA) allows for a maximum over-expansion of 0.5mm compared to the nominal scaffold diameter. Post-dilatation with balloons inflated >0.5mm above the indicated scaffold diameter increases the risk of fracture. OCT can accurately determine lumen and vessel dimensions as well as lesion characteristics and thus guide treatment strategy, in terms of the selection of an appropriate balloon and scaffold diameter and length.[6]

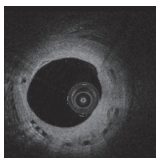

OCT can precisely assess scaffold expansion and strut apposition

The major concern in inadequate scaffold expansion and incomplete strut apposition is that it can cause non-laminar and turbulent blood flow that can trigger platelet activation, thrombosis or restenosis.[24, 25] OCT allows for the assessment of scaffold expansion in relation to the distal and proximal reference segments and to side branches, as well as strut apposition against the vessel wall. The accurate evaluation of scaffold expansion and apposition decreases the risk of incomplete scaffold expansion, recoil, fracture or thrombosis.[26, 27]

OCT can reliably assess scaffold strut distribution

Scaffold strut distribution can influence the concentrations of drug reached within the vessel wall, the radial support of the vessel wall and the access to side branches. Therefore, assessment of the scaffold strut distribution is important. Non-uniform strut distribution, which is hypothesized to be caused by calcified deposits occupying >75° of the vessel circumference,[28] may cause non-uniform drug-concentrations within the vessel wall, potentially affecting long-term outcome.[29] OCT allows for detailed analysis of the composition of the atherosclerotic lesion, including the size and extent of calcium, and of the strut distribution pattern, including the assessment of the maximum circular unsupported surface area as well as the assessment of side branch access through the scaffold struts and the impact of struts on side branch patency.[30-33]

OCT can accurately assess scaffold strut coverage

The absence and the exaggerated development of neointimal coverage, potentially with the subsequent development of neoatherosclerosis, have been related to late (drug-eluting) stent thrombosis.[34, 35] OCT can reliably detect early and very thin layers of coverage on top of scaffold struts and permits the quantification of the coverage with high reliability.[27, 36] OCT allows the assessment of scaffold area, neointimal area and symmetry as well as lumen area [37-39] and permits the qualitative characterization of neointimal tissue.[40, 41]

OCT allows for detailed assessment of scaffold strut degradation

Scaffold strut degradation is of growing clinical interest. OCT can visualize with detail the appearance of the scaffold struts and changes in the strut-appearance over time.[4]

In the first-in-man evaluation of the Absorb bioresorbable vascular scaffold (BVS), OCT demonstrated changes in the optical properties of the scaffold struts.

Preclinical observations in coronary arteries of healthy swine demonstrated that OCT can accurately diagnose individual struts as well as the strut/vessel wall interaction acutely (**Figure 4**) and over time. At the 4 year follow-up, OCT demonstrated absence of struts in the vascular wall, with complete degradation of the scaffold confirmed by histology. It is important to note that at the mid-term follow-up (2 years) OCT demonstrated a box-shaped appearance of the scaffold strut that can be associated with strut replacement by proteoglycan.[42]

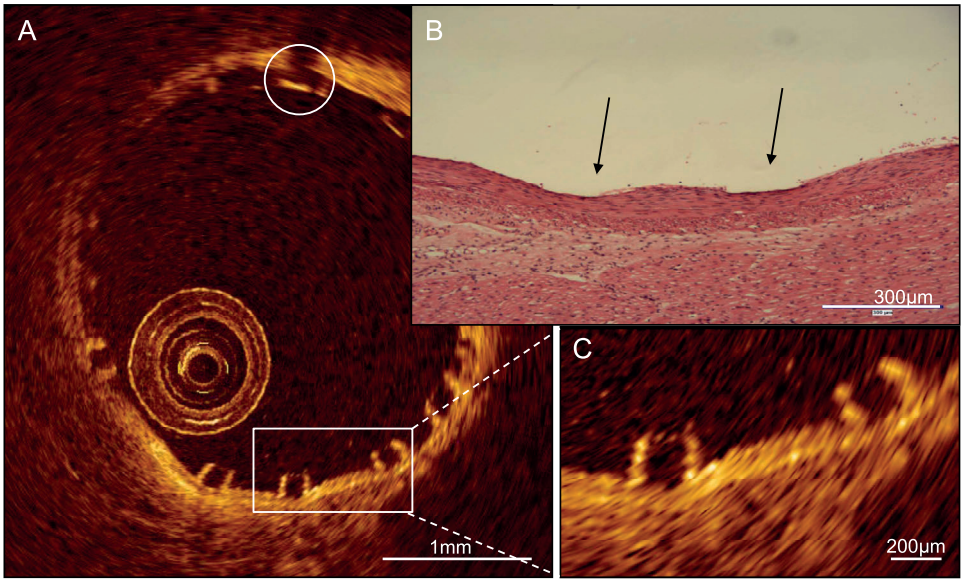

Figure 4 OCT and histology of the Absorb BVS immediately after implantation in a healthy, young swine

OCT (A and C) can accurately visualize the vessel/ wall interaction after implantation of an Absorb bioresorbable vascular scaffold (Abbott Vascular, Santa Clara, CA, USA) in a coronary artery of a healthy, young swine. In the magnification the typical box-shaped appearance of the scaffold struts can be appreciated, which slightly compress the media (C), as confirmed by the histological cross-section (B). The circle indicates the platinum marker of the scaffold strut, the arrows indicate the indentation of the scaffold on histology

Advantage of three-dimensional OCT

The unique ability of OCT to reconstruct three-dimensional (3D) images allows better visualization of the scaffold surface and can provide additive information on the result of PCI, particularly in complex lesions.[43, 44] The application of 3D OCT within the coronary bifurcation seems promising, as the visualization of the complex anatomy of

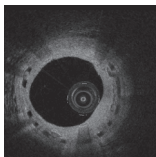

the bifurcation and the effects of intervention are difficult and not always reliable with two-dimensional imaging.[32, 45] 3D-OCT can identify the configuration of overhanging struts in front of the side branch ostium and can be helpful to assess and correctly position the guidewire.

Clinical Experience

Numerous bioresorbable scaffolds have been investigated in humans.[46] Some have demonstrated disappointing first findings,[47] while others, e.g. the ABSORB trials, have proven more encouraging findings.[4]

Polymeric bioresorbable scaffolds

Igaki-Tamai

The Igaki-Tamai (Igaki Medical Planning Co., Kyoto, Japan) represents the first fully biodegradabable scaffold tested in humans in the 1990's.[2] It was a self-expanding, poly-l-lactic acid (PLLA) based, non drug-eluting scaffold with a zigzag design and a strut thickness of 170µm. The scaffold was compatible with 8F guide catheters and required storage and expansion at a pre-specified temperature.

A clinical trial in 15 patients proved feasibility and demonstrated remarkable results with a target lesion revascularization rate per patient of 6.7% at 6 months.[2] Six-month intravascular imaging demonstrated no degradation of the scaffold and the absence of scaffold shrinkage. At the 10-year follow-up, similar major adverse cardiac event (MACE) rates to those of bare metal stents (MACE-free survival was 50% at 10 years) were documented [48] and OCT demonstrated that just the scaffold markers were still visible (**Figure 5**). Despite the good results, however, further use of the scaffold for treatment of coronary disease was put on hold, mainly because of the pre-specified temperature required for storage and expansion.

Absorb BVS

The Absorb bioresorbable vascular scaffold (Abbott Vascular, Santa Clara, CA) represents the scaffold with the vastest clinical experience. The scaffold is constructed of a poly-L-lactic acid (PLLA) backbone coated with poly-D,L-lactic acid (PDLLA) that contains the antiproliferative drug everolimus and controls its release (**Figure 4**).[49]

In the *ABSORB Cohort A trial*, a prospective, multi-center registry in 30 patients with a single, *de-novo* target lesion in a native coronary artery, the first-generation BVS

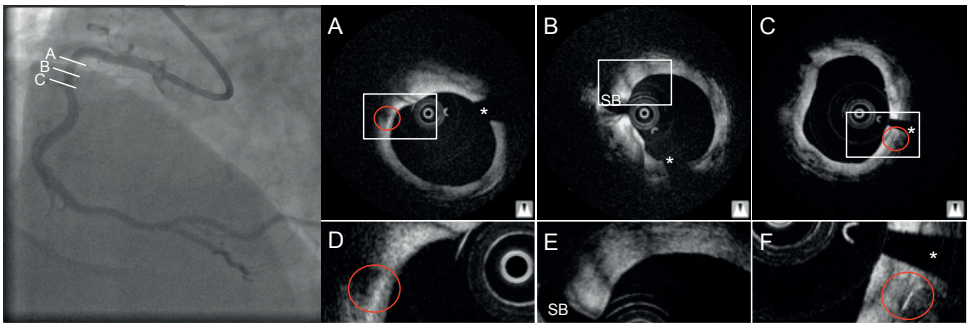

Figure 5 Angiography and OCT 10 years after implantation of an Igaki-Tamai scaffold in a patient with stable angina

Optical coherence tomography cross-sections (A to F) demonstrate that only the markers of the scaffold are still visible (A and C), while the remaining struts are not. The asterisk (*) indicates the guidewire artifact, SB = side branch, the rectangles indicate the magnifications on the bottom and the red circles indicate the markers of the scaffold

(BVS1.0) was investigated.[4] The majority of patients received a 3.0x12.0mm scaffold, 2 patients received a 3.0x18mm scaffold. The BVS1.0 was designed with a crossing profile of 1.4 mm in circumferential hoops and a strut thickness of 150µm that were either directly joined or linked by straight bridges. The scaffolds had to be kept at a minimum temperature of -20˚C to prevent physical aging of the polymer and to ensure device stability.

This first-in-man-trial trial demonstrated the feasibility of the everolimus-eluting BVS1.0. Procedural success was 100%, and device success, 94%.[4, 50, 51] At one year, the MACE-rate was 3.3% of 30 patients. One patient suffered a non-Q wave myocardial infarction. There were no late stent thromboses. At 2 years vasomotion restored, and the scaffold was clinically safe without cardiac death, ischaemia-driven target lesion revascularisation, or stent thrombosis.[4, 50] Long-term results up to 5 years confirmed favourable clinical outcomes, without any cardiac death or scaffold thrombosis and ischaemia-driven MACE rate remained unchanged (3.4% of 29 patients).[52] Furthermore, late luminal enlargement (**Figure 6**) without adaptive vessel remodelling was observed up to 5 year follow-up.[53-56]

The OCT substudy of this first-in-man trial, including 13 patients, described changes of the strut appearance at follow-up that were thought to be associated with degradation of the scaffold over time.

In the preclinical study of the BVS1.0 implanted in healthy young swine, however, the assessment of polymer degradation by chemical analysis demonstrated that the preservation of the box-shaped appearance did not exclude resorption of polymeric

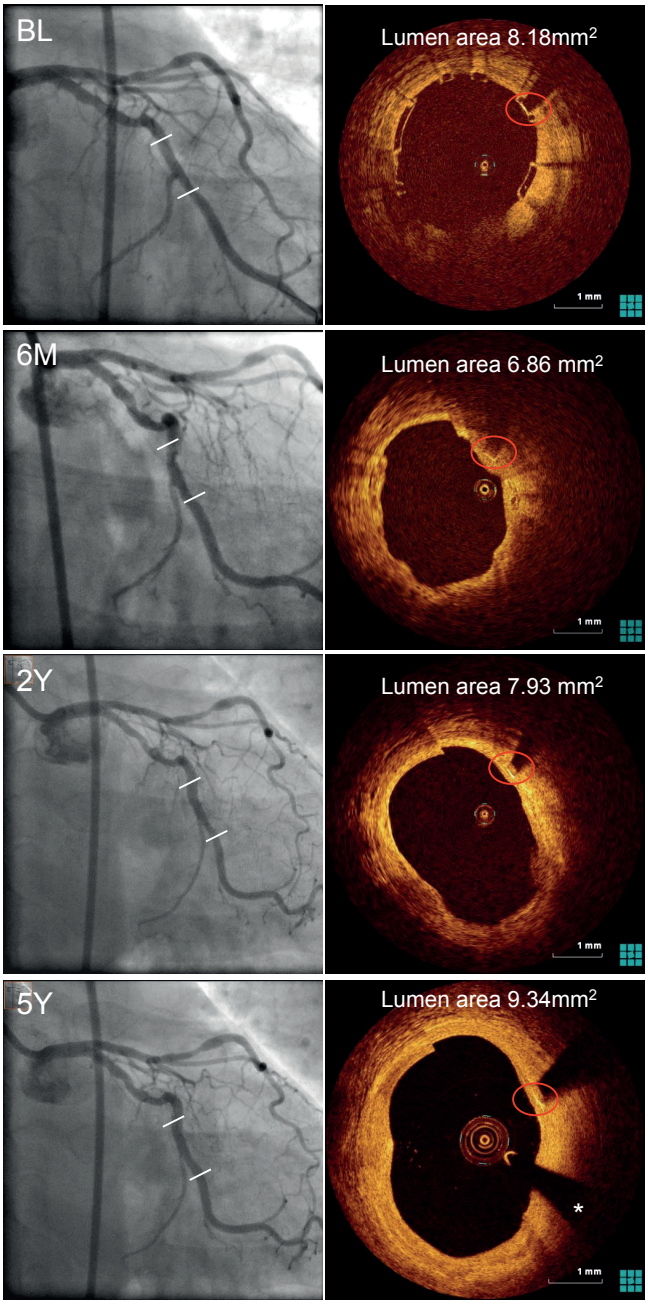

Figure 6 Angiography and OCT of an Absorb BVS immediately after, 6 months and 2 and 5 years after implantation in a patient with stable angina

The distal and proximal edge of the scaffold are depicted by white lines in the coronary angiogram (left). The box-shaped appearance of the scaffold struts can be clearly visualized by OCT immediately after implantation. At 5 year follow-up, the marker of the scaffold strut is visible (red circle), while the remaining scaffold struts are not. The asterisk (*) indicates the guidewire artefact

struts.[42] Two years after implantation, the polymer was no longer accurately quantifiable by chemical degradation analysis, but the structures observed with OCT represented regions corresponding to the location of the scaffold struts. At the 4-year follow-up, OCT demonstrated an absence of struts in the vascular wall, indicating its ability to assess complete degradation of the scaffold *in-vivo*.

In the *ABSORB Cohort B trial*, a prospective, multi-center registry of patients with a single, *de-novo* target lesion in a native coronary artery, the second-generation Absorb BVS (BVS 1.1) was investigated. The BVS1.1 is similar to the BVS1.0 with the same polymer mass, strut thickness and drug coating. The manufacturing process of the BVS1.1 has however been modified to enhance the mechanical strength and durability of the struts.[30] The BVS1.1 has in-phase zigzag hoops linked by bridges that allow for more uniform strut distribution, reducing the maximum circular unsupported surface area and providing more uniform vessel wall support and drug transfer.[33]

Clinical results demonstrated a low MACE-rate at 6 months (4.4%), representing one myocardial infraction and one target lesion revascularization. No death or thrombosis occurred.[57] At 1 year, the MACE-rate was 7.1%, representing two myocardial infarctions and 2 target lesion revascularizations, whereas no cardiac death occurred. At 3 years, the MACE-rate was 10.0% without any scaffold thrombosis. The return of vasomotion was observed at 12 months and more pronounced at 24 months, suggesting a link between scaffold degradation and restoration of vasomotion in the treated segments.[58]

The OCT substudy demonstrated preservation of the box-shaped appearance of the scaffold struts at 6 months, [30] which is in line with preclinical observations in atherosclerotic swine [59] 6 months after Absorb BVS1.1 implantation (**Figure 7**).

In the *ABSORB EXTEND trial*, a non-randomized, single-arm, continued access trial, 800 patients with up to two *de novo* lesions in a native coronary artery were treated with BVS 1.1 to continue the assessment of the safety and performance of the BVS1.1 in a large and more complex population. The preliminary report of the twelve-month clinical outcomes for the first 512 patients demonstrated that the composite endpoints of ischaemia-driven MACE and ischaemia-driven target vessel failure were low (4.3% and 4.9%, respectively). The cumulative rate of definite and probable scaffold thrombosis was 0.8%.[60]

Other clinical trials that are underway include the *ABSORB II* and *the ABSORB III and IV pivotal clinical trial programs*. The *ABSORB II trial* is the first randomized trial designed to compare the safety and efficacy of the BVS1.1 versus Xience prime in 500 patients with stable angina and single or two vessel disease.[61] The *ABSORB III and IV pivotal clinical trial programs* are randomized trials designed to achieve approval of

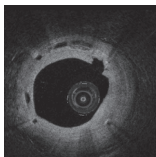

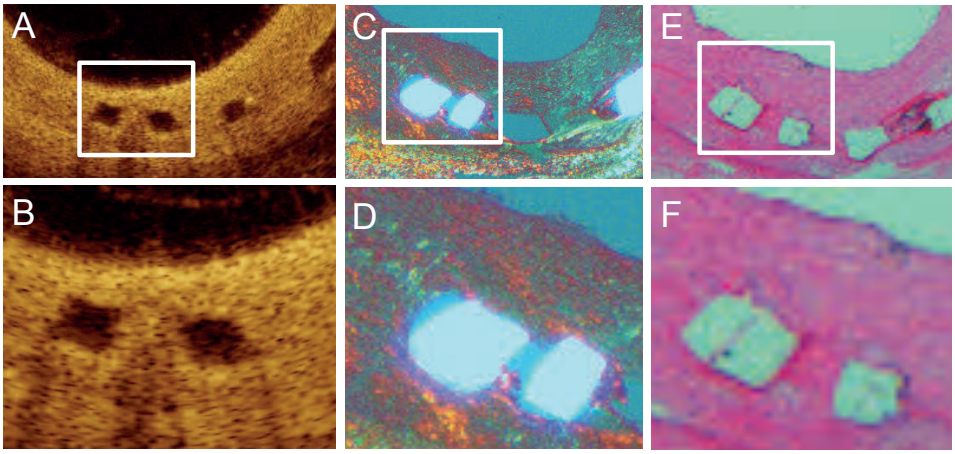

Figure 7 OCT and histology 6 months after Absorb BVS1.1 implantation in an atherosclerotic swine

The OCT cross-sections (A, magnification in B) clearly demonstrate the box-shaped appearance of the scaffold struts. Preservation of the scaffold struts is confirmed by histology, demonstrating presence of the polymeric struts under polarization light microscopy (C, magnification in D) and of the strut voids on haematoxylin eosin staining (E, magnification in F).

BVS1.1 in the United States of America and to demonstrate the superiority of BVS1.1 compared to drug-eluting stents.[62]

DESolve

The DESolve (Elixir Medical, Sunnyvale, USA) scaffold is a PLLA-based scaffold that contains the anti-proliferative drug myolimus, has a strut thickness of 150µm, 2 platinum-based radiopaque markers at either end of the scaffold, provides vessel support for 3-4 months and fully resorbs in about 1 year.

In *the DESolve First-in-Man* study, a prospective, non-randomized, multi-center study, 16 patients with *de novo* native coronary artery lesions were included and the feasibility and efficacy of the DESolve scaffold were demonstrated.[5] Acute procedural success was 100%. At 12 months, no scaffold thrombosis or MACE directly attributable to the scaffold occurred and invasive imaging demonstrated low neointimal hyperplasia and no evidence of scaffold recoil or late malapposition.[5]

In *the DESolve Nx study*, a prospective, multi-center study presented at the transcatheter-therpeutic-interventions (TCT) conference in San Francisco in 2013, the second iteration of the DESolve containing the antiproliferative drug novolimus was evaluated. In the first 126 patients included, a 1-year MACE rate of 5.69% was observed,

representing 2 cardiac deaths, 1 target vessel myocardial infarction and 4 clinically indicated target lesion revascularizations. No scaffold thrombosis was documented.[63]

REVA

The first-generation REVA (REVA Medical Inc., San Diego, USA) is a non-drug-eluting scaffold composed of tyrosine-derived polycarbonate, with a unique radio-opaque slide-and-lock mechanism to allow for safe expansion and visualization under X-ray (**Figure 8**).[3]

In *the RESORB study*, a non-randomized, multicenter registry that assessed the safety and performance of the scaffold, 25 patients with a *de novo* coronary lesion were included. Radial strength was sufficient during the first 3 months following implantation without appreciable shrinkage. However, focal mechanical failures led to a high rate of target lesion revascularization (66.7%) between the 4 and 6 months follow-up.[64]

In *the RESTORE trial*, the ReZolve Sirolimus-eluting bioresorbable coronary scaffold clinical trial, a new iteration of the REVA scaffold, the ReZolve, was evaluated for its safety and performance in 26 patients. The 12 months results, presented at the TCT conference in Miami in 2012, demonstrated safety and good performance. Two MACE, one target lesion revascularization for focal in-stent restenosis, and one directly related to protocol deviation at implant were documented up through the 6 months follow-up.[65]

In *the RESTORE II trial*, the second-generation ReZolve (ReZolve2), which has a lower profile and is sheathless, will be evaluated in 125 patients with the aim of attaining Conformité Européenne (CE) mark approval.

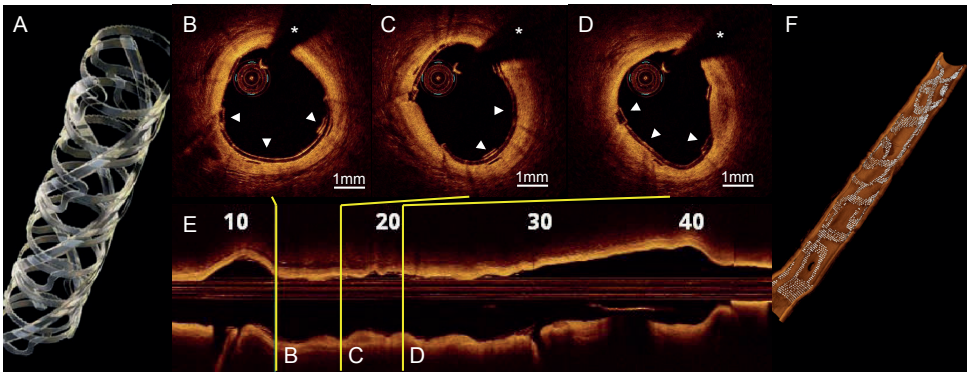

Figure 8 OCT immediately after REVA scaffold implantation in a patient with stable angina
The REVA is designed with a unique slide-and-lock design, as can be visualized in the cartoon (A), the OCT cross-sections (arrowheads in B, C and D) that correspond to the letters B, C and D in the longitudinal view (E) of the OCT-pullback and the three-dimensional reconstruction (F). The asterisk (*) indicates the guide wire artifact.

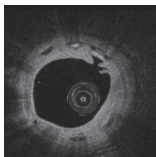

ART

The ART (Arterial Remodeling Technologies, Noisy le Roi, France) is a drug-free, flexible, bioresorbable PDLLA-polymer scaffold. Dismantling starts at 3 months with recovery of arterial function, and full resorption expected within 18-24 months.

In *the ARTDIVA* (Arterial Remodelling Transient Dismantling Vascular Angioplasty) trial, a prospective, multicenter, single-arm investigation, 30 patients with single *de novo* native coronary artery lesions with mandatory balloon pre-dilatation were included. Preliminary results, presented at the TCT conference in San Francisco in 2013, demonstrated 100% procedural and 94% device success, good apposition, 30-day event-free survival and 4.0% angiographic recoil at 30 days.[66]

IDEAL

The IDEAL (Xenogenics Corp., Canton, MA, USA) is a fully bioresorbable balloon-expandable scaffold that consists of a polylactide, anhydride and a trimer of two salicyclic acid molecules joined by a sebacic acid, while the top coat is comprised of salicylate and the antiproliferative drug sirolimus.[67]

In *the WHISPER study*, a prospective, first-in-man study, the safety and efficacy of the scaffold was evaluated. Although the study has not been fully reported, an increased neointimal formation, attributed to an inadequate drug dose and fast drug-elution, was documented in eleven patients, and a new iteration of the scaffold was developed.

The revised scaffold, the IDEAL BioStent, has a higher drug dose with slower release kinetics and is currently under preclinical evaluation.

Xinsorb

The Xinsorb (Shandong Huaan Biotechnology Co., Ltd, China) is a sirolimus-eluting, balloon-expandable, PLLA scaffold that has radiopaque markers to facilitate its expansion. The scaffold has a strut thickness of 160μm and is available in sizes ranging from 2.75 to 4.0mm in diameter, and from 12 to 28mm in length.[68]

In the first-in-man, prospective, bi-centre trial, the feasibility, safety and efficacy of the Xinsorb will be evaluated in 30 patients at 1, 3, 6, 9 and 12 months. The six-months angiography of the first 6 patients demonstrates effective suppression of neointimal hyperplasia.[69]

ON-ABS

The ON-ABS BRS is composed of three distinct bioabsorbable polymer systems: Poly-D-lactide, PLLA, and L-lactide-co-ε-caprolactone, and incorporates a partitioned

coating technology that allows the scaffold to be covered by abluminal sirolimus and luminal endothelial progenitor cell capture (+CD34) antibodies. Preliminary preclinical data presented at the TCT conference in San Francisco in 2013 demonstrated optimal device implantation without evidence of fracture.[70]

The first-in-man evaluation of the ON-ABS is underway.

FORTITUDE

The FORTITUDE (Amaranth Medical Inc Mountain View, CA, USA) is a non-drug-eluting PLLA-based scaffold that contains structural integrity for 3-6 months and completely resorbs within 1-2 years. The scaffold was evaluated in a study of 13 patients with single *de novo* coronary artery lesions and, as presented at the TCT conference in San Francisco in 2013, demonstrated maintained mechanical integrity with late lumen loss comparable to that observed for bare metal stents at the 6 months follow-up.[71]

Currently, the second-generation FORTITUDE, which has thinner struts and sirolimus drug-elution capabilities, is already in advanced development.

Metallic bioresorbable scaffolds

AMS

The absorbable metal stent (AMS) (Biotronik, Berlin, Germany) is a tubular, slotted, magnesium-based balloon-expandable scaffold, available in 10 and 15mm lengths with 3.0 and 3.5mm diameters, respectively.

In the first-in-man *PROGRESS-AMS trial*, a prospective, non-randomized, multi-center clinical trial, 63 patients with single *de novo* native coronary artery lesions were enrolled.[72] No myocardial infarction, subacute or late thrombosis, or death was documented. Target lesion revascularization rates were, however, high: 23.8% after 4 months, and 45% after 1 year.

In *the BIOSOLVE-1 trial*, a prospective, multi-center study, a new generation drug-eluting absorbable metal scaffolds (DREAMS), characterized by a prolonged scaffolding time and the anti-proliferative drug paclitaxel, was evaluated in 46 patients with single *de novo* native coronary artery lesions. One-year results demonstrated feasibility and safety of the DREAMS with 100% procedural and device success, a target lesion revascularization rate of 7% and no cardiac death or scaffold thrombosis.[73]

In *the BIOSOLVE-II trial*, a prospective, international, multi-centre study, the safety and clinical performance of the second-generation sirolimus-eluting DREAMS will be evaluated.

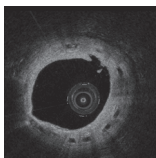

Other Bioresorbable Scaffolds Currently Under Investigation

Several other bioresorbable scaffolds that are currently under development include the MeRes (Meril Life Science, India), Lifetech Iron (Lifetech Scientific, Shenzhen, China), Sahajanand (Sahajanand Medica Technologies, India), Avatar (S3V Vascular Technologies, India), FADES (Zorion Medical, Indianapolis, IN, USA) and Arterius (Arterius Ltd, Bradford, UK).

OCT Imaging Of Bioresorbable Scaffolds – A Step Towards Routine Clinical Practice

Bioresorbable scaffolds are increasingly used in clinical practice, with the extension to patients with more complex lesions,[60] including ST-elevation myocardial infarction patients,[74] patients with long lesions requiring overlapping scaffolds, or patients with small vessels and bifurcation lesions.[75-78] The detailed evaluation of the behaviour and performance of bioresorbable scaffolds – such as the expansion, apposition and degradation of the scaffolds as well as the vascular response to the scaffold – is of growing clinical interest and thus the longitudinal, *in-vivo* intracoronary OCT, which has proven safe, highly accurate and reliable, is more widely used. Additionally, with the development of 3D OCT and software that allows co-registration of quantitative coronary angiography and OCT,[79] OCT can accurately guide treatment strategy (**Figure 9**) and assess treatment outcome (**Figure 10**) and thus provide advantages for the evaluation of scaffold behaviour and performance in routine clinical practice.

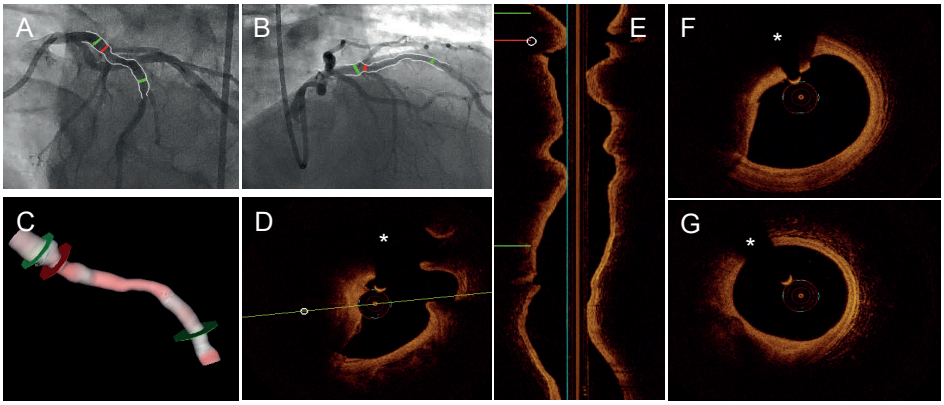

Figure 9 Three-dimensional (3D) QCA and OCT for optimal scaffold selection

Two angiographic views (A and B) were used to reconstruct the color-coded vessel segment (C). The red line corresponds to the OCT cross-section that is used as landmark (D), also visible in the longitudinal view of the OCT pullback (E). The green lines indicate the distal (F) and proximal (G) landing zones. After the registration, the corresponding markers in the different views (A to G) were synchronized, allowing the assessment of lumen dimensions from both imaging modalities at every corresponding position along the vessel segment (QAngioOCT; Medis Specials, Leiden, Netherlands). The asterisk (*) indicates the guide wire artifact

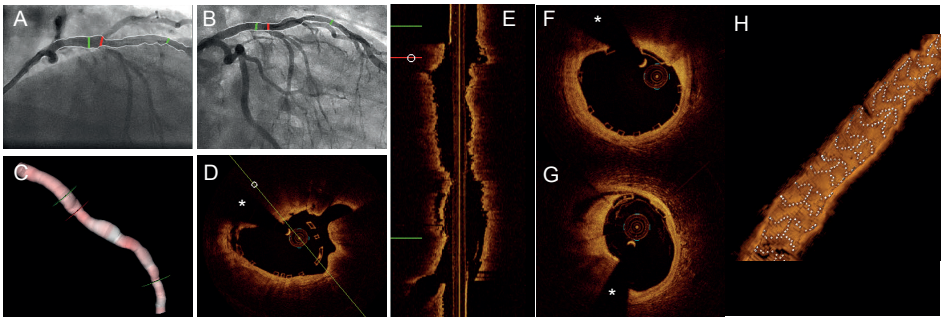

Figure 10 Three-dimensional QCA and OCT to assess scaffold-implantation

Two angiographic views (A and B) were used to reconstruct the color-coded vessel segment (C). The red line corresponds to the OCT cross-section that is used as landmark (D), also visible in the longitudinal view of the OCT pullback (E). The green lines indicate the distal (F) and proximal (G) landing zones. After the registration, the corresponding markers in the different views (A to G) were synchronized, allowing for assessment of the scaffold from both imaging modalities. The 3D reconstruction of the scaffold clearly demonstrates the in-phase zigzag hoops that are linked by bridges (H) (QAngioOCT; Medis Specials, Leiden, Netherlands). The asterisk (*) indicates the guide wire artifact

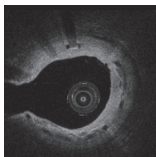

References

1. Serruys PW, Garcia-Garcia HM, Onuma Y. From metallic cages to transient bioresorbable scaffolds: change in paradigm of coronary revascularization in the upcoming decade? Eur Heart J 2012;**33**(1):16-25b.
2. Tamai H, Igaki K, Kyo E, Kosuga K, Kawashima A, Matsui S, Komori H, Tsuji T, Motohara S, Uehata H. Initial and 6-month results of biodegradable poly-l-lactic acid coronary stents in humans. Circulation 2000;**102**(4):399-404.
3. Pollman MJ. Engineering a bioresorbable stent: REVA programme update. EuroIntervention 2009;**5 Suppl F**:F54-7.
4. Ormiston JA, Serruys PW, Regar E, Dudek D, Thuesen L, Webster MW, Onuma Y, Garcia-Garcia HM, McGreevy R, Veldhof S. A bioabsorbable everolimus-eluting coronary stent system for patients with single de-novo coronary artery lesions (ABSORB): a prospective open-label trial. Lancet 2008;**371**(9616):899-907.
5. Verheye S, Ormiston JA, Stewart J, Webster M, Sanidas E, Costa R, Costa JR, Jr., Chamie D, Abizaid AS, Pinto I, Morrison L, Toyloy S, Bhat V, Yan J, Abizaid A. A next-generation bioresorbable coronary scaffold system: from bench to first clinical evaluation: 6- and 12-month clinical and multimodality imaging results. JACC Cardiovasc Interv 2014;**7**(1):89-99.
6. Gutierrez-Chico JL, Serruys PW, Girasis C, Garg S, Onuma Y, Brugaletta S, Garcia-Garcia H, van Es GA, Regar E. Quantitative multi-modality imaging analysis of a fully bioresorbable stent: a head-to-head comparison between QCA, IVUS and OCT. Int J Cardiovasc Imaging 2012;**28**(3):467-78.
7. Tsuchida K, van der Giessen WJ, Patterson M, Tanimoto S, Garcia-Garcia HM, Regar E, Ligthart JM, Maugenest AM, Maatrijk G, Wentzel JJ, Serruys PW. In vivo validation of a novel three-dimensional quantitative coronary angiography system (CardiOp-B): comparison with a conventional two-dimensional system (CAAS II) and with special reference to optical coherence tomography. EuroIntervention 2007;**3**(1):100-8.
8. Huang D, Swanson EA, Lin CP, Schuman JS, Stinson WG, Chang W, Hee MR, Flotte T, Gregory K, Puliafito CA, et al. Optical coherence tomography. Science 1991;**254**(5035):1178-81.
9. Sarno G, Bruining N, Onuma Y, Garg S, Brugaletta S, De Winter S, Regar E, Thuesen L, Dudek D, Veldhof S, Dorange C, Garcia-Garcia HM, Ormiston JA, Serruys PW. Morphological and functional evaluation of the bioresorption of the bioresorbable everolimus-eluting vascular scaffold using IVUS, echogenicity and vasomotion testing at two year follow-up: a patient level insight into the ABSORB A clinical trial. Int J Cardiovasc Imaging 2012;**28**(1):51-8.
10. Van Ditzhuijzen NS, Van Beusekom HM, Ligthart JM, Regar E. Invasive imaging of the coronary atherosclerotic plaque. Minerva Cardioangiol 2012;**60**(3):305-29.
11. Regar E, van Leeuwen AMGJ, Serruys PW. *Optical coherence tomography in cardiovascular research.* London: Informa Healthcare; 2007.
12. Gonzalo N, Serruys PW, Garcia-Garcia HM, van Soest G, Okamura T, Ligthart J, Knaapen M, Verheye S, Bruining N, Regar E. Quantitative ex vivo and in vivo comparison of lumen dimensions measured by optical coherence tomography and intravascular ultrasound in human coronary arteries. Rev Esp Cardiol 2009;**62**(6):615-24.
13. van Ditzhuijzen NS, Karanasos A, Bruining N, van den Heuvel M, Sorop O, Ligthart J, Witberg K, Garcia-Garcia HM, Zijlstra F, Duncker DJ, van Beusekom HM, Regar E. The impact

of Fourier-Domain optical coherence tomography catheter induced motion artefacts on quantitative measurements of a PLLA-based bioresorbable scaffold. Int J Cardiovasc Imaging 2014.

14. Jamil Z, Tearney G, Bruining N, Sihan K, van Soest G, Ligthart J, van Domburg R, Bouma B, Regar E. Interstudy reproducibility of the second generation, Fourier domain optical coherence tomography in patients with coronary artery disease and comparison with intravascular ultrasound: a study applying automated contour detection. Int J Cardiovasc Imaging 2013;**29**(1):39-51.
15. Okamura T, Onuma Y, Garcia-Garcia HM, van Geuns RJ, Wykrzykowska JJ, Schultz C, van der Giessen WJ, Ligthart J, Regar E, Serruys PW. First-in-man evaluation of intravascular optical frequency domain imaging (OFDI) of Terumo: a comparison with intravascular ultrasound and quantitative coronary angiography. EuroIntervention 2011;**6**(9):1037-45.
16. Gonzalo N, Tearney GJ, Serruys PW, van Soest G, Okamura T, Garcia-Garcia HM, Jan van Geuns R, van der Ent M, Ligthart J, Bouma BE, Regar E. Second-generation optical coherence tomography in clinical practice. High-speed data acquisition is highly reproducible in patients undergoing percutaneous coronary intervention. Rev Esp Cardiol 2010;**63**(8):893-903.
17. Okamura T, Gonzalo N, Gutierrez-Chico JL, Serruys PW, Bruining N, de Winter S, Dijkstra J, Commossaris KH, van Geuns RJ, van Soest G, Ligthart J, Regar E. Reproducibility of coronary Fourier domain optical coherence tomography: quantitative analysis of in vivo stented coronary arteries using three different software packages. EuroIntervention 2010;**6**(3):371-9.
18. G Z, Karanasos A, Van Soest G, E R, Niessen WJ, Gijsen FJ, van Walsum T. Semi-automated quantification of fibrous cap thickness in intra- coronary optical coherence tomography. IPCAI in press 2014.
19. Takarada S, Imanishi T, Liu Y, Ikejima H, Tsujioka H, Kuroi A, Ishibashi K, Komukai K, Tanimoto T, Ino Y, Kitabata H, Kubo T, Nakamura N, Hirata K, Tanaka A, Mizukoshi M, Akasaka T. Advantage of next-generation frequency-domain optical coherence tomography compared with conventional time-domain system in the assessment of coronary lesion. Catheter Cardiovasc Interv 2010;**75**(2):202-6.
20. Prati F, Regar E, Mintz GS, Arbustini E, Di Mario C, Jang IK, Akasaka T, Costa M, Guagliumi G, Grube E, Ozaki Y, Pinto F, Serruys PW, Expert's OCTRD. Expert review document on methodology, terminology, and clinical applications of optical coherence tomography: physical principles, methodology of image acquisition, and clinical application for assessment of coronary arteries and atherosclerosis. Eur Heart J 2010;**31**(4):401-15.
21. Prati F, Guagliumi G, Mintz GS, Costa M, Regar E, Akasaka T, Barlis P, Tearney GJ, Jang IK, Arbustini E, Bezerra HG, Ozaki Y, Bruining N, Dudek D, Radu M, Erglis A, Motreff P, Alfonso F, Toutouzas K, Gonzalo N, Tamburino C, Adriaenssens T, Pinto F, Serruys PW, Di Mario C, Expert's OCTRD. Expert review document part 2: methodology, terminology and clinical applications of optical coherence tomography for the assessment of interventional procedures. Eur Heart J 2012;**33**(20):2513-20.
22. Tanimoto S, Bruining N, van Domburg RT, Rotger D, Radeva P, Ligthart JM, Serruys PW. Late stent recoil of the bioabsorbable everolimus-eluting coronary stent and its relationship with plaque morphology. J Am Coll Cardiol 2008;**52**(20):1616-20.
23. Tearney GJ, Regar E, Akasaka T, Adriaenssens T, Barlis P, Bezerra HG, Bouma B, Bruining N, Cho JM, Chowdhary S, Costa MA, de Silva R, Dijkstra J, Di Mario C, Dudek D, Falk E,

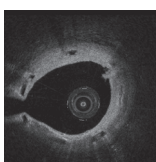

Feldman MD, Fitzgerald P, Garcia-Garcia HM, Gonzalo N, Granada JF, Guagliumi G, Holm NR, Honda Y, Ikeno F, Kawasaki M, Kochman J, Koltowski L, Kubo T, Kume T, Kyono H, Lam CC, Lamouche G, Lee DP, Leon MB, Maehara A, Manfrini O, Mintz GS, Mizuno K, Morel MA, Nadkarni S, Okura H, Otake H, Pietrasik A, Prati F, Raber L, Radu MD, Rieber J, Riga M, Rollins A, Rosenberg M, Sirbu V, Serruys PW, Shimada K, Shinke T, Shite J, Siegel E, Sonoda S, Suter M, Takarada S, Tanaka A, Terashima M, Thim T, Uemura S, Ughi GJ, van Beusekom HM, van der Steen AF, van Es GA, van Soest G, Virmani R, Waxman S, Weissman NJ, Weisz G. Consensus standards for acquisition, measurement, and reporting of intravascular optical coherence tomography studies: a report from the International Working Group for Intravascular Optical Coherence Tomography Standardization and Validation. J Am Coll Cardiol 2012;**59**(12):1058-72.

24. Foin N, Gutierrez-Chico JL, Nakatani S, Torii R, Bourantas CV, Sen S, Nijjer S, Petraco R, Kousera C, Ghione M, Onuma Y, Garcia-Garcia HM, Francis DP, Wong P, Di Mario C, Davies JE, Serruys PW. Incomplete stent apposition causes high shear flow disturbances and delay in neointimal coverage as a function of strut to wall detachment distance: implications for the management of incomplete stent apposition. Circ Cardiovasc Interv 2014;**7**(2):180-9.
25. Karanasos A, van Geuns RJ, Zijlstra F, Regar E. Very late bioresorbable scaffold thrombosis after discontinuation of dual antiplatelet therapy. Eur Heart J 2014.
26. Gomez-Lara J, Diletti R, Brugaletta S, Onuma Y, Farooq V, Thuesen L, McClean D, Koolen J, Ormiston JA, Windecker S, Whitbourn R, Dudek D, Dorange C, Veldhof S, Rapoza R, Regar E, Garcia-Garcia HM, Serruys PW. Angiographic maximal luminal diameter and appropriate deployment of the everolimus-eluting bioresorbable vascular scaffold as assessed by optical coherence tomography: an ABSORB cohort B trial sub-study. EuroIntervention 2012;**8**(2):214-24.
27. Gomez-Lara J, Radu M, Brugaletta S, Farooq V, Diletti R, Onuma Y, Windecker S, Thuesen L, McClean D, Koolen J, Whitbourn R, Dudek D, Smits PC, Regar E, Veldhof S, Rapoza R, Ormiston JA, Garcia-Garcia HM, Serruys PW. Serial analysis of the malapposed and uncovered struts of the new generation of everolimus-eluting bioresorbable scaffold with optical coherence tomography. JACC Cardiovasc Interv 2011;**4**(9):992-1001.
28. Sato K, Latib A, Naganuma T, Panoulas VF, Miyazaki T, Colombo A. Impact of calcified plaque for stent struts distribution of the bioabsorbable everolimus-eluting device - Optical coherence tomography analysis. In: *EuroPCR. Paris, 2014*.
29. Suzuki Y, Ikeno F, Yeung AC. Drug-eluting stent strut distribution: a comparison between Cypher and Taxus by optical coherence tomography. J Invasive Cardiol 2006;**18**(3):111-4.
30. Gomez-Lara J, Brugaletta S, Diletti R, Garg S, Onuma Y, Gogas BD, van Geuns RJ, Dorange C, Veldhof S, Rapoza R, Whitbourn R, Windecker S, Garcia-Garcia HM, Regar E, Serruys PW. A comparative assessment by optical coherence tomography of the performance of the first and second generation of the everolimus-eluting bioresorbable vascular scaffolds. Eur Heart J 2011;**32**(3):294-304.
31. Burzotta F, De Vita M, Sgueglia G, Todaro D, Trani C. How to solve difficult side branch access? EuroIntervention 2010;**6 Suppl J**:J72-80.
32. Okamura T, Onuma Y, Garcia-Garcia HM, Regar E, Wykrzykowska JJ, Koolen J, Thuesen L, Windecker S, Whitbourn R, McClean DR, Ormiston JA, Serruys PW, Investigators ACB. 3-Dimensional optical coherence tomography assessment of jailed side branches by bioresorbable vascular scaffolds: a proposal for classification. JACC Cardiovasc Interv 2010;**3**(8):836-44.

33. Okamura T, Garg S, Gutierrez-Chico JL, Shin ES, Onuma Y, Garcia-Garcia HM, Rapoza RJ, Sudhir K, Regar E, Serruys PW. In vivo evaluation of stent strut distribution patterns in the bioabsorbable everolimus-eluting device: an OCT ad hoc analysis of the revision 1.0 and revision 1.1 stent design in the ABSORB clinical trial. EuroIntervention 2010;**5**(8):932-8.
34. Cook S, Wenaweser P, Togni M, Billinger M, Morger C, Seiler C, Vogel R, Hess O, Meier B, Windecker S. Incomplete stent apposition and very late stent thrombosis after drug-eluting stent implantation. Circulation 2007;**115**(18):2426-34.
35. Park SJ, Kang SJ, Virmani R, Nakano M, Ueda Y. In-stent neoatherosclerosis: a final common pathway of late stent failure. J Am Coll Cardiol 2012;**59**(23):2051-7.
36. Gutierrez-Chico JL, Regar E, Nuesch E, Okamura T, Wykrzykowska J, di Mario C, Windecker S, van Es GA, Gobbens P, Juni P, Serruys PW. Delayed coverage in malapposed and side-branch struts with respect to well-apposed struts in drug-eluting stents: in vivo assessment with optical coherence tomography. Circulation 2011;**124**(5):612-23.
37. Tanimoto S, Rodriguez-Granillo G, Barlis P, de Winter S, Bruining N, Hamers R, Knappen M, Verheye S, Serruys PW, Regar E. A novel approach for quantitative analysis of intracoronary optical coherence tomography: high inter-observer agreement with computer-assisted contour detection. Catheter Cardiovasc Interv 2008;**72**(2):228-35.
38. Gonzalo N G-GH, Serruys PW, Commissaris K, Bezerra H, Gobbens P, Costa MA, Regar E. Reproducibility of quantitative optical coherence tomography for stent analysis. Eurointervention 2009;**In press**.
39. Brugaletta S, Radu MD, Garcia-Garcia HM, Heo JH, Farooq V, Girasis C, van Geuns RJ, Thuesen L, McClean D, Chevalier B, Windecker S, Koolen J, Rapoza R, Miquel-Hebert K, Ormiston J, Serruys PW. Circumferential evaluation of the neointima by optical coherence tomography after ABSORB bioresorbable vascular scaffold implantation: can the scaffold cap the plaque? Atherosclerosis 2012;**221**(1):106-12.
40. Gomez-Lara J, Brugaletta S, Farooq V, Onuma Y, Diletti R, Windecker S, Thuesen L, McClean D, Koolen J, Whitbourn R, Dudek D, Smits PC, Chevalier B, Regar E, Veldhof S, Rapoza R, Ormiston JA, Garcia-Garcia HM, Serruys PW. Head-to-head comparison of the neointimal response between metallic and bioresorbable everolimus-eluting scaffolds using optical coherence tomography. JACC Cardiovasc Interv 2011;**4**(12):1271-80.
41. Gonzalo N, Serruys PW, Okamura T, van Beusekom HM, Garcia-Garcia HM, van Soest G, van der Giessen W, Regar E. Optical coherence tomography patterns of stent restenosis. Am Heart J 2009;**158**(2):284-93.
42. Onuma Y, Serruys PW, Perkins LE, Okamura T, Gonzalo N, Garcia-Garcia HM, Regar E, Kamberi M, Powers JC, Rapoza R, van Beusekom H, van der Giessen W, Virmani R. Intracoronary optical coherence tomography and histology at 1 month and 2, 3, and 4 years after implantation of everolimus-eluting bioresorbable vascular scaffolds in a porcine coronary artery model: an attempt to decipher the human optical coherence tomography images in the ABSORB trial. Circulation 2010;**122**(22):2288-300.
43. Farooq V, Gogas BD, Okamura T, Heo JH, Magro M, Gomez-Lara J, Onuma Y, Radu MD, Brugaletta S, van Bochove G, van Geuns RJ, Garcia-Garcia HM, Serruys PW. Three-dimensional optical frequency domain imaging in conventional percutaneous coronary intervention: the potential for clinical application. Eur Heart J 2013;**34**(12):875-85.
44. van Geuns RJ, Gogas BD, Farooq V, Regar E, Serruys PW. 3-Dimensional reconstruction of a bifurcation lesion with double wire after implantation of a second generation everolimus-eluting bioresorbable vascular scaffold. Int J Cardiol 2011;**153**(2):e43-5.

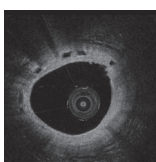

45. Okamura T, Serruys PW, Regar E. Cardiovascular flashlight. The fate of bioresorbable struts located at a side branch ostium: serial three-dimensional optical coherence tomography assessment. Eur Heart J 2010;**31**(17):2179.
46. Van Ditzhuijzen N, Ligthart J, Bruining N, E R, Van Beusekom HMM. Invasive Imaging of Bioresorbable Coronary Scaffolds - A Review. Interventional Cardiology Review 2013;**8**(1):23-35.
47. Erbel R, Di Mario C, Bartunek J, Bonnier J, de Bruyne B, Eberli FR, Erne P, Haude M, Heublein B, Horrigan M, Ilsley C, Bose D, Koolen J, Luscher TF, Weissman N, Waksman R. Temporary scaffolding of coronary arteries with bioabsorbable magnesium stents: a prospective, non-randomised multicentre trial. Lancet 2007;**369**(9576):1869-75.
48. Nishio S, Kosuga K, Igaki K, Okada M, Kyo E, Tsuji T, Takeuchi E, Inuzuka Y, Takeda S, Hata T, Takeuchi Y, Kawada Y, Harita T, Seki J, Akamatsu S, Hasegawa S, Bruining N, Brugaletta S, de Winter S, Muramatsu T, Onuma Y, Serruys PW, Ikeguchi S. Long-Term (>10 Years) clinical outcomes of first-in-human biodegradable poly-l-lactic acid coronary stents: Igaki-Tamai stents. Circulation 2012;**125**(19):2343-53.
49. Oberhauser J, Hossainy S, Rapoza R. Design principles and performance of bioresorbable polymeric coronary scaffolds. EuroIntervention 2009;**5**(Supplement F):F15-F23.
50. Serruys PW, Ormiston JA, Onuma Y, Regar E, Gonzalo N, Garcia-Garcia HM, Nieman K, Bruining N, Dorange C, Miquel-Hebert K, Veldhof S, Webster M, Thuesen L, Dudek D. A bioabsorbable everolimus-eluting coronary stent system (ABSORB): 2-year outcomes and results from multiple imaging methods. Lancet 2009;**373**(9667):897-910.
51. Onuma Y, Serruys PW, Ormiston JA, Regar E, Mark Webster, Thuesen L, Dudek D, Veldhof S, Rapoza R. Three-year results of clinical follow-up after a bioresorbable everolimus-eluting scaffold in patients with de novo coronary artery disease: the ABSORB trial. EuroInterv 2010;**In press**.
52. Onuma Y, Dudek D, Thuesen L, Webster M, Nieman K, Garcia-Garcia HM, Ormiston JA, Serruys PW. Five-year clinical and functional multislice computed tomography angiographic results after coronary implantation of the fully resorbable polymeric everolimus-eluting scaffold in patients with de novo coronary artery disease: the ABSORB cohort A trial. JACC Cardiovasc Interv 2013;**6**(10):999-1009.
53. Brugaletta S, Heo JH, Garcia-Garcia HM, Farooq V, van Geuns RJ, de Bruyne B, Dudek D, Smits PC, Koolen J, McClean D, Dorange C, Veldhof S, Rapoza R, Onuma Y, Bruining N, Ormiston JA, Serruys PW. Endothelial-dependent vasomotion in a coronary segment treated by ABSORB everolimus-eluting bioresorbable vascular scaffold system is related to plaque composition at the time of bioresorption of the polymer: indirect finding of vascular reparative therapy? Eur Heart J 2012;**33**(11):1325-33.
54. Karanasos A, Simsek C, Serruys P, Ligthart J, Witberg K, van Geuns RJ, Sianos G, Zijlstra F, Regar E. Five-year optical coherence tomography follow-up of an everolimus-eluting bioresorbable vascular scaffold: changing the paradigm of coronary stenting? Circulation 2012;**126**(7):e89-91.
55. Garcia-Garcia HM, Schultz C, Duckers E, Regar E, Ligthart J, Serruys PW, van Geuns RJ. Five-year follow-up of the ABSORB bioresorbable everolimus-eluting vascular scaffold system: multimodality imaging assessment. EuroIntervention 2013;**8**(10):1126-7.
56. Simsek C, Karanasos A, Magro M, Garcia-Garcia HM, Onuma Y, Regar E, Boersma E, Serruys PW, van Geuns RJ. Long-term invasive follow-up of the everolimus-eluting bioresorbable

vascular scaffold: five-year results of multiple invasive imaging modalities. EuroIntervention 2016;**11**(9):996-1003.

57. Serruys PW, Onuma Y, Ormiston JA, de Bruyne B, Regar E, Dudek D, Thuesen L, Smits PC, Chevalier B, McClean D, Koolen J, Windecker S, Whitbourn R, Meredith I, Dorange C, Veldhof S, Miquel-Hebert K, Rapoza R, Garcia-Garcia HM. Evaluation of the second generation of a bioresorbable everolimus drug-eluting vascular scaffold for treatment of de novo coronary artery stenosis: six-month clinical and imaging outcomes. Circulation 2010;**122**(22):2301-12.
58. Serruys PW, Onuma Y, Dudek D, Smits PC, Koolen J, Chevalier B, de Bruyne B, Thuesen L, McClean D, van Geuns RJ, Windecker S, Whitbourn R, Meredith I, Dorange C, Veldhof S, Hebert KM, Sudhir K, Garcia-Garcia HM, Ormiston JA. Evaluation of the second generation of a bioresorbable everolimus-eluting vascular scaffold for the treatment of de novo coronary artery stenosis: 12-month clinical and imaging outcomes. J Am Coll Cardiol 2011;**58**(15):1578-88.
59. van Ditzhuijzen NS, van den Heuvel M, Sorop O, van Duin RW, Krabbendam-Peters I, van Haeren R, Ligthart JM, Witberg KT, Duncker DJ, Regar E, van Beusekom HM, van der Giessen WJ. Invasive coronary imaging in animal models of atherosclerosis. Neth Heart J 2011;**19**(10):442-6.
60. Abizaid A, Costa JR, Jr., Bartorelli AL, Whitbourn R, van Geuns RJ, Chevalier B, Patel T, Seth A, Stuteville M, Dorange C, Cheong WF, Sudhir K, Serruys PW. The ABSORB EXTEND study: preliminary report of the twelve-month clinical outcomes in the first 512 patients enrolled. EuroIntervention 2014.
61. Diletti R, Serruys PW, Farooq V, Sudhir K, Dorange C, Miquel-Hebert K, Veldhof S, Rapoza R, Onuma Y, Garcia-Garcia HM, Chevalier B. ABSORB II randomized controlled trial: a clinical evaluation to compare the safety, efficacy, and performance of the Absorb everolimus-eluting bioresorbable vascular scaffold system against the XIENCE everolimus-eluting coronary stent system in the treatment of subjects with ischemic heart disease caused by de novo native coronary artery lesions: rationale and study design. Am Heart J 2012;**164**(5):654-63.
62. Stone GW. ABSORB III and IV: pivotal clinical trial program. In: *Transcatheter Cardiovascular Therapeutics*. *Miami*, *2012*.
63. Abizaid A, Schofer, J., Maeng, M., Witzenbichler, B., Botelho, R., Ormiston, J.A., Costa, R.A., Costa Jr, J.D., Chamie, D., Castro, J.P., Abizaid, A., John, Y., Bhat, V., Morrison, L., Toyloy, S., Verheye, S. Prospective, Multi-Center Evaluation of the DESolve Nx Novolimus-Eluting Bioresorbable Coronary Scaffold: First Report of One Year Clinical and Imaging Outcomes. In: *Transcatheter Cardiovascular Therapeutics (TCT)*. *San Francisco*, *2013*.
64. Grube E. Bioabsorbable stents: the Boston Scientific & REVA technology. In: *EuroPCR*. *Barcelona, Spain*, *2009*.
65. Costa RA. REVA ReZolve Clinical Program Update. In: *Transcatheter Cardiovascular Therapeutics*. *Miami*, *2012*.
66. Fajadet J. The ART BRS: Design and FIH Experiences: Can a polymer-only scaffold do it alone? In: *Transcatheter Cardiovascular Therapeutics*. *San Francisco*, *2013*.
67. Jabara R, Pendyala L, Geva S, Chen J, Chronos N, Robinson K. Novel fully bioabsorbable salicylate-based sirolimus-eluting stent. EuroIntervention 2009;**5 Suppl F**:F58-64.

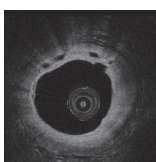

68. Wu Y, Shen L, Wang Q, Ge L, Xie J, Hu X, Sun A, Qian J, Ge J. Comparison of acute recoil between bioabsorbable poly-L-lactic acid XINSORB stent and metallic stent in porcine model. J Biomed Biotechnol 2012;**2012**:413956.
69. Ge J, Chen Y, Qian J, Ge L, Wang Q, Yao K, Zhang F, Huang D, Shen L, Wu Y, Liu H, Sun Z, Guo J, Liu C, Chen G, Xie J, Hu X. A first-in-man study of XINSORB scaffold for patients with single de-novo coronary lesions. In: *EuroPCR*. *Paris*, *2014*.
70. Cottone RJ. Pre-clinical Evaluations of Combination Drug Eluting and CD34 Antibody - Coated Bioabsorbable Scaffold - Program Update. In: *Transcatheter Cardiovascular Therapeutics*. *San Francisco*, *2013*.
71. Granada JF. The Amaranth PLLA Based Bioresorbable Scaffold (ABRS) - Experimental and Early Human Results. In: *Transcatheter Cardiovascular Therapeutics*. *San Fransisco*, *2013*.
72. Erbel R, Di Mario C, Bartunek J, Bonnier J, de Bruyne B, Eberli FR, Erne P, Haude M, Heublein B, Horrigan M, Ilsley C, Bose D, Koolen J, Luscher TF, Weissman N, Waksman R, Investigators P-A. Temporary scaffolding of coronary arteries with bioabsorbable magnesium stents: a prospective, non-randomised multicentre trial. Lancet 2007;**369**(9576):1869-75.
73. Haude M, Erbel R, Erne P, Verheye S, Degen H, Bose D, Vermeersch P, Wijnbergen I, Weissman N, Prati F, Waksman R, Koolen J. Safety and performance of the drug-eluting absorbable metal scaffold (DREAMS) in patients with de-novo coronary lesions: 12 month results of the prospective, multicentre, first-in-man BIOSOLVE-I trial. Lancet 2013.
74. Diletti R, Karanasos A, Muramatsu T, Nakatani S, Van Mieghem NM, Onuma Y, Nauta ST, Ishibashi Y, Lenzen MJ, Ligthart J, Schultz C, Regar E, de Jaegere PP, Serruys PW, Zijlstra F, van Geuns RJ. Everolimus-eluting bioresorbable vascular scaffolds for treatment of patients presenting with ST-segment elevation myocardial infarction: BVS STEMI first study. Eur Heart J 2014;**35**(12):777-86.
75. Van Mieghem N, Wilschut J, Ligthart J, Witberg K, Van Geuns RJ, E R. Modified T-Technique with Bioresorbable Scaffolds ensures Complete Carina Coverage – an Optical Coherence Tomography Study. JACC Cardiovasc Interv 2014.
76. Ruzsa Z, van der Linden M, Van Mieghem NM, Regar E, Ligthart JM, Serruys P, van Geuns RJ. Culotte stenting with bioabsorbable everolimus-eluting stents. Int J Cardiol 2013;**168**(2):e35-7.
77. Diletti R, Onuma Y, Farooq V, Gomez-Lara J, Brugaletta S, van Geuns RJ, Regar E, de Bruyne B, Dudek D, Thuesen L, Chevalier B, McClean D, Windecker S, Whitbourn R, Smits P, Koolen J, Meredith I, Li D, Veldhof S, Rapoza R, Garcia-Garcia HM, Ormiston JA, Serruys PW. 6-month clinical outcomes following implantation of the bioresorbable everolimus-eluting vascular scaffold in vessels smaller or larger than 2.5 mm. J Am Coll Cardiol 2011;**58**(3):258-64.
78. Diletti R, Farooq V, Girasis C, Bourantas C, Onuma Y, Heo JH, Gogas BD, van Geuns RJ, Regar E, de Bruyne B, Dudek D, Thuesen L, Chevalier B, McClean D, Windecker S, Whitbourn RJ, Smits P, Koolen J, Meredith I, Li X, Miquel-Hebert K, Veldhof S, Garcia-Garcia HM, Ormiston JA, Serruys PW. Clinical and intravascular imaging outcomes at 1 and 2 years after implantation of absorb everolimus eluting bioresorbable vascular scaffolds in small vessels. Late lumen enlargement: does bioresorption matter with small vessel size? Insight from the ABSORB cohort B trial. Heart 2013;**99**(2):98-105.
79. Reiber JH, Tu S, Tuinenburg JC, Koning G, Janssen JP, Dijkstra J. QCA, IVUS and OCT in interventional cardiology in 2011. Cardiovasc Diagn Ther 2011;**1**(1):57-70.

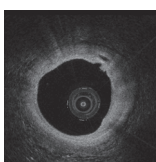

OCT assessment of the long-term vascular healing response 5 years after everolimus-eluting bioresorbable vascular scaffold

A Karanasos, C Simsek, M Gnanadesigan, NS van Ditzhuijzen, R Freire, J Dijkstra, S Tu, N Van Mieghem, G van Soest, P de Jaegere, PW Serruys, F Zijlstra, RJ van Geuns, E Regar

J Am Coll Cardiol. 2014 Dec 9;64(22):2343-56

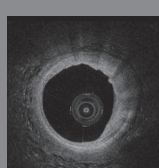

Abstract

Introduction Although recent observations suggest a favorable initial healing process of the everolimus-eluting bioresorbable vascular scaffold (BVS), little is known regarding the long-term healing response. This study assessed the in-vivo vascular healing response using optical coherence tomography (OCT) 5 years after elective first-in-man BVS implantation.

Methods Of the 14 living patients enrolled in the Thoraxcenter Rotterdam cohort of the ABSORB A study, 8 patients underwent invasive follow-up, including OCT, 5 years after implantation. Advanced OCT image analysis included luminal morphometry, assessment of the adluminal signal-rich layer separating the lumen from other plaque components, visual and quantitative tissue characterization, and assessment of side-branch ostia "jailed" at baseline.

Results In all patients, BVS struts were integrated in the vessel wall and were not discernible. Both minimum and mean luminal area increased from 2 years to 5 years, whereas lumen eccentricity decreased over time. In most patients, plaques were covered by a signal-rich, low-attenuating layer. Minimum cap thickness over necrotic core was 155±90μm. One patient showed plaque progression and discontinuity of this layer. Side-branch ostia were preserved with tissue bridge thinning that had developed in the place of side-branch struts, creating a neo-carina.

Conclusions At long-term BVS follow-up, we observed a favourable tissue response, with late luminal enlargement, side-branch patency and development of a signal-rich, low-attenuating layer that covered thrombogenic plaque components. The small size of the study and the observation of a different tissue response in 1 patient warrant judicious interpretation of our results and confirmation in larger studies.

Introduction

Metallic stents for percutaneous revascularization have been associated with late complications, such as neoatherosclerosis, late restenosis and thrombosis.[1] Bioresorbable vascular scaffolds (BVS) could help overcome such pitfalls. In the ABSORB A study (ABSORB [A bioabsorbable everolimus-eluting coronary stent system] Clinical Investigation, Cohort A), the first-generation everolimus-eluting BVS (Absorb BVS 1.0; Abbott Vascular, Santa Clara, California) was associated with a good long-term clinical outcome after 2 and 5 years.[2, 3] Plaque regression from 2 to 5 years and recovery of vasomotion in the scaffolded segment were documented in a patient subset.[4] Moreover, recent clinical observations of a signal-rich layer separating potentially thrombogenic plaque components from the lumen [5, 6] suggest a favourable long-term healing response with potential plaque sealing.

We aimed to provide a comprehensive optical coherence tomography (OCT) analysis of the vascular healing response in the longest follow-up available to date (5 years) in the first series of patients who received everolimus-eluting BVS

Methods

Patient population

The study population [4] and index procedure [2] have been described (**Supplementary Material; Appendix A**). Briefly, all 14 living patients from the Thoraxcenter Rotterdam cohort of ABSORB A were asked to participate. Eight consented and were included. The protocol was approved by the institutional ethics committee and conformed to the Declaration of Helsinki.

OCT image acquisition

All 8 subjects underwent frequency-domain OCT at the 5-year invasive follow-up.[7] Six patients at baseline, 7 patients at 6-month follow-up and 7 patients at 2-year follow-up had undergone occlusive time-domain OCT per the study protocol, with serial OCT imaging at all intervals available for 5 patients. For details see **Supplementary Material; Appendix A**.

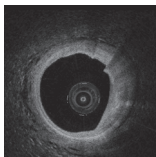

Definitions

OCT analysis of bioresorbable scaffolds reveals essential differences from metal stents (**Figure 1**). With metal stents, struts are preserved and neointimal area is clearly defined as the area between stent and lumen contour. In BVS, when scaffold struts are still discernible, the neointimal area can be assessed similarly to metal stents. However, at long-term follow-up, BVS scaffold struts are no longer visible and the area corresponding to struts and neointima has similar optical properties as the underlying fibrous layer.[5, 8] Consequently, it is impossible to distinguish between strut area, neointimal area and underlying plaque. Therefore, the vascular structure observed at the scaffolded segment, a product of the consolidation of underlying plaque, biodegraded struts, and neointima, resembled a native atherosclerotic plaque and was defined as neoplaque (**Figure 1**).

Because OCT cannot distinguish the scaffold area, and thus neointimal area, from the underlying plaque, neointimal thickness cannot be assessed directly. Hence, we aimed to provide an indirect assessment that focused on the signal-rich layer, which consisted of the neointimal layer, resorbed struts and pre-existing fibrous tissue. We analysed this signal-rich layer, between the lumen border and internal elastic lamina,

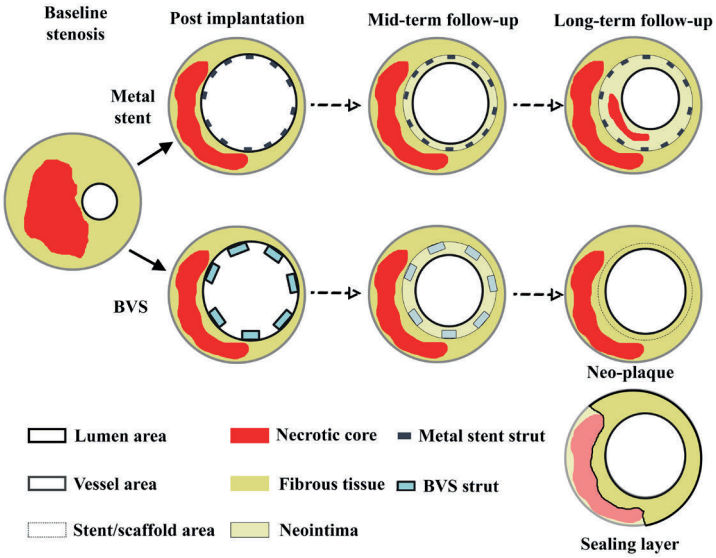

Figure 1 Long-term vascular healing response in metal stents and bioresorbable scaffolds
After metal stent implantation, struts are preserved and the neointimal area clearly delineated between stent and lumen contour even at long-term, with possible development of vneoatherosclerosis within the neointima. Conversely, in long-term follow-up of bioresorbable scaffolds, neointimal boundaries are unclear after bioresorption (dotted line), and the intima resembles a native plaque, defined as 'neo-plaque'. The signal-rich layer is the layer that separates the underlying plaque components from the lumen. BVS = Bioresorbable vascular scaffold

for providing a measure of separation of the lumen from the underlying plaque components.[5, 6] In situations in which signal-poor regions (e.g., calcifications, necrotic core, deeply located fibrous plaque) obscured delineation of the internal elastic lamina, the signal-rich layer was delineated between lumen border and the boundary of signal-rich and signal-poor regions (**Figures 1 and 2**).

OCT image analysis

The platinum scaffold markers defined the region of interest. Quantitative and qualitative 5-year OCT image analysis was per- formed per frame. Analysis included the assessment of discernible struts, lumen morphometry, signal-rich layer thickness measurement, neoplaque characterization, attenuation analysis, and ostial side-branch assessment. Metal stents implanted in the same vessels were also analyzed.[1]

Luminal measurements and variability analysis

For details, see **Supplementary Material (Appendix A)**. Measurements included mean and minimum lumen area and eccentricity, calculated as the ratio [(maximum lumen diameter – minimum lumen diameter)/maximum lumen diameter].[7] Lumen measurements were assessed for intra-observer, inter-observer and intra-study variability.

Quantification of signal-rich layer thickness

The signal-rich layer was quantified following segmentation of its luminal and abluminal contour by measuring minimum, mean and maximum thickness and symmetry (ratio of minimal-to-maximal thickness) (**Figure 2**).

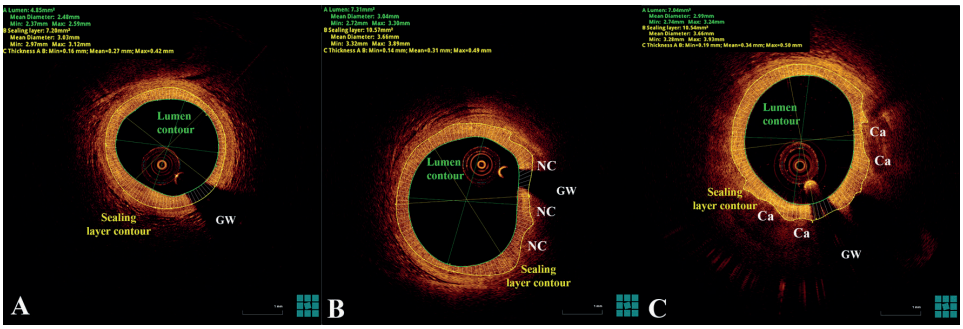

Figure 2 Quantifying signal-rich layer thickness in different plaque types
In the absence of attenuating intimal regions, the contour is traced at the internal elastic lamina (A). In plaques with necrotic core, the abluminal contour is traced at the attenuating region boundary (B). In plaques with calcifications, the signal-rich layer is segmented at the calcification edge (C). GW=guidewire; NC=necrotic core; Ca=calcium

'Neo-plaque' characterization

'Neo-plaque' morphology was assessed per frame at 5 years, according to native atherosclerosis definitions,[7] and the arc of calcifications, necrotic core and mixed plaque was measured with QCU-CMS (LKEB, Leiden University, The Netherlands; research version of QIvus, Medis medical imaging systems, Leiden, The Netherlands). Fibrous cap contours were traced over necrotic core with mean and minimum cap thickness calculated per patient. Spread-out maps representing 'neo-plaque' morphology and cap thickness throughout the scaffolded segment were generated (**Figure 3**), and colour-coded by plaque type. The presence of sharply delineated signal-poor voids, which corresponded to intimal microchannels,[7] was recorderd. In neoplaques with necrotic core, OCT images were compared with previous follow-ups to look for de novo accumulation of necrotic core of adluminal origin, possibly corresponding to neoatherosclerosis.

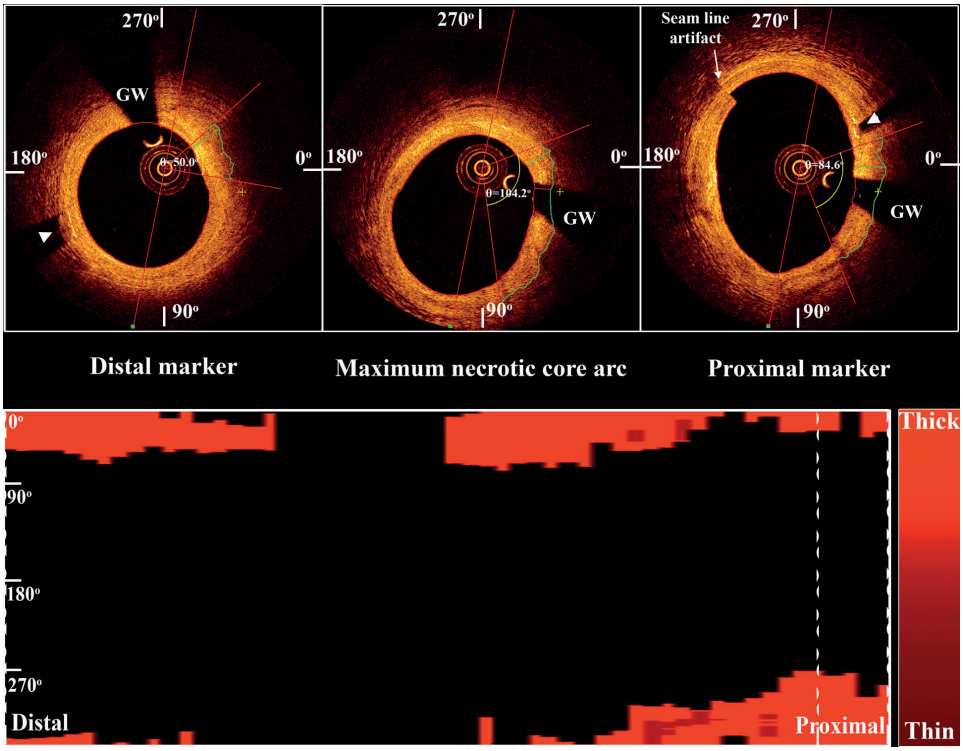

Figure 3 Plaque characterization and cap tracing

In frames with necrotic core, calcifications, or mixed plaque within the scaffolded segment, the overlying fibrous cap was segmented and minimum thicknesses are recorded. A spread-out map was generated that showed the component distribution within the 'neo-plaque', with lighter colours corresponding to thicker caps. Arrowhead indicates scaffold marker. GW=guidewire

Attenuation analysis

We used attenuation analysis for quantitative tissue characterization of the signal-rich layer and the 'neo-plaque' (**Figure 4**). In ex-vivo validation experiments, highly-attenuating regions (attenuation coefficient $\mu_t \geq 8mm^{-1}$) have been associated with necrotic core or macrophages. Conversely, $\mu_t < 6mm^{-1}$ were associated with healthy vessel, intimal thickening or calcified plaque.[9, 10] Attenuation was quantified circumferentially at different depths from the lumen surface by custom-made software.[11] Results were plotted in spread-out maps demonstrating 1) maximum attenuation coefficient per A-line throughout the pullback, and 2) attenuation coefficient values in different depths from the vessel surface.

Side-branch assessment

To assess anatomical side-branch jailing over time, three-dimensional images of side-branch ostia were obtained by volume-rendering software (INTAGE Realia, KGT, Tokyo, Japan).[12] No struts were identifiable by OCT, but neointimal bridges had developed in their place and were classified based on their relative location to the ostium as proximal, distal, proximal and distal, or crossing (**Figure 5**). Mean and minimal thickness

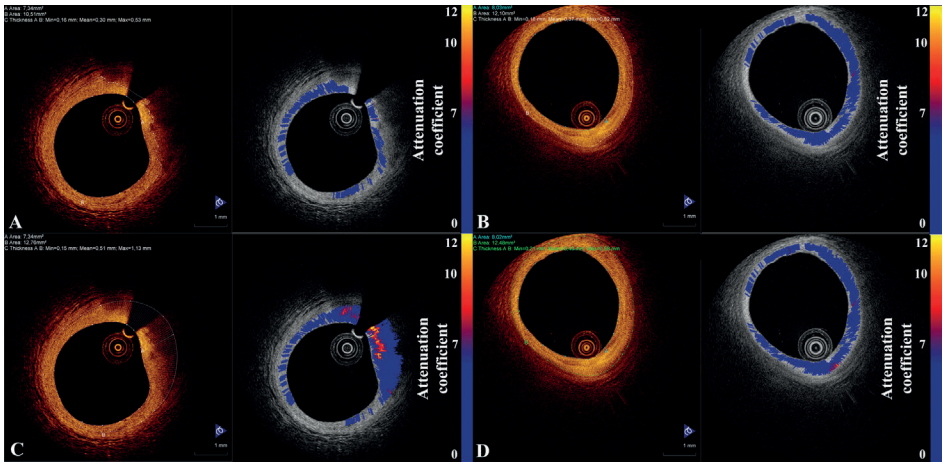

Figure 4 Example of attenuation analysis

In all frames, tissue attenuation properties within adluminal and abluminal contour were measured and displayed on a colour scale (blue represents low-attenuation regions, whereas red and yellow represent high-attenuation regions). Analysis was performed in the signal-rich layer (A and B), as defined in **Figure 2**, *and in the entire 'neo-plaque', up to the internal elastic lamina (C and D). Note the lack of highly attenuating regions within the signal-rich layer (A and B), whereas attenuation properties deeper in the 'neo-plaque' depended on tissue type (high attenuation in necrotic core; C). In intimal thickness <200µm, as in 6 to 7 o'clock in A and C and 8 to 9 o'clock in B and D, analysis was not performed because of lack of sufficient imaging window. Abbreviations as in* **Figure 2**

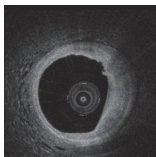

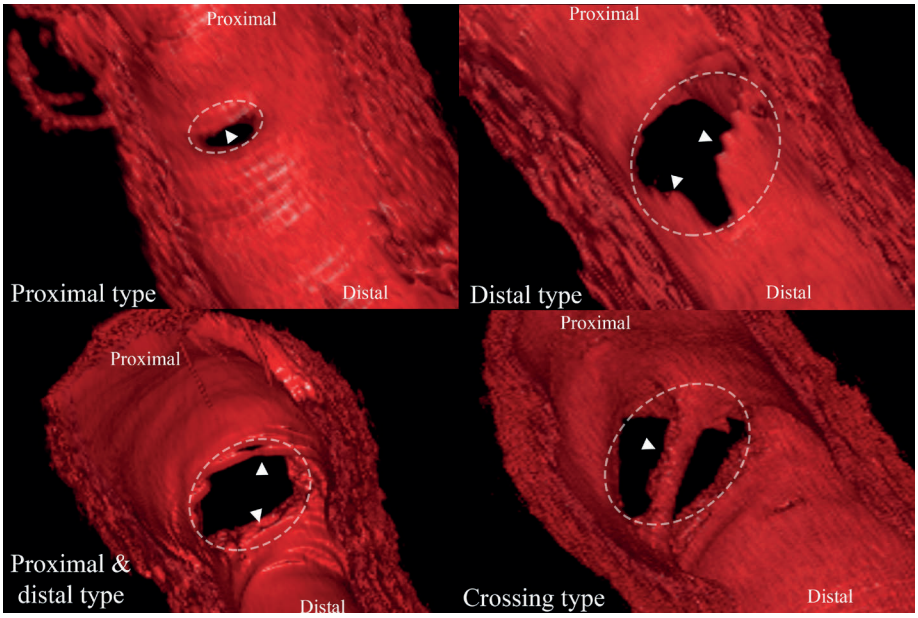

Figure 5 Different types of tissue bridges overlying side-branches
The classification is based on the relative location of the tissue bridge with the side-branch ostium. Four different types could be identified: proximal, distal, proximal and distal, or crossing. Dotted lines indicate side-branch ostia and arrowheads tissue bridges

was measured in matched frames at the 2- and the 5-year follow-up using QCU-CMS (**Supplementary Figure 1;Appendix C**).

Side-branch ostium area was assessed with dedicated software (QAngioOCT 1.0, Medis Specials, Leiden, The Netherlands). Following three-dimensional reconstruction, a cut-plane perpendicular to the side-branch centreline was selected and side-branch ostium planimetry was performed (**Figure 6**).[13]

Statistical analysis

Continuous variables are presented as mean ± SD or median (interquartile range; [IQR]) and nominal variables as n (%). Significance level was set at $p < 0.05$. Luminal measurements were compared by Wilcoxon signed rank test. All other paired comparisons were performed by paired Student *t*-test. No corrections were made for multiple comparisons. Variability was assessed with intraclass correlation coefficients (ICCs) for absolute agreement and Bland-Altman statistics. Statistical analysis was performed with SPSS version 20.0 (IBM, Armonk, New York).

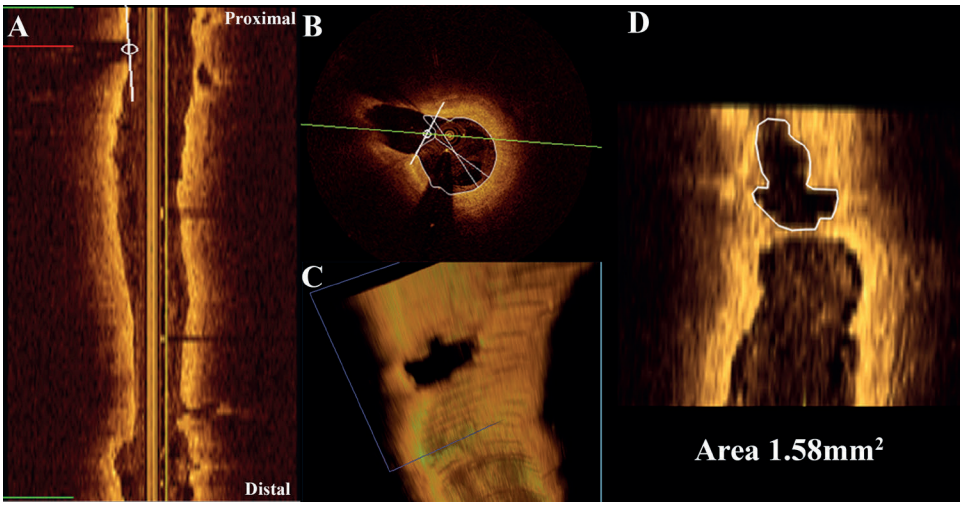

Figure 6 Side-branch ostium area measurement by cut-plane analysis
After three-dimensional rendering, side-branch ostium area can be measured in a cut-plane perpendicular to the side-branch ostium: L-mode display (A); Cross-sectional image (B); Three-dimensional rendering (C) Derived perpendicular cut-plane (D)

Results

Lumen and strut measurements

No binary restenosis was witnessed in the 5-year angiograms. In all patients, scaffold struts were no longer discernible as a result of complete bioresorption, and lumen area increased significantly from 2 to 5 years (**Figure 7**). Lumen eccentricity declined over time (baseline: 0.24±0.13; 6-month: 0.29±0.12; 2-year: 0.21±0.08; 5-year: 0.15±0.02; p<0.05 for all comparisons versus previous studies). The total strut count was reduced in 5 patients with serial observations: 278 struts at baseline, 248 at 6 months, 174 at 2 years, and no visible struts at 5 years. Two cases with incomplete scaffold apposition at baseline or 6 months demonstrated complete resolution of incomplete scaffold apposition at 2 years and complete strut bioresorption at 5 years.

Quantification of signal-rich layer

Median values (IQR) for the mean, minimum, and maximum signal-rich layer thickness and symmetry were 330μm (290μm-378μm), 150μm (120μm–190μm), 570μm (500μm–640μm), and 0.26 (0.20–0.33), respectively. **Supplementary Figure 2 (Appendix C)** demonstrates frequency distributions of these thickness measurements.

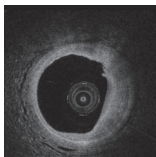

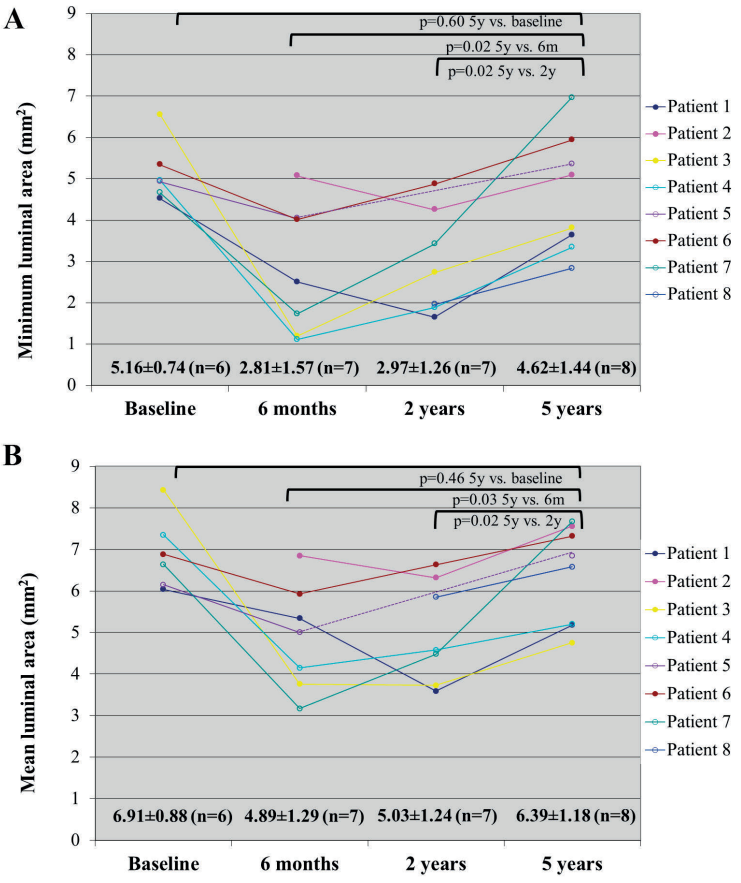

Figure 7 Serial luminal measurements

Despite an initial decrease in lumen dimensions from baseline to 6 months, minimal (A) and mean (B) lumen areas were increased at 5 years compared to previous follow-ups and were not significantly different from baseline

'Neo-plaque' characterization

Figure 8 presents spread-out 'neo-plaque' maps. The mean value of minimum cap thickness was 310±113μm, whereas the minimum value was 155±90μm. Mean and maximum values were 92˚±49˚ and 156˚±72˚ for necrotic core arc, 80˚ and 104˚ for calcification arc, 104˚±145˚ and 146˚±80˚ for mixed plaque arc.

Microchannels were identified in 7 of 8 patients and in 66 of 468 frames (14.1%). Per the 'neo-plaque' maps, necrotic core or mixed plaque >1 quadrant was observed in 7 patients. Comparison with previous follow-ups did not reveal evidence of de novo necrotic core accumulation of adluminal origin.

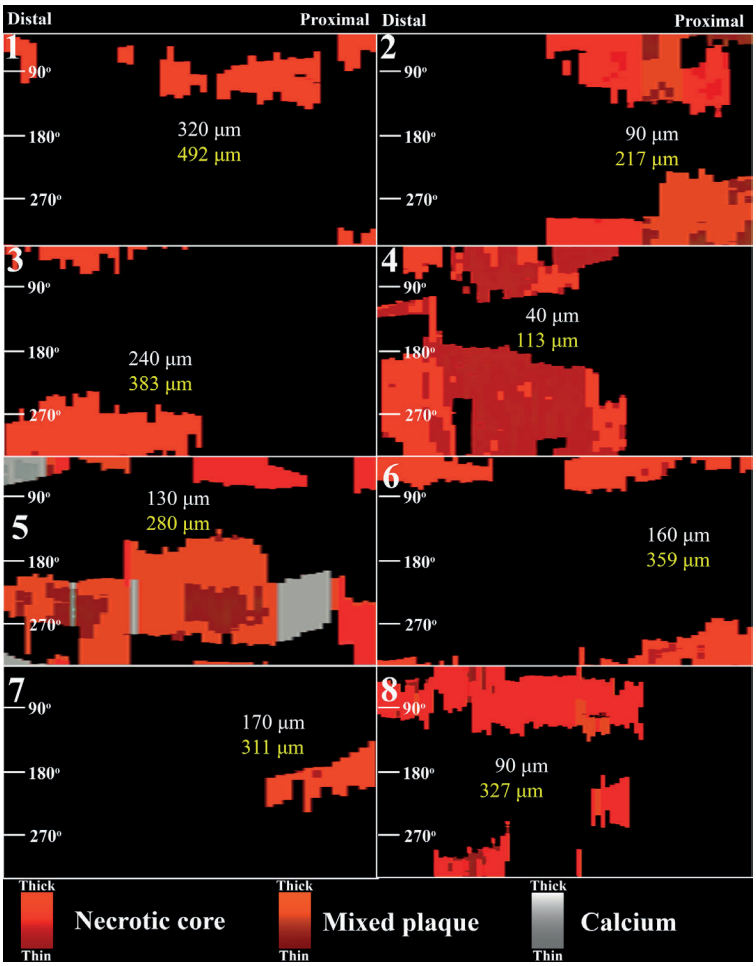

Figure 8 Neo-plaque morphology

Spread-out maps from all patients demonstrating 'neo-plaque' composition. Red represents necrotic core, orange mixed plaque, and white calcification. Lighter colours indicate a thicker fibrous cap (>250µm). The minimum and mean values of minimum cap thickness per patient are presented in white and yellow, respectively

Two patients had a focally irregular lumen contour: Patient #8 had a short intimal dissection, not present at earlier investigations, at the overlap between BVS and a metallic stent implanted at baseline. This minor, angiographically not visible dissection was most likely iatrogenic, induced by the guidewire. In Patient #4, a thin cap fibroatheroma was observed at the distal scaffold segment with cap disruption and small thrombus (**Figure 9**). Post-hoc revision of previous OCT examinations revealed possible scaffold discontinuity near the distal edge at 4 months, with the scaffold being dislocated opposite to the rupture site.

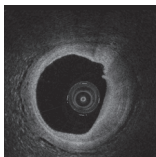

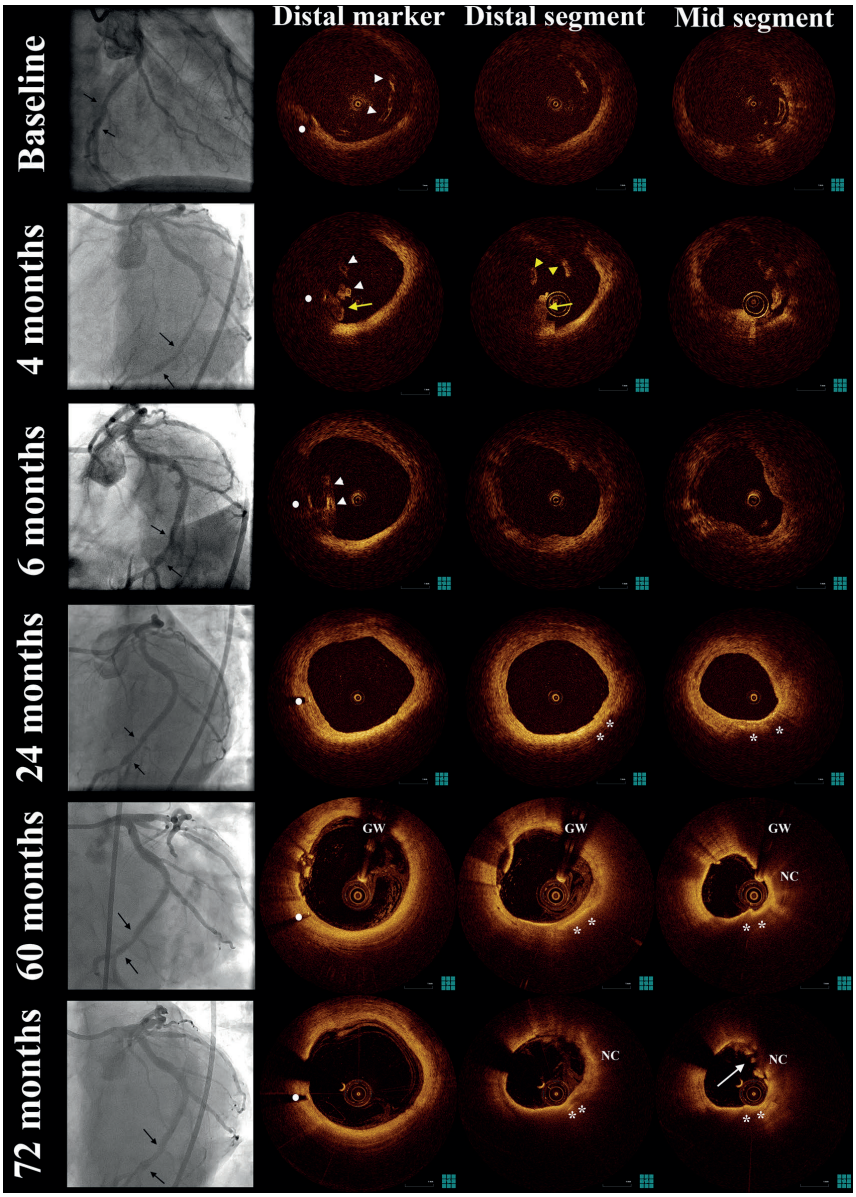

Figure 9 Vascular response in Patient #4

At baseline, there is malapposition (white arrowheads) at the distal segment. At 106-day follow-up, scaffold collapse (white arrowheads) at the site of the distal marker (white bullet), overhanging struts (yellow arrowheads), and thrombus (yellow arrow) were observed that suggested late scaffold discontinuity. At 6 months, a tissue bridge was formed (white arrowheads) at the site of the collapsed scaffold, and integrated into the vascular wall by 24 months. Note the macrophage accumulation (white asterisks) at the opposite side at 24 months. At 60-month follow-up, lesion progression with macrophages and necrotic core was evident, as well as intimal disruption. At 72-months follow-up, there was further luminal narrowing and plaque rupture with thrombus (white arrow). Black arrows indicate scaffold markers. Abbreviations as in **Figure 2**

Attenuation analysis

Mean per-patient attenuation within the signal-rich layer was 1.77 ± 0.32 mm^{-1} and the median was 1.28±0.25 mm^{-1} (**Supplementary Figure 3; Appendix C**). This value was higher within the entire 'neo-plaque' (mean per patient: 2.87±0.54 mm^{-1}, median per patient: 2.33±0.49 mm^{-1}, p<0.001) (**Supplementary Figure 4; Appendix C**). Spread-out attenuation maps at different depths from the luminal surface (100μm, 200 μm, and 400μm) are displayed in **Figure 10**. The surface layers (first 200μm) had low attenuation, overlying high-attenuation areas located deeper in the plaque.

Side-branch assessment

All side branches were patent with TIMI (Thrombolysis In Myocardial Infarction) flow grade 3. Overall, 14 side-branches were associated with incompletely apposed struts at previous examinations. Neointimal bridges at 5 years were identified in 13 side-branches, whereas in one no bridge was visible (**Table 1**).

Minimal and mean thickness of neointimal bridges overlying side-branches were respectively reduced from 241 ± 92μm and 341 ± 106μm at 2 years to 161 ± 107μm and 227 ± 119μm at 5 years (p<0.001) (**Supplementary Figure 5; Appendix C**).

Metal drug-eluting stent analysis

Metal drug-eluting stent (DES) analysis is presented in **Supplementary Table 1 (Appendix B)** and **Figure 11**. In all metal stents, coverage was >95%, without malapposed struts, whereas neoatherosclerosis was identified in all.

Variability analysis

Inter-observer and intra-observer variability for both frame- and patient-level analysis was low (inter-observer: difference 0.23±0.29mm, ICC 0.98; inter-observer [core laboratory]: difference 0.13±0.32mm, ICC 0.98; intra-observer: difference 0.17±0.19mm, ICC 0.99) (**Supplementary Table 2; Appendix B** and **Supplementary Figure 6; Appendix C**). As seen in the Bland-Altman plots, there were few measurements with significant differences, all of which in the polygon of confluence of larger side-branches with complex geometry lacking a priori definitions for contour tracing. ICCs for mean and minimal signal-rich layer thickness were respectively 0.95 and 0.86 for intra-observer variability and 0.80 and 0.80 for inter-observer variability.

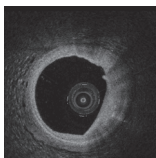

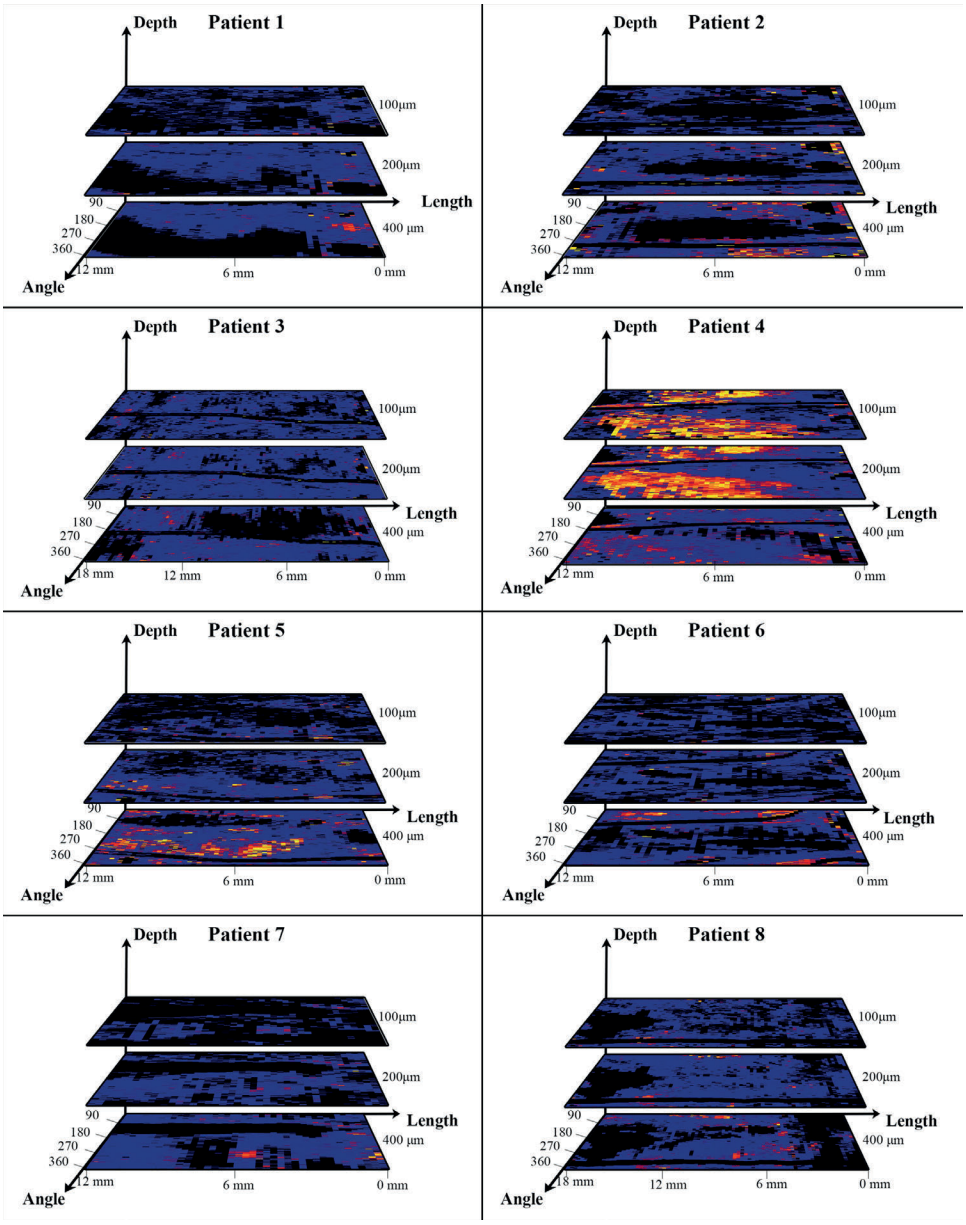

Figure 10 Attenuation spread-out

Spread-out maps demonstrating attenuation coefficient in pre-defined depths from the vessel surface (100µm, 200µm, and 400µm) per patient. In most patients, there was a low-attenuating layer of 200µm separating the underlying plaque (starting at ~400µm) from the lumen. In Patient #4, this layer was absent and attenuating areas were close to the lumen

Table 1 Side-branch analysis

	Bifurcation type	SB ostium area(mm²)	Jailing pattern
Patient #1-SB 1	OM-LCx	4.81	Proximal and distal
Patient #2-SB 1	LAD-septal	6.22	Crossing
Patient #2-SB 2	LAD-diagonal	1.14	Distal
Patient #2-SB 3	LAD-septal	1.89	Proximal
Patient #3-SB 1	LAD-diagonal	1.58	Distal
Patient #3-SB 2	LAD-septal	1.42	N/A*
Patient #4-SB 1	LCx-OM	1.11	Proximal and distal
Patient #5-SB 1	LAD-septal	1.93	Crossing
Patient #5-SB 2	LAD-diagonal	0.46	Distal
Patient #6-SB 1	LCx-OM	1.37	Crossing
Patient #6-SB 2	OM-LCx	2.23	Distal
Patient #8-SB 1	LCx-OM	N/A‡	Proximal
Patient #8-SB 2	LCx–posterolateral	0.3	Proximal
Patient #8-SB 3	LCx-OM	0.78	Proximal

**The bridge was not present at 5 years; distal location at previous studies. ‡Exact area not measurable. N/A = not available, SB=side-branch, OM=obtuse marginal branch, LCx=left circumflex artery LAD=left anterior descending artery*

Discussion

We present the first in-vivo long-term OCT data after BVS implantation. Despite the small sample size, these first patients treated with BVS offer a unique opportunity to study the long-term vascular response after BVS implantation (**Figure 12**). Our main findings are that 5 years after BVS 1.0 implantation: 1) there is late lumen enlargement with simultaneous increase in luminal symmetry; 2) all struts have disappeared and have been integrated within the neointima and the underlying plaque, forming a homogeneous, signal-rich, low-attenuating layer; 3) this signal-rich layer separates the lumen from the underlying plaque with a minimum thickness of 150µm (IQR: 120 to190µm); 4) this effect is not universal, with 1 case showing thinning and disruption of the signal-rich layer; 5) jailed side-branch ostia are preserved, whereas side-branch related struts have been replaced by thin tissue bridges; and 6) metal DES in the same vessels are lacking a distinct signal-rich layer and show neoatherosclerosis despite good coverage and apposition.

In our series, we observed a consistent luminal enlargement from 2 to 5 years in all patients. Late luminal enlargement in bioresorbable scaffolds has been attributed

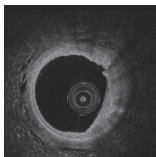

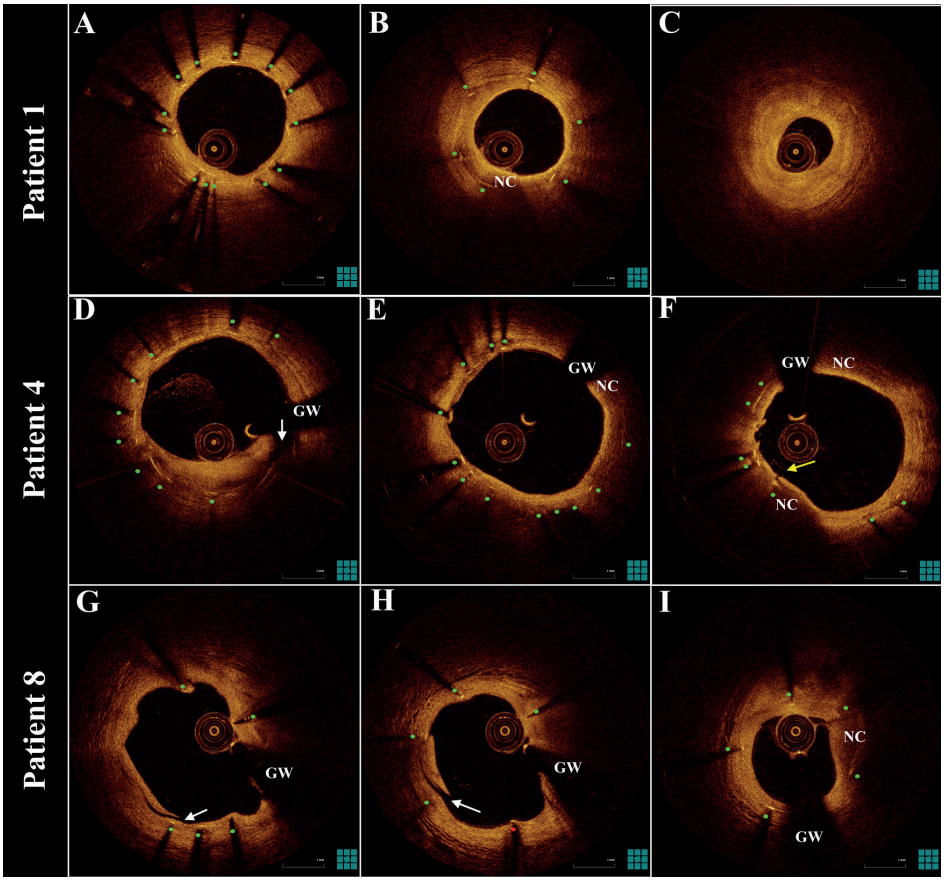

Figure 11 Representative optical coherence tomography images of metal drug-eluting stents
Covered struts (A, green bullet), Neoatherosclerosis (B), Distal edge stenosis (C) (area=1.74mm^2;), Heterogeneous neointima with discontinuity (D, white arrow), Neoatherosclerosis (E), Neointimal disruption (yellow arrow) over necrotic core with mural micro-thrombi (F), Evaginations - neointimal discontinuity (white arrow) possibly iatrogenic (G), Uncovered strut (H, red bullet), Neoatherosclerosis (I). Abbreviations as in **Figure 2**

to outward remodelling in animal studies,[14] and plaque burden reduction in clinical trials.[4, 15] Our findings echo larger-scale intravascular ultrasound (IVUS) observations of lumen area increases from 6 months to 2 years after BVS implantation.[2, 15] IVUS observations in our study population were consistent with our findings, dis- playing a trend for further lumen enlargement from 2 to 5 years, driven by a persistent decrease in plaque size from 6 months to 2 years caused by either true plaque regression or pseudoregression from strut resorption.[2, 4] A similar trend was observed in the 5-year multi-slice computed tomography follow-up of ABSORB A.[3] We observed recovery of the luminal symmetry, a finding of unclear significance. Simultaneous observations of

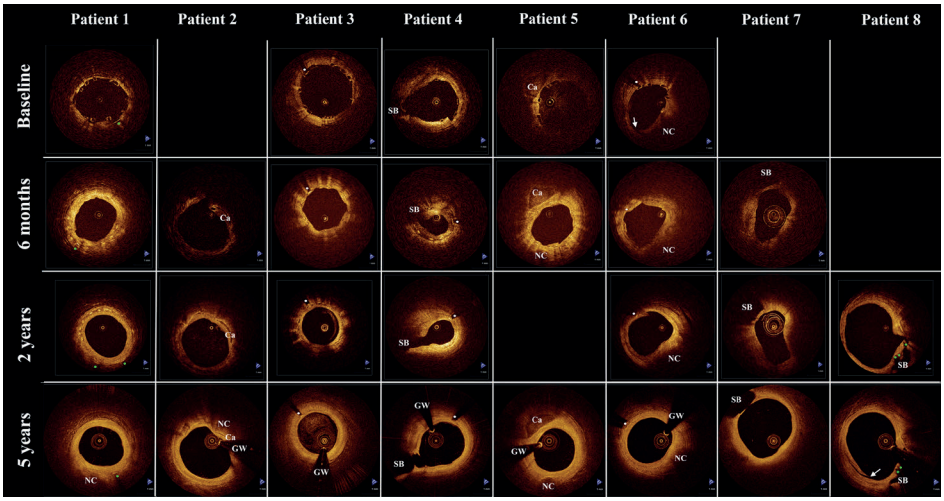

Figure 12 Serial assessment of vascular response

Matched representative images from serial examinations of all patients. Note the complete strut integration at 5 years, together with lumen enlargement compared with 6-month and 2-year follow-ups. In Patient #8, intimal discontinuity (arrow), presumably iatrogenic, was observed. White bullets indicate scaffold markers, green bullets indicate metal struts. SB = side branche; other abbreviations as in **Figure 2**

strut bioresorption and signal-rich layer development suggest a potentially favourable biological effect, which parallels IVUS studies showing increased plaque rupture in eccentric vessels.[16] The observed complete strut bio- resorption tracks with vasomotion findings demonstrating a lack of mechanical vessel constraint, with positive acetylcholine response in 4 patients, negative response in 2 patients, and absence of significant change in 2 patients.[4]

It has been suggested that neointimal growth after BVS resorption could serve as a mechanical barrier that prevents potentially thrombogenic plaque components from reaching the bloodstream, a concept dubbed "plaque sealing" or "recapping the plaque".[5, 6] With this hypothesis in mind, we scrutinized BVS morphology in our cohort, using sophisticated algorithms for in-depth analysis. We focused on the developed adluminal signal-rich layer, which corresponds to neointima, bioresorbed struts and fibrous components of the underlying plaque. The minimum signal-rich layer thickness was 150µm, and the minimum cap thickness over necrotic core was 155 ± 90µm, both well beyond the 65-µm threshold generally accepted as high-risk for plaque rupture[17], which suggests that this layer could reliably separate the lumen from potentially thrombogenic plaque components. Importantly, this layer showed remarkable homogeneity in the attenuation analysis, with low attenuation values hinting at the

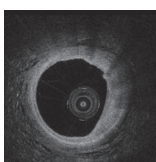

absence of high-risk wall components such as necrotic core and macrophages.[9, 10] This signal-rich layer could be protective against very late scaffold thrombosis or de novo thrombosis by plaque progression and rupture.[1, 17]

The complete scaffold integration into the vascular wall has shaped a 'neo-plaque' phenotype that resulted from the complex interaction of pre-existing plaque, morphological changes of the pre-existing plaque subject to dynamic local rheologic factors[18, 19], strut resorption, and neointima formation.[8] We visually characterized 'neo-plaque' using standardized OCT criteria.[7] Quantitative attenuation analysis corroborated these qualitative findings, revealing co-localization of necrotic core regions with high attenuation regions (**Supplementary Figure 7; Appendix C**), generally located deeper in the vessel wall and rarely observed within the first 200 μm from luminal surface. Of note, most patients were receiving intensive medical therapy (statins, 75%; beta-blockers, 75%; angiotensin receptor blocker, 62.5%), which possibly contributed to this favourable phenotype.

Metal stents covered with well-organized and functional neointima can likewise present a mechanical barrier between underlying plaque and lumen. However, neointimal proliferation and neo- atherosclerosis development over time have been reported for bare-metal stents and are even more accelerated for DES. The permanent nature of the metallic structure further limits the vessel's capacity for remodeling, plaque regression, and lumen enlargement over time. Consequently, lumen narrowing develops inevitably over time, and indeed, 3 metal DES in our cohort showed adluminal neoatherosclerosis, with minimum cap thickness ranging from 70 to 110mm. This is notable because thin fibrous cap emerges as a risk factor for neointimal rupture and acute coronary syndrome not only in native atherosclerosis but also in neoatherosclerosis.[1]

We analyzed the fate of side-branches "jailed" by BVS, because high strut thickness and tissue bridge formation have raised questions regarding long-term patency.[12] Three-dimensional rendering demonstrated side-branch patency, allowed reliable ostial measurements, and identified different intimal bridge patterns. Strut integration into these tissue bridges was completed, accompanied by bridge thinning from 341 ± 106 mm at 2 years to 227 ± 119 mm at 5 years. Together with the angiographically confirmed absence of flow impairment, we consider these findings a favorable long-term outcome. However, the implications of BVS over large SBs or in true bifurcation lesions remain unknown,[20, 21] because these were excluded per protocol.

Overall, our long-term OCT observations suggest a favourable vascular healing response with late lumen enlargement, increased luminal symmetry, side-branch pa-

tency, complete strut resorption and formation of a potentially protective tissue layer, giving an appearance consistent with the hypothetical concept of plaque sealing. Patient #4 did show a different response, which captured our attention. We observed target-lesion progression, with OCT findings consistent with macrophage infiltration, abluminal necrotic core accumulation, fibrous cap thinning and plaque rupture at follow-up, while the patient was treated only with aspirin and clopidogrel. This patient had diffuse disease that necessitated non–target-lesion revascularization with a metal paclitaxel-eluting stent in the same artery 106 days after BVS implantation. This stent developed subsequent neoatherosclerosis with neointimal disruption and micro-thrombus formation (**Figure 11**). This evidence of accelerated atherosclerosis, combined with mechanical factors (baseline incomplete scaffold apposition followed by late structural discontinuity) might have contributed to the adverse 'neo-plaque' phenotype. Notably, the patient did not have a clinically apparent acute coronary syndrome regardless of these impressive findings.

Despite the limited scale of our study, it provides crucial information on the long-term vascular response 5 years after BVS implantation. Although we consider the overall vascular response favourable and in line with larger-scale clinical reports, there might be lessons to learn from observations in the single patient who showed a different biological reaction, with recurring plaque rupture after BVS implantation. This finding might underscore the need for an optimal acute mechanical result with optimal lesion coverage, while simultaneously raising questions regarding a possible responder/non-responder reaction to BVS and the need for intensified secondary prevention in selected patients.[22] As such, our findings might guide further research for optimizing the clinical efficacy of BVS in the light of the 1.1 version modifications and herald observations in more complex populations.[23]

Study limitations

This is a small first-in-man study, so selection bias cannot be excluded, although the baseline clinical and angiographic characteristics were not different from the entire ABSORB A Cohort. The BVS 1.0 assessed in our study differs in geometry and resorption rate from the currently used BVS 1.1, which might affect the temporal course and pattern of the healing response.

Attenuation analysis has only been validated in ex vivo specimens of native atherosclerosis and not in device-induced tissue responses. However, because attenuation is an optical property of tissue components, we expect the absence of high- attenuating regions to correspond to absence of necrotic core or macrophages in this setting.

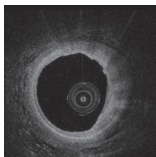

Five-year OCT follow-up was performed with a non-occlusive frequency-domain system; previous OCT examinations were performed with an occlusive time-domain system. Frequency-domain OCT offers better image quality and higher dynamic range, which allows superior visualization of deeply located plaques.[24] Because of these limitations of time-domain sys- tems, serial assessment of plaque morphology was not performed systematically and was only examined with reference to possible neoatherosclerosis, although changes over time would be expected.[19] Occlusive time-domain OCT slightly underestimates lumen area.[25] Nevertheless, 4 patients in our study underwent additional non-occlusive OCT imaging at 2-year follow-up. When we compared non-occlusive data at 2 and 5 years, findings of late lumen enlargement were consistent, albeit not reaching significance because of the smaller sample size (minimum lumen area: 3.54±1.43mm^2; at 2 years versus 4.06±1.33mm^2; at 5 years, p=0.14; mean lumen area: 5.12±1.62mm^2; at 2 years versus 5.95±1.20mm^2; at 5 years, p=0.07).

Conclusions

At long-term follow-up 5 years after BVS implantation, we observed a favourable tissue response with late luminal enlargement, complete strut bioresorption, and development of a low-attenuating signal-rich layer that covered the underlying thrombogenic plaque components. The small scale of our study and the observation of a different tissue response in 1 patient warrant judicious interpretation of our results and further confirmation in larger studies.

References

1. Karanasos A, Ligthart J, Witberg K, Toutouzas K, Daemen J, van Soest G, Gnanadesigan M, van Geuns R-J, de Jaegere P, Regar E. Association of neointimal morphology by optical coherence tomography with rupture of neoatherosclerotic plaque very late after coronary stent implantation. In: *SPIE conference proceedings. 2013*: Abstract 8565, p. 856542-856542-13.
2. Serruys PW, Ormiston JA, Onuma Y, Regar E, Gonzalo N, Garcia-Garcia HM, Nieman K, Bruining N, Dorange C, Miquel-Hébert K, Veldhof S, Webster M, Thuesen L, Dudek D. A bioabsorbable everolimus-eluting coronary stent system (ABSORB): 2-year outcomes and results from multiple imaging methods. The Lancet 2009;373(9667):897-910.
3. Onuma Y, Dudek D, Thuesen L, Webster M, Nieman K, Garcia-Garcia HM, Ormiston JA, Serruys PW. Five-Year Clinical and Functional Multislice Computed Tomography Angiographic Results After Coronary Implantation of the Fully Resorbable Polymeric Everolimus-Eluting Scaffold in Patients With De Novo Coronary Artery Disease: The ABSORB Cohort A Trial. JACC Cardiovasc Interv 2013;6(10):999-1009.
4. Simsek C, Karanasos A, Magro M, Garcia-Garcia HM, Onuma Y, Regar E, Boersma E, Serruys P, van Geuns R-J. Long-term Invasive Follow-Up of the Everolimus-Eluting Bioresorbable Vascular Scaffold: Five-year Results of Multiple Invasive Imaging Modalities. EuroIntervention 2014;under revision.
5. Karanasos A, Simsek C, Serruys P, Ligthart J, Witberg K, Geuns R-Jv, Sianos G, Zijlstra F, Regar E. Five-Year Optical Coherence Tomography Follow-Up of an Everolimus-Eluting Bioresorbable Vascular Scaffold Changing the Paradigm of Coronary Stenting? Circulation 2012;126(7):e89-e91.
6. Brugaletta S, Radu MD, Garcia-Garcia HM, Heo JH, Farooq V, Girasis C, van Geuns RJ, Thuesen L, McClean D, Chevalier B, Windecker S, Koolen J, Rapoza R, Miquel-Hebert K, Ormiston J, Serruys PW. Circumferential evaluation of the neointima by optical coherence tomography after ABSORB bioresorbable vascular scaffold implantation: can the scaffold cap the plaque? Atherosclerosis 2012;221(1):106-12.
7. Tearney GJ, Regar E, Akasaka T, Adriaenssens T, Barlis P, Bezerra HG, Bouma B, Bruining N, Cho J-m, Chowdhary S, Costa MA, de Silva R, Dijkstra J, Di Mario C, Dudeck D, Falk E, Feldman MD, Fitzgerald P, Garcia H, Gonzalo N, Granada JF, Guagliumi G, Holm NR, Honda Y, Ikeno F, Kawasaki M, Kochman J, Koltowski L, Kubo T, Kume T, Kyono H, Lam CCS, Lamouche G, Lee DP, Leon MB, Maehara A, Manfrini O, Mintz GS, Mizuno K, Morel M-a, Nadkarni S, Okura H, Otake H, Pietrasik A, Prati F, Räber L, Radu MD, Rieber J, Riga M, Rollins A, Rosenberg M, Sirbu V, Serruys PWJC, Shimada K, Shinke T, Shite J, Siegel E, Sonada S, Suter M, Takarada S, Tanaka A, Terashima M, Troels T, Uemura S, Ughi GJ, van Beusekom HMM, van der Steen AFW, van Es G-A, van Soest G, Virmani R, Waxman S, Weissman NJ, Weisz G. Consensus Standards for Acquisition, Measurement, and Reporting of Intravascular Optical Coherence Tomography Studies: A Report From the International Working Group for Intravascular Optical Coherence Tomography Standardization and Validation. J Am Coll Cardiol 2012;59(12):1058-1072.
8. Onuma Y, Serruys PW, Perkins LEL, Okamura T, Gonzalo N, García-García HM, Regar E, Kamberi M, Powers JC, Rapoza R, Beusekom Hv, Giessen Wvd, Virmani R. Intracoronary Optical Coherence Tomography and Histology at 1 Month and 2, 3, and 4 Years After Implantation of Everolimus-Eluting Bioresorbable Vascular Scaffolds in a Porcine Coronary

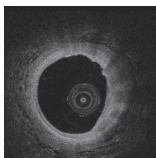

Artery Model An Attempt to Decipher the Human Optical Coherence Tomography Images in the ABSORB Trial. Circulation 2010;122(22):2288-2300.
9. van Soest G, Goderie T, Regar E, Koljenović S, van Leenders GLJH, Gonzalo N, van Noorden S, Okamura T, Bouma BE, Tearney GJ, Oosterhuis JW, Serruys PW, van der Steen AFW. Atherosclerotic tissue characterization in vivo by optical coherence tomography attenuation imaging. J Biomed Opt 2010;15(1):011105.
10. Ughi GJ, Adriaenssens T, Sinnaeve P, Desmet W, D'Hooge J. Automated tissue characterization of in vivo atherosclerotic plaques by intravascular optical coherence tomography images. Biomed Opt Express 2013;4(7):1014-30.
11. Gnanadesigan M, van Soest G, White S, Scoltock S, Ughi GJ, Baumbach A, van der Steen AFW, Regar E, Johnson TW. Effect of temperature and fixation on the optical properties of atherosclerotic tissue: a validation study of an ex-vivo whole heart cadaveric model. Biomed Opt Express 2014;5(4):1038-1049.
12. Okamura T, Onuma Y, García-García HM, Regar E, Wykrzykowska JJ, Koolen J, Thuesen L, Windecker S, Whitbourn R, McClean DR, Ormiston JA, Serruys PW. 3-Dimensional Optical Coherence Tomography Assessment of Jailed Side Branches by Bioresorbable Vascular Scaffolds: A Proposal for Classification. JACC Cardiovasc Interv 2010;3(8):836-844.
13. Karanasos A, Tu S, van Ditzhuijzen NS, Ligthart J, Witberg K, van Mieghem NM, van Geuns RJ, de Jaegere P, Zijlstra F, Reiber JHC, Regar E. A novel method to assess coronary artery bifurcations by OCT: Cut-plane analysis for side-branch ostial assessment from a main vessel pullback. under review.
14. Strandberg E, Zeltinger J, Schulz DG, Kaluza GL. Late Positive Remodeling and Late Lumen Gain Contribute to Vascular Restoration by a Non-Drug Eluting Bioresorbable Scaffold A Four-Year Intravascular Ultrasound Study in Normal Porcine Coronary Arteries. Circulation Cardiovasc Interv 2012;5(1):39-46.
15. Serruys PW, Onuma Y, Garcia-Garcia HM, Muramatsu T, van Geuns R-J, de Bruyne B, Dudek D, Thuesen L, Smits PC, Chevalier B, McClean D, Koolen J, Windecker S, Whitbourn R, Meredith I, Dorange C, Veldhof S, Hebert KM, Rapoza R, Ormiston JA. Dynamics of vessel wall changes following the implantation of the Absorb everolimus-eluting bioresorbable vascular scaffold: a multi-imaging modality study at 6, 12, 24 and 36 months. EuroIntervention 2013.
16. von Birgelen C, Klinkhart W, Mintz GS, Papatheodorou A, Herrmann J, Baumgart D, Haude M, Wieneke H, Ge J, Erbel R. Plaque distribution and vascular remodeling of ruptured and nonruptured coronary plaques in the same vessel: an intravascular ultrasound study in vivo. J Am Coll Cardiol 2001;37(7):1864-1870.
17. Virmani R, Burke AP, Farb A, Kolodgie FD. Pathology of the vulnerable plaque. J Am Coll Cardiol 2006;47(8 Suppl):C13-8.
18. Wentzel JJ, Schuurbiers JC, Gonzalo Lopez N, Gijsen FJ, van der Giessen AG, Groen HC, Dijkstra J, Garcia-Garcia HM, Serruys PW. In vivo assessment of the relationship between shear stress and necrotic core in early and advanced coronary artery disease. EuroIntervention 2013;9(8):989-95.
19. Kubo T, Maehara A, Mintz GS, Doi H, Tsujita K, Choi S-Y, Katoh O, Nasu K, Koenig A, Pieper M, Rogers JH, Wijns W, Böse D, Margolis MP, Moses JW, Stone GW, Leon MB. The dynamic nature of coronary artery lesion morphology assessed by serial virtual histology intravascular ultrasound tissue characterization. J Am Coll Cardiol 2010;55(15):1590-1597.

20. Ruzsa Z, van der Linden M, Van Mieghem NM, Regar E, Ligthart JM, Serruys P, van Geuns RJ. Culotte stenting with bioabsorbable everolimus-eluting stents. Int J Cardiol 2013;168(2):e35-7.
21. van Mieghem NM, Wilschut J, Ligthart J, Witberg K, van Geuns RJ, Regar E. Modified T-Technique with Bioresorbable Scaffolds ensures Complete Carina Coverage – an Optical Coherence Tomography Study. JACC Cardiovasc Interv 2014;in press.
22. Karanasos A, Geuns R-Jv, Zijlstra F, Regar E. Very late bioresorbable scaffold thrombosis after discontinuation of dual antiplatelet therapy. Eur Heart J 2014.
23. Diletti R, Karanasos A, Muramatsu T, Nakatani S, Van Mieghem NM, Onuma Y, Nauta ST, Ishibashi Y, Lenzen MJ, Ligthart J, Schultz C, Regar E, de Jaegere PP, Serruys PW, Zijlstra F, van Geuns RJ. Everolimus-eluting bioresorbable vascular scaffolds for treatment of patients presenting with ST-segment elevation myocardial infarction: BVS STEMI first study. Eur Heart J 2014.
24. Manfrini O, Mont E, Leone O, Arbustini E, Eusebi V, Virmani R, Bugiardini R. Sources of error and interpretation of plaque morphology by optical coherence tomography. Am J Cardiol 2006;98(2):156-9.
25. Gonzalo N, Serruys PW, García-García HM, van Soest G, Okamura T, Ligthart J, Knaapen M, Verheye S, Bruining N, Regar E. Quantitative ex vivo and in vivo comparison of lumen dimensions measured by optical coherence tomography and intravascular ultrasound in human coronary arteries. Rev Esp Cardiol 2009;62(6):615-624.

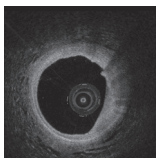

Appendix A - Supplementary Material

Patient population

The population of this study has been previously described.[1] Briefly, all living patients of the Thoraxcenter Rotterdam cohort of the ABSORB Cohort A study (n=14) were asked to participate, with the exclusion of patients with any of the following: hypersensitivity or contra-indication to treatment with heparin or contrast that could not be adequately pre-medicated, left ventricular ejection fraction<30%, renal insufficiency (serum creatinine >2.5 mg/dL or patient on dialysis), bleeding diathesis or coagulopathy and stroke within the past year. Eight patients gave final consent and were finally enrolled in the study. Invasive follow-up including OCT imaging was performed between March 8, and July 20, 2012.

Study device

The study device is a first-generation bioresorbable everolimus-eluting scaffold (BVS version 1.0; 3.0x12 mm; Abbott Vascular, Santa Clara, California), consisting of out-of-phase circumferential zig-zag poly-L-lactic acid struts (150 μm thickness) with a poly-D-L-lactic acid coating containing everolimus (98 μg/cm^2 of surface area).

OCT image acquisition

The ABSORB study included optional OCT imaging at baseline, 6 months and 2 years. Methodology of OCT image acquisition for these studies, using time-domain OCT system (M2/M3®, Lightlab Imaging/St. Jude Medical, St. Paul, Minnesota, USA) with occlusive technique, has been previously described.[2] For the population of the current study, serial OCT pullbacks with good quality images were available for a total of 8 patients, specifically 6 patients at baseline, 7 patients at 6-months follow-up and 7 patients at 2-year follow-up. All 8 subjects underwent Frequency-domain OCT at 5-year invasive follow-up. OCT was performed with the C7XR® imaging console and the Dragonfly® intravascular imaging catheter (Lightlab Imaging/St. Jude Medical, St. Paul, Minnesota), as previously described.[3] Briefly, after positioning the OCT catheter distally to the scaffold, the catheter is pulled back automatically at 20mm/sec with simultaneous infusion by a power injector (flush rate 3 to 4 ml/s) of contrast (Iodixanol 370, Visipaque™, GE Health Care, Ireland) warmed at 37˚C.

Luminal measurements and variability analysis

Lumen area and diameters for all time points were measured at ~200μm intervals in the region of interest, and mean and minimum cross-sectional areas were calculated. Lumen eccentricity was calculated as the ratio (maximum lumen diameter – minimum lumen diameter)/maximum lumen diameter[3]. The analysis was performed with the proprietary LightLab/St. Jude software for off-line analysis. The z-offset was checked and corrected if necessary in all the pullbacks before any measurement. The lumen contour was obtained with an automated detection algorithm and additional manual corrections, if necessary.

Intra-observer variability was assessed by re-analysis of 5-year lumen area measurements by the same observer 3 weeks later. Inter-observer variability analysis was performed by re-analysis of 5-year lumen area measurements by 1) a second observer and 2) by an independent core-lab (Clinfact, Leiden, Netherlands) blinded to the study content. In all cases, analysis was performed with the same pre-defined region of interest. The second observer used the same offline analysis software as the first observer, with individual adjustment of the z-offset. Analysis by the core-lab was performed by offline software (QCU-CMS; LKEB, Leiden University, The Netherlands which is the research version of QIvus, Medis medical imaging systems bv, Leiden, The Netherlands) with automated contour detection and manual correction when necessary.[4] Inter-study variability was assessed by analysis of a second OCT pullback by the same observer, in 4 of the cases in which a second OCT pullback was available.

Variability was assessed on a frame-level and on a scaffold-level basis. In the frame-level analysis, area measurements from each frame in the region of interest were assessed for intra- and inter-observer variability. In the scaffold-level analysis, mean and minimal lumen area measurements were assessed for intra-, inter-observer and inter-study variability.

Analysis of metal first-generation drug eluting stents (DES)

Although the ABSORB A study was a single-arm study, the implantation of metal sirolimus-eluting stents (SES) was allowed as a bail-out procedure. Thus, two patients had SES implanted at the index BVS implantation, both distally overlapping the BVS. Moreover, another patient had a paclitaxel-eluting stent implantation 7mm proximally to the scaffolded segment in the left circumflex artery, 106 days after BVS implantation. Metal stents were analysed on a frame-level basis, including volumetric measurements of stented segments and assessment of strut coverage and apposition. The presence of neoatherosclerosis and neointimal rupture was recorded, and in stents

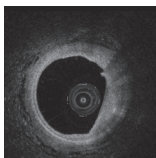

with neoatherosclerosis the lipid core arc and the minimum fibrous cap thickness were measured[5].

References

1. Simsek C, Karanasos A, Magro M et al. Long-term Invasive Follow-Up of the Everolimus-Eluting Bioresorbable Vascular Scaffold: Five-year Results of Multiple Invasive Imaging Modalities. EuroIntervention 2014;in press
2. Serruys PW, Ormiston JA, Onuma Y et al. A bioabsorbable everolimus-eluting coronary stent system (ABSORB): 2-year outcomes and results from multiple imaging methods. The Lancet 2009;373:897-910.
3. Tearney GJ, Regar E, Akasaka T et al. Consensus Standards for Acquisition, Measurement, and Reporting of Intravascular Optical Coherence Tomography Studies: A Report From the International Working Group for Intravascular Optical Coherence Tomography Standardization and Validation. J Am Coll Cardiol 2012;59:1058-1072.
4. Okamura T, Gonzalo N, Gutiérrez-Chico JL et al. Reproducibility of coronary Fourier domain optical coherence tomography: quantitative analysis of in vivo stented coronary arteries using three different software packages. EuroIntervention 2010;6:371-379.
5. Karanasos A, Ligthart J, Witberg K et al. Association of neointimal morphology by optical coherence tomography with rupture of neoatherosclerotic plaque very late after coronary stent implantation. SPIE conference proceedings, 2013:856542-856542-13.

Appendix B - Supplementary Tables

Supplementary Table 1 Assessment of metal drug-eluting stents at 5 years follow-up

	Patient 1	Patient 4	Patient 8
Type of stent	SES 3.0x13mm, distal overlap, implanted at baseline	PES 3.5x20mm, non-overlapping, implanted 106 days post BVS implantation	3 overlapping SES 3.0x13mm, distal overlap, implanted at baseline
Minimum luminal area (mm^2)	2.38	7.05	2.07
Mean luminal area (mm^2)	5.59	9.44	5.67
Minimum stent area (mm^2)	6.11	10.34	3.76
Mean stent area (mm^2)	7.16	12.89	7.13
Mean neointimal thickness (μm)	193	249	178
Uncovered/total struts n, (%)	1/627 (0.16)	25/920 (2.71)	5/1434 (0.34)
Incompletely apposed struts n, (%)	0/630 (0)	0/920 (0)	0/1434 (0)
Cross-sections with >30% uncovered struts/ total n, (%)	0/59 (0)	0/103 (0)	0/146 (0)
Cross-sections with incompletely apposed struts/total n, (%)	0/59 (0)	0/103 (0)	0/ 146 (0)
Neoatherosclerosis	Yes	Yes	Yes
Neointimal rupture	No	Yes	No
Thrombus	No	Yes	No
Maximum necrotic core arc in neointima (°)	160	170	67
Minimum cap thickness in neoatherosclerosis (μm)	110	70	80

SES=sirolimus-eluting stents, PES=paclitaxel eluting stents, BVS=bioresorbable scaffold

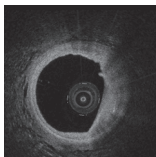

Supplementary Table 2

Study-level inter- and intra-observer variability (n=8)

	Observer 1 Measurement 1	Observer 2	Difference (Observer 1 – Observer 2)	ICC	Core lab measurements	Difference (Observer 1 – Core lab)	ICC	Observer 1 Measurement 2	Difference (Measurement 1 – Measurement 2)	ICC
Mean lumen area (mm^2)	6.39±1.18	6.16±1.29	0.23±0.29	0.98	6.26±1.15	0.13±0.32	0.98	6.22±1.32	0.17±0.19	0.99
Minimum lumen area (mm^2)	4.62±1.44	4.55±1.51	0.07±0.23	0.99	4.59±1.48	0.03±0.25	0.99	4.55±1.51	0.07±0.20	0.99

Inter-study variability (n=4)

	Pullback 1	Pullback 2	Difference (Pullback 1 – Pullback 2)	ICC
Mean lumen area (mm^2)	6.93±1.18	6.74±1.42	0.20±0.32	0.98
Minimum lumen area (mm^2)	5.41±1.40	5.38±1.56	0.03±0.34	0.98

Frame-level inter- and intra-observer variability (n=468)

	Observer 1 Measurement 1	Observer 2	Difference (Observer 1 – Observer 2)	ICC	Core lab measurements	Difference (Observer 1 – Core lab)	ICC	Observer 1 Measurement 2	Difference (Measurement 1 – Measurement 2)	ICC
Lumen area (mm^2)	6.23±2.19	6.00±2.18	0.23±0.62	0.95	6.14±2.07	0.08±0.54	0.97	6.06±2.26	0.16±0.30	0.99

ICC=intraclass correlation coefficient

Appendix C - Supplementary Figures

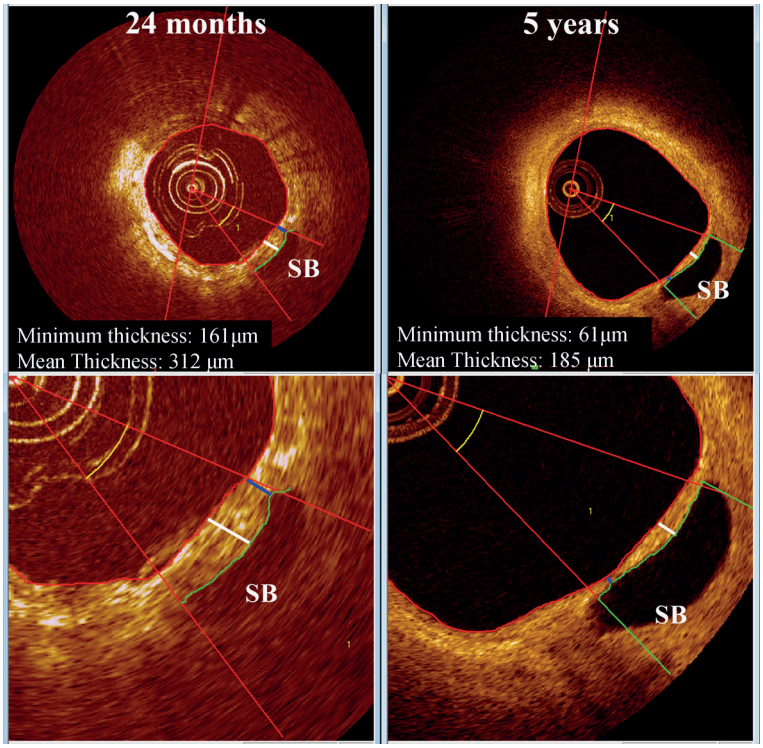

Supplementary Figure 1 Measurement of thickness of tissue bridges associated with side-branch ostia

The tissue bridge is manually segmented at the adluminal (red line) and abluminal (green line) contour, and minimum and mean thickness are measured. Note the presence of scaffold struts at the 24-month follow-up. Blue line indicates minimum thickness and white line indicates maximum thickness

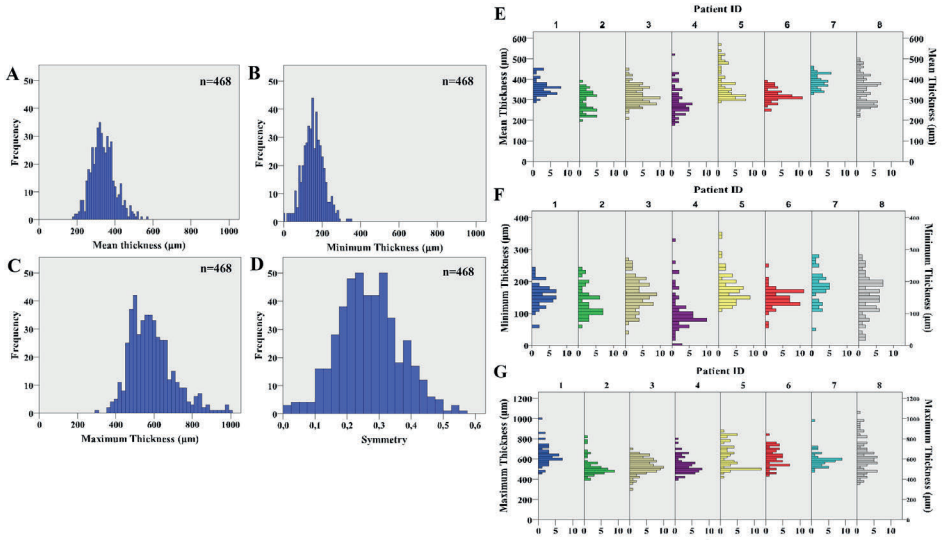

Supplementary Figure 2 Frequency distribution of signal-rich layer thickness

Frequency distribution of mean (A), minimum (B) and maximum (C) signal-rich layer thickness, as well as thickness symmetry in all analyzed frames (D). Distributions of mean (E), minimum (F) and maximum (G) signal-rich layer thickness are also presented per individual patient

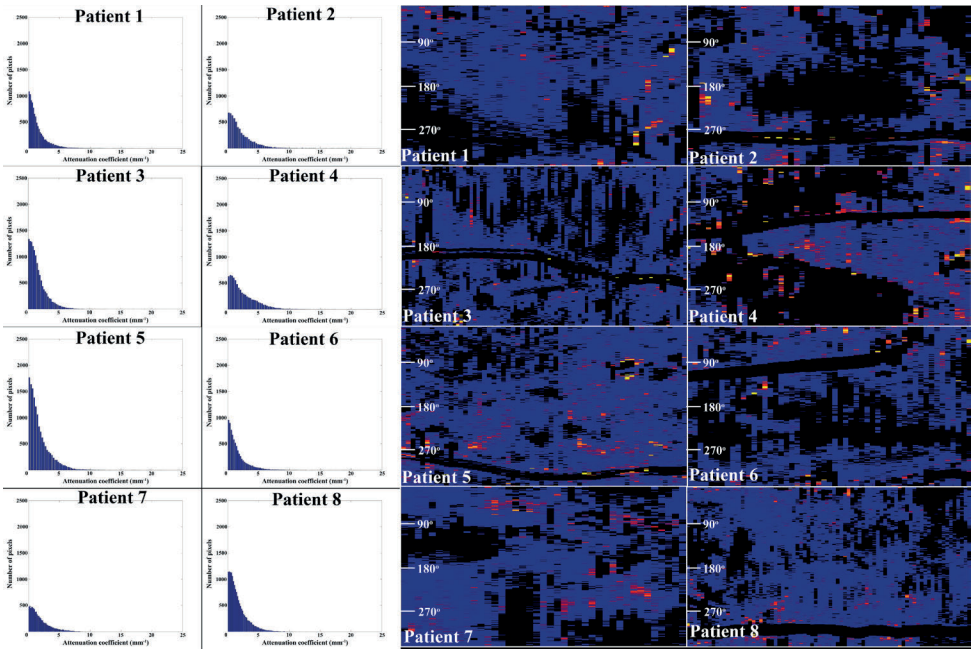

Supplementary Figure 3 Frequency distribution of attenuation coefficient and maximum attenuation maps at the signal-rich layer

Frequency distribution of all attenuation values in the signal-rich layer in all frames per patient (left panels). The attenuation values are low, with the 90th percentile ≤4mm^{-1} with the exeption of patient #4. Spread-out maps demonstrate the maximum attenuation per A-line in the signal-rich layer (Right panels). There is mainly blue colour indicating low-attenuation regions. Note that in cases with a signal-rich layer <200microm, the region is displayed as black due to the lack of sufficient imaging window for the analysis

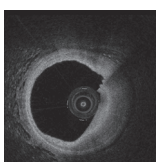

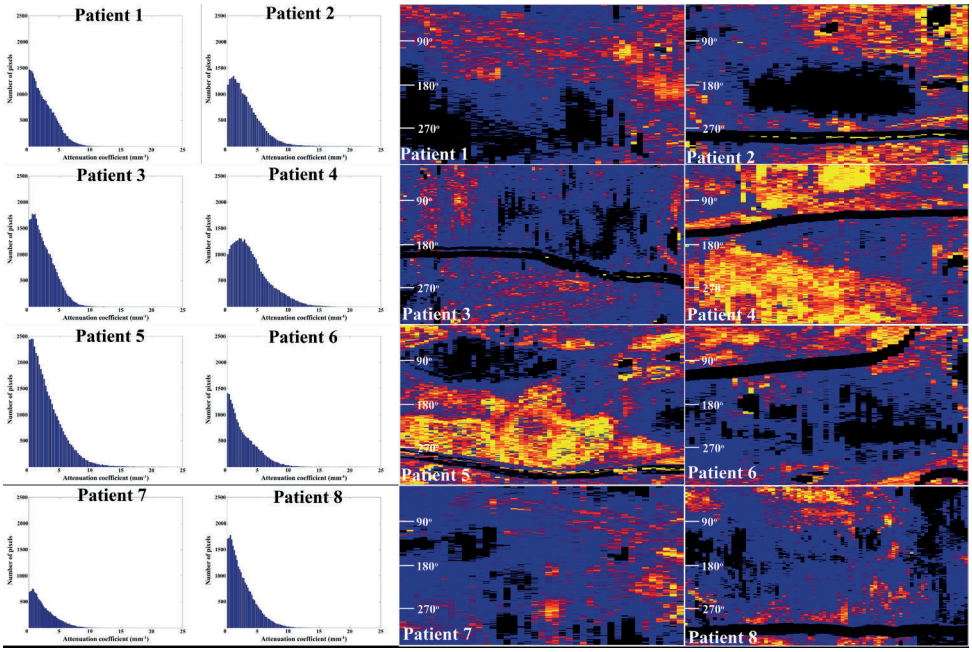

Supplementary Figure 4 Frequency distribution of attenuation coefficient and maximum attenuation maps in the 'neo-plaque' region

Frequency distribution of all attenuation values in the 'neo-plaque' region in all frames per patient (Left panels). Attenuation values vary depending on plaque type. Spread-out maps demonstrating the maimum attenuation per A-line in the 'neo-plaque' region (Right panels). Regions with yellow or red colour indicate highly attenuating areas corresponding to plaque. Similarly to **Supplementary Figure 3**, *'neo-plaque' regions with intimal thickness <200microm are displayed as black*

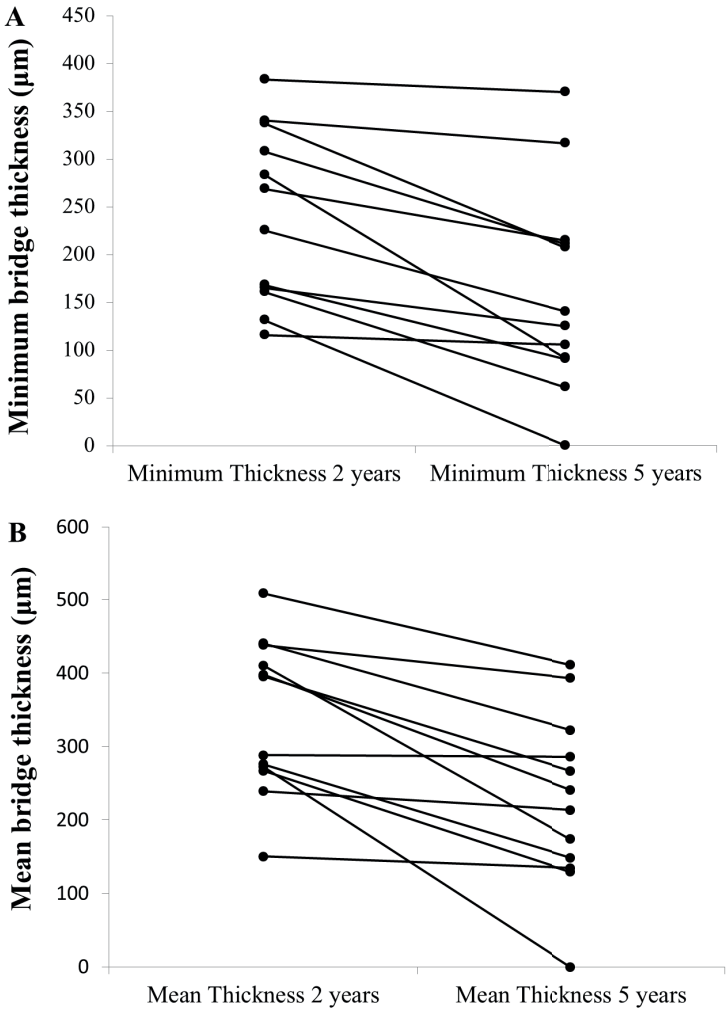

Supplementary Figure 5 Thickness of tissue bridges overlying side-branches at 2 years and 5 years

There is a decrease of the minimal (A) and mean (B) thickness of tissue bridges associated with side-branches in almost all cases (minimum: 241 ± 92µm at 2 years versus 161 ± 107µm at 5 years, P<0.001; mean 341 ± 106µm at 2 years versus 227 ± 119µm at 5 years, P=0.001)

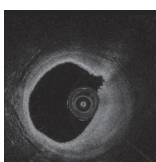

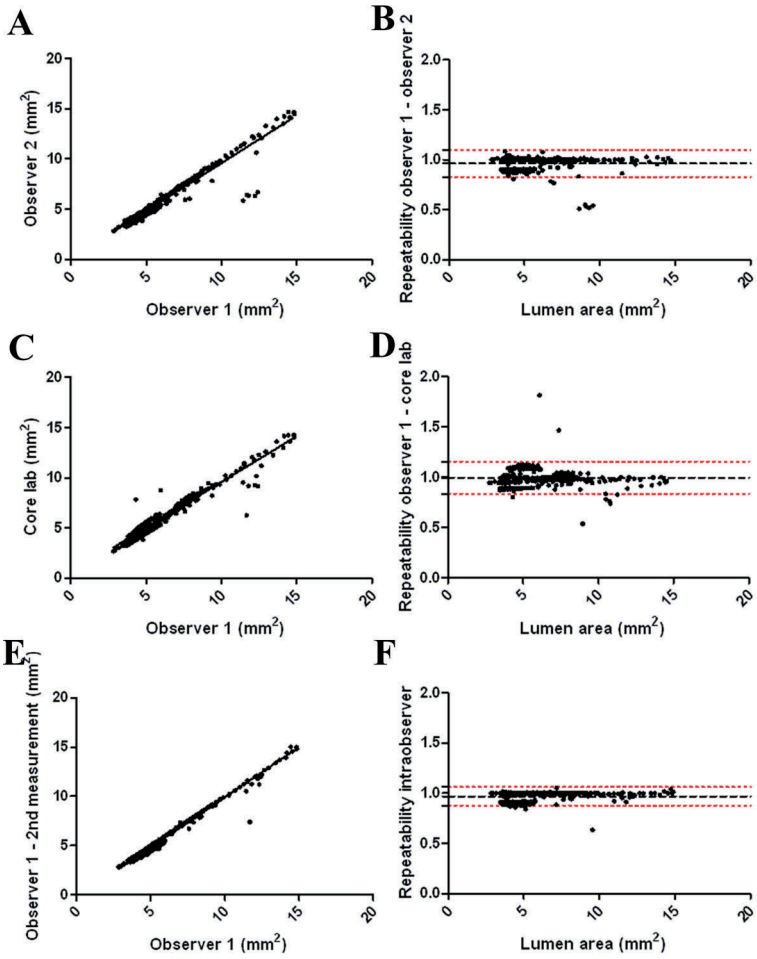

Supplementary Figure 6 Correlation and Bland-Altman plots for inter- and intra-observer variability in a frame-level analysis

Correlation plots and Bland-Altman repeatability plots for inter-observer variability (A and B), inter-observer variability with core-lab measurements (C and D) en intra-observer variability (E and F). Note the presence of outliers, corresponding to contour tracing discrepancies in regions of side-branch ostia. Black striped line corresponds to mean repeatability and red striped lines to 95% limits of agreement (mean ± 2 SD)

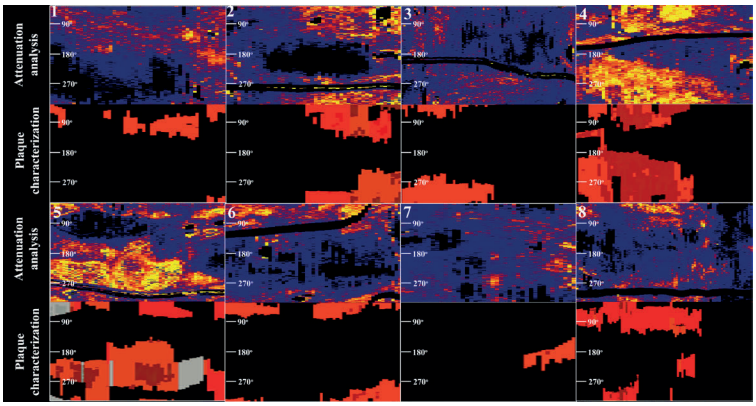

Supplementary Figure 7 Comparison of quantitative attenuation analysis with visual plaque characterization

Spread-out maps generated by visual plaque characterization and maximum attenuation analysis of the entire plaque in all patients. Note the spatial correspondence of necrotic core sites with regions of high attenuation

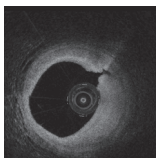

Neoatherosclerosis development following bioresorbable vascular scaffold implantation in diabetic and non-diabetic swine coronary arteries

N.S. van Ditzhuijzen, M. van den Heuvel, M. Kurata, O. Sorop, R.W.B. van Duin, I. Krabbendam-Peters, J. Ligthart, K. Witberg, M. Murawska, Hector M. Garcia-Garcia, M. Mulder, F. Zijlstra, D.J. Duncker, H.M.M. van Beusekom, E. Regar

Under consideration at Plos One

10

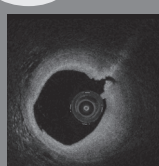

Abstract

Introduction Diabetes mellitus (DM) remains a risk factor for poor outcome after stent-implantation, but little is known if and how DM affects the vascular response to bioresorbable vascular scaffolds (BVS). We aimed to examine coronary responses to BVS in swine with and without diabetes mellitus fed a 'fast-food' diet (FF-DM and FF-NDM, respectively) by sequential optical coherence tomography (OCT)-imaging and histology.

Materials and methods Fifteen male swine were evaluated. Eight received streptozotocin-injection to induce DM. After 9 months (M), 32 single BVS were implanted in epicardial arteries with a stent to artery (S/A)-ratio of 1.1:1 under quantitative coronary angiography (QCA) and OCT guidance. Lumen, scaffold, neointimal coverage and composition were assessed by QCA, OCT and near-infrared spectroscopy (NIRS) pre- and/or post-procedure, at 3M and 6M. Additionally, polarization-sensitive (PS)-OCT was performed in 7 swine at 6M. After sacrifice at 3M and 6M, histology and polymer degradation analysis were performed.

Results Late lumen loss was high (~60%) within the first 3M after BVS-implantation ($P<0.01$ FF-DM vs. FF-NDM) and stabilized between 3M and 6M (<5% change in FF-DM, ~10% in FF-NDM; $P>0.20$). Neointimal coverage was highly heterogeneous in all swine (DM vs. NDM $P>0.05$), with focal lipid accumulation, irregular collagen distribution and neointimal calcification. Likewise, polymer mass loss was low (~2% at 3M, ~5% at 6M;$P>0.20$) and not associated with DM or inflammation.

Conclusions Scaffold coverage showed signs of neo-atherosclerosis in all FF-DM and FF-NDM swine, scaffold polymer was preserved and the vascular response to BVS was not influenced by diabetes.

Introduction

Patients with diabetes mellitus (DM) are generally at risk for worse outcome after stent-implantation than patients without DM.[1] Due to the complex and multifactorial nature of the disease process, including metabolic abnormalities and vascular dysfunction, the vascular response to stent-implantation is generally impaired, complicating current stenting strategies.[2-4]

The everolimus-eluting bioresorbable vascular scaffold (BVS) may offer advantages. It elutes everolimus in the first 3 to 6 months after implantation, inhibiting excessive neointimal growth [5] and starts losing structural integrity 3 months after implantation,[5] potentially enabling vascular function restoration.[6]

Histology in healthy swine demonstrated that struts are covered at 28 days and resorbed around 3 years with minimal calcification and inflammation.[7, 8] In selected patients from the ABSORB Cohort A (BVS 1.0) and B (BVS 1.1) trials, excellent results for treatment of coronary artery lesions were observed.[9, 10] However, only 3%-20% of the study population suffered DM and no studies were performed in diabetic animals. Thus, little is known about the effect of DM on the vascular response to BVS. DM may cause inflammation, which could influence scaffold degradation by disregulated acid-base balance or body-temperature.[11]

Animal models reflecting the impact of atherosclerosis and DM can be useful, as they allow us to study vascular responses and scaffold degradation in a more complex setting.[12] Moreover, swine can be rendered diabetic and in combination with an atherogenic diet they develop atherosclerosis comparable to humans.[13] Scaffolds can be placed in coronary arteries and in-vivo sequential intracoronary imaging can be performed by optical coherence tomography (OCT), polarization-sensitive (PS)-OCT and near-infrared spectroscopy (NIRS). After sacrifice, histology and gel permeation chromatography (GPC) can be performed to assess scaffold coverage and degradation of the polymer.

We examined the mechanistic and morphological aspects of the coronary response to BVS1.1 in DM and non-DM swine fed a fast-food diet (FF-DM, FF-NDM respectively) using longitudinal intracoronary imaging and histology.

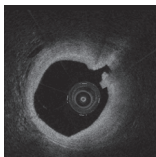

Materials and methods

Experimental design

The Erasmus MC Animal Ethics committee approved the study, performed in accordance with the Guide for Care and Use of Laboratory Animals.[14] Fifteen male [Yorkshire x Landrace] swine with an age of ~11 weeks and a body weight of ~30kg were included (see **Supplementary Material (Appendix A)** for a detailed description). DM was induced by streptozotocin (140mg/kg iv, single dose) in 8 randomly selected male crossbred swine.[15] Four weeks after start of the study, all 15 swine started a fast-food diet (FF), which is a diet containing 10% sucrose, 15% fructose, 25% (swine) lard, 1% cholesterol and 0.7% sodiumcholate (bile salts).

All 8 FF-DM and 5 FF-NDM received single 3.0x18.0mm Absorb BVS1.1 implants in 2, and 2 FF-NDM received single Absorb BVS1.1 implants in all 3 coronary arteries to ensure an even amount of scaffolds in FF-DM (N=16) and FF-NDM (N=16) (see **Supplementary Material; Appendix A**).

Sequential coronary imaging included QCA and OCT pre-, immediately, 3 and 6 months (M) post-implantation and NIRS pre-, 3M and 6M post-implantation. PS-OCT was performed in N=3 FF-DM and N=4 FF-NDM BVS at 6M. 3M imaging was included when pre and/or post-implantation imaging were available and 6M imaging was included when pre- and/or post –and 3M imaging were available. After the 3M imaging assessment, 3 FF-DM and 2 FF-NDM were sacrificed and after the 6M imaging assessment the remaining swine were sacrificed. After sacrifice, hearts were removed, the coronary tree dissected free and coronary arteries containing BVS randomized to histological (3M N=5/10, 6M N=12/22) or GPC analysis (3M N=5/10, 6M N=10/22) (**Figure 1**).

Fasting blood samples were obtained at baseline, 3M and 6M to measure glucose, total, low- and high-density lipoprotein cholesterol (TC, LDL, HDL) and triglyceride levels.

In-vivo QCA, (PS)-OCT and NIRS analysis

See **Supplementary Material (Appendix A)** for a detailed description of the imaging analyses. Coronary angiograms were obtained in two orthogonal views and QCA-analysis was performed (CAAS, version 5.9.2 Pie Medical Imaging BV). Mean (LD) and minimal lumen diameter (MLD), scaffold to artery (S/A) ratio, acute gain and late lumen loss were documented. Longitudinal matching of OCT pullbacks (C7XR Fourier-

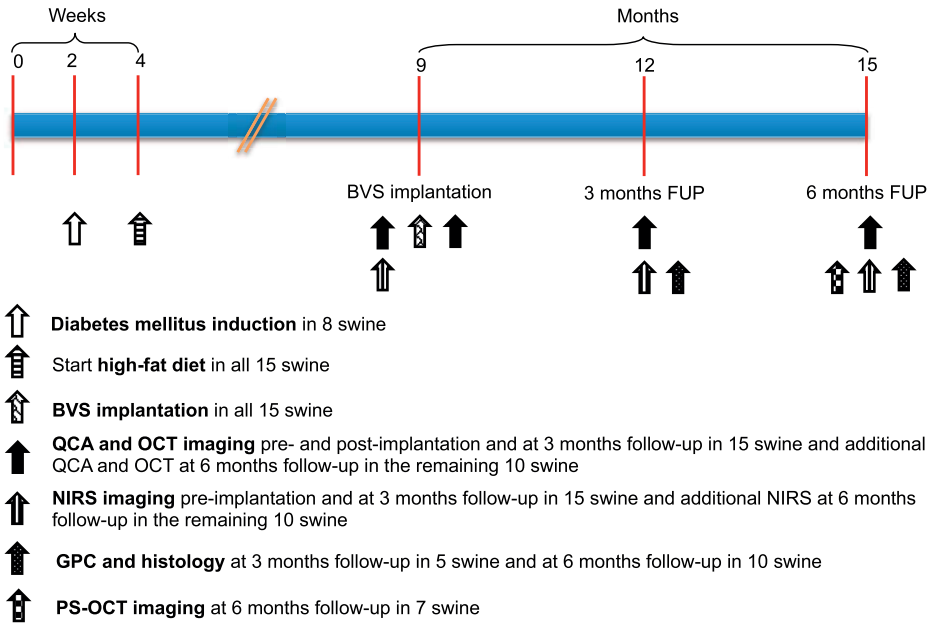

Figure 1 Study Design

BVS = bioresorbable vascular scaffold, FUP = follow-up, QCA = quantitative coronary angiography, PS = Polarization Sensitive, OCT = optical coherence tomography, NIRS = near-infrared spectroscopy, GPC = gel permeation chromatography

Domain, St. Jude Medical) was performed as described previously using dedicated CURAD analysis software (CURAD BV).[16]

OCT parameters for vascular reaction, including lumen and scaffold dimensions and scaffold strut appearance, apposition, neointimal coverage and coverage morphology were assessed in 1-mm intervals using off-line OCT analysis software according to previously published methodology.[17] In pre-implantation lesions not exceeding the penetration depth of OCT, plaque burden (PB) was determined. Mean number of discernible struts were documented immediately post-implantation and at follow-up. Changes in strut appearances were categorised as preserved, open, dissolved bright, and dissolved black box.[18] Struts were scored as covered or uncovered and the morphology of the coverage – defined as [SA – LA][16] – was described as homogeneous or heterogeneous. Heterogeneous coverage was furthermore described as lipid-laden, calcified, surrounding the struts or subluminal, or mixed (**Supplementary Figure 1; Appendix C**).[19]

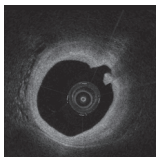

PS-OCT was performed using a prototype imaging system. PS-OCT provides a measure of tissue birefringence, an optical tissue property that describes the interaction with polarized light. It grossly relates to microscopic tissue organization, and enables characterization of collagen content and smooth muscle cell (SMC) density in atherosclerotic plaques.[20]

NIRS analysis (LipiScan, InfraReDx) was used for lipid core plaque (LCP) characterization.[21] Lipid-core burden index (LCBI) was documented, indicating high probability that LCP is present. To evaluate the agreement between OCT and NIRS for detection of lipid, we compared – per scaffold – the LCBI score to the percentage of OCT cross-sections with lipid-containing morphology.

Ex-vivo degradation analysis

GPC was performed as described previously (see **Supplementary Material; Appendix A**).[7] Degradation in our model was studied in relation to DM, time, inflammation, scaffold recoil, OCT-derived strut appearance and pre-implantation plaque burden.

Ex-vivo histological analysis

See **Supplementary Material (Appendix A)** for a detailed analysis. Proximal, middle and distal sections within each BVS were obtained. Tissue sections were stained by Hematoxylin-Eosin (HE) as an overview stain, Resorcin-Fuchsin for elastin, Alcian-Blue for proteoglycans, Oil-red-O (ORO) for lipids, Picrosirius Red (PSR) for collagen, von Kossa for calcium, and immunohistochemistry for smooth muscle cells (aSMA, clone 1A4, Dako, the Netherlands) and leukocytes (CD45, clone MCA 1447, AbD Serotec, UK). Polarization microscopy was performed to assess scaffold struts.

Histological analysis included neointimal healing and organization, collagen distribution, injury and inflammation score, lipid accumulation and presence of calcium classified as subluminal or surrounding struts (**Supplementary Figure 2; Appendix C**).

Statistical analysis

Statistical analysis (SPSS 20.0) entailed the Kolmogorov-Smirnov test for normality of the data. Normal distribution was expressed as mean ± standard deviation. Non-normally distributed data were presented as median with interquartile range. Comparison of in-vivo imaging between FF-DM and FF-NDM was performed by generalized estimating equations (GEE) modeling. A linear response model was applied with an exchangeable structure for the within-cluster correlation matrix. For repeated measures,

GEE modeling was performed using a linear response model with an autoregressive (AR(1)) structure for the within-cluster correlation matrix. Comparison of ex-vivo GPC between FF-DM and FF-NDM swine was performed by independent samples t-test. To assess variable relations, the Spearman correlation coefficient was computed. All statistical tests were 2 tailed, and P<0.05 was considered statistically significant.

Results

Plasma measurements

Average TC, LDL and HDL were similar between FF-DM and FF-NDM (TC 18.7±5.0mmol/l and 19.0±5.8mmol/l (P=0.86); LDL 15.1±5.1mmol/l and 15.6±5.1mmol/l (P=0.75); HDL 5.4±0.8mmol/l and 5.7±0.7mmol/l (P=0.13) in FF-DM and FF-NDM respectively). In the 8 swine that received a steptozotocin-injection, DM was successfully induced. Average plasma glucose and triglyceride levels were elevated in FF-DM compared to FF-NDM (15.0±7.8mmol/l vs. 4.5±1.0 mmol/l (P<0.01), 1.1±0.8mmol/l vs. 0.6±0.5mmol/l (P=0.02), respectively).

In-vivo QCA, (PS)-OCT and NIRS

All 32 BVS were successfully implanted with a mean S/A-ratio of 1.1±0.1 in FF-DM and FF-NDM (P=0.20).

QCA findings are presented in **Figure 2A and B** and **Supplementary Table 1 (Appendix B)**. Pre-implantation lesions were mild and similar between FF-DM and FF-NDM (P=0.33). In all swine, mean LD decreased from post-implantation to 3M (P<0.01) and remained fairly stable from 3M to 6M (P=0.34 and P=0.54, respectively).

Quantitative OCT findings are presented in **Figure 2C to F** and **Supplementary Table 1 (Appendix B).** Pre-implantation lumen dimensions (LD, LA and MLA) were similar between FF-DM and FF-NDM (P=0.46, P=0.46 and P=0.74) and pre-implantation %PB was mild (9±2% FF-DM, 10±1% FF-NDM; P=0.58). Scaffolds were implanted according to protocol with an S/A ratio ≥1.1. Thus, LD increased in all swine from pre- to post-implantation (P>0.10). No signs of scaffold damage nor procedure-related injury were documented. No edge dissection or thrombus was observed and minor tissue prolapse was documented. Mild acute ISA was observed in 2 FF-DM BVS (mean ISA area 0.26±0.11mm^2) and 1 FF-NDM BVS (mean ISA area 0.03mm^2; P<0.01). From post-implantation to 3M, mean LD, LA and MLA decreased (~60%). At 3M, all ISA resolved, no late acquired ISA developed and all struts were covered. Restenosis, however, hampered OCT imaging at 3M in one FF-NDM. At 6M, OCT demonstrated a substantial

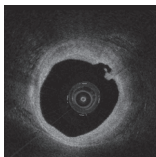

neointima with a highly heterogeneous morphology, which was confirmed by histology (**Supplementary Figure 3; Appendix C**). From 3M to 6M, mean LD, LA, MLA, SD and SA remained fairly stable in all swine (**Figure 2 C to E**; **Supplementary Table 1 (Appendix B)**)

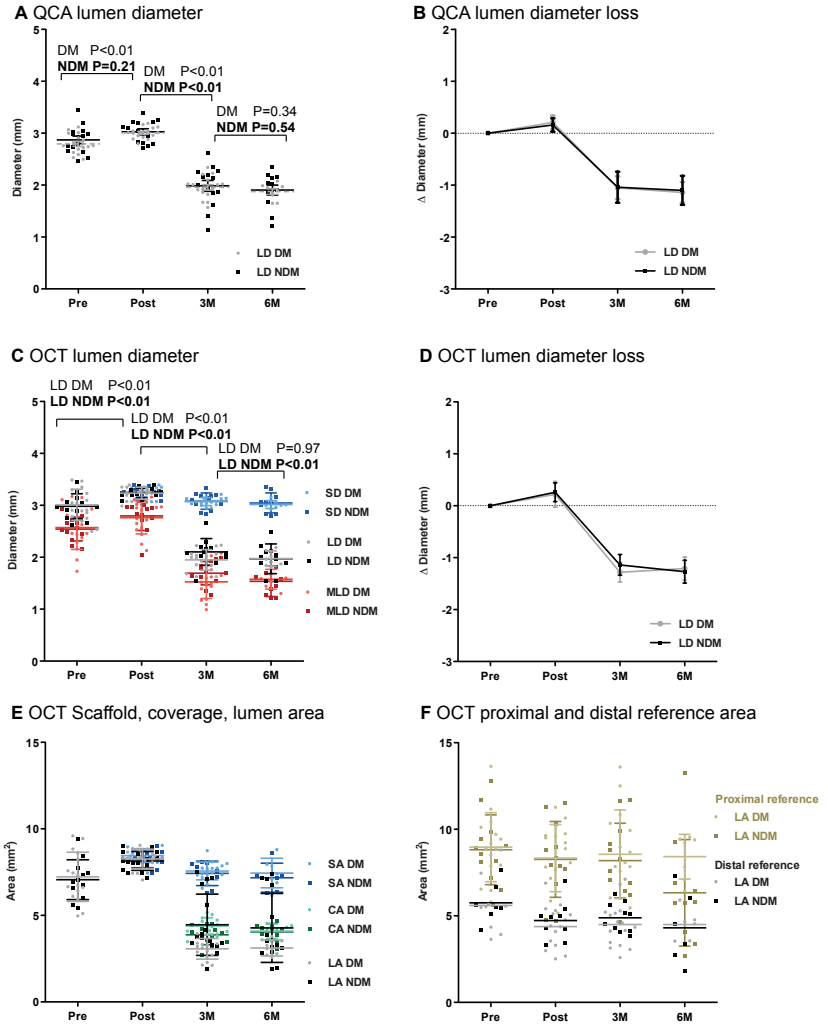

Figure 2 QCA and OCT analysis results

A and B) Mean lumen diameter (LD) slightly increased from pre-to post-implantation, decreased from post-implantation to 3M and remained stable from 3M to 6M. Grey: FF-DM, black: FF-NDM. C to E) Mean lumen area (LA), lumen diameter (LD) and minimal lumen diameter (MLD) increased slightly from pre- to post-implantation. Mean LA, LD and MLD and mean scaffold area (SA) and scaffold diameter (SD) decreased from post-implantation to 3M and mean LA, LD, MLD, SA, SD and coverage area (CA) remained stable from 3M to 6M. F) Proximal and distal reference LA slightly decrease from pre- to post-implantation and stabilized from post-implantation to 3M and 6M

Table 1. OCT coverage analysis

	3M			6M			P‡	
	FF-DM	FF-NDM	P*	FF-DM	FF-NDM	P*	FF-DM	FF-NDM
Coverage thickness, mm	0.42±0.08	0.39±0.11	0.50	0.39±0.06	0.41±0.11	0.59	0.05	0.38
Coverage area, mm^2	4.38±0.48	4.03±0.67	0.19	4.09±0.42	4.20±0.59	0.65	0.03	0.10
Coverage appearance								
Homogeneous, %	0 (0;6)	0 (0;4)	0.17	0 (0;0)	0 (0;4)	0.51	0.05	0.09
Heterogeneous, %	100 (94;100)	100 (96;100)	0.17	100 (100;100)	100 (96;100)	0.51	0.05	0.09
Lipid-laden, %	0 (0;12)	0 (0;14)	0.57	6 (6;11)	6 (0;15)	0.97	0.54	0.79
Calcified, %	25 (16;43)	16 (5;40)	0.49	41 (33; 66)	72 (37;87)	0.64	0.01	<0.01
Strut area, %	19 (10;31)	13 (0;34)	0.70	29 (13;63)	15 (5;47)	0.49	0.14	0.05
Subluminal, %	3 (0;7)	0 (0;4)	0.51	5 (0;6)	3 (0;29)	0.29	0.49	0.07
Strut area + subluminal, %	0 (0;0)	0 (0;0)	0.55	5 (0;8)	19 (3;29)	0.11	0.09	<0.01
Mixed, %	0 (0;7)	0 (0;9)	0.99	22 (12;48)	13 (1;40)	0.71	<0.01	0.04

*Normally distributed data are presented as mean±SD, non-normally distributed data as median (interquartile range). FF-DM = fast-food fed diabetic swine, FF-NDM = fast-food fed non-diabetic swine, OCT = optical coherence tomography, 3M = 3 months follow-up, 6M = 6 months follow-up. *P-value for the comparison between FF-DM and FF-NDM swine, ‡P-value for the difference between 3M and 6M*

Changes in coverage morphology

See **Table 1** for OCT findings. A heterogeneous morphology predominated in all swine at 3M, with a relatively high prevalence of calcium (25% (16%; 43%) in FF-DM and 16% (5%; 36%) in FF-NDM; P=0.49). At 6M, the heterogeneous pattern predominated and was mainly characterized by calcium (41% (33%; 66%) in FF-DM and 59% (37%; 85%) in FF-NDM) (P=0.82) (**Supplementary Video 1 and 2**). Moreover, the accumulation of calcium increased (P<0.05), whereas the accumulation of lipid remained moderate (FF-DM P=0.67, FF-NDM P=0.97).

PS-OCT was only qualitatively analyzed and showed a heterogeneous neointima with spots of elevated birefringence (**Figure 3B and M**). Rapid depolarization of the signal was often observed, focally (**Figure 3C**) and in areas with the appearance of lipid-rich plaque and inflammation (**Figure 3E and F**).

See **Supplementary Table 2 (Appendix B)** for NIRS findings. Similar to OCT, the prevalence of lipid was relatively low in FF-DM (9/15 BVS) and FF-NDM (3/11 BVS) at 3M with relatively low LCBI scores (3.00 (0.00; 22.50) in FF-DM, 0.00 (0.00; 3.00) in FF-NDM; P=0.69). From 3M to 6M, the prevalence of lipid increased numerically, in FF-DM

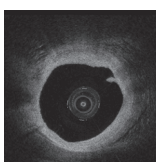

(6/6 BVS) and FF-NDM (5/8 BVS). Subsequently, LCBI scores slightly increased (17.50 (9.75; 26.00) in FF-DM, 6.50 (0.00; 47.25) in FF-NDM; P=0.49).

The association of LCBI-score and percentage of OCT cross-sections with a lipid-laden or mixed appearance was modest at 3M (Spearman's rho 0.397; P=0.05) but became stronger at 6M (Spearman's rho 0.666; P<0.01).

Changes in strut appearance

See **Supplementary Table 3 (Appendix B)**. The number of discernible struts per OCT cross-section was similar post-implantation (8±2 in FF-DM, 8±1 in FF-NDM) and at 3M (8±1 in FF-DM, FF-NDM) and decreased to 6M (7±1 in FF-DM, 6±2 in FF-NDM). The

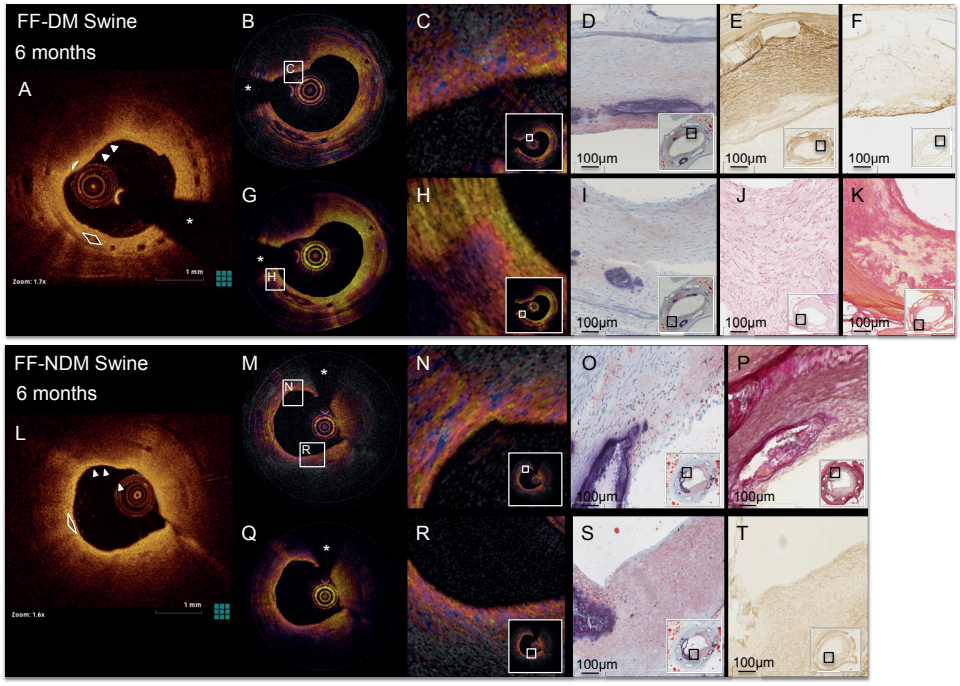

Figure 3 (PS)-OCT and corresponding histology at 6M

OCT demonstrated the development of a highly heterogeneous neointima with lipid and calcium accumulation in FF-DM and FF-NDM swine at 6 months (A and L), which was confirmed by histology (D, I, O and S; Oil-red-O). Phase retardation corresponding to tissue birefringence (B and M) and depolarization (G and Q) imaged by PS-OCT, demonstrated enhanced birefringence and depolarization (C) in an SMC-poor area (E; αSMA) with inflammation (F; CD45). Furthermore, PS-OCT demonstrated focal depolarization (H) in a collagen-poor area with loss of structure and evidence of early necrosis (J and K; HE, PSR). N shows coarse-grained high birefringence in an area with strongly circumferentially organized intimal SMCs (P; RF); lipid-rich, SMC-poor tissue (T; SMA) exhibits a more finely speckled heterogeneity, associated with a rapid loss of polarization degree (R). Asterisk (*) indicates guidewire artefact, arrowheads lipid, white lines calcium

majority kept a preserved box appearance from 3M (79% in FF-DM, 81% in FF-NDM) to 6M (77% in FF-DM, 68% in FF-NDM). Interestingly, a substantial amount of struts appeared as dissolved black box at 3M (20% in FF-DM, 18% in FF-NDM) and 6M (22% in FF-DM, 31% in FF-NDM).[22]

Ex-vivo GPC

See **Table 2**. The initial Mn, Mw and PDI were 109.55 KDa, 229.68 KDa and 2.10 respectively. The initial mass was 8.53±0.08mg in FF-DM and 8.50±0.07mg in FF-NDM. Up to 6M, Mn, Mw and PDI decreased and mass loss was low: 5.5±1.9% in FF-DM and 4.3±1.4% in FF-NDM (P=0.28).

There was no relationship between scaffold degradation and DM (P>0.10), or with OCT-derived pre-implantation %PB (P=0.22), scaffold recoil (P=0.59), preserved (P=0.92), open (P=0.45) or dissolved black box appearance (P=0.99) at 3M, or at 6M (P=0.29, P=0.73 P=0.27, P=0.36 and P=0.64 respectively).

Ex-vivo histology

See **Table 2**. All struts were covered by neointima 3M post-implantation (FF-DM 0.76±0.1mm, FF-NDM 0.62±0.1mm; P>0.10). Neointimal organization score was higher at 3M than 6M (P<0.01) in FF-DM and FF-NDM (P=0.14). Injury was moderate. Injury scores were 1.30±0.42 and 1.10±0.14 (P=0.58) at 3M and 1.10±0.13 and 1.04±0.33 (P=0.74) at 6M in FF-DM and FF-NDM, respectively.

Collagen poor regions were observed within the neointima. They contained leukocytes, were evident at sites with extracellular lipids and often coincided with calcifications (**Figure 4**). Collagen poor but SMC positive tissue generally contained lipid accumulation (P>0.10 for FF-DM vs. FF-NDM) (**Figure 4 G to I**). Mainly intra- and extracellular lipid deposits with few cholesterol crystals were observed and advanced necrotic cores were absent.

Neointimal and peristrut calcifications were observed in FF-DM and FF-NDM **(P=0.04)** at 3M and 6M (**Figure 3**, **Table 2)**, with varying size, shape and location between animals, suggesting an inter-animal difference. From 3M to 6M, lipid-accumulation remained (**Figure 5**) and calcifications were observed more frequently subluminally (in 3/5 FF-DM BVS, 6/7 FF-NDM BVS).

At 6M, signs of myxoid degeneration with lipid accumulation were present (**Supplementary Figure 4; Appendix C**). In 3 BVS (N=1 FF-DM, N=2 FF-NDM) thrombus remnants were observed at 6M but not at 3M.

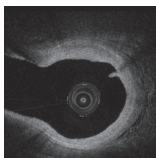

Table 2. GPC and histology results

	3M			6M		
	FF-DM	**FF-NDM**	**P***	**FF-DM**	**FF-NDM**	**P***
GPC results						
BVS evaluated, n	3	2		5	5	
Mn, KDa	82.76±4.36	80.13±0.85	0.41	67.17±3.11	65.55±3.40	0.46
Mw, KDa	159.31±7.07	160.39±4.03	0.84	134.55±2.47	132.23±8.03	0.56
PDI	1.93±0.02	2.00±0.03	0.10	2.01±0.09	2.02±0.04	0.84
%Mass loss	2.6±0.6	2.0±6.6	0.86	5.5±1.9	4.3±1.4	0.28
Histological results						
BVS evaluated, n	3	2		5	7	
Neointimal thickness, mm	0.76±0.08	0.62±0.07	0.13	0.60±0.06	0.65±0.11	0.38
Medial thickness, mm	0.06±0.01	0.06±0.03	1.00	0.07±0.02	0.09±0.03	0.17
Adventitial thickness, mm	0.13±0.02	0.14±0.09	0.95	0.10±0.02	0.11±0.03	0.32
Scaffold area, mm^2	7.20±0.36	6.53±0.97	0.50	5.61±0.73	5.65±0.63	0.92
Injury sore	1.30±0.42	1.10±0.14	0.58	1.10±0.13	1.04±0.33	0.74
Inflammation score	0.95±0.32	0.32±0.08	0.08	0.22±0.18	0.30±0.47	0.71
Lipid accumulation, %	7.2 (5.4;17.3) 3.72.8;5.3)	15.8 (9.5;20.0) (9.0;(0.9;1.4)	0.83	19.5 (15.8;19.8)	9.4 (6.1;24.6)	0.76
Calcium						
Surrounding strut, %	88.03±8.21	94.05±8.41	0.48	72.54±11.63	74.21±19.63	0.87
Score per-strut	1.23±0.24	1.20±0.14	0.87	0.86±0.38	0.94±0.26	0.67
Subluminal, n	2	1	0.79	3	6	0.36

GPC = gel permeation chromatography, Mn = number average molecular weight, Mw = weight average molecular weight, PDI = polydispersity index [Mn/Mw]. Percentage (%) mass loss = [(Initial mass prior to scaffold implantation [T=0] (mg) – Found mass (mg)) / Initial mass [T=0] (mg) x 100]. Footnotes and the remaining abbreviations are as listed in **Table 1**

Furthermore, the polymeric scaffold struts demonstrated birefringence with polarized light, confirming preservation of scaffold struts in all swine.

Discussion

The present study describes the coronary artery response to BVS1.1 in FF-DM and FF-NDM swine. A remarkable neotintima burden with a highly heterogeneous appearance was observed in all swine, with lipid accumulation and calcification, indicative for the formation of neoatherosclerosis. The scaffold polymer was preserved up to 6M, independent of inflammation or the presence of DM in FF-swine.

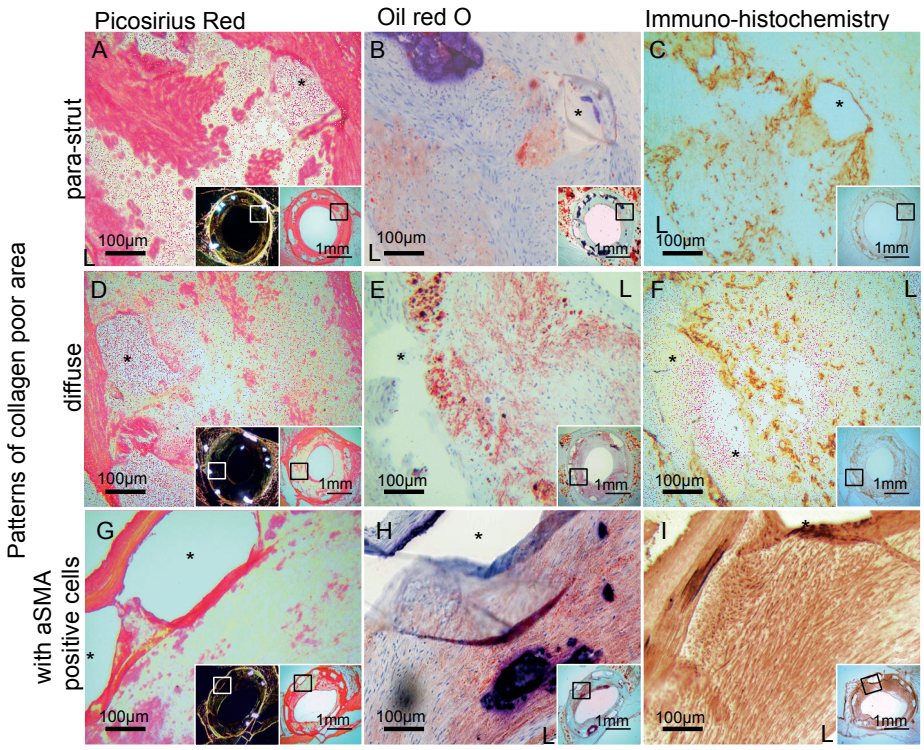

Figure 4 Irregular collagen distribution in the neointima

*Collagen poor areas in peri-strut regions and neointima (A and D; Picrosirius Red) often demonstrated lipid accumulation (B and E; Oil-red-O), and leucocytes (C and F; CD45). Additionally, G (Picrosirius Red) demonstrates a patchy collagen poor lesion with lipid accumulation (H; Oil-red-O) and smooth muscle cells (I; aSMA). *: strut void, L: lumen*

Neoatherosclerosis development following BVS-implantation

Interestingly, considerable neointima formation with complete strut coverage was observed in all swine, independent of the presence of DM. This is relevant, as uncovered struts have been associated with adverse events like stent thrombosis.[23] However, the neointima was highly heterogeneous in all swine, with substantial lipid- and calcium accumulation and lack of intimal organization at 6M, consistent with neoatherosclerosis formation. This is of note, as previously published experimental studies in healthy swine and clinical studies in selected patients demonstrated a favorable vascular response with rather homogeneous coverage following BVS-implantation.[7, 10, 24] We hypothesize that the vascular response observed in our study is likely model specific, and may be caused by a hypersensitive vascular response in relatively young swine, which, in combination with hypercholesterolemia, enhanced lipid- and calcium-accumulation within the scaffolded vessel wall.[25, 26] In humans, calcification is accelerated by young

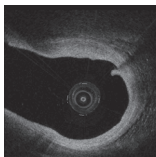

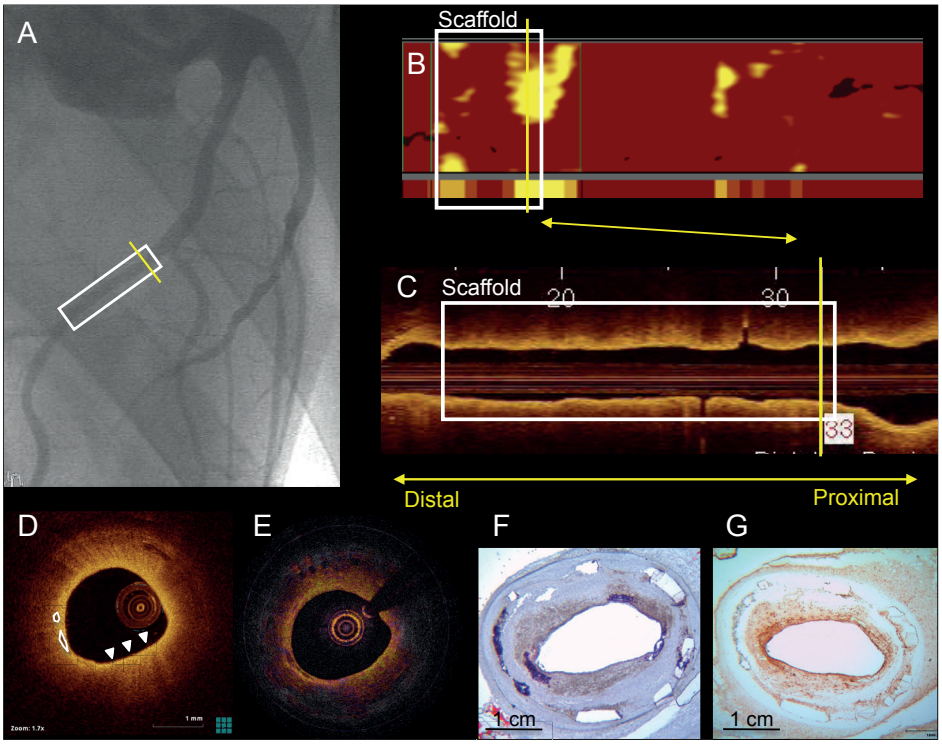

Figure 5 Corresponding QCA, OCT, NIRS and histology at 6M

QCA (A) demonstrates the scaffolded region (white block), with the yellow line indicating the region corresponding to the NIRS, (PS)-OCT and histology images (B to G). The NIRS chemogram demonstrates presence of lipid (B), also observed by OCT (D; arrowheads) that additionally demonstrates the presence of calcium (white circles). The PS-OCT phase retardation image demonstrates a finely grained pattern (E) consistent with lipid-rich neointima (F; Oil-Red-O) and active inflammation (G; CD45)

age and mechanical stress and this might explain why we found such a high incidence in our swine model.[27] Furthermore, scaffold-implantation with an SA-ratio of >1.1 might have caused injury to the endothelium that diminished the vascular wall barrier-function against excessive uptake of circulating lipids, resulting in neoatherosclerosis formation.[25, 28] While it is not completely clear to what extent our observations can be extrapolated to the clinical setting, our observation of considerable neoatherosclerosis formation under diet induced dyslipidemia might point at neoatherosclerosis as an important contributor to BVS failure at long term, similar to that described for DES and BMS.[29, 30] It might also be in line with individual observations of asyptomatic neoplaque rupture after BVS-implantation and recently reported cases of BVS thrombosis.[10, 17, 24, 31]

Neoatherosclerosis characterization by PS-OCT

This study presents the first data of neoatheroasclerotic tissue organization characterized with PS-OCT. We observed enhanced tissue birefringence in areas with SMC alignment in the neointima, as well as in areas with inflammation. Macrophage recruitment in atherosclerosis has been associated with formation of cholesterol crystals [32], which are highly birefringent [33]. The contrast provided by PS-OCT, consisting of birefringence and depolarization, reflects tissue organization, which has an impact on structural plaque stability. A fuller understanding of the features highlighted by PS-OCT may complete our comprehension of neoatherogenesis and its impact on clinical sequelae.

Preserved scaffold integrity

GPC and histology demonstrated preserved scaffold integrity up to 6M after BVS1.1-implantation in all swine, which was not affected by DM or inflammation. This is expected as the scaffold starts losing structural integrity at 3-6 months, and scaffold resorption is driven by hydration, rather than inflammation. Although, theoretically, other factors associated with inflammation such as deregulated acid-base balance or body-temperature could influence scaffold degradation, this was not seen in the present study.[11]

Interestingly, OCT demonstrated morphological changes at individual strut levels despite preserved scaffold integrity. The OCT classification of strut appearances was developed in the ABSORB Cohort A trial to characterize the optical changes of the struts during the process of bioresorption.[9] However, preclinical evaluation of BVS1.0 demonstrated full degradation of the scaffold struts by GPC, while OCT demonstrated the presence of so-called 'preserved black boxes' within the vascular wall.[7] As the OCT signal is arising from the interface of structures with different optical indices, OCT reflects changes of tissue surrounding the struts, rather than changes in strut morphology. This should be kept in mind when interpreting in-vivo clinical and preclinical OCT observations in BVS.

Methodological considerations

Sacrifice was planned for 1/3 of the swine at 3M, and thus the serial BL, 3M and 6M sample size was relatively small. The aim of our study, however, was to longitudinally examine mechanistic and morphological aspects of the coronary response to BVS1.1 in FF-DM and FF-NDM swine. To accurately assess the mechanistic aspects – e.g. scaffold resorption – at various time points, additional planned sacrifice at 3M was

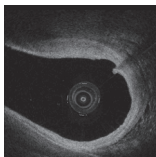

beneficial. Furthermore, atherosclerotic lesions that developed in FF-DM and FF-NDM swine before scaffold-implantation were relatively small. However, distribution and size of the lesions were similar in both groups, allowing for adequate comparison of vascular responses following BVS-implantation between FF-DM and FF-NDM swine.

References

1. Scheen AJ, Warzee F, Legrand VM. Drug-eluting stents: meta-analysis in diabetic patients. Eur Heart J 2004;**25**(23):2167-8; author reply 2168-9.
2. Berry C, Tardif JC, Bourassa MG. Coronary heart disease in patients with diabetes: part I: recent advances in prevention and noninvasive management. J Am Coll Cardiol 2007;**49**(6):631-42.
3. Creager MA, Luscher TF, Cosentino F, Beckman JA. Diabetes and vascular disease: pathophysiology, clinical consequences, and medical therapy: Part I. Circulation 2003;**108**(12):1527-32.
4. Qin SY, Zhou Y, Jiang HX, Hu BL, Tao L, Xie MZ. The association of diabetes mellitus with clinical outcomes after coronary stenting: a meta-analysis. PLoS One 2013;**8**(9):e72710.
5. Oberhauser JP, Hossainy S, Rapoza RJ. Design principles and performance of bioresorbable polymeric vascular scaffolds. EuroIntervention 2009;**5 Suppl F**:F15-22.
6. Gomez-Lara J, Brugaletta S, Diletti R, Garg S, Onuma Y, Gogas BD, van Geuns RJ, Dorange C, Veldhof S, Rapoza R, Whitbourn R, Windecker S, Garcia-Garcia HM, Regar E, Serruys PW. A comparative assessment by optical coherence tomography of the performance of the first and second generation of the everolimus-eluting bioresorbable vascular scaffolds. Eur Heart J 2011;**32**(3):294-304.
7. Onuma Y, Serruys PW, Perkins LE, Okamura T, Gonzalo N, Garcia-Garcia HM, Regar E, Kamberi M, Powers JC, Rapoza R, van Beusekom H, van der Giessen W, Virmani R. Intracoronary optical coherence tomography and histology at 1 month and 2, 3, and 4 years after implantation of everolimus-eluting bioresorbable vascular scaffolds in a porcine coronary artery model: an attempt to decipher the human optical coherence tomography images in the ABSORB trial. Circulation 2010;**122**(22):2288-300.
8. Otsuka F, Pacheco E, Perkins LE, Lane JP, Wang Q, Kamberi M, Frie M, Wang J, Sakakura K, Yahagi K, Ladich E, Rapoza RJ, Kolodgie FD, Virmani R. Long-term safety of an everolimus-eluting bioresorbable vascular scaffold and the cobalt-chromium XIENCE V stent in a porcine coronary artery model. Circ Cardiovasc Interv 2014;**7**(3):330-42.
9. Serruys PW, Ormiston JA, Onuma Y, Regar E, Gonzalo N, Garcia-Garcia HM, Nieman K, Bruining N, Dorange C, Miquel-Hebert K, Veldhof S, Webster M, Thuesen L, Dudek D. A bioabsorbable everolimus-eluting coronary stent system (ABSORB): 2-year outcomes and results from multiple imaging methods. Lancet 2009;**373**(9667):897-910.
10. Serruys PW, Onuma Y, Garcia-Garcia HM, Muramatsu T, van Geuns RJ, de Bruyne B, Dudek D, Thuesen L, Smits PC, Chevalier B, McClean D, Koolen J, Windecker S, Whitbourn R, Meredith I, Dorange C, Veldhof S, Hebert KM, Rapoza R, Ormiston JA. Dynamics of vessel wall changes following the implantation of the Absorb everolimus-eluting bioresorbable vascular scaffold: a multi-imaging modality study at 6, 12, 24 and 36 months. EuroIntervention 2013.
11. Liu L, Li S, Garreau H, Vert M. Selective enzymatic degradations of poly(L-lactide) and poly(epsilon-caprolactone) blend films. Biomacromolecules 2000;**1**(3):350-9.
12. Koopmans SJ, Mroz Z, Dekker R, Corbijn H, Ackermans M, Sauerwein H. Association of insulin resistance with hyperglycemia in streptozotocin-diabetic pigs: effects of metformin at isoenergetic feeding in a type 2-like diabetic pig model. Metabolism 2006;**55**(7):960-71.

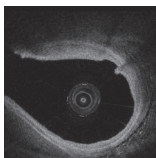

13. Dixon JL, Stoops JD, Parker JL, Laughlin MH, Weisman GA, Sturek M. Dyslipidemia and vascular dysfunction in diabetic pigs fed an atherogenic diet. Arterioscler Thromb Vasc Biol 1999;**19**(12):2981-92.
14. *Guide for the Care and Use of Laboratory Animals, 8th edition*. Washington, DC: National Academies Press (US); 2011.
15. van den Heuvel M, Sorop O, Koopmans SJ, Dekker R, de Vries R, van Beusekom HM, Eringa EC, Duncker DJ, Danser AH, van der Giessen WJ. Coronary microvascular dysfunction in a porcine model of early atherosclerosis and diabetes. Am J Physiol Heart Circ Physiol 2012;**302**(1):H85-94.
16. van Ditzhuijzen NS, Karanasos A, Bruining N, van den Heuvel M, Sorop O, Ligthart J, Witberg K, Garcia-Garcia HM, Zijlstra F, Duncker DJ, van Beusekom HM, Regar E. The impact of Fourier-Domain optical coherence tomography catheter induced motion artefacts on quantitative measurements of a PLLA-based bioresorbable scaffold. Int J Cardiovasc Imaging 2014;**30**(6):1013-26.
17. Serruys PW, Onuma Y, Ormiston JA, de Bruyne B, Regar E, Dudek D, Thuesen L, Smits PC, Chevalier B, McClean D, Koolen J, Windecker S, Whitbourn R, Meredith I, Dorange C, Veldhof S, Miquel-Hebert K, Rapoza R, Garcia-Garcia HM. Evaluation of the second generation of a bioresorbable everolimus drug-eluting vascular scaffold for treatment of de novo coronary artery stenosis: six-month clinical and imaging outcomes. Circulation 2010;**122**(22):2301-12.
18. Ormiston JA, Serruys PW, Regar E, Dudek D, Thuesen L, Webster MW, Onuma Y, Garcia-Garcia HM, McGreevy R, Veldhof S. A bioabsorbable everolimus-eluting coronary stent system for patients with single de-novo coronary artery lesions (ABSORB): a prospective open-label trial. Lancet 2008;**371**(9616):899-907.
19. Kang SJ, Mintz GS, Akasaka T, Park DW, Lee JY, Kim WJ, Lee SW, Kim YH, Whan Lee C, Park SW, Park SJ. Optical coherence tomographic analysis of in-stent neoatherosclerosis after drug-eluting stent implantation. Circulation 2011;**123**(25):2954-63.
20. Nadkarni SK, Pierce MC, Park BH, de Boer JF, Whittaker P, Bouma BE, Bressner JE, Halpern E, Houser SL, Tearney GJ. Measurement of collagen and smooth muscle cell content in atherosclerotic plaques using polarization-sensitive optical coherence tomography. J Am Coll Cardiol 2007;**49**(13):1474-81.
21. Waxman S, Dixon SR, L'Allier P, Moses JW, Petersen JL, Cutlip D, Tardif JC, Nesto RW, Muller JE, Hendricks MJ, Sum ST, Gardner CM, Goldstein JA, Stone GW, Krucoff MW. In vivo validation of a catheter-based near-infrared spectroscopy system for detection of lipid core coronary plaques: initial results of the SPECTACL study. JACC Cardiovasc Imaging 2009;**2**(7):858-68.
22. van Soest G, Regar E, Goderie TP, Gonzalo N, Koljenovic S, van Leenders GJ, Serruys PW, van der Steen AF. Pitfalls in plaque characterization by OCT: image artifacts in native coronary arteries. JACC Cardiovasc Imaging 2011;**4**(7):810-3.
23. Finn AV, Joner M, Nakazawa G, Kolodgie F, Newell J, John MC, Gold HK, Virmani R. Pathological correlates of late drug-eluting stent thrombosis: strut coverage as a marker of endothelialization. Circulation 2007;**115**(18):2435-41.
24. Karanasos A, Simsek C, Gnanadesigan M, van Ditzhuijzen NS, Freire R, Dijkstra J, Tu S, Van Mieghem N, van Soest G, de Jaegere P, Serruys PW, Zijlstra F, van Geuns RJ, Regar E. OCT Assessment of the Long-Term Vascular Healing Response 5 Years After Everolimus-Eluting Bioresorbable Vascular Scaffold. J Am Coll Cardiol 2014;**64**(22):2343-56.

25. Ross R. Atherosclerosis--an inflammatory disease. N Engl J Med 1999;**340**(2):115-26.
26. van Beusekom HM, Post MJ, Whelan DM, de Smet BJ, Duncker DJ, van der Giessen WJ. Metalloproteinase inhibition by batimastat does not reduce neointimal thickening in stented atherosclerotic porcine femoral arteries. Cardiovasc Radiat Med 2003;**4**(4):186-91.
27. Schoen FJ, Levy RJ. Calcification of tissue heart valve substitutes: progress toward understanding and prevention. Ann Thorac Surg 2005;**79**(3):1072-80.
28. van Beusekom HM, Whelan DM, Hofma SH, Krabbendam SC, van Hinsbergh VW, Verdouw PD, van der Giessen WJ. Long-term endothelial dysfunction is more pronounced after stenting than after balloon angioplasty in porcine coronary arteries. J Am Coll Cardiol 1998;**32**(4):1109-17.
29. Nakazawa G, Otsuka F, Nakano M, Vorpahl M, Yazdani SK, Ladich E, Kolodgie FD, Finn AV, Virmani R. The pathology of neoatherosclerosis in human coronary implants bare-metal and drug-eluting stents. J Am Coll Cardiol 2011;**57**(11):1314-22.
30. van Beusekom HM, van der Giessen WJ, van Suylen R, Bos E, Bosman FT, Serruys PW. Histology after stenting of human saphenous vein bypass grafts: observations from surgically excised grafts 3 to 320 days after stent implantation. J Am Coll Cardiol 1993;**21**(1):45-54.
31. Karanasos A, Van Mieghem N, van Ditzhuijzen N, Felix C, Daemen J, Autar A, Onuma Y, Kurata M, Diletti R, Valgimigli M, Kauer F, van Beusekom H, de Jaegere P, Zijlstra F, van Geuns RJ, Regar E. Angiographic and optical coherence tomography insights into bioresorbable scaffold thrombosis: single-center experience. Circ Cardiovasc Interv 2015;**8**(5).
32. Duewell P, Kono H, Rayner KJ, Sirois CM, Vladimer G, Bauernfeind FG, Abela GS, Franchi L, Nunez G, Schnurr M, Espevik T, Lien E, Fitzgerald KA, Rock KL, Moore KJ, Wright SD, Hornung V, Latz E. NLRP3 inflammasomes are required for atherogenesis and activated by cholesterol crystals. Nature 2010;**464**(7293):1357-1361.
33. Ioannou GN, Haigh WG, Thorning D, Savard C. Hepatic cholesterol crystals and crown-like structures distinguish NASH from simple steatosis. Journal of Lipid Research 2013;**54**(5):1326-1334.

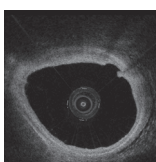

Appendix A - Supplementary Material

Experimental design

Fifteen male [Yorkshire x Landrace] swine with an age of ~11 weeks and a body weight of ~30 kg entered this study. Two weeks after start of the study, diabetes mellitus (DM) was induced in 8 anesthetized swine by a single injection of streptozotocin (140 mg/kg i.v.; Enzo Life Sciences, Raamsdonksveer, The Netherlands). During streptozotocin injection, the swine were anesthetized with intramuscular azaperone 2 mg/kg (Stressnil, Janssen, Tilburg, The Netherlands), followed by intravenous thiopental 15 mg/kg (Nesdonal, Rhone Merieux, Lyon, France). Four weeks after start of the study, all 15 swine started a fast-food diet (FF), which is a diet containing 10% sucrose, 15% fructose, 25% (swine) lard, 1% cholesterol and 0.7% sodiumcholate (bile salts).

Scaffold implantation procedure

Nine months after start of the study, 32 single 3.0 x 18.0mm Bioresorbable Vascular Scaffold (BVS) revision 1.1 (Abbott Vascular, Santa Clara, CA) were implanted via carotid access under the guidance of quantitative coronary angiography (QCA) and optical coherence tomography (OCT). In case of major discrepancy (>0,5mm in diameter lumen) between angiography and OCT, OCT was considered the gold standard for selection of BVS position and sizing. To achieve a stent to artery ratio of ≥ 1.1:1 delivery balloons were inflated with a mean pressure of 12±2 atm according to the measured lumen diameter and the compliance chart of the balloons. One day prior to BVS1.1-implantation the swine received 300 mg acetylsalicylic acid and a loading dose of 300 mg clopidogrel (Plavix, Sanofi). After an overnight fast, the swine were sedated using ketamine/ midazolam (20 mg/kg / 1 mg/kg i.m.) and atropine (1mg/30kg i.m.). After induction of anesthesia with thiopental (15 mg /kg i.v.; Nesdonal, Aventis), the swine were connected to a ventilator that administered a mixture of oxygen and nitrous oxide (1:2 [vol/vol]). Vascular access was obtained with an 8F vascular sheath in the carotid artery, 10.000 IU heparin was administered initially and thereafter 5000 IU of heparin was administered every hour. Anesthesia was maintained using 0.5-2.5 vol% isoflurane (Forence, Abbott Laboratories). Antibiotic prophylaxis was administered by an intramuscular injection of 8 mL 200 mg/mL procaine-benzylpenicillin and 250 mg/mL streptomycin. After scaffold implantation, all swine were treated with acetylsalicylic acid (300mg) and clopidogrel (75mg) daily until the end of the study.

Intracoronary imaging and sacrifice at 3M and 6M

After an overnight fast, the swine were sedated using ketamine/ midazolam (20 mg/ kg/1 mg/kg i.m.) and atropine (1mg/30kg i.m.). Induction of anesthesia was performed using thiopental (15 mg/kg i.v.). Vascular access was obtained with an 8F vascular sheath in the carotid artery, 10.000 IU heparin was administered initially and thereafter 5000 IU of heparin was administered every hour. The swine were connected to a ventilator that administered a mixture of oxygen and nitrous oxide (1:2 [vol/vol]) and anesthesia was maintained using 0.5-2.5 vol% isoflurane. Antibiotic prophylaxis was administered by an intramuscular injection of 8 mL of 200 mg/mL procaine-benzylpenicillin and 250 mg/mL streptomycin. Sacrifice of the swine was performed by an intravenous injection of pentobarbital euthanasia solution (100mg/kg).

Due to the increased weight of the swine at 6M, pentobarbital (5mg/ kg i.m.) instead of ketamine/ midazolam was used for sedation after an overnight fast. Induction of anesthesia was performed as described for the 3 months follow-up but anesthesia was maintained using pentobarbital (5mg/ kg i.m.) and sacrifice of the swine was performed by an intravenous injection of pentobarbital euthanasia solution (100mg/kg).

QCA analysis

S/A ratio was calculated as the maximum balloon diameter during implantation of the scaffold divided by the mean lumen diameter pre-implantation. Acute gain was defined by the difference between mean lumen diameter before scaffold implantation and immediately after scaffold implantation. Late lumen loss was defined by the difference between mean lumen diameter immediately post-implantation and at 3M or 6M.

OCT analysis

OCT analysis of the serial data was performed off-line according to previously published methodology.[1, 2] Before OCT analysis, the Z-offset was checked in all pullbacks and corrected if necessary. The region of interest was defined as the scaffolded segment plus 5mm proximal and 5mm distal from the scaffolded segment. Pre-implantation we measured mean lumen area (LA), EEM area and mean plaque burden (%PB). Contours of the lumen area were obtained with a semi-automated detection algorithm using the LightLab proprietary software for off-line OCT analysis (St. Jude medical, Westford, MA, USA) and additional manual corrections were performed if necessary. Contours of the EEM area were obtained to calculate the mean % plaque burden and were measured by the *multiple point trace* function of the offline OCT analysis software. Mean plaque burden (%PB) was calculated as [(EEM area – LA)/ EEM area] * 100.

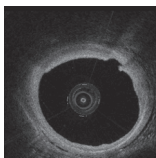

Post-implantation and at 3M and 6M we measured mean lumen area, scaffold area (SA) and incomplete strut apposition (ISA) area. The lumen area can be imaged because of the translucency of the polymeric struts, and is delineated by the endoluminal contour of the vessel wall. Scaffold area is measured by joining the middle point of the abluminal side of the black core of the struts. Incomplete strut apposition (ISA) is defined as a clear separation, by a contrast-filled gap, between the back (abluminal) side of the strut and the vessel wall and ISA area is delineated by the area between the abluminal side of the frame border of the malapposed strut and the endoluminal contour of the vessel wall.[3] In case of complete strut apposition immediately post-implantation, scaffold area is identical to lumen area. In case of prolapse protruding between struts into the lumen immediately post-implantation, the prolapse area was calculated as difference between the lumen area and the scaffold area. A thrombus was identified as an intra-luminal mass, with no direct continuity with the surface of the vessel wall or as a highly backscattered luminal protrusion in continuity with the vessel wall and resulting in signal-free shadowing.[4]

Coverage area (CA) and coverage thickness (CT) were calculated at 3M and 6M. Lumen area is drawn by following the endoluminal contour of the neointima between and on top of the struts. Scaffold area is measured as post-implantation. Due to high heterogeneity of the coverage at follow-up, the contours of the black core area of the scaffold struts could not always be clearly identified. In case the contours of the black core areas could not be traced, the scaffold area contour could be interpolated from a cross-section distal or proximal to the cross-section selected for analysis.

From previous animal studies we know that each polymeric strut is ultimately replaced by proteoglycan and connective tissue, therefore, in order to have a representative measure of the coverage of the lesion treated with BVS, coverage area was defined as [scaffold area – lumen area].[5] To evaluate whether the clearly visible struts were covered or uncovered, the coverage thickness (CT) of these struts was measured as the length between the abluminal border of the black core area of the strut and the lumen contour following the center of gravity of the lumen area.[6] The threshold for coverage is 30 microns of the endoluminal light backscattering frame of the strut.

The morphology the scaffold coverage – defined as [SA – LA], as has been described previously [2] – was described per OCT cross-section as homogeneous or heterogeneous. Homogeneous coverage is defined as coverage that contains uniform optical properties and does not demonstrate focal variations in backscattering pattern and heterogeneous coverage as coverage that contains focally changing optical properties and shows various backscattering patterns. The heterogeneous coverage was

furthermore classified into lipid-laden, calcified or mixed. [7] Lipid-laden coverage was defined as coverage clearly containing signal poor regions with diffusely delineated borders, calcified as coverage clearly containing signal poor regions with sharply delineated borders either present around the struts or subluminal, and mixed coverage was defined as coverage containing both a lipid-laden and calcified appearance (**Supplementary Figure 2; Appendix C**). The presence of calcium was furthermore classified as a) surrounding the struts, defined as calcium located in the abluminal half of the neointima (towards the scaffold struts), and b) subluminal, defined as calcium located in the adluminal half of the neointima (in contact with the luminal arterial wall).

NIRS analysis

The NIRS catheter was advanced distally in the coronary artery over a 0.14inch guide wire through an 8F guiding catheter and pulled back automatically with a pullback speed of 0.5mm/sec. Quantitative NIRS analysis was performed in the region of interest, thus scaffolded segment + 5mm proximal and distal, that was matched between all time-points, using the off-line LipiScan analyzer software. A quantitative lipid-core burden index (LCBI) is provided as a summary metric of the LCP over the scaffolded segment and is computed as a fraction of valid pixels within the scanned region that exceed an LCP probability of 0.6, multiplied by 1000.[8] Moreover, the LCP(+) signal is indicated by yellow in the chemogram when the algorithm indicates there is a high probability of the presence of an LCP of interest.

Ex-vivo degradation analysis

For the GPC-analysis, the initial mass was determined for all scaffolds. As a control, weight-average molecular weight (Mw), number-average molecular weight (Mn) and polydispersity index [PDI = Mw/ Mn] were determined in 5 scaffolds that were not implanted but were from the same batch as the implanted scaffolds. After sacrifice of the swine at 3M and 6M, Mw, Mn, PDI and polymer mass loss [% mass loss = (Initial mass [T=0] – Found mass) / Initial mass [T=0] * 100] were determined for GPC-analysis.

Ex-vivo histological analysis

BVS designated for histology were embedded in tissue-tek (Sakura Finetek, Japan) and frozen in N_2-cooled isopentane (n=17). All tissue sections were stained by Hematoxylin-Eosin (HE) as an overview stain, Resorcin-Fuchsin for elastin, Alcian-Blue for low pH and proteoglycans, Oil-red-O (ORO) for fat, Picrosirius Red (PSR) for collagen, von

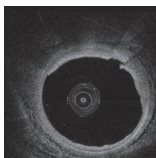

Kossa for calcium, and immunohistochemistry for smooth muscle cells (αSMA, clone 1A4, Dako, the Netherlands) and leukocytes (CD45, clone MCA 1447, AbD Serotec, UK).

Neointimal healing and organization Struts covered with neointima without remnant thrombus or fibrin, were defined as healed. Luminal organization was scored as 2 if present in more than 50% of the circumference with 3 or more layers of SMA positive cells, as 1 if present in less than 50% of the circumference or as 0 if not present at all. Signs of myxoid degeneration were noted.

Neointimal collagen distribution If PSR staining was diminished in bright field and absent under polarized light, tissue was stratified as collagen poor.

Injury and inflammation Injury was scored on Elastin stained sections (Schwartz score). [9] Inflammation around struts was scored using HE, ranking from 0 (no inflammatory cells) to 3 (>20 inflammatory cell per strut) (Cheneau score).

Neointimal calcification Subluminal calcification was scored as present or not. Para-strut calcification was calculated as % calcification-positive struts regardless of severity (100x(calcified struts/total struts)). Severity of para-strut calcification was scored as rank 0 for none, rank 1 for partial rims of circumstrut calcium, rank 2 if extending beyond a rim, and rank 3 when extensive and connecting struts and given as the maximum score per scaffold.

Injury, inflammation and calcification scores were calculated per section as the sum of strut scores divided by the number of struts. Mean scores per segment were averaged per scaffold. Subluminal calcifications and collagen poor areas are given as presence per scaffold.

Lipid accumulation Was documented as the proportion of ORO-positivity within the neointimal area.

References

1. Serruys PW, Onuma Y, Ormiston JA, de Bruyne B, Regar E, Dudek D, Thuesen L, Smits PC, Chevalier B, McClean D, Koolen J, Windecker S, Whitbourn R, Meredith I, Dorange C, Veldhof S, Miquel-Hebert K, Rapoza R, Garcia-Garcia HM. Evaluation of the second generation of a bioresorbable everolimus drug-eluting vascular scaffold for treatment of de novo coronary artery stenosis: six-month clinical and imaging outcomes. Circulation 2010;**122**(22):2301-12.
2. van Ditzhuijzen NS, Karanasos, A., Bruining, N., van den Heuvel, M., Sorop, O., Ligthart, J., Witberg, K., Garcia-Garcia, H.M., Zijlstra, F., Duncker, D.J., van Beusekom, H.M.M., Regar, E. The impact of Fourier-Domain optical coherence tomography catheter induced motion artefacts on quantitative measurements of a PLLA-based bioresorbable scaffold. Accepted in Int J Cardiovasc Imaging 2014.
3. Prati F, Guagliumi G, Mintz GS, Costa M, Regar E, Akasaka T, Barlis P, Tearney GJ, Jang IK, Arbustini E, Bezerra HG, Ozaki Y, Bruining N, Dudek D, Radu M, Erglis A, Motreff P, Alfonso F, Toutouzas K, Gonzalo N, Tamburino C, Adriaenssens T, Pinto F, Serruys PW, Di Mario C. Expert review document part 2: methodology, terminology and clinical applications of optical coherence tomography for the assessment of interventional procedures. Eur Heart J;**33**(20):2513-20.
4. Kume T, Akasaka T, Kawamoto T, Ogasawara Y, Watanabe N, Toyota E, Neishi Y, Sukmawan R, Sadahira Y, Yoshida K. Assessment of coronary arterial thrombus by optical coherence tomography. Am J Cardiol 2006;**97**(12):1713-7.
5. Onuma Y, Serruys PW, Perkins LE, Okamura T, Gonzalo N, Garcia-Garcia HM, Regar E, Kamberi M, Powers JC, Rapoza R, van Beusekom H, van der Giessen W, Virmani R. Intracoronary optical coherence tomography and histology at 1 month and 2, 3, and 4 years after implantation of everolimus-eluting bioresorbable vascular scaffolds in a porcine coronary artery model: an attempt to decipher the human optical coherence tomography images in the ABSORB trial. Circulation 2010;**122**(22):2288-300.
6. Brugaletta S, Radu MD, Garcia-Garcia HM, Heo JH, Farooq V, Girasis C, van Geuns RJ, Thuesen L, McClean D, Chevalier B, Windecker S, Koolen J, Rapoza R, Miquel-Hebert K, Ormiston J, Serruys PW. Circumferential evaluation of the neointima by optical coherence tomography after ABSORB bioresorbable vascular scaffold implantation: can the scaffold cap the plaque? Atherosclerosis 2012;**221**(1):106-12.
7. Kang SJ, Mintz GS, Akasaka T, Park DW, Lee JY, Kim WJ, Lee SW, Kim YH, Whan Lee C, Park SW, Park SJ. Optical coherence tomographic analysis of in-stent neoatherosclerosis after drug-eluting stent implantation. Circulation 2011;**123**(25):2954-63.
8. van Ditzhuijzen NS, van Beusekom HM, Ligthart JM, Regar E. Invasive imaging of the coronary atherosclerotic plaque. Minerva Cardioangiol 2012;**60**(3):305-29.
9. Schwartz RS, Huber KC, Murphy JG, Edwards WD, Camrud AR, Vlietstra RE, Holmes DR. Restenosis and the proportional neointimal response to coronary artery injury: results in a porcine model. J Am Coll Cardiol 1992;**19**(2):267-74.

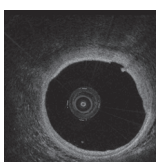

Appendix B - Supplementary Tables

Supplementary Table 1 Quantitative QCA and OCT analysis results

	Pre-procedure			Post-procedure		
	FF-DM	**FF-NDM**	**P***	**FF-DM**	**FF-NDM**	**P***
QCA results						
BVS evaluated	16	14		16	14	
Mean scaffold to artery ratio	-	-	-	1.1±0.1	1.1±0.1	0.20
Mean lumen diameter, mm	2.79±0.19	2.87±0.27	0.33	3.01±0.11	3.03±0.22	0.75
Minimal lumen diameter, mm	-	-	-	-	-	-
Acute gain, mm	-	-	-	0.21±0.13	0.16±0.13	0.22
Late loss, mm	-	-	-	-	-	-
OCT results						
BVS evaluated, n	16	14		16	14	
Mean discernible struts per cross-section, n	-	-	-	8.16±1.57	8.25±0.69	0.90
Mean lumen area, mm^2	7.23±1.42	6.79±1.37	0.46	8.26±0.57	8.27±0.52	0.99
Mean lumen diameter, mm	3.01±0.30	2.92±0.31	0.46	3.23±0.12	3.24±0.10	0.94
Minimal lumen diameter, mm	2.57±0.42	2.53±0.26	0.74	2.76±0.31	2.83±0.28	0.55
Mean scaffold area, mm^2	-	-	-	8.29±0.55	8.31±0.52	0.92
Mean scaffold diameter, mm	-	-	-	3.24±0.11	3.25±0.10	0.85
Mean prolapse area, mm^2 [n]	-	-	-	0.22 (0.04;0.55) [6]	0.29 (0.20;0.35) [10]	0.51
Distal reference lumen area, mm^2	5.60±1.66	5.20±1.51	0.59	4.38±1.27	4.59±1.05	0.66
Proximal reference lumen area, mm^2	8.97±1.99	8.71±1.88	0.72	8.34±194	8.26±2.02	0.91

*Normally distributed data are presented as mean ± SD, non-normally distributed data as median (inter-quartile range). FF-DM = fast-food fed diabetic swine, FF-NDM = fast-food fed non-diabetic swine, QCA = Quantitative coronary angiography, OCT = optical coherence tomography, BVS = bioresorbable vascular scaffold, post = post-implantation, 3M = 3 months follow-up, 6M = 6 months follow-up. *P-value for the comparison between FF-DM and FF-NDM swine, ǂP-value for the difference between post-procedure and 3M, ǂP-value for the difference between 3M and 6M*

3M			6M			P†		P‡	
FF-DM	**FF-NDM**	**P***	**FF-DM**	**FF-NDM**	**P***	**FF-DM**	**FF-NDM**	**FF-DM**	**FF-NDM**
16	14		8	12					
-	-	-	-	-	-	-	-	-	-
1.96±0.21	1.99±0.39	0.82	1.87±0.16	1.90±0.34	0.11	<0.01	<0.01	0.34	0.54
1.61±0.36	1.62±0.44	0.75	1.56±0.26	1.69±0.41	0.46	-	-	0.95	0.83
-	-	-	-	-	-	-	-	-	-
1.05±0.22	1.04±0.30	0.93	1.14±0.20	1.10±0.28	0.78	-	-	0.24	0.65
16	14		7	12		16	14	7	12
7.94±1.07	8.05±0.91	0.72	6.58±1.18	6.65±1.78	0.95	0.66	0.53	0.01	<0.01
3.07±0.59	3.25±1.12	0.64	3.12±0.46	2.85±1.06	0.55	<0.01	<0.01	0.92	<0.01
1.95±0.20	1.99±0.38	0.79	1.97±0.15	1.86±0.37	0.45	<0.01	<0.01	0.97	<0.01
1.53±0.32	1.62±0.27	0.29	1.58±0.19	1.48±0.29	0.34	<0.01	<0.01	0.71	0.01
7.45±0.36	7.32±0.84	0.71	7.17±0.36	7.16±0.94	0.88	<0.01	<0.01	0.19	0.35
3.07±0.08	3.04±0.18	0.70	3.02±0.08	3.01±0.20	0.92	<0.01	<0.01	0.19	0.33
-	-	-	-	-	-	-	-	-	-
4.50±1.32	4.59±1.19	0.81	4.50±0.88	4.01±1.99	0.29	0.34	0.82	0.91	0.02
8.56±2.56	8.03±2.03	0.54	8.42±1.29	6.45±2.80	0.15	0.90	0.60	0.62	0.04

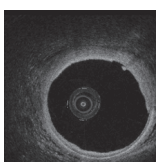

Supplementary Table 2 NIRS analysis results

	Pre-procedure			3M			6M			P§		P‡	
	FF-DM	FF-NDM	P*	FF-DM	FF-NDM	P*	FF-DM	FF-NDM	P*	FF-DM	FF-NDM	FF-DM	FF-NDM
BVS evaluated, n	15	11		15	11		6	8					
LCBI	0.00 (0.00;5.00)	0.00 (0.00;1.00)	0.34	2.00 (0.00;15.50)	0.00 (0.00;3.00)	0.69	17.50 (9.75;26.00)	6.50 (0.00;47.25)	0.49	0.88	0.50	0.80	0.18

NIRS = Near-infrared spectroscopy, LCBI = lipid core burden index. §P-value for the difference between pre-procedure and 3M. Remaining footnotes and abbreviations are as listed in **Table 1**

Supplementary Table 3 OCT strut appearance

	3M			**6M**			**P‡**	
	FF-DM	**FF-NDM**	**P***	**FF-DM**	**FF-NDM**	**P***	**FF-DM**	**FF-NDM**
BVS evaluated, n	16	12		7	12			
Mean discernible struts per cross-section, n	8±1	8±1	0.72	7±1	6±2	0.79	0.01	<0.01
Box classification								
Preserved box, %	79±8	81±11	0.63	77±13	68±17	0.30	0.68	0.05
Open box, %	1.0±1.5	1.1±2.3	0.88	0.3±0.9	1.4±1.3	<0.01	0.29	0.50
Dissolved black box, %	20±8	18±12	0.61	22±14	31±17	0.35	0.53	0.06
Dissolved bright box, %	0	0	-	0	0	-	-	

Percentages are calculated as mean from the total (100%). Footnotes and abbreviations are as listed in Table

Appendix C - Supplementary Figures

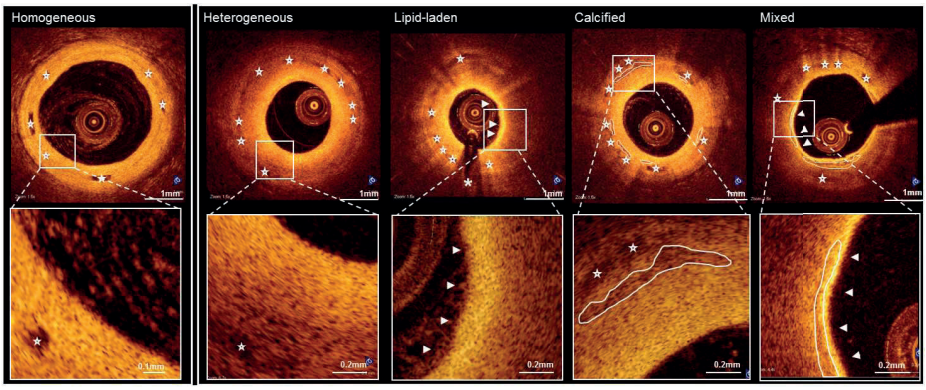

Supplementary Figure 1 Qualitative OCT analysis of the scaffold coverage
In the top OCT cross-sections of a homogeneous, heterogeneous, lipid-laden, calcified and mixed appearance of the coverage are depicted and on the bottom the magnifications. The 'open' stars indicate the black boxes of the scaffold struts at follow-up. The asterix (*) indicates the guide wire artifact. The arrowheads indicate the region containing lipid and the drawn white lines indicate calcified regions

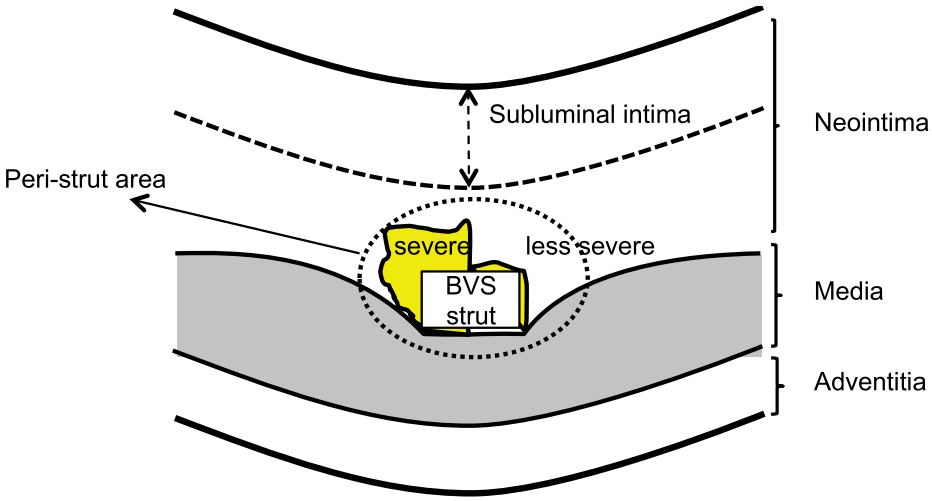

Supplementary Figure 2 Schematic representation of histological regions of interest
Within the neointima, 2 specific regions were discerned: peri-strut neointima, defined as in contact with the struts, and subluminal: located near the lumen

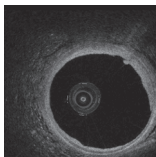

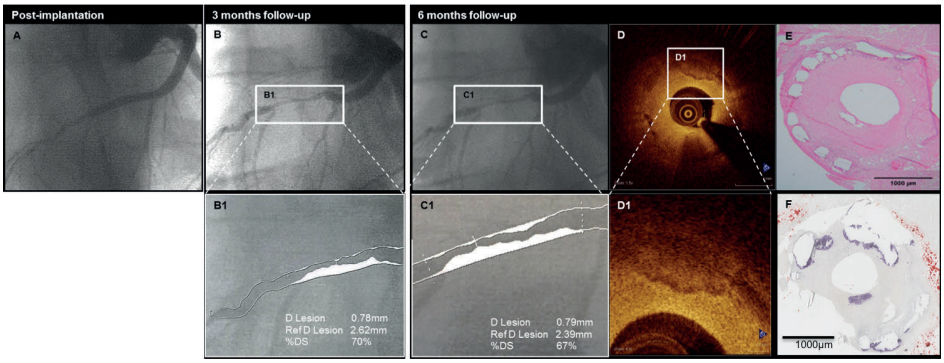

Supplementary Figure 3 Restenosis at 3M

Restenosis of a BVS implanted in an FF-NDM swine at 3M. Coronary angiography post-implantation (A) and at 3M (B) demonstrates a significant lumen loss, with a percentage diameter stenosis (%DS) of 70% which persisted at 6M, (C). At 3M OCT was not performed as the lesion was considered too tight to allow passage of an OCT catheter without risk of causing ischemia and all the potential sequelae thereof. Therefore OCT was restricted to 6M follow-up, the scheduled sacrifice time point. OCT demonstrated a highly heterogeneous neointima (D), which is confirmed by histology demonstrating a large neointimal burden with calcification subluminal and surrounding the struts (E H&E + F, ORO). D Lesion= Diameter of the lesion, Ref D Lesion= Reference diameter

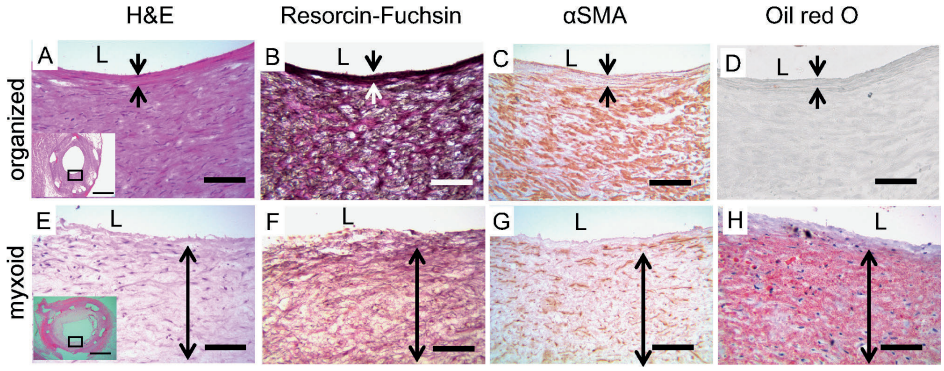

Supplementary Figure 4 Organized and non-organized luminal layers in the neointima

The vessels with well-organized neointimal layers (two arrows in A-D) showed dense elastic fibers (B) with 3 or more layers of αSMA positive cells (C) without lipid accumulation (D). The unorganized neointima showed myxoid degeneration (double arrow in E-H) with disarray and low density of αSMA positive cells (G). In the same area, lipid accumulation was clearly seen (H). αSMA: alpha smooth muscle cell actin, L: lumen, A-D: 3 months DM, E-H: 6 months non-DM, A and E: H&E, B and F: Resorcin-Fuchsin, C and G: αSMA, E and H: Oil red O, Scale bar in A -H: 100 µm, insert bar of A and E: 1000 µm

Supplementary video legends

Video 1 6M OCT pullback of a BVS implanted in a FF-DM swine
OCT imaging at 6M in a FF-DM swine demonstrates a highly heterogeneous appearance of the coverage. The red line in the longitudinal view of the OCT pullback (middle panel) corresponds to the location of the OCT catheter in the 2D pullback (left panel) and 3D pullback (right panel). The asterisk (*) indicates the guidewire artefact, the green line delineates the contour of the lumen area, the stars indicate scaffold struts, the arrowheads lipid, the white circles calcium and the red circle indicates the marker of the scaffold.

Video 2 6M OCT pullback of BVS in an FF-NDM swine
OCT imaging at 6M in an FF-NDM swine demonstrates a highly heterogeneous appearance of the coverage. The red line in the longitudinal view of the OCT pullback (middle panel) corresponds to the location of the OCT catheter in the 2D pullback (left panel) and 3D pullback (right panel). The green line delineates the contour of the lumen area, the stars indicate scaffold struts, the arrowheads lipid and the white circles indicate calcium.

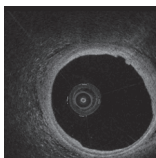

Summary

General discussion

11

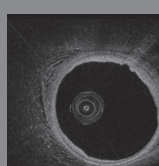

Summary

Coronary artery disease (CAD) is one of the main causes of morbidity and mortality worldwide.[1, 2] Animal models have increased our understanding of the development and treatment of CAD, but there is an ongoing need to further increase our understanding of the disease, especially in more complex situations, such as in a background of diabetes mellitus (DM).[3] Diabetic patients have a 2 to 6 fold higher risk to encounter adverse events associated with CAD than non-diabetic patients.[4] With an expected DM epidemic, a deeper understanding of the development and treatment of CAD is becoming increasingly important.[3] For this purpose, a swine model seems most representative. Moreover, swine can be rendered diabetic mimicking the human situation of multiple co-morbidities, develop atherosclerotic lesions at anatomical locations similar to humans [5-7] and allow for coronary stent-implantation as well as invasive assessment of the coronary vasculature.[8]

Compared to the traditionally used coronary angiography that solely provides a representation of the lumen, invasive imaging techniques such as optical coherence tomography (OCT) and near-infrared spectroscopy (NIRS) enable highly detailed imaging of the coronary morphology and the vascular response to stent-implantation.[9-11] This is important, as understanding the vascular response to stent-implantation can improve CAD treatment. Thorough evaluation of the vascular response to drug-eluting stent (DES) implantation increased our understanding of not only the advantages, but also the disadvantages of DES, such as permanent caging with or without malapposition, jailing of side branches and late stent thrombosis.[12, 13] Consequently, bioresorbable vascular scaffolds (BVS) have been developed in an attempt to overcome these limitations.[12]

This thesis evaluates the development of CAD in a background of diabetes mellitus and the treatment of CAD by BVS, using intracoronary imaging techniques.

Intracoronary imaging of coronary artery disease development

Part I describes the intravascular imaging techniques that can be used to assess coronary atherosclerosis and discusses the safety and methodological considerations of OCT.

A number of catheter-based intravascular imaging techniques have been developed to overcome one of the major limitations of coronary angiography, namely the direct assessment of specific morphological components in the coronary vessel wall.[9-11] In **Chapter 2** the abilities of these intravascular imaging techniques, including intravas-

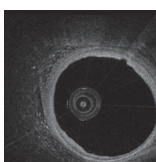

cular ultrasound (IVUS), IVUS-VH, iMAP IVUS, integrated-backscatter-IVUS, OCT, NIRS and angioscopy, to diagnose coronary atherosclerosis and their potential to guide clinical decision-making, are discussed.

Chapter 3 reports on a large single-center registry investigating the safety of intracoronary imaging by OCT in an unselected patient population of 1142 patients with varying indications for imaging. OCT was successfully performed with a low incidence of imaging-related complications (0.6%). This incidence was similar to the incidence of imaging-related complications observed in 2476 patients undergoing IVUS during the same study period in the same center. Importantly, the observed complications were self-limiting after retrieval of the imaging catheter or easily treatable in the catheterization laboratory. These findings indicate that OCT is safe to use in an unselected and heterogeneous group of patients with a very low event rate.

Quantitative OCT analysis can however be complicated by catheter displacement. The impact of longitudinal catheter displacement during image acquisition on the quantitative assessment of BVS is examined in an experimental setting in **Chapter 4**. Variation in the assessment of the imaged scaffold length was high. Although this did not affect global measurements such as mean lumen, mean scaffold and mean coverage area, measurements in specific scaffold regions were affected, hampering serial evaluation of matched cross-sections. Importantly, longitudinal catheter displacement due to coronary artery motion has also been described in humans, suggesting that such quantitative measurements are also vulnerable to errors in human studies.[14] Dedicated analysis methods with per frame analysis or using software allowing for synchronized evaluation of matched segments, could be more suitable for serial analysis in specific scaffold regions in cases with apparent longitudinal catheter displacement.

Preclinical evaluation of coronary artery disease

In **Part II**, animal models used to assess coronary atherosclerosis are discussed and micro- and macrovascular coronary dysfunction and atherosclerosis development is investigated in swine with and without diabetes mellitus.

Several animal models have been used for the evaluation of experimental atherosclerosis. However, most of the studies are performed in transgenic and knockout mice, rats or rabbits, not taking into account the multifactorial nature of the disease. Non-transgenic animal models that more closely mimic human CAD seem more appropriate. In **Chapter 5** several animal models used for the assessment of experimental atherosclerosis are discussed and the preliminary results of a study evaluating CAD development in swine using OCT, IVUS and histology are presented. The presence

of metabolic alterations resulted in coronary lesion development in swine within 9 to 12 months. OCT and IVUS enabled plaque characterization in-vivo in a diseased swine model and proved to be complementary to each other for the evaluation of CAD development, which may be ideal for studying in-vivo CAD development as well as new coronary diagnostic and therapeutic interventions.

In **Chapter 6** the development of CAD was investigated in swine with and without DM using in-vivo OCT, NIRS and coronary computed tomography angiography (CCTA) and ex-vivo vascular function testing and histology. OCT and NIRS enabled the assessment of the gradual development of early atherosclerosis, whereas CCTA was not able to detect the mainly small, non-calcified lesions. Throughout the study, OCT, NIRS, CCTA, vascular function testing and histology demonstrated no differences in early atherosclerosis development between diabetic and non-diabetic swine, suggesting that macroscopic atherosclerosis development was not influenced by hyperglycemia in these swine.

The effect of hyperglycemia and hypercholesterolemia on vascular function of small coronary arteries, e.g. side branches of the main conduit coronary arteries, was investigated in swine in **Chapter 7**. Ex-vivo vascular function testing demonstrated that the balance of the different contributors to vascular tone of small coronary arteries changes during the progression of the atherosclerotic disease in both diabetic and non-diabetic swine. Early in the disease, at 2.5 months follow-up, impaired endothelium-mediated vasodilation in response to bradykinin was compensated by a reduced endothelin-1 (ET-1) dependent vasoconstriction in DM swine, while no alterations in either bradykinin or ET-1 responses were observed in non-DM swine. In contrast, at 15 months follow-up the balance was dominated by increased vasoconstriction to ET-1 in both DM and non-DM swine, while the endothelium-dependent vasodilator mechanisms seemed paradoxically restored in DM swine and were no longer different from non-DM swine. Hence, findings obtained early on in the disease are not a predictor for the future evolution of the dysfunction, emphasizing the importance of longitudinal studies of vascular function in DM and CAD.

Bioresorbable vascular scaffolds for the treatment of coronary artery disease

Part III elaborates on BVS for the treatment of CAD and the vascular response to BVS-implantation is investigated at long-term follow-up in patients, and shorter-term follow-up in diabetic and non-diabetic swine.

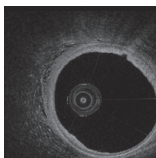

Various types of bioresorbable scaffolds are discussed in **Chapter 8**. Some of them are used in an experimental setting, whereas others are already used in clinical practice. Before BVS can be widely used in clinical practice, it is important to understand the vascular healing response to BVS-implantation. Intravascular imaging by OCT can improve our understanding of the vascular healing response. Therefore, in **Chapter 9,** the vascular healing response 5 years after first-in-man BVS-implantation was investigated by OCT. Implantation of the bioresorbable scaffold led to a restoration of the vascular phenotype at long term by configuration of a non-obstructive plaque, which was created by the consolidation of the underlying plaque, neointima, and resorbed struts. Tissue characterization of the formed 'neo-plaque' was performed both by a human analyst and automated software assessing tissue attenuation. Both assessments were consistent, showing in the majority of cases the formation of a stable plaque with low amount of necrotic core that was covered by a signal-rich tissue layer separating the underlying thrombogenic plaque components from the lumen, potentially shielding the plaque. However, this favorable response was not universal and the observation of a patient with recurrent asymptomatic plaque rupture suggests a need for optimum lesion coverage and continued secondary prevention strategies to optimize vascular healing after BVS-implantation.

Hence, the need to understand the vascular response to BVS-implantation remains, especially in more complex situations. In **Chapter 10**, the vascular response to BVS-implantation was investigated in swine with and without DM. Swine with and without DM, fed a fast-food diet, received single BVS in two or more coronary arteries and were investigated using in-vivo intracoronary OCT, polarization-sensitive (PS)-OCT and NIRS. After sacrifice at either 3 or 6 months after BVS-implantation, ex-vivo histology and polymer degradation analysis were performed. Late lumen loss was relatively high in all swine within 3 months after BVS-implantation (~60%), stabilized from 3 to 6 months follow-up, and demonstrated a highly heterogeneous neointima, suggestive of neoatherosclerosis formation. Between diabetic and non-diabetic swine, no difference was observed, suggesting that neoatherosclerosis developed in these swine, independent of the presence of DM. Although it is not completely clear to what extent these observations can be extrapolated to the clinical arena, the considerable neoatherosclerosis development under diet-induced dyslipidemia may point at neoatherosclerosis as an important contributor to BVS failure at long-term.

Discussion and future outlook

Considerations for the assessment of coronary artery disease

Compared to the traditionally used coronary angiography, intracoronary imaging offers new levels of anatomical detail and new dimensions of information for the diagnosis and treatment of CAD (**Chapter 2**), paving the way to an improved understanding and therapeutic targeting of atherosclerosis.[9-11, 15] However, a routine use of intracoronary imaging in guidance of CAD treatment is currently not supported, although intracoronary imaging is safe (**Chapter 3**) and indications for clinical use were proposed.[16] Further establishment of the indications for clinical application seems warranted and may be accommodated by randomized studies assessing intracoronary imaging versus angiography guidance.

In addition, a number of methodological shortcomings of current analysis techniques should be overcome in order to enhance the prognostic potential of the currently available intracoronary imaging techniques. Our observation in **Chapter 4** that significant errors in the accurate analysis of lumen measurements by intracoronary OCT can occur due to a relatively slow pullback speed and frame rate acquisition of the catheter, suggests that the development of OCT imaging with faster pullback speeds and higher frame rates could help improve such analysis.[17] Additional developments should be aimed at more detailed and user-independent quantitative tissue characterization. OCT, for example, offers possibilities for quantitative tissue characterization by exploiting the optical attenuation coefficient for tissue identification or measure tissue birefringence using polarization sensitive OCT (PS-OCT).[18-20] Dual-modality intracoronary imaging tools, such as a combination of OCT and NIRS or NIRS and IVUS imaging for simultaneous microstructural and molecular imaging, may also improve intracoronary atherosclerosis assessment.[21] Furthermore interesting is the development of photoacoustic imaging. Photoacoustic tomography uses a short-pulsed laser beam to diffusively penetrate into tissue. Upon absorption of the light by the target, photoacoustic waves are generated and used to reconstruct, at ultrasound resolution, the optical absorption distribution that reveals optical contrast.[22, 23] Ongoing development of these new intracoronary imaging techniques that allow for the accurate and longitudinal assessment of structural information of plaques, intraplaque biochemical activity or plaque features at cellular level, may improve our understanding of atherosclerosis development and its therapeutic targets.

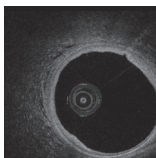

The need for a sophisticated animal model mimicking human-like coronary artery disease

Several animal models for the assessment of atherosclerosis have been discussed in the past decades.[8, 24-28] However, only a few allow evaluation of coronary atherosclerosis that closely resembles coronary atherosclerosis in humans.[29] Besides the porcine diabetes/ hypercholesterolemia model[30] studied by our group, the low-density lipoprotein (LDL) receptor knockout swine, mimicking familial hypercholesterolemia,[31-33] and the more recently developed D374Y-PCSK9 transgenic swine,[28] that exhibit increased plasma LDL levels, demonstrated promising results regarding the assessment of 'human-like' coronary atherosclerosis.[8, 27, 34] However, although swine enable in-vivo longitudinal intracoronary imaging as well as ex-vivo vascular function testing and histological examination of coronary atherosclerosis as demonstrated in **Chapter 6**, conflicting results have been reported regarding the severity of the atherosclerotic disease and the effect of hyperglycemia on the development of coronary atherosclerosis.[5, 28, 30-32, 35] Several factors, including strain difference, age of the swine, duration of the disease, the toxins used to induce diabetes and the type and amount of diet given to the swine may be responsible for the differences observed between the different studies. Moreover, the LDL-receptor knockout swine fed a normal, low calorie, diet demonstrate atheromas by 18 months of age and fully developed coronary atherosclerotic lesions by 24 months of age,[31] whereas the PCSK9 transgenic swine fed a high fat/ high cholesterol diet develop complex progressive human-like coronary atherosclerotic lesions at approximately 12 months of age.[28] Furthermore, in **Chapter 7** we demonstrated a different vascular dysfunction at 2.5 months follow-up than at 15 months follow-up in hypercholesterolemic swine fed a fast-food diet with and without diabetes mellitus, suggesting that the type and amount of vascular dysfunction depends on the time of evaluation. The need to understand what constitutes the most optimal swine model to assess coronary atherosclerosis development remains.[27, 36] A study evaluating several swine strains under different 'atherosclerotic' conditions may improve our understanding of atherosclerosis development in swine, and may help to construct the ideal model to study experimental 'human like' coronary atherosclerosis. Additionally, future studies should consider longitudinal assessment of coronary atherosclerosis development in aging swine with or without diabetes mellitus and include risk factors such as hypertension.

The future of bioresorbable vascular scaffolds

BVS were introduced in an attempt to overcome the limitations of the current gold standard treatment of CAD, namely DES-implantation, which is hampered by permanent caging with or without malapposition, jailing of side branches and late stent thrombosis.[12, 37, 38] In **Chapter 9** we demonstrated that BVS are associated with a favorable healing response at long-term follow-up in a selected group of patients with relatively non-complex lesions. However, clinical studies demonstrating that the vascular healing response following BVS-implantation in an unselected patient population translates into a better clinical outcome at long-term are needed. Although non-inferiority of BVS compared to metallic stents in relatively selected non-complex situations was demonstrated in a number of studies, [39-45] a recent comparison between the BVS and everolimus-eluting DES demonstrated a similar vasomotor reactivity and a larger late luminal loss in the BVS group than the DES group 3 years after implantation.[46] Additionally, conflicting results from registries with several studies demonstrating increased rates of scaffold thrombosis following BVS-implantation in more complex lesions have been reported.[47-50] In the first clinical study assessing the pathomechanisms of BVS thrombosis in-vivo, suboptimal implantation appeared the main substrate for BVS thrombosis, highlighting the need for optimal lesion preparation and possibly for the use of intracoronary imaging techniques to optimize stent implantation.[51] Additionally, we documented neoatherosclerosis development within 3 months after BVS-implantation in swine with and without DM fed a fast-food diet (**Chapter 10**), which may point at neoatherosclerosis as an important contributor to BVS failure at long-term. The distinct healing patterns observed in our preclinical and clinical studies (**Chapter 9 and 10**) need to be better understood. Future studies should consider investigating the use of intracoronary imaging to optimize lesion preparation, sizing of the device and accurate scaffold implantation. Furthermore, larger randomized studies focused on outcome in more complex patient populations are needed to support the use of BVS in complex lesions.

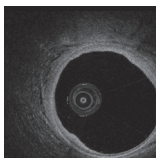

References

1. Roger VL, Go AS, Lloyd-Jones DM, Benjamin EJ, Berry JD, Borden WB, Bravata DM, Dai S, Ford ES, Fox CS, Fullerton HJ, Gillespie C, Hailpern SM, Heit JA, Howard VJ, Kissela BM, Kittner SJ, Lackland DT, Lichtman JH, Lisabeth LD, Makuc DM, Marcus GM, Marelli A, Matchar DB, Moy CS, Mozaffarian D, Mussolino ME, Nichol G, Paynter NP, Soliman EZ, Sorlie PD, Sotoodehnia N, Turan TN, Virani SS, Wong ND, Woo D, Turner MB, American Heart Association Statistics C, Stroke Statistics S. Heart disease and stroke statistics--2012 update: a report from the American Heart Association. Circulation 2012;**125**(1):e2-e220.
2. Murray CJ, Lopez AD. Mortality by cause for eight regions of the world: Global Burden of Disease Study. Lancet 1997;**349**(9061):1269-76.
3. Fox CS, Evans JC, Larson MG, Kannel WB, Levy D. Temporal trends in coronary heart disease mortality and sudden cardiac death from 1950 to 1999: the Framingham Heart Study. Circulation 2004;**110**(5):522-7.
4. Norhammar A, Malmberg K, Diderholm E, Lagerqvist B, Lindahl B, Ryden L, Wallentin L. Diabetes mellitus: the major risk factor in unstable coronary artery disease even after consideration of the extent of coronary artery disease and benefits of revascularization. J Am Coll Cardiol 2004;**43**(4):585-91.
5. Dixon JL, Stoops JD, Parker JL, Laughlin MH, Weisman GA, Sturek M. Dyslipidemia and vascular dysfunction in diabetic pigs fed an atherogenic diet. Arterioscler Thromb Vasc Biol 1999;**19**(12):2981-92.
6. Swindle MM, Makin A, Herron AJ, Clubb FJ, Jr., Frazier KS. Swine as models in biomedical research and toxicology testing. Vet Pathol 2012;**49**(2):344-56.
7. M.M. Swindle DCMaLDP. *Swine as Models in Biomedical Research*: Iowa State University Press, IA; 1992.
8. Granada JF, Kaluza GL, Wilensky RL, Biedermann BC, Schwartz RS, Falk E. Porcine models of coronary atherosclerosis and vulnerable plaque for imaging and interventional research. EuroIntervention 2009;**5**(1):140-8.
9. Hodgson JM, Graham SP, Sheehan H, Savakus AD. Percutaneous intracoronary ultrasound imaging: initial applications in patients. Echocardiography 1990;**7**(4):403-13.
10. Huang D, Swanson EA, Lin CP, Schuman JS, Stinson WG, Chang W, Hee MR, Flotte T, Gregory K, Puliafito CA, et al. Optical coherence tomography. Science 1991;**254**(5035):1178-81.
11. Gardner CM, Tan H, Hull EL, Lisauskas JB, Sum ST, Meese TM, Jiang C, Madden SP, Caplan JD, Burke AP, Virmani R, Goldstein J, Muller JE. Detection of lipid core coronary plaques in autopsy specimens with a novel catheter-based near-infrared spectroscopy system. JACC Cardiovasc Imaging 2008;**1**(5):638-48.
12. Serruys PW, Garcia-Garcia HM, Onuma Y. From metallic cages to transient bioresorbable scaffolds: change in paradigm of coronary revascularization in the upcoming decade? Eur Heart J 2012;**33**(1):16-25b.
13. Ong AT, McFadden EP, Regar E, de Jaegere PP, van Domburg RT, Serruys PW. Late angiographic stent thrombosis (LAST) events with drug-eluting stents. J Am Coll Cardiol 2005;**45**(12):2088-92.
14. Schmidt EJ, Yoneyama R, Dumoulin CL, Darrow RD, Klein E, Kiruluta AJ, Hayase M. 3D coronary motion tracking in swine models with MR tracking catheters. J Magn Reson Imaging 2009;**29**(1):86-98.

15. Wijns W, Shite J, Jones MR, Lee SW, Price MJ, Fabbiocchi F, Barbato E, Akasaka T, Bezerra H, Holmes D. Optical coherence tomography imaging during percutaneous coronary intervention impacts physician decision-making: ILUMIEN I study. Eur Heart J 2015;**36**(47):3346-55.
16. Windecker S, Kolh P, Alfonso F, Collet JP, Cremer J, Falk V, Filippatos G, Hamm C, Head SJ, Juni P, Kappetein AP, Kastrati A, Knuuti J, Landmesser U, Laufer G, Neumann FJ, Richter DJ, Schauerte P, Sousa Uva M, Stefanini GG, Taggart DP, Torracca L, Valgimigli M, Wijns W, Witkowski A. 2014 ESC/EACTS Guidelines on myocardial revascularization: The Task Force on Myocardial Revascularization of the European Society of Cardiology (ESC) and the European Association for Cardio-Thoracic Surgery (EACTS)Developed with the special contribution of the European Association of Percutaneous Cardiovascular Interventions (EAPCI). Eur Heart J 2014;**35**(37):2541-619.
17. Wang T, Wieser W, Springeling G, Beurskens R, Lancee CT, Pfeiffer T, van der Steen AF, Huber R, van Soest G. Intravascular optical coherence tomography imaging at 3200 frames per second. Opt Lett 2013;**38**(10):1715-7.
18. van Soest G, Goderie T, Regar E, Koljenovic S, van Leenders GL, Gonzalo N, van Noorden S, Okamura T, Bouma BE, Tearney GJ, Oosterhuis JW, Serruys PW, van der Steen AF. Atherosclerotic tissue characterization in vivo by optical coherence tomography attenuation imaging. J Biomed Opt 2010;**15**(1):011105.
19. Nadkarni SK, Pierce MC, Park BH, de Boer JF, Whittaker P, Bouma BE, Bressner JE, Halpern E, Houser SL, Tearney GJ. Measurement of collagen and smooth muscle cell content in atherosclerotic plaques using polarization-sensitive optical coherence tomography. J Am Coll Cardiol 2007;**49**(13):1474-81.
20. Giattina SD, Courtney BK, Herz PR, Harman M, Shortkroff S, Stamper DL, Liu B, Fujimoto JG, Brezinski ME. Assessment of coronary plaque collagen with polarization sensitive optical coherence tomography (PS-OCT). Int J Cardiol 2006;**107**(3):400-9.
21. Yoo H, Kim JW, Shishkov M, Namati E, Morse T, Shubochkin R, McCarthy JR, Ntziachristos V, Bouma BE, Jaffer FA, Tearney GJ. Intra-arterial catheter for simultaneous microstructural and molecular imaging in vivo. Nat Med 2011;**17**(12):1680-4.
22. Kumavor PD, Xu C, Aguirre A, Gamelin J, Ardeshirpour Y, Tavakoli B, Zanganeh S, Alqasemi U, Yang Y, Zhu Q. Target detection and quantification using a hybrid hand-held diffuse optical tomography and photoacoustic tomography system. J Biomed Opt 2011;**16**(4):046010.
23. Cai X, Kim C, Pramanik M, Wang LV. Photoacoustic tomography of foreign bodies in soft biological tissue. J Biomed Opt 2011;**16**(4):046017.
24. Shiomi M, Ito T. The Watanabe heritable hyperlipidemic (WHHL) rabbit, its characteristics and history of development: a tribute to the late Dr. Yoshio Watanabe. Atherosclerosis 2009;**207**(1):1-7.
25. Rosenfeld ME, Polinsky P, Virmani R, Kauser K, Rubanyi G, Schwartz SM. Advanced atherosclerotic lesions in the innominate artery of the ApoE knockout mouse. Arterioscler Thromb Vasc Biol 2000;**20**(12):2587-92.
26. Li Y, Fuchimoto D, Sudo M, Haruta H, Lin QF, Takayama T, Morita S, Nochi T, Suzuki S, Sembon S, Nakai M, Kojima M, Iwamoto M, Hashimoto M, Yoda S, Kunimoto S, Hiro T, Matsumoto T, Mitsumata M, Sugitani M, Saito S, Hirayama A, Onishi A. Development of Human-Like Advanced Coronary Plaques in Low-Density Lipoprotein Receptor Knockout Pigs and Justification for Statin Treatment Before Formation of Atherosclerotic Plaques. J Am Heart Assoc 2016;**5**(4):e002779.
27. Shim J, Al-Mashhadi RH, Sorensen CB, Bentzon JF. Large animal models of atherosclerosis--new tools for persistent problems in cardiovascular medicine. J Pathol 2016;**238**(2):257-66.

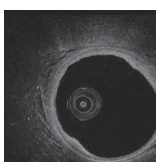

28. Al-Mashhadi RH, Sorensen CB, Kragh PM, Christoffersen C, Mortensen MB, Tolbod LP, Thim T, Du Y, Li J, Liu Y, Moldt B, Schmidt M, Vajta G, Larsen T, Purup S, Bolund L, Nielsen LB, Callesen H, Falk E, Mikkelsen JG, Bentzon JF. Familial hypercholesterolemia and atherosclerosis in cloned minipigs created by DNA transposition of a human PCSK9 gain-of-function mutant. Sci Transl Med 2013;**5**(166):166ra1.
29. Vesselinovitch D. Animal models and the study of atherosclerosis. Arch Pathol Lab Med 1988;**112**(10):1011-7.
30. Gerrity RG, Natarajan R, Nadler JL, Kimsey T. Diabetes-induced accelerated atherosclerosis in swine. Diabetes 2001;**50**(7):1654-65.
31. Hasler-Rapacz J, Ellegren H, Fridolfsson AK, Kirkpatrick B, Kirk S, Andersson L, Rapacz J. Identification of a mutation in the low density lipoprotein receptor gene associated with recessive familial hypercholesterolemia in swine. Am J Med Genet 1998;**76**(5):379-86.
32. Prescott MF, McBride CH, Hasler-Rapacz J, Von Linden J, Rapacz J. Development of complex atherosclerotic lesions in pigs with inherited hyper-LDL cholesterolemia bearing mutant alleles for apolipoprotein B. Am J Pathol 1991;**139**(1):139-47.
33. Davis BT, Wang XJ, Rohret JA, Struzynski JT, Merricks EP, Bellinger DA, Rohret FA, Nichols TC, Rogers CS. Targeted disruption of LDLR causes hypercholesterolemia and atherosclerosis in Yucatan miniature pigs. PLoS One 2014;**9**(4):e93457.
34. Hamamdzic D, Wilensky RL. Porcine models of accelerated coronary atherosclerosis: role of diabetes mellitus and hypercholesterolemia. J Diabetes Res 2013;**2013**:761415.
35. Duff GL, Mc MG. The effect of alloxan diabetes on experimental cholesterol atherosclerosis in the rabbit. J Exp Med 1949;**89**(6):611-30.
36. Iqbal J, Chamberlain J, Francis SE, Gunn J. Role of Animal Models in Coronary Stenting. Ann Biomed Eng 2016;**44**(2):453-65.
37. Otsuka F, Pacheco E, Perkins LE, Lane JP, Wang Q, Kamberi M, Frie M, Wang J, Sakakura K, Yahagi K, Ladich E, Rapoza RJ, Kolodgie FD, Virmani R. Long-term safety of an everolimus-eluting bioresorbable vascular scaffold and the cobalt-chromium XIENCE V stent in a porcine coronary artery model. Circ Cardiovasc Interv 2014;**7**(3):330-42.
38. Raber L, Magro M, Stefanini GG, Kalesan B, van Domburg RT, Onuma Y, Wenaweser P, Daemen J, Meier B, Juni P, Serruys PW, Windecker S. Very late coronary stent thrombosis of a newer-generation everolimus-eluting stent compared with early-generation drug-eluting stents: a prospective cohort study. Circulation 2012;**125**(9):1110-21.
39. Ellis SG, Kereiakes DJ, Metzger DC, Caputo RP, Rizik DG, Teirstein PS, Litt MR, Kini A, Kabour A, Marx SO, Popma JJ, McGreevy R, Zhang Z, Simonton C, Stone GW. Everolimus-Eluting Bioresorbable Scaffolds for Coronary Artery Disease. N Engl J Med 2015;**373**(20):1905-15.
40. Gao R, Yang Y, Han Y, Huo Y, Chen J, Yu B, Su X, Li L, Kuo HC, Ying SW, Cheong WF, Zhang Y, Xu B, Popma JJ, Stone GW. Bioresorbable Vascular Scaffolds Versus Metallic Stents in Patients With Coronary Artery Disease: ABSORB China Trial. J Am Coll Cardiol 2015;**66**(21):2298-309.
41. Kimura T, Kozuma K, Tanabe K, Nakamura S, Yamane M, Muramatsu T, Saito S, Yajima J, Hagiwara N, Mitsudo K, Popma JJ, Serruys PW, Onuma Y, Ying S, Cao S, Staehr P, Cheong WF, Kusano H, Stone GW. A randomized trial evaluating everolimus-eluting Absorb bioresorbable scaffolds vs. everolimus-eluting metallic stents in patients with coronary artery disease: ABSORB Japan. Eur Heart J 2015;**36**(47):3332-42.
42. Sabate M, Windecker S, Iniguez A, Okkels-Jensen L, Cequier A, Brugaletta S, Hofma SH, Raber L, Christiansen EH, Suttorp M, Pilgrim T, Anne van Es G, Sotomi Y, Garcia-Garcia HM,

Onuma Y, Serruys PW. Everolimus-eluting bioresorbable stent vs. durable polymer everolimus-eluting metallic stent in patients with ST-segment elevation myocardial infarction: results of the randomized ABSORB ST-segment elevation myocardial infarction-TROFI II trial. Eur Heart J 2016;**37**(3):229-40.

43. Chevalier B, Onuma Y, van Boven AJ, Piek JJ, Sabate M, Helqvist S, Baumbach A, Smits PC, Kumar R, Wasungu L, Serruys PW. Randomised comparison of a bioresorbable everolimus-eluting scaffold with a metallic everolimus-eluting stent for ischaemic heart disease caused by de novo native coronary artery lesions: the 2-year clinical outcomes of the ABSORB II trial. EuroIntervention 2016;**12**(9):1102-1107.
44. Onuma Y, Sotomi Y, Shiomi H, Ozaki Y, Namiki A, Yasuda S, Ueno T, Ando K, Furuya J, Igarashi K, Kozuma K, Tanabe K, Kusano H, Rapoza R, Popma JJ, Stone GW, Simonton C, Serruys PW, Kimura T. Two-year clinical, angiographic, and serial optical coherence tomographic follow-up after implantation of an everolimus-eluting bioresorbable scaffold and an everolimus-eluting metallic stent: insights from the randomised ABSORB Japan trial. EuroIntervention 2016;**12**(9):1090-1101.
45. Serruys PW, Chevalier B, Dudek D, Cequier A, Carrie D, Iniguez A, Dominici M, van der Schaaf RJ, Haude M, Wasungu L, Veldhof S, Peng L, Staehr P, Grundeken MJ, Ishibashi Y, Garcia-Garcia HM, Onuma Y. A bioresorbable everolimus-eluting scaffold versus a metallic everolimus-eluting stent for ischaemic heart disease caused by de-novo native coronary artery lesions (ABSORB II): an interim 1-year analysis of clinical and procedural secondary outcomes from a randomised controlled trial. Lancet 2015;**385**(9962):43-54.
46. Serruys PW, Chevalier B, Sotomi Y, Cequier A, Carrie D, Piek JJ, Van Boven AJ, Dominici M, Dudek D, McClean D, Helqvist S, Haude M, Reith S, de Sousa Almeida M, Campo G, Iniguez A, Sabate M, Windecker S, Onuma Y. Comparison of an everolimus-eluting bioresorbable scaffold with an everolimus-eluting metallic stent for the treatment of coronary artery stenosis (ABSORB II): a 3 year, randomised, controlled, single-blind, multicentre clinical trial. Lancet 2016.
47. Capodanno D, Joner M, Zimarino M. What about the risk of thrombosis with bioresorbable scaffolds? EuroIntervention 2015;**11 Suppl V**:V181-4.
48. Capodanno D, Gori T, Nef H, Latib A, Mehilli J, Lesiak M, Caramanno G, Naber C, Di Mario C, Colombo A, Capranzano P, Wiebe J, Araszkiewicz A, Geraci S, Pyxaras S, Mattesini A, Naganuma T, Munzel T, Tamburino C. Percutaneous coronary intervention with everolimus-eluting bioresorbable vascular scaffolds in routine clinical practice: early and midterm outcomes from the European multicentre GHOST-EU registry. EuroIntervention 2015;**10**(10):1144-53.
49. Sotomi Y, Suwannasom P, Serruys PW, Onuma Y. Possible Mechanical Causes of Scaffold Thrombosis: Insights from Case Reports with Intracoronary Imaging. EuroIntervention 2016.
50. Cassese S, Byrne RA, Ndrepepa G, Kufner S, Wiebe J, Repp J, Schunkert H, Fusaro M, Kimura T, Kastrati A. Everolimus-eluting bioresorbable vascular scaffolds versus everolimus-eluting metallic stents: a meta-analysis of randomised controlled trials. Lancet 2016;**387**(10018):537-44.
51. Karanasos A, Van Mieghem N, van Ditzhuijzen N, Felix C, Daemen J, Autar A, Onuma Y, Kurata M, Diletti R, Valgimigli M, Kauer F, van Beusekom H, de Jaegere P, Zijlstra F, van Geuns RJ, Regar E. Angiographic and optical coherence tomography insights into bioresorbable scaffold thrombosis: single-center experience. Circ Cardiovasc Interv 2015;**8**(5).

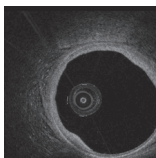

Nederlandse samenvatting

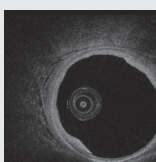

Nederlandse samenvatting

Coronair vaatlijden is één van de meest voorkomende oorzaken van morbiditeit en mortaliteit wereldwijd.[1, 2] Diermodellen hebben onze kennis over de ontwikkeling en behandeling van coronair vaatlijden vergroot. Het is echter belangrijk om onze kennis hierover nog verder te verbreden, met name in meer complexe situaties, zoals in een achtergrond van diabetes mellitus (DM).[3] Patiënten met coronair vaatlijden en DM hebben een 2 tot 6 maal verhoogd risico op een negatieve uitkomst dan patiënten met coronair vaatlijden zonder DM.[4] Met een verwachtte epidemie van DM wordt een betere kennis over de ontwikkeling en behandeling van coronair vaatlijden steeds belangrijker.[3] Voor het onderzoek hiernaar lijkt een varkensmodel het meest representatief. Varkens kunnen diabetisch gemaakt worden, waarbij ze de menselijke situatie kunnen nabootsen met diverse co-morbiditeiten en de ontwikkeling van atherosclerotische laesies op verschillende anatomische locaties.[5-7] Tevens faciliteren ze de implantatie van coronaire stents en staan ze invasieve beeldvorming van de coronair vasculatuur toe.[8]

In vergelijking met de traditioneel gebruikte coronaire angiografie, dat alleen een representatie van het lumen geeft, faciliteren invasieve beeldvormingstechnieken, zoals optische coherentie tomografie (OCT) en near-infrared spectroscopie (NIRS), hoge resolutie beeldvorming van de morfologie van de coronairen en de vasculaire respons van de coronairen na stent-implantatie.[9-11] Dit is belangrijk, omdat het begrijpen van de vasculaire respons na stent-implantatie de behandeling van coronair vaatlijden kan verbeteren.

Gedetailleerde evaluatie van de vasculaire respons na drug-eluting stent (DES) implantatie heeft niet alleen onze kennis vergroot over de voordelen, maar ook over de nadelen van DES, zoals het permanent vastzetten van de vaatwand door het metaal van de stent met of zonder malappositie, het blokkeren van zijtakken en de ontwikkeling van late stent trombose.[12, 13] De bioresorbeerbare vasculaire stent (BVS) is ontwikkeld in een poging de limitaties van DES te omzeilen.[12]

In dit proefschrift wordt de ontwikkeling van coronair vaatlijden in een achtergrond van diabetes mellitus onderzocht en wordt de behandeling van coronair vaatlijden door middel van BVS, met behulp van intracoronaire beeldvorming, onderzocht.

Intracoronaire beeldvorming van coronair atherosclerose

Deel I beschrijft de intravasculaire beeldvormingstechnieken die gebruikt kunnen worden om coronair atherosclerose te onderzoeken en bediscussieerd de veiligheid

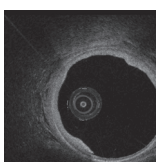

en mogelijke nadelen van het gebruik van de intracoronaire beeldvormingstechniek OCT.

Een aantal intracoronaire beeldvormingstechnieken zijn ontwikkeld om de limitaties van coronair angiografie, zoals de onmogelijkheid om de specifieke componenten van de morfologie van de coronaire vaatwand direct te beoordelen, te omzeilen.[9-11] In **Hoofdstuk 2** worden de mogelijkheden van deze intracoronaire beeldvormingstechnieken, zoals intravascular ultrasound (IVUS), IVUS-VH, iMAP IVUS, integrated-backscatter-IVUS, OCT, NIRS en angioscopie, om coronair vaatlijden te diagnosticeren, besproken.

Hoofdstuk 3 beschrijft een grote single-center registry die de veiligheid en haalbaarheid van intracoronaire beeldvorming met behulp van OCT onderzoekt in een ongeselecteerde patiëntenpopulatie van 1142 patiënten met verscheidene indicaties voor beeldvorming. OCT was succesvol uitgevoerd met een lage incidentie complicaties (0.6%). Deze incidentie was gelijk aan de incidentie complicaties onderzocht in 2476 patiënten die IVUS onderging gedurende dezelfde periode in hetzelfde ziekenhuis. Een belangrijke bevinding bij dit onderzoek is dat de geobserveerde complicaties vanzelf overgingen na het terugtrekken van de katheter of makkelijk te behandelen waren in het katheterisatie laboratorium. Concluderend kan gezegd worden dat de bevindingen in dit onderzoek aantonen dat OCT veilig is in een ongeselecteerde patiëntenpopulatie met een zeer laag percentage complicaties.

Kwantitatieve OCT analyse kan echter bemoeilijkt worden door verplaatsing van de katheter gedurende de beeldvorming. De impact van longitudinale verplaatsing van de katheter op de kwantitatieve analyse van BVS is onderzocht in een experimenteel onderzoek in **Hoofdstuk 4**. De variatie van de gemeten lengte van de BVS was hoog. Hoewel dit niet de globale metingen, zoals de gemiddelde oppervlakte van het lumen, de stent of de weefsel bedekking van de stent beïnvloedde, waren de metingen van specifieke stent regio's wel aangedaan, wat het moeilijker maakte serieel gelijke cross-secties te beoordelen. Belangrijk om te weten is dat longitudinale katheter verplaatsing ook beschreven is in mensen, wat suggereert dat de kwantitatieve analyse van specifieke (stent) locaties ook onderhevig is aan fouten in patiënten.[14] Analysemethoden toegewijd aan het per frame analyseren van de coronairen, of die gesynchroniseerde analyse van segmenten uit dezelfde regio mogelijk maken, zouden meer geschikt kunnen zijn voor de seriële analyse van specifieke stent regio's in gevallen waar duidelijk sprake is van longitudinale katheter verplaatsing.

Preklinische evaluatie van coronair vaatlijden

In **deel II** van dit proefschrift worden diermodellen die gebruikt kunnen worden voor de evaluatie van atherosclerose beschreven en de micro- en macrovasculaire coronaire dysfunctie en atherosclerose ontwikkeling wordt onderzocht in varkens met en zonder DM.

Verschillende diermodellen kunnen worden gebruikt voor de evaluatie van experimentele atherosclerose. Echter, de meeste studies zijn uitgevoerd in transgene of knockout muizen, ratten of konijnen, waarbij geen rekening wordt gehouden met het multifactoriele aspect van de ziekte. Niet-transgene diermodellen die beter het menselijk coronair vaatlijden kunnen nabootsen lijken meer geschikt. In **Hoofdstuk 5** worden verschillende diermodellen die gebruikt kunnen worden voor experimentele atherosclerose beschreven en worden de voorlopige resultaten van een studie die de ontwikkeling van coronair vaatlijden in varkens onderzoekt met behulp van OCT, IVUS en histologie gepresenteerd. De aanwezigheid van metabole veranderingen in de varkens resulteerde in de ontwikkeling van coronaire laesies binnen 9 tot 12 maanden. OCT en IVUS faciliteerden in-vivo plaque karakterisatie in een varkens ziektemodel en lieten zien dat ze complementair aan elkaar gebruikt kunnen worden voor de evaluatie van de ontwikkeling van coronair vaatlijden. Dit kan ideaal zijn voor het in-vivo bestuderen van de ontwikkeling van coronair vaatlijden en voor de ontwikkeling van nieuwe diagnostische en therapeutische interventies.

In **Hoofdstuk 6** wordt de ontwikkeling van coronair vaatlijden bestudeerd in varkens met en zonder DM, waarbij gebruik wordt gemaakt van in-vivo OCT, NIRS en 'coronary computed tomography angiography' (CCTA) en ex-vivo vaatfunctie onderzoek en histologie. OCT en NIRS faciliteerden de evaluatie van de geleidelijke ontwikkeling van vroege coronair atherosclerose, terwijl CCTA niet in staat was de, voornamelijk kleine, niet gecalcificeerde laesies te detecteren. Gedurende de studie lieten OCT, NIRS, CCTA, vaatfunctie onderzoek en histologie geen verschillen zien in de vroege atherosclerose ontwikkeling tussen diabetische en niet-diabetische varkens. Deze bevinding suggereert dat de macroscopisch zichtbare ontwikkeling van atherosclerose in deze varkens niet beïnvloed was door hyperglykemie.

Het effect van hyperglykemie of hypercholesterolemie op de vaatfunctie van de kleine coronairvaten, ofwel de zijtakken van de hoofdtakken van de coronairen, is onderzocht in varkens in **Hoofdstuk 7**. Ex-vivo vaatfunctie onderzoek toonde aan dat de balans van de verschillende factoren die bepalend zijn voor de vaattonus van de kleine coronairen veranderde gedurende de ontwikkeling van coronair atherosclerose in zowel de diabetische als de niet-diabetische varkens. Vroeg in het ziekteproces, 2.5

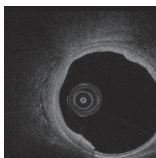

maand na start van de studie, werd een verzwakte endotheel-gemedieerde vasodilatatie in respons op bradykinine gecompenseerd door een verminderde endotheline-1 afhankelijke vasoconstrictie in varkens met DM, terwijl er geen veranderingen werden gezien in de respons op bradykinine of endotheline-1 in varkens zonder DM. In tegenstelling tot de bevindingen bij 2.5 maand, was de balans op 15 maanden na start van de studie voornamelijk gedomineerd door een verhoogde endotheline-1 afhankelijke vasoconstrictie in zowel varkens met als zonder DM, terwijl de endotheel-gemedieerde vasodilatatie paradoxaal leek te zijn hersteld in varkens met DM en nu niet verschillend was van de varkens zonder DM. Uit deze bevindingen kan geconcludeerd worden dat de bevindingen die gedaan zijn vroeg in de studie (2.5 maand) niet voorspellend zijn voor de toekomstige ontwikkeling van de dysfunctie, waardoor het belang van longitudinale studies naar veranderingen van de vaatfunctie in een achtergrond van DM benadrukt wordt.

Bioresorbeerbare stents voor de behandeling van coronair vaatlijden

Deel III van dit proefschrift gaat in op bioresorbeerbare stents die gebruikt kunnen worden voor de behandeling van coronair vaatlijden en de vasculaire respons na BVS-implantatie wordt onderzocht na een lange follow-up in patiënten (5 jaar) en een kortere follow-up (tot 15 maanden) in varkens met en zonder DM.

Verschillende typen bioresorbeerbare stents worden beschreven in **Hoofdstuk 8**. Een aantal van deze stents worden gebruikt in een experimentele setting, terwijl anderen al gebruikt worden in de kliniek. Voordat BVS echter gebruikt kunnen worden in patiënten, is het belangrijk om de vasculaire respons na BVS-implantatie te begrijpen. Intravasculaire beeldvorming met behulp van OCT kan onze kennis over de vasculaire respons na BVS-implantatie vergroten. Daarom is in **Hoofdstuk 9** onderzoek gedaan naar de vasculaire respons 5 jaar na BVS-implantatie in de eerste patiënten die hiermee behandeld zijn. Implantatie van de BVS leidde op lange termijn tot restoratie van het vasculaire fenotype door het ontstaan van een non-obstructieve plaque, welke was gecreëerd door het samenvloeien van de onderliggende plaque, de neointima en de geresorbeerde struts. Weefsel karakterisatie van de 'neo-plaque' die ontstaan was, was gedaan door een menselijk analyst en geautomatiseerde software waarmee weefsel attenuatie geanalyseerd kan worden. De analyses waren consistent en lieten in de meeste gevallen de ontwikkeling van een stabiele plaque met een lage hoeveelheid necrotische kern zien die was beschermd door een weefsellaag met een hoge signaal intensiteit, die de onderliggende thrombogene plaque onderscheidde van het

lumen en daarmee mogelijk de plaque afschermt. Echter niet in alle patiënten werd deze gunstige respons gezien. De observatie van een patiënt met een terugkerende asymptomatische plaque ruptuur versterkte het belang van optimale bescherming van de laesie en het aanhouden van secundaire preventie maatregelen om de vasculaire respons na BVS-implantatie te optimaliseren.

Het blijft belangrijk de vasculaire respons na BVS-implantatie te begrijpen. In **Hoofdstuk 10** wordt de vasculaire respons na BVS-implantatie onderzocht in varkens met en zonder DM. In varkens met en zonder DM, die een ongezond (fast-food) dieet kregen, werden enkele BVS in 2 of 3 van de coronairen geïmplanteerd en onderzocht met behulp van in-vivo intracoronaire OCT, polarization-sensitive (PS)-OCT en NIRS. Na de opoffering van de dieren op 3 of 6 maanden na BVS-implantatie werden ex-vivo histologie en chemische analyse van de degradatie van de polymeer van de scaffold, onderzocht. Late lumen verkleining was relatief hoog in alle varkens binnen 3 maanden na BVS-implantatie (~60%), stabiliseerde tussen 3 en 6 maanden follow-up en toonde een heel heterogene neontima, suggestief voor de ontwikkeling van neoatherosclerose. Tussen varkens met en zonder DM werd er geen verschil geobserveerd. Deze bevinding suggereert dat neoatherosclerose ontwikkeling plaatsvind in varkens op een ongezond dieet, onafhankelijk van de aanwezigheid van DM. Hoewel het nog niet helemaal duidelijk is in welke mate deze bevindingen geëxtrapoleerd kunnen worden naar de klinische setting, is de ontwikkeling van een aanzienlijke hoeveelheid neoatherosclerse die gezien is in deze studie, mogelijk een aanwijzing voor neoathoerscleorose als een belangrijke bijdrager aan het falen van de BVS op lange termijn.

Discussie en toekomstige vooruitzichten

Overwegingen bij de beoordeling van coronair vaatlijden

Vergeleken met de traditioneel gebruikte coronair angiografie, biedt intracoronaire beeldvorming een verbeterd anatomisch detail en informatie over de diagnose en behandeling van coronair vaatlijden (**Hoofdstuk 2**), waardoor betere kennis over therapeutische middelen en atherosclerose ontwikkeling verkregen kan worden.[9-11, 15] Intracoronaire beeldvorming wordt momenteel echter niet routinematig gebruikt voor het bepalen van de juiste behandeling van coronair vaatlijden, hoewel intracoronaire beeldvorming wel veilig is (**Hoofdstuk 3**) en indicaties voor klinisch gebruik zijn voorgesteld. Verdere ontwikkeling van indicaties voor klinisch gebruik lijkt genoodzaakt en kan mogelijk bereikt worden door het uitvoeren van gerandomiseerde studies die de

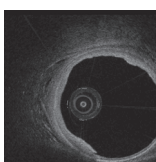

toepassing van intracoronaire beeldvorming vergelijken met coronair angiografie voor het bepalen van de strategie voor behandeling van coronair vaatlijden.[16]

Om het prognostisch potentieel van de momenteel verkrijgbare intracoronaire beeldvormingstechnieken te verhogen, moeten er echter een aantal tekortkomingen van de huidige analyse technieken overwonnen worden. Onze bevindingen in **Hoofdstuk 4** dat er door een te langzame pullback snelheid en lage frame rate van intracoronair OCT significante fouten kunnen voorkomen bij de analyse van specifieke regio's, suggereert dat de ontwikkeling van OCT technieken met een hogere pullback snelheid en hogere frame rate dit soort analyse kan verbeteren.[17] Daarbij zouden nieuwe ontwikkelingen gericht moeten worden op gebruiksvriendelijke kwantitatieve weefsel analyse. OCT faciliteert bijvoorbeeld de mogelijkheid tot verbeterde kwantitatieve weefsel karakterisatie door het gebruik van de optische attenuatie coefficient voor weefsel identificatie of door het meten van het dubbelbrekingseffect van PS-OCT.[18-20] Gecombineerde intracoronaire beeldvormingstechnieken, zoals de combinatie van OCT en NIRS of NIRS en IVUS voor het gelijktijdig gebruik van microstructurele en moleculaire beeldvorming, zouden daarnaast ook de beoordeling van intracoronaire atheroslcerose kunnen verbeteren.[21] Een andere interessante ontwikkeling, zoals de ontwikkeling van foto-akoestische beeldvorming zou ook kunnen bijdragen aan een verbeterde beoordeling van coronair atherosclerose. Foto-akoestische tomografie maakt gebruik van een laserstraal met korte puls om diffuus het weefsel te penetreren. Door absorptie van het licht door het weefsel worden foto-akoestische golven geproduceerd en gebruikt om, met ultrasound resolutie, de distributie van de optische absorptie weer te geven en daarmee het optische contrast aan te tonen.[22, 23] De blijvende ontwikkeling van dit soort nieuwe intracoronaire beeldvormingstechnieken, die accurate en longitudinale beoordeling van structurele informatie van plaques, intraplaque biochemische activiteit of kenmerken van plaques op cellulair niveau mogelijk maken, dragen mogelijk bij aan ons begrip van atherosclerose ontwikkeling en de therapeutische opties.

Het belang van een geavanceerd diermodel dat de menselijke situatie met coronair vaatlijden kan nabootsen

Verscheidene diermodellen zijn de laatste decennia gebruikt voor onderzoek naar de ontwikkeling van atheroslcerose.[8, 24-28] Slechts een aantal van deze diermodellen faciliteren echter de evaluatie van de coronair atherosclerose lijkend op dat in mensen.[29] Naast het varkensmodel met DM en hypercholesterolemie [30] dat onder andere door onze groep bestudeerd wordt, zijn er nog andere varkensmodellen,

zoals de low-density lipoprotein (LDL) receptor knockout varkens, die familiaire hypercholesterolemie nabootsen,[31-33] en de meer recent ontwikkelde D374-PCSK9 transgene varkens, die verhoogde plasma LDL levels hebben,[28] die veelbelovende resultaten laten zien wat betreft het onderzoek naar de ontwikkeling van op het in de mens gelijkende coronair atherosclerose.[8, 27, 34] Hoewel varkens in-vivo longitudinale intracoronaire beeldvorming en ex-vivo vasculair functie onderzoek en histologisch onderzoek van coronair atherosclerose faciliteren, zoals aangegeven in **Hoofdstuk 6**, zijn er tegenstrijdige resultaten gepubliceerd over de ernst van de atherosclerose en het effect van hyperglykemie op de ontwikkeling van coronair atherosclerose.[5, 28, 30-32, 35] Een aantal factoren, waaronder verschillen tussen soort en leeftijd van de varkens, duur van de ziekte, de toxines die gebruikt zijn om DM te induceren en het type en de hoeveelheid dieet dat gegeven wordt aan de varkens, zouden een rol kunnen spelen bij de verschillen die worden gezien tussen de studies. Bijvoorbeeld, de LDL-receptor knockout varkens die een normaal, laag calorisch dieet ontvingen ontwikkelde bij een leeftijd van 18 maanden atheromateuze laesies en bij een leeftijd van 24 maanden atherosclerotische plaques,[31] terwijl de PCSK9 transgene varkens die een dieet ontvingen met een hoog vet en cholesterol gehalte, ontwikkelde bij een leeftijd van 12 maanden complexe, progressieve atherosclerotische plaques, lijkend op de plaques zoals deze gezien worden in mensen.[28] Daarbij hebben wij in **Hoofdstuk 7** laten zien dat er in varkens met hypercholesterolemie met en zonder DM die een 'fast-food' dieet ontvingen, een verschil bestond in de mate van vasculaire dysfunctie tussen een leeftijd van 2.5 maand en 15 maanden. De behoefte te weten wat het beste varkensmodel is om coronair atherosclerose ontwikkeling te onderzoeken blijft.[27, 36] Een studie waarin verschillende varkens soorten worden vergeleken onder verschillende 'atherosclerotische' condities zou hier mogelijk aan kunnen bijdragen en helpt mogelijk bij het ontwikkelen van een varkensmodel dat ideaal is voor onderzoek naar atherosclerose ontwikkeling dat lijkt op dat van de mens. Toekomstige studies zouden tevens kunnen overwegen oudere varkens te gebruiken met of zonder DM met de toevoeging van risicofactoren zoals hypertensie.

De toekomst van bioresorbeerbare vasculaire scaffolds

BVS zijn geïntroduceerd in een poging de limitaties van de huidige gouden standaard behandeling van coronair vaatlijden: DES-implantatie, dat wordt belemmerd door permanent vastzetten van de vaatwand door het metaal van de stent met of zonder malappositie, het bedekken van openingen naar zijtakken en late stent trombose, te omzeilen.[12, 37, 38] In **Hoofdstuk 9** laten we zien dat BVS geassocieerd zijn met een po-

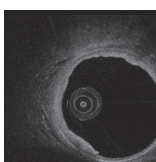

sitieve helingsreactie van de vaatwand na een lange follow-up in een geselecteerde groep patiënten met relatief non-complexe laesies. Er zijn echter klinische studies nodig naar de lange termijn effecten van BVS-implantatie in een niet-geselecteerde patiëntenpopulatie. Hoewel non-inferioriteit is aangetoond van BVS vergeleken met metalen stents in een relatief geselecteerde non-complexe groep patiënten,[39-45] heeft een recente studie aangetoond dat BVS eenzelfde vasomotore reactie toont als everolimus-eluting DES en dat er een grotere lumenverkleining was in de BVS dan de DES groep 3 jaar na implantatie.[46] Daarbij zijn er meerdere registries die verhoogde aantallen scaffold trombose na BVS-implantatie in meer complexe laesies laten zien.[47-50] In de eerste klinische studie waarin het pathomechanisme van BVS trombose in-vivo is onderzocht, leek de meest voorkomende oorzaak voor BVS trombose suboptimale implantatie. Het belang van optimale voorbereiding van de laesie wordt hierdoor benadrukt en intracoronaire beeldvorming zou mogelijk hiervoor en daarmee voor optimale stent-implantatie gebruikt kunnen worden.[51] Tevens hebben we in **Hoofdstuk 10** laten zien dat 3 maanden na BVS-implantatie in varkens op een fast-food dieet met en zonder DM neoatherosclerose ontwikkeling plaatsvind, wat mogelijk een aanwijzing is voor het falen van BVS op langere termijn. Het is van belang dat we de onderscheidende helingspatronen die wij hebben gezien na BVS-implantatie in onze preklinische en klinische studies (**Hoofdstuk 9 en 10**) beter leren begrijpen. Toekomstige studies zouden moeten overwegen onderzoek te doen naar het gebruik van intracoronaire beeldvorming voor het optimaal voorbereiden van een laesie, het uitzoeken van de optimale diameter en lengte van de scaffold en het accuraat plaatsen van de scaffold. Daarbij zijn er grotere gerandomiseerde studies nodig die onderzoek doen naar de uitkomst in meer complexe patientenpopulaties om het gebruik van BVS in complexe laesies te ondersteunen.

Referenties

1. Roger VL, Go AS, Lloyd-Jones DM, Benjamin EJ, Berry JD, Borden WB, Bravata DM, Dai S, Ford ES, Fox CS, Fullerton HJ, Gillespie C, Hailpern SM, Heit JA, Howard VJ, Kissela BM, Kittner SJ, Lackland DT, Lichtman JH, Lisabeth LD, Makuc DM, Marcus GM, Marelli A, Matchar DB, Moy CS, Mozaffarian D, Mussolino ME, Nichol G, Paynter NP, Soliman EZ, Sorlie PD, Sotoodehnia N, Turan TN, Virani SS, Wong ND, Woo D, Turner MB, American Heart Association Statistics C, Stroke Statistics S. Heart disease and stroke statistics--2012 update: a report from the American Heart Association. Circulation 2012;**125**(1):e2-e220.
2. Murray CJ, Lopez AD. Mortality by cause for eight regions of the world: Global Burden of Disease Study. Lancet 1997;**349**(9061):1269-76.
3. Fox CS, Evans JC, Larson MG, Kannel WB, Levy D. Temporal trends in coronary heart disease mortality and sudden cardiac death from 1950 to 1999: the Framingham Heart Study. Circulation 2004;**110**(5):522-7.
4. Norhammar A, Malmberg K, Diderholm E, Lagerqvist B, Lindahl B, Ryden L, Wallentin L. Diabetes mellitus: the major risk factor in unstable coronary artery disease even after consideration of the extent of coronary artery disease and benefits of revascularization. J Am Coll Cardiol 2004;**43**(4):585-91.
5. Dixon JL, Stoops JD, Parker JL, Laughlin MH, Weisman GA, Sturek M. Dyslipidemia and vascular dysfunction in diabetic pigs fed an atherogenic diet. Arterioscler Thromb Vasc Biol 1999;**19**(12):2981-92.
6. Swindle MM, Makin A, Herron AJ, Clubb FJ, Jr., Frazier KS. Swine as models in biomedical research and toxicology testing. Vet Pathol 2012;**49**(2):344-56.
7. M.M. Swindle DCMaLDP. *Swine as Models in Biomedical Research*: Iowa State University Press, IA; 1992.
8. Granada JF, Kaluza GL, Wilensky RL, Biedermann BC, Schwartz RS, Falk E. Porcine models of coronary atherosclerosis and vulnerable plaque for imaging and interventional research. EuroIntervention 2009;**5**(1):140-8.
9. Hodgson JM, Graham SP, Sheehan H, Savakus AD. Percutaneous intracoronary ultrasound imaging: initial applications in patients. Echocardiography 1990;**7**(4):403-13.
10. Huang D, Swanson EA, Lin CP, Schuman JS, Stinson WG, Chang W, Hee MR, Flotte T, Gregory K, Puliafito CA, et al. Optical coherence tomography. Science 1991;**254**(5035):1178-81.
11. Gardner CM, Tan H, Hull EL, Lisauskas JB, Sum ST, Meese TM, Jiang C, Madden SP, Caplan JD, Burke AP, Virmani R, Goldstein J, Muller JE. Detection of lipid core coronary plaques in autopsy specimens with a novel catheter-based near-infrared spectroscopy system. JACC Cardiovasc Imaging 2008;**1**(5):638-48.
12. Serruys PW, Garcia-Garcia HM, Onuma Y. From metallic cages to transient bioresorbable scaffolds: change in paradigm of coronary revascularization in the upcoming decade? Eur Heart J 2012;**33**(1):16-25b.
13. Ong AT, McFadden EP, Regar E, de Jaegere PP, van Domburg RT, Serruys PW. Late angiographic stent thrombosis (LAST) events with drug-eluting stents. J Am Coll Cardiol 2005;**45**(12):2088-92.
14. Schmidt EJ, Yoneyama R, Dumoulin CL, Darrow RD, Klein E, Kiruluta AJ, Hayase M. 3D coronary motion tracking in swine models with MR tracking catheters. J Magn Reson Imaging 2009;**29**(1):86-98.

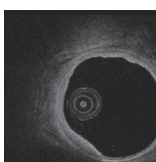

15. Wijns W, Shite J, Jones MR, Lee SW, Price MJ, Fabbiocchi F, Barbato E, Akasaka T, Bezerra H, Holmes D. Optical coherence tomography imaging during percutaneous coronary intervention impacts physician decision-making: ILUMIEN I study. Eur Heart J 2015;**36**(47):3346-55.
16. Windecker S, Kolh P, Alfonso F, Collet JP, Cremer J, Falk V, Filippatos G, Hamm C, Head SJ, Juni P, Kappetein AP, Kastrati A, Knuuti J, Landmesser U, Laufer G, Neumann FJ, Richter DJ, Schauerte P, Sousa Uva M, Stefanini GG, Taggart DP, Torracca L, Valgimigli M, Wijns W, Witkowski A. 2014 ESC/EACTS Guidelines on myocardial revascularization: The Task Force on Myocardial Revascularization of the European Society of Cardiology (ESC) and the European Association for Cardio-Thoracic Surgery (EACTS)Developed with the special contribution of the European Association of Percutaneous Cardiovascular Interventions (EAPCI). Eur Heart J 2014;**35**(37):2541-619.
17. Wang T, Wieser W, Springeling G, Beurskens R, Lancee CT, Pfeiffer T, van der Steen AF, Huber R, van Soest G. Intravascular optical coherence tomography imaging at 3200 frames per second. Opt Lett 2013;**38**(10):1715-7.
18. van Soest G, Goderie T, Regar E, Koljenovic S, van Leenders GL, Gonzalo N, van Noorden S, Okamura T, Bouma BE, Tearney GJ, Oosterhuis JW, Serruys PW, van der Steen AF. Atherosclerotic tissue characterization in vivo by optical coherence tomography attenuation imaging. J Biomed Opt 2010;**15**(1):011105.
19. Nadkarni SK, Pierce MC, Park BH, de Boer JF, Whittaker P, Bouma BE, Bressner JE, Halpern E, Houser SL, Tearney GJ. Measurement of collagen and smooth muscle cell content in atherosclerotic plaques using polarization-sensitive optical coherence tomography. J Am Coll Cardiol 2007;**49**(13):1474-81.
20. Giattina SD, Courtney BK, Herz PR, Harman M, Shortkroff S, Stamper DL, Liu B, Fujimoto JG, Brezinski ME. Assessment of coronary plaque collagen with polarization sensitive optical coherence tomography (PS-OCT). Int J Cardiol 2006;**107**(3):400-9.
21. Yoo H, Kim JW, Shishkov M, Namati E, Morse T, Shubochkin R, McCarthy JR, Ntziachristos V, Bouma BE, Jaffer FA, Tearney GJ. Intra-arterial catheter for simultaneous microstructural and molecular imaging in vivo. Nat Med 2011;**17**(12):1680-4.
22. Kumavor PD, Xu C, Aguirre A, Gamelin J, Ardeshirpour Y, Tavakoli B, Zanganeh S, Alqasemi U, Yang Y, Zhu Q. Target detection and quantification using a hybrid hand-held diffuse optical tomography and photoacoustic tomography system. J Biomed Opt 2011;**16**(4):046010.
23. Cai X, Kim C, Pramanik M, Wang LV. Photoacoustic tomography of foreign bodies in soft biological tissue. J Biomed Opt 2011;**16**(4):046017.
24. Shiomi M, Ito T. The Watanabe heritable hyperlipidemic (WHHL) rabbit, its characteristics and history of development: a tribute to the late Dr. Yoshio Watanabe. Atherosclerosis 2009;**207**(1):1-7.
25. Rosenfeld ME, Polinsky P, Virmani R, Kauser K, Rubanyi G, Schwartz SM. Advanced atherosclerotic lesions in the innominate artery of the ApoE knockout mouse. Arterioscler Thromb Vasc Biol 2000;**20**(12):2587-92.
26. Li Y, Fuchimoto D, Sudo M, Haruta H, Lin QF, Takayama T, Morita S, Nochi T, Suzuki S, Sembon S, Nakai M, Kojima M, Iwamoto M, Hashimoto M, Yoda S, Kunimoto S, Hiro T, Matsumoto T, Mitsumata M, Sugitani M, Saito S, Hirayama A, Onishi A. Development of Human-Like Advanced Coronary Plaques in Low-Density Lipoprotein Receptor Knockout Pigs and Justification for Statin Treatment Before Formation of Atherosclerotic Plaques. J Am Heart Assoc 2016;**5**(4):e002779.

27. Shim J, Al-Mashhadi RH, Sorensen CB, Bentzon JF. Large animal models of atherosclerosis--new tools for persistent problems in cardiovascular medicine. J Pathol 2016;**238**(2):257-66.
28. Al-Mashhadi RH, Sorensen CB, Kragh PM, Christoffersen C, Mortensen MB, Tolbod LP, Thim T, Du Y, Li J, Liu Y, Moldt B, Schmidt M, Vajta G, Larsen T, Purup S, Bolund L, Nielsen LB, Callesen H, Falk E, Mikkelsen JG, Bentzon JF. Familial hypercholesterolemia and atherosclerosis in cloned minipigs created by DNA transposition of a human PCSK9 gain-of-function mutant. Sci Transl Med 2013;**5**(166):166ra1.
29. Vesselinovitch D. Animal models and the study of atherosclerosis. Arch Pathol Lab Med 1988;**112**(10):1011-7.
30. Gerrity RG, Natarajan R, Nadler JL, Kimsey T. Diabetes-induced accelerated atherosclerosis in swine. Diabetes 2001;**50**(7):1654-65.
31. Hasler-Rapacz J, Ellegren H, Fridolfsson AK, Kirkpatrick B, Kirk S, Andersson L, Rapacz J. Identification of a mutation in the low density lipoprotein receptor gene associated with recessive familial hypercholesterolemia in swine. Am J Med Genet 1998;**76**(5):379-86.
32. Prescott MF, McBride CH, Hasler-Rapacz J, Von Linden J, Rapacz J. Development of complex atherosclerotic lesions in pigs with inherited hyper-LDL cholesterolemia bearing mutant alleles for apolipoprotein B. Am J Pathol 1991;**139**(1):139-47.
33. Davis BT, Wang XJ, Rohret JA, Struzynski JT, Merricks EP, Bellinger DA, Rohret FA, Nichols TC, Rogers CS. Targeted disruption of LDLR causes hypercholesterolemia and atherosclerosis in Yucatan miniature pigs. PLoS One 2014;**9**(4):e93457.
34. Hamamdzic D, Wilensky RL. Porcine models of accelerated coronary atherosclerosis: role of diabetes mellitus and hypercholesterolemia. J Diabetes Res 2013;**2013**:761415.
35. Duff GL, Mc MG. The effect of alloxan diabetes on experimental cholesterol atherosclerosis in the rabbit. J Exp Med 1949;**89**(6):611-30.
36. Iqbal J, Chamberlain J, Francis SE, Gunn J. Role of Animal Models in Coronary Stenting. Ann Biomed Eng 2016;**44**(2):453-65.
37. Otsuka F, Pacheco E, Perkins LE, Lane JP, Wang Q, Kamberi M, Frie M, Wang J, Sakakura K, Yahagi K, Ladich E, Rapoza RJ, Kolodgie FD, Virmani R. Long-term safety of an everolimus-eluting bioresorbable vascular scaffold and the cobalt-chromium XIENCE V stent in a porcine coronary artery model. Circ Cardiovasc Interv 2014;**7**(3):330-42.
38. Raber L, Magro M, Stefanini GG, Kalesan B, van Domburg RT, Onuma Y, Wenaweser P, Daemen J, Meier B, Juni P, Serruys PW, Windecker S. Very late coronary stent thrombosis of a newer-generation everolimus-eluting stent compared with early-generation drug-eluting stents: a prospective cohort study. Circulation 2012;**125**(9):1110-21.
39. Ellis SG, Kereiakes DJ, Metzger DC, Caputo RP, Rizik DG, Teirstein PS, Litt MR, Kini A, Kabour A, Marx SO, Popma JJ, McGreevy R, Zhang Z, Simonton C, Stone GW. Everolimus-Eluting Bioresorbable Scaffolds for Coronary Artery Disease. N Engl J Med 2015;**373**(20):1905-15.
40. Gao R, Yang Y, Han Y, Huo Y, Chen J, Yu B, Su X, Li L, Kuo HC, Ying SW, Cheong WF, Zhang Y, Xu B, Popma JJ, Stone GW. Bioresorbable Vascular Scaffolds Versus Metallic Stents in Patients With Coronary Artery Disease: ABSORB China Trial. J Am Coll Cardiol 2015;**66**(21):2298-309.
41. Kimura T, Kozuma K, Tanabe K, Nakamura S, Yamane M, Muramatsu T, Saito S, Yajima J, Hagiwara N, Mitsudo K, Popma JJ, Serruys PW, Onuma Y, Ying S, Cao S, Staehr P, Cheong WF, Kusano H, Stone GW. A randomized trial evaluating everolimus-eluting Absorb bioresorbable scaffolds vs. everolimus-eluting metallic stents in patients with coronary artery disease: ABSORB Japan. Eur Heart J 2015;**36**(47):3332-42.

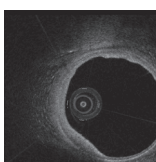

42. Sabate M, Windecker S, Iniguez A, Okkels-Jensen L, Cequier A, Brugaletta S, Hofma SH, Raber L, Christiansen EH, Suttorp M, Pilgrim T, Anne van Es G, Sotomi Y, Garcia-Garcia HM, Onuma Y, Serruys PW. Everolimus-eluting bioresorbable stent vs. durable polymer everolimus-eluting metallic stent in patients with ST-segment elevation myocardial infarction: results of the randomized ABSORB ST-segment elevation myocardial infarction-TROFI II trial. Eur Heart J 2016;**37**(3):229-40.
43. Chevalier B, Onuma Y, van Boven AJ, Piek JJ, Sabate M, Helqvist S, Baumbach A, Smits PC, Kumar R, Wasungu L, Serruys PW. Randomised comparison of a bioresorbable everolimus-eluting scaffold with a metallic everolimus-eluting stent for ischaemic heart disease caused by de novo native coronary artery lesions: the 2-year clinical outcomes of the ABSORB II trial. EuroIntervention 2016;**12**(9):1102-1107.
44. Onuma Y, Sotomi Y, Shiomi H, Ozaki Y, Namiki A, Yasuda S, Ueno T, Ando K, Furuya J, Igarashi K, Kozuma K, Tanabe K, Kusano H, Rapoza R, Popma JJ, Stone GW, Simonton C, Serruys PW, Kimura T. Two-year clinical, angiographic, and serial optical coherence tomographic follow-up after implantation of an everolimus-eluting bioresorbable scaffold and an everolimus-eluting metallic stent: insights from the randomised ABSORB Japan trial. EuroIntervention 2016;**12**(9):1090-1101.
45. Serruys PW, Chevalier B, Dudek D, Cequier A, Carrie D, Iniguez A, Dominici M, van der Schaaf RJ, Haude M, Wasungu L, Veldhof S, Peng L, Staehr P, Grundeken MJ, Ishibashi Y, Garcia-Garcia HM, Onuma Y. A bioresorbable everolimus-eluting scaffold versus a metallic everolimus-eluting stent for ischaemic heart disease caused by de-novo native coronary artery lesions (ABSORB II): an interim 1-year analysis of clinical and procedural secondary outcomes from a randomised controlled trial. Lancet 2015;**385**(9962):43-54.
46. Serruys PW, Chevalier B, Sotomi Y, Cequier A, Carrie D, Piek JJ, Van Boven AJ, Dominici M, Dudek D, McClean D, Helqvist S, Haude M, Reith S, de Sousa Almeida M, Campo G, Iniguez A, Sabate M, Windecker S, Onuma Y. Comparison of an everolimus-eluting bioresorbable scaffold with an everolimus-eluting metallic stent for the treatment of coronary artery stenosis (ABSORB II): a 3 year, randomised, controlled, single-blind, multicentre clinical trial. Lancet 2016.
47. Capodanno D, Joner M, Zimarino M. What about the risk of thrombosis with bioresorbable scaffolds? EuroIntervention 2015;**11 Suppl V**:V181-4.
48. Capodanno D, Gori T, Nef H, Latib A, Mehilli J, Lesiak M, Caramanno G, Naber C, Di Mario C, Colombo A, Capranzano P, Wiebe J, Araszkiewicz A, Geraci S, Pyxaras S, Mattesini A, Naganuma T, Munzel T, Tamburino C. Percutaneous coronary intervention with everolimus-eluting bioresorbable vascular scaffolds in routine clinical practice: early and midterm outcomes from the European multicentre GHOST-EU registry. EuroIntervention 2015;**10**(10):1144-53.
49. Sotomi Y, Suwannasom P, Serruys PW, Onuma Y. Possible Mechanical Causes of Scaffold Thrombosis: Insights from Case Reports with Intracoronary Imaging. EuroIntervention 2016.
50. Cassese S, Byrne RA, Ndrepepa G, Kufner S, Wiebe J, Repp J, Schunkert H, Fusaro M, Kimura T, Kastrati A. Everolimus-eluting bioresorbable vascular scaffolds versus everolimus-eluting metallic stents: a meta-analysis of randomised controlled trials. Lancet 2016;**387**(10018):537-44.
51. Karanasos A, Van Mieghem N, van Ditzhuijzen N, Felix C, Daemen J, Autar A, Onuma Y, Kurata M, Diletti R, Valgimigli M, Kauer F, van Beusekom H, de Jaegere P, Zijlstra F, van Geuns

RJ, Regar E. Angiographic and optical coherence tomography insights into bioresorbable scaffold thrombosis: single-center experience. Circ Cardiovasc Interv 2015;**8**(5).

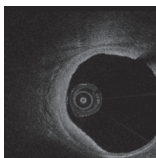

Curriculum vitae

PhD Portfolio

Publicatielijst

Dankwoord

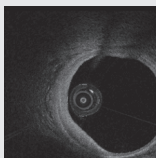

Curriculum vitae

Nienke Simone van Ditzhuijzen was born on November 1st, 1988 in Utrecht, the Netherlands. In 2006 she graduated from secondary school (Gymnasium, Nature & Health, Het Nieuwe Lyceum, Bilthoven) and started medical school at the Erasmus University Medical Center (Erasmus MC) in Rotterdam.

In November 2010 she graduated from the preclinical years of medical school after she successfully performed her elective research at the Harrington McLaughlin Cardiovascular Institute in Cleveland, Ohio, under supervision of Prof. Dr. W.J. van der Giessen from the Erasmus MC and Prof. Dr. M. Costa from the Case Western Reserve University in Cleveland, Ohio. Hereafter, she initiated her PhD project entitled "Coronary Artery Disease – Assessing the development and treatment of coronary atherosclerosis" at the divisions of experimental and interventional cardiology of the department of cardiology, thoraxcenter, Erasmus MC, Rotterdam under supervision of Prof. Dr. W.J. van der Giessen, which was, due to his unfortunate decease, later taken over by Prof. Dr. F. Zijlstra, Prof. Dr. D.J.G.M. Duncker and Dr. E. Regar.

During her PhD project, she investigated, by using intracoronary imaging techniques, the development of coronary atherosclerosis and the vascular response to bioresorbable scaffold implantation as treatment of coronary atherosclerosis in coronary arteries of swine with and without diabetes mellitus. Additionally, she co-authored several preclinical and clinical research papers, investigating intracoronary imaging techniques, coronary artery disease and the treatment of coronary artery disease.

In January 2015 she started her medical internships and on February 24th 2017 she obtained the degree of medical doctor at the Erasmus MC in Rotterdam. Currently, she is working as a resident (ANIOS) at the department of Surgery of the St. Antonius hospital in Nieuwegein.

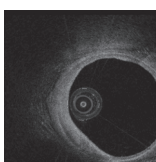

PhD Portfolio

Name PhD student: Nienke Simone van Ditzhuijzen	PhD period: Nov 2010 – May 2017
Erasmus MC Department: Cardiology	Promotor(s): Prof. Dr. F. Zijlstra
Research School: COEUR	Prof. Dr. D.J. Duncker
	Supervisor: Dr. E. Regar

1. PhD training

	Year	Workload (ECTS)
General academic skills		
- Biomedical English Writing and Communication	Aug/Sept 2011	4
- Laboratory animal science	Sept 2011	4.5
Research skills		
- Statistics: Biostatistical methods I: Basic principles (CCO2)	Sept/Okt 2012	5.7
- BROK course	Nov 2012	0.7
In-depth courses (e.g. Research school, Medical Training)		
- IVUS course 1.5 days 09.00-18.00	9 sept 2010	0.5
- OCT course 1.5 days 09.00 – 18.00	7 okt 2010	0.5
- CPO minicourse 09.00 – 17.00 "Methodologie voor patientgebonden Onderzoek en Voorbereiding van Subsidieaanvragen"	15 feb 2011	0.3
- COEUR Course Cardiovascular Medicine	17/18 nov 2011	1.5
- COEUR Course Pathophysiology of ischemic heart disease	9 feb 2012	1.5
- OCT course 1 day 09:00 – 18:00	30 okt 2012	0.3
- NHS Papendal PhD training course "Cardiac Function"	30 sept – 04 okt 2013	2.0
International conferences		
- Cardiovascular Conference (2 days 09.00 – 17.00)	17-18 mrt 2011	0.6
- Transcatheter Cardiovascular Therapeutics (TCT) Conference, 2011	7-11 nov 2011	1.5
- Optics in Cardiology 2011, Rotterdam	1-2 dec 2011	0.6
- NVVC conference	Apr 2012	0.3
- European Society of Cardiology (ESC) conference, Munich, 2012	25-29 Aug 2012	1.5
- Optics in Cardiology 2012, Rotterdam	21-22 Mrt 2013	0.6
- EuroPCR congress, Paris, 2013	21-24 May 2013	1.5
- European Society of Cardiology (ESC) conference, Amsterdam, 2013	31 Aug – 4 Sept 2013	1.5
- American Heart Association conference, Dallas, 2013	16-20 Nov 2013	1.5
- Transcatheter Cardiovascular Therapeutics (TCT) conference, Washington, 2014	13-17 Sept 2014	1.5
Seminars and workshops		
- Coeur seminars	2010 – 2013	2.5

Other

- Abbott symposium (2 days 09.00 – 17.00)	10/11 mrt 2011	0.6
- EUR PhD day 10.00 – 16.00	15 apr 2011	0.4
- Symposium Microcirculation in Health and Disease (9.00-12.00)	28 apr 2011	0.1
- PcR focusgroup Abbott BVS 2012	Mrt 2012	0.6
- Erasmus MC PhD day	Jun 2012	0.1

2. Teaching activities

	Year	**Workload (ECTS)**
Supervising		
- 2nd year review	2013	0.5
- Msc and Bsc studens	2012 - 2013	6

3. Awards and grants

	Year	
Awards		
- Dirk Durrer prize	2011	
Grants		
- European Society of Cardiology (ESC) Council on Basic Cardiovascular Science grant for travel to the ESC conference in Munich	2012	
- Erasmus Trustfund grant for travel to the American Heart Association conference in Dallas	2013	
	Total ECTS	43.4

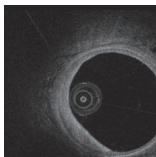

List of publications

Original & peer-reviewed papers

1. Gnanadesigan M, Kameyama T, Karanasos A, **van Ditzhuijzen NS**, van der Sijde JN, van Geuns RJ, Ligthart J, Witberg K, Ughi GJ, van der Steen AF, Regar E, van Soest G. Automated characterisation of lipid core plaques in vivo by quantitative optical coherence tomography tissue type imaging. EuroIntervention. 2016 Dec 20;12(12):1490-1497. doi: 10.4244/EIJ-D-15-00320
2. **N.S. van Ditzhuijzen**, M. van den Heuvel, O. Sorop, A. Rossi, N. Bruining, S. Roest, J. Ligthart, K. Witberg, F. Zijlstra, D.J. Duncker, H.M.M. van Beusekom, E. Regar. Serial coronary imaging of early atherosclerosis development in fast-food fed diabetic and non-diabetic swine. *JACC: Basic to Transl Scie Vol.1 No.6 Oct 2016:449-6. doi:* 10.1016/j.jacbts.2016.08.006
3. Diletti R, Ishibashi Y, Felix C, Onuma Y, Nakatani S, van Mieghem NM, Regar E, Valgimigli M, de Jaegere PP, **van Ditzhuijzen N**, Fam JM, Ligthart JM, Lenzen MJ, Serruys PW, Zijlstra F, Jan van Geuns R. Expanded clinical use of everolimus eluting bioresorbable vascular scaffolds for treatment of coronary artery disease. *Catheter Cardiovasc Interv. 2016 Nov 29. doi: 10.1002/ccd.26832. [Epub ahead of print]*
4. Sorop O, van den Heuvel M, **van Ditzhuijzen NS**, de Beer VJ, Heinonen I, van Duin RW, Zhou Z, Koopmans SJ, Merkus D, van der Giessen W, Danser AH, Duncker DJ. Coronary microvascular dysfunction after long-term diabetes and hypercholesterolemia. Am J Physiol Heart Circ Physiol. 2016 Sep 2:ajpheart.00458.2015. doi: 10.1152/ajpheart.00458.2015. [Epub ahead of print]
5. Hoogendoorn A, Gnanadesigan M, Zahnd G, **van Ditzhuijzen NS**, Schuurbiers JC, van Soest G, Regar E, Wentzel JJ. *OCT-measured plaque free wall angle is indicative for plaque burden: overcoming the main limitation of OCT?* Int J Cardiovasc Imaging. 2016 Jul 20. [Epub ahead of print]
6. De Paolis M, Felix C, **van Ditzhuijzen N**, Fam JM, Karanasos A, de Boer S, van Mieghem NM, Daemen J, Costa F, Bergoli LC, Ligthart JM, Regar E, de Jaegere PP, Zijlstra F, van Geuns RJ, Diletti R. *Everolimus-eluting bioresorbable vascular scaffolds implanted in coronary bifurcation lesions: Impact of polymeric wide struts on side-branch impairment.* Int J Cardiol. 2016 Jun 25;221:656-664. doi: 10.1016/j.ijcard.2016.06.153.
7. Prabhu D, Mehanna E, Gargesha M, Wen D, Brandt E, **van Ditzhuijzen NS**, Chamie D, Yamamoto H, Fujino Y, Farmazilian A, Patel J, Costa M, Bezerra HG, Wilson DL. *3D registration of intravascular optical coherence tomography and cryo-image volumes for microscopic-resolution validation.* Proc SPIE Int Soc Opt Eng. 2016 Feb 27;9788. pii: 97882C. Epub 2016 Mar 29
8. van der Sijde JN, Karanasos A, **van Ditzhuijzen NS**, Okamura T, van Geuns RJ, Valgimigli M, Ligthart JM, Witberg KT, Wemelsfelder S, Fam JM, Zhang B, Diletti R, de Jaegere PP, van Mieghem NM, van Soest G, Zijlstra F, van Domburg RT, Regar E. *Safety of optical coherence tomography in daily practice: a comparison with intravascular ultrasound.* Eur Heart J Cardiovasc Imaging. 2016 Mar 18
9. Schrauwen JT, Karanasos A, **van Ditzhuijzen NS**, Aben JP, van der Steen AF, Wentzel JJ, Gijsen FJ.*Influence of the Accuracy of Angiography-Based Reconstructions on Velocity and Wall Shear Stress Computations in Coronary Bifurcations: A Phantom Study.* PLoS One. 2015 Dec 21;10(12):e0145114. doi: 10.1371/journal.pone.0145114. eCollection 2015

10. Karanasos A, Van Mieghem N, **van Ditzhuijzen N**, Felix C, Daemen J, Autar A, Onuma Y, Kurata M, Diletti R, Valgimigli M, Kauer F, van Beusekom H, de Jaegere P, Zijlstra F, van Geuns RJ, Regar E. *Angiographic and optical coherence tomography insights into bioresorbable scaffold thrombosis: single-center experience.* Circ Cardiovasc Interv. 2015 May;8(5). pii: e002369
11. Khairoun M, van den Heuvel M, van den Berg BM, Sorop O, de Boer R, **van Ditzhuijzen NS**, Bajema IM, Baelde HJ, Zandbergen M, Duncker DJ, Rabelink TJ, Reinders ME, van der Giessen WJ, Rotmans JI. *Early systemic microvascular damage in pigs with atherogenic diabetes mellitus coincides with renal angiopoietin dysbalance.* PLoS One. 2015 Apr 24;10(4):e0121555
12. **van Ditzhuijzen NS**, Regar E. *Shedding light on in-stent restenosis: are bioresorbable vascular scaffolds the solution for a vexing problem?* Can J Cardiol. 2015 Mar;31(3):253-4
13. Karanasos A, Simsek C, Gnanadesigan M, **van Ditzhuijzen NS**, Freire R, Dijkstra J, Tu S, Van Mieghem N, van Soest G, de Jaegere P, Serruys PW, Zijlstra F, van Geuns RJ, Regar E. *OCT assessment of the long-term vascular healing response 5 years after everolimus-eluting bioresorbable vascular scaffold.* J Am Coll Cardiol. 2014 Dec 9;64(22):2343-56
14. Karanasos A, Tu S, **van Ditzhuijzen NS**, Ligthart JM, Witberg K, Van Mieghem N, van Geuns RJ, de Jaegere P, Zijlstra F, Reiber JH, Regar E. *A novel method to assess coronary artery bifurcations by OCT: cut-plane analysis for side-branch ostial assessment from a main-vessel pullback.* Eur Heart J Cardiovasc Imaging. 2015 Feb;16(2):177-89
15. **Nienke S van Ditzhuijzen**, Jurgen MR Ligthart, Shengxian Tu, Marc van der Linden, Evelyn Regar. *Optical Coherence Tomography-guided Bifurcation Stenting of a Coronary Artery Dissection.* Can J Cardiol. 2014 Apr 12. pii: S0828-282X(14)00239-6. doi: 10.1016/j.cjca.2014.04.009
16. **van Ditzhuijzen NS**, Karanasos A, Bruining N, van den Heuvel M, Sorop O, Ligthart J, Witberg K, Garcia-Garcia HM, Zijlstra F, Duncker DJ, van Beusekom HM, Regar E. *The impact of Fourier-Domain optical coherence tomography catheter induced motion artefacts on quantitative measurements of a PLLA-based bioresorbable scaffold.* Int J Cardiovasc Imaging. 2014 May 16. [Epub ahead of print]
17. Mehanna E, Bezerra H, Prabhu D, Brandt E, Chamie D, Yamamoto H, Attizani G, Tahara S, **van Ditzhuijzen N**, Fujimo Y, Kanaya T, Stefano G, Wang W, Gargesha M, Wilson D, Costa M. *Volumetric Characterization of Human Coronary Calcification by Frequency Domain Optical Coherence Tomography.* Circ J. 2013;77(9):2334-40. Epub 2013 Jun 19
18. **Nienke S van Ditzhuijzen**, Jurgen MR Ligthart, Nico Bruining, Evelyn Regar and Heleem MM van Beusekom. *Invasive imaging of Bioresorbable Coronary Scaffolds – A review.* Interventional Cardiology Review, 2013;8(1):23-25
19. **van Ditzhuijzen NS**, van Beusekom HMM, Ligthart JM, Regar E. *Invasive imaging of the coronary atherosclerotic plaque.* Minerva Cardioangiol. 2012 Jun;60(3):305-29
20. **van Ditzhuijzen NS**, van den Heuvel M, Sorop O, van Duin RW, Krabbendam-Peters I, van Haeren R, Ligthart JM, Witberg KT, Duncker DJ, Regar E, van Beusekom HM, van der Giessen WJ. *Invasive coronary imaging in animal models of atherosclerosis.* Neth Heart J. 2011 Oct;19(10):442-6
21. Diletti R, Garcia-Garcia HM, Gomez-Lara J, Brugaletta S, Wykrzykowska JJ, **van Ditzhuijzen N**, van Geuns RJ, Regar E, Ambrosio G, Serruys PW. *Assessment of coronary atherosclerosis progression and regression at bifurcations using combined IVUS and OCT.* JACC Cardiovasc Imaging. 2011 Jul;4(7):774-80

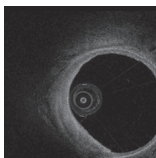

22. Kubo T, Xu C, Wang Z, **van Ditzhuijzen NS**, Bezerra HG. *Plaque and thrombus evaluation by optical coherence tomography.* Int J Cardiovasc Imaging. 2011 Feb;27(2):289-98

Book chapters

23. Regar E, **van Ditzhuijzen NS**, van der Sijde JN, Ligthart J, Witberg K, van Soest G, Karanasos A. *Identifying stable coronary plaques with OCT technology.* In: Continuing Cardiology Education: Stable Coronary Artery Disease 2016
24. Fam JM, **van Ditzhuijzen NS**, van der Sijde JN, Zhang BC, Karanasos A, van Geuns RJ, Regar E. *OCT is the way to go.* In: Textbook on Bioresorbable Scaffolds: from basic concept to clinical application by Onuma Y et al. 2016
25. **Nienke Simone van Ditzhuijzen**, Antonios Karanasos, Jors van der Sijde, Gijs van Soest, and Evelyn Regar. *Bioabsorbable stent.* In: Cardiovascular OCT Imaging by Jang IK et al. 2015
26. Antonios Karanasos, MD, Konstantinos Toutouzas, MD, PhD, Jors van der Sijde, MD, **Nienke van Ditzhuijzen**, MSc, Evelyn Regar, MD, PhD. *Optical coherence tomography imaging in acute myocardial infarction.* In: Myocardial infarctions; Risk factors, emergency management and long-term health outcomes by Wilkonson P et al. 2014

Publications in preparation

27. **N.S. van Ditzhuijzen**, M. van den Heuvel, M. Kurata, O. Sorop, R.W.B. van Duin, I. Krabbendam-Peters, J. Ligthart, K. Witberg, M. Murawska, Hector M. Garcia-Garcia, M. Mulder, F. Zijlstra, D.J. Duncker, H.M.M. van Beusekom, E. Regar. *Neoatherosclerosis development following bioresorbable vascular scaffold implantation in diabetic and non-diabetic swine coronary arteries. Under consideration at Plos One*
28. Bu-Chun Zhang; Muthukaruppan Gnanadesigan; Johannes N van der Sijde; **Nienke S van Ditzhuijzen**; Karen T Witberg; Jurgen M Ligthart; Roberto Diletti; Robert-Jan van Geuns; Jouke Dijkstra; Felix Zijlstra; Gijs van Soest; Evelyn Regar; Antonios Karanasos. *Qualitative and quantitative evaluation of dynamic changes in non-culprit coronary atherosclerotic lesion morphology. A longitudinal OCT study*

Abstracts

29. **N.S. van Ditzhuijzen**, M. van den Heuvel, O. Sorop, S. Roest, J. Ligthart, F. Zijlstra, D.J. Duncker, H.M.M. van Beusekom, E. Regar. *Serial optical coherence tomography imaging of early atherosclerosis progression in diabetic versus non-diabetic swine. J Am Coll Cardiol*. 2014;64(11_S):. doi:10.1016/j.jacc.2014.07.436 TCT 2014, Washington, DC
30. **N.S. van Ditzhuijzen**, M. Kurata, O. Sorop, M. van den Heuvel, R. van Duin, I. Krabbendam-Peters, J. Ligthart, K. Witberg, P.W. Serruys, R. Rapoza, F. Zijlstra, D.J. Duncker, H.M.M. van Beusekom, E. Regar. *Diabetes mellitus does not influence long-term coverage of the everolimus-eluting bioresorbable scaffold.* Circulation 2013 Nov 26;128(22)(Supplement S):17519 AHA 2013, Dallas – Travel grant Erasmus Trustfonds

31. **N.S. van Ditzhuijzen**, N. Bruining, O. Sorop, J. Ligthart, K. Witberg, D.J. Duncker, F. Zijlstra, H.M.M. van Beusekom, E. Regar (Rotterdam, NL). *Bioresorbable stents: serial measurements using optical coherence tomography - the impact of respiratory and cardiac movement.* Eur Heart J 2013 Aug;34(Supplement 1):713-713 ESC 2013, Amsterdam
32. **N.S. Van Ditzhuijzen**, H.M.M. Van Beusekom, O. Sorop, M. Van Den Heuvel, J. Ligthart, K. Witberg, F. Zijlstra, D.J. Duncker, E. Regar (Rotterdam, NL). *Optical coherence tomography analysis of atherosclerosis development in swine fed a high-cholesterol diet.* Eur Heart J 2013 Aug;34(Supplement 1):444-445 ESC 2013, Amsterdam
33. **N.S. van Ditzhuijzen**, N. Bruining, O. Sorop, J. Ligthart, K. Witberg, D.J. Duncker, F. Zijlstra, H.M.M van Beusekom, E. Regar. *The impact of respiratory and cardiac movement on lumen and stent dimension measurements using optical coherence tomography.* EuroPCR 2013, Paris
34. **N.S. Van Ditzhuijzen**, O. Sorop, J.M.R. Ligthart, K.T. Witberg, N. Ramesh, R. Rapoza, D.J. Duncker, E. Regar, H.M.M. Van Beusekom, W.J. Van Der Giessen (Rotterdam, NL; Santa Clara, US). *Quantitative optical coherence tomography analysis of in-stent tissue growth after implantation of a bioresorbable vascular scaffold in a diabetic animal model*. Eur Heart J 2012;33(Supplement 1):999-999 ESC 2012, Munich – CBCS travel grant
35. **N.S. Van Ditzhuijzen**, O. Sorop, J.M.R. Ligthart, K.T. Witberg, N. Ramesh, R. Rapoza, D.J. Duncker, E. Regar, H.M.M. Van Beusekom, W.J. Van Der Giessen (Rotterdam, NL; Santa Clara, US). *Quantitative OCT analysis of in-stent tissue growth after implantation of a bioresorbable vascular scaffold in a diabetic animal model*. EuroPCR 2012, Paris
36. **N.S. Van Ditzhuijzen**, O. Sorop, M. van den Heuvel, J.M.R. Ligthart, K.T. Witberg, R. van Duin, I. Krabbendam-Peters, D. Follett, N. Ramesh, R. Rapoza, D.J. Duncker, E.Regar, H.M.M van Beusekom, H. Garcia-Garcia, W.J. van der Giessen. *Quantitative OCT analysis of in-stent neointimal growth after implantation of ABSORB BVS in a diabetic pig.* J Am Coll Cardiol 2011 Nov 8;58(20)(Supplement B):B127-B127 TCT 2011, San Francisco
37. **Nienke S van Ditzhuijzen**, Jurgen Ligthart, Karen T Witberg, Dirk-Jan Duncker, Felix Zijlstra, Marc van der Linden, Evelyn Regar. *OCT-guided bifurcation stenting of a coronary artery dissection.* TCT 2013, San Francisco

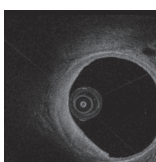

Dankwoord

De totstandkoming van mijn proefschrift is voor mij een belangrijke reis geweest. Een avontuur waaraan ik ben begonnen met de steun en het vertrouwen van mijn familie en vrienden en waarin ik bijzondere mensen heb leren kennen, nieuwe vrienden heb gemaakt en, bovenal, waarin ik veel heb geleerd.

Om iedereen te bedanken die mij tijdens mijn reis heeft geholpen en geïnspireerd, moet ik terug naar 2010. In dat jaar ben ik naar Cleveland, Ohio in de Verenigde Staten gegaan voor mijn keuzeonderzoek. Bedankt dr. Klootwijk dat je mij in contact hebt gebracht met prof.dr. Wim van der Giessen, die mij samen met prof.dr. Marco Costa superviseerde.

Ik vergeet nooit dat ik bij Wim op de kamer zat. Hij zat daar, rustig als altijd, achter zijn bureau en ik zat zenuwachtig aan de andere kant. Wim legde uit welke universiteiten positief hadden gereageerd op mijn applicatie, in welke steden deze universiteiten stonden en wat voor onderzoek ze deden. Mijn keuze was snel gemaakt, ik wilde in Cleveland onderzoek doen naar de ontwikkeling van atherosclerose met behulp van intracoronaire beeldvorming. Wim vroeg vervolgens of ik niet liever in Rotterdam wilde blijven. Op de experimentele cardiologie zou namelijk een groot project starten, waarbij ze ook intracoronaire beeldvorming zouden gebruiken. Mijn keuze had ik echter al gemaakt.

Voordat ik naar Cleveland ging hebben Jurgen en Karen mij veel geleerd over invasieve beeldvorming, met name over optical coherence tomography (OCT) en intravascular ultrasound (IVUS). Bedankt voor jullie hulp toen en de hulp die jullie nu nog steeds bieden. Zelfs met de kaft van dit boekje hebben jullie nog mee gedacht! Jurg, bedankt dat ik nog altijd bij je terecht kan voor advies. Ik hoop dat waar ik ook terecht kom, wij het contact niet zullen verliezen.

In Cardialysis heb ik veel geleerd over het analyseren van OCT. Prof. Serruys, Dr. Roberto Diletti, Dr. Yoshinobu Onuma, Dr. Guiseppe Gomez-Lara, Dr. Juan-Luiz Gutierrez-Chico, Dr Salvatore Brugaletta, Dr. Maria Radu, Dr. Lorenz Raber, Dr. Vasim Farooq, Dr. Bill Gogas, and Dr. Hector Garcia-Garcia, thank you so much for your help!

In Cleveland kreeg ik meteen een warm welkom en werd ik opgenomen in een geweldig team. I admire the hard work of the corelab in Cleveland, led by Dr. Hiram Bezerra and Prof. Marco Costa. Dear Marco and Hiram, thank you for making me part of the corelab family in Cleveland in the short time I spent there. Dear Dr. Satoko Tahara, Dr. Hiroyuki Kyono, Dr. Guilherme Attizani and Dr. Andrej Kupec, thank you for teaching me about OCT, cardiology and your culture. Dear Dina Nshisso, Matt Gillespie and Stan

Pokras, it was great getting to know you. Also the collaboration with the Biomedical Engineering department of the Case Western Reserve University was an educational experience. Thank you Dr. David Wilson, David Prabhu and Zhao Wang. Emile Mehanna, without you my time in Cleveland wouldn't have been as fun as it was, thank you for the great memories. You are a very eager person, I am sure you will become a great cardiologist.

Maaike Roefs, Maaik, Maaikuh, oeps! Ik ben blij dat ik je in Steiner House heb leren kennen en dat we elkaar nog steeds af en toe zien. Bedankt voor de, soms niet zo goed georganiseerde, weekendjes weg, voor de fantastische 'Dutch nights', onze vakantie naar India, die gelukkig wel goed georganiseerd was, en de etentjes die we regelmatig hebben. Ik weet dat promoveren voor jou niet zo'n succes was, maar ik weet dat je alles wat je doet, goed doet. Jij komt er wel!

Eenmaal terug in Nederland was ik zo enthousiast over het onderzoek dat ik in Cleveland had gedaan, dat ik op de experimentele cardiologie als onderzoeksmederwerker ben gaan werken. Oorspronkelijk voor een jaar, om daarna met mijn coschappen te beginnen, maar uiteindelijk zit ik hier nu een aantal jaar later het dankwoord van mijn proefschrift te schrijven.

Uiteraard wil ik Prof. Wim van der Giessen bedanken. Beste Wim, helaas moeten we je missen. Zonder jou was ik nooit geweest waar ik nu ben. Je hebt mij geholpen de beste keuze te maken voor mijn keuzeonderzoek, je hebt me aangenomen als onderzoeksmederwerker en je hebt ervoor gezorgd dat ik nu dit proefschrift heb. Bedankt!!

Wie ik ook zeker wil bedanken zijn prof. Felix Zijlstra en prof. Dirk-Jan Duncker. Beste Felix, na het overlijden van Wim werd jij mijn 1e promotor. Bedankt dat je mij hebt geholpen op de juiste momenten de juiste beslissingen te maken.

Beste Dirk, hoewel het onderwerp van mijn proefschrift niet direct aansluit op jouw onderzoekslijn, heb je me wel altijd kunnen helpen door de juiste vragen te stellen en suggesties te geven voor onderzoek. Onze gesprekken over mijn onderzoek en de toekomst heb ik altijd erg gewaardeerd. Heel erg bedankt hiervoor!

Heel belangrijk voor al het onderzoek dat ik heb gedaan was Dr. Evelyn Regar. Evelyn, ik ben blij dat jij mijn co-promotor was. Er is niemand die zo veel weet van intracoronaire beeldvorming, en zeker niet over OCT. Ik bewonder je harde werken, je kennis en de precisie waarmee je werkt. Je wist altijd mijn artikelen naar een hoger niveau te tillen. Ik heb veel van je geleerd, over de cardiologie, over het doen van onderzoek, maar vooral over OCT.

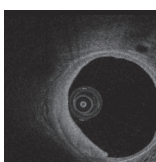

Elles, Monique, Anja en Wil, bedankt voor het regelen van alle administratieve zaken en bedankt voor het regelen van afspraken met Wim, Dirk, Evelyn of Felix. Een afspraak plannen met zowel Dirk, Evelyn als Felix was zonder jullie nooit gelukt!

Zonder kleine en grote commissie zou ik mijn proefschrift niet kunnen verdedigen. Bedankt Prof.dr.ir. Ton van der Steen, Prof.Dr. Clemens von Birgelen en Dr. Manel Sabaté voor het lezen van mijn proefschrift. Het is een eer om jullie in mijn kleine commissie te hebben. Prof.Dr. Eric Boersma, bedankt dat u in mijn grote commissie wilt plaatsnemen. Ik kan me nog goed herinneren dat ik naar u toe kwam met vragen over een klinische studie. Het is jammer dat deze nooit door is gegaan, maar ik hecht veel waarde aan het gesprek dat wij toen hebben gehad en uw aangeboden hulp. Dr. Gijs van Soest, ik heb veel waardering voor het werk dat je doet en de enorme kennis die je hebt. Het was altijd fijn om met je samen te werken. Zelfs op het moment dat je in Australië zat nam je meerdere malen de tijd om te skypen en te overleggen over ons onderzoek. Bedankt dat je onderdeel uit wilt maken van mijn grote commissie!

De eerste tijd van mijn promotietraject heb ik doorgebracht bij de experimentele cardiologie op de 23^{e} verdieping van de faculteit. Een gezellige, sportieve en leergierige afdeling! Bedankt Mieke en Oana voor alle dingen die jullie mij op het lab geleerd hebben en voor jullie adviezen. Heleen, bedankt voor je altijd kritische blik. Bedankt Richard, Bianca, Charlotte, Ilona en Rorry voor alle tijd die we samen hebben doorgebracht op het lab en voor de gezellige borrels en BBQ's in het park! Tuncay, Stefan en André, bedankt dat jullie mij over hebben gehaald hard te gaan lopen. Mijn knie is kapot, de klimmuur was een beter idee! Tuncay, Dokter Yetgin! Bedankt voor alle koffie-uurtjes, bedankt dat ik mijn frustraties bij je kwijt kon en bedankt voor het filosoferen over de toekomst in het ziekenhuis. Ik ben blij dat ik je heb leren kennen. Ik weet zeker dat je een fantastische dokter zult worden.

A special thanks to Mie, who tought me about the Japanese culture, who was always kind and helpful and who did a tremendous job with the histology.

Ook de studenten, Janna, Raiza, Stefan en Ayla bedankt! Het was leuk om jullie te begeleiden. Ayla, goed om je weer op de 23^{e} te zien. Veel succes met je promotietraject!

Naarmate ik langer bezig was met mijn onderzoek, ben ik naar het Thoraxcentrum verhuisd. Eerst tijdelijk op de kamer van Evelyn, en later hebben Antonios en ik een kamer weten te krijgen op de 4^{e} verdieping van het Thoraxcentrum. Antonios, thank you for being a great friend and colleague. There is still so much I can learn from you. I hope we'll keep in touch. Later kwam Jors er ook bij. Nog zo'n super collega,

waarmee ik naast serieuze dingen, ook gezellige vrijdagmiddagborrels of congressen kon hebben. Bedankt Jors!!

Maria, Wail, Buchun, Jiang Ming, Sebastiaan, Mustafa en Stefan. Jullie ook bedankt voor de leuke tijd op de 4e!

De cardiologie telt te veel onderzoekers en arts-assistenten om allemaal op te noemen. De educatieve en leuke momenten met jullie zal ik niet snel vergeten. Heel erg bedankt voor de gezellige congressen, vrijdagmiddag borrels en een super ski weekend.

Zonder mijn familie en vrienden had ik deze reis echter nooit kunnen maken.

Lieve Lau, Fee, Va, Mitch en Max, lieve "mooiste oud-homies", ik ben blij dat we elkaar nog zo vaak zien. Het is heerlijk om na een drukke dag of week met jullie leuke dingen te doen. Lieve Lau, of ik nu wel of niet nog veel in Rotterdam zal zijn, ik hoop dat wij elkaar veel blijven zien!

Lieve homies & oud-homies van HA, laten we nog vaak samen brunchen of andere leuke dingen doen!

Lieve Tjits, bedankt voor de gezellige borrels en bedankt voor je altijd luisterend oor. Het is maar goed dat de vrijdagmiddag altijd zal blijven bestaan!

Lot en Leev, kanjers! Bedankt dat jullie altijd geïnteresseerd waren in mijn promotie, voor de gezellige weekenden en de super vakanties. Ga maar snel trouwen, ik heb wel zin in een feestje!

Lieve Annette en Pieter, wat ben ik blij dat jullie mijn vrienden zijn. En wat hebben jullie een prachtig gezinnetje! Bedankt voor alle gezellige barbecues, skivakanties en het super weekend in Zeeland. Wanneer gaan we weer?

Lieve Tim en Joyce, ook al zo'n mooi gezinnetje. We zien elkaar wat minder dan vroeger, maar dat maakt de vriendschap niet minder gemeend. Dat we nog veel mooie herinneringen mogen maken samen!

Lieve Bas, bedankt voor alle super feestjes, skivakanties, oud & nieuw in München en het varen door de Amsterdamse grachten. Koningsdag zal ik niet snel vergeten!

Lieve huisgenootjes van de Jonker Fransstraat, lieve Miek, bedankt voor de gezelligheid en borrels. Lieve Lies, bedankt voor de heerlijke en gezellige etentjes en bedankt dat ik altijd mijn verhaal bij je kwijt kon als ik een leuke of minder leuke dag had gehad. Ook al wonen we inmiddels beiden in een andere stad, het is fijn dat we elkaar blijven zien!

Lieve 'Rotterdammers', lieve Lo, Eef, Myrth en Ber, ik hoop dat we nog vaak samen zullen eten. Lo en Myrth, bedankt voor alle gezellige koffie-uurtjes in het Erasmus MC.

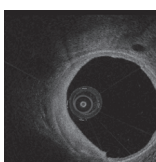

Lieve Lo, bedankt voor je altijd goede tips. Ber! Wat gezellig dat je in de buurt bent komen wonen. Ik hoop dat we elkaar veel zullen blijven zien.

Clau, Li U, Val, An, Fleur, Lo, Eef, Ber, Myrth, Li B, Miek en Noor, bedankt voor een super studententijd en een geweldige reis naar Maleisië. Laten we snel nog eens zo'n reis maken!

Lieve Kim, ik ben blij dat we elkaar weer wat vaker zien. Bedankt voor de gezellige en gekke dingen die we altijd samen doen en jouw altijd lieve en enthousiaste woorden. Je bent een fantastische vriendin.

Paulien, Plien, stoomboot! We zien elkaar misschien niet zo veel meer als vroeger, maar onze etentjes blijven altijd gezellig. Laten we dat niet vergeten!

Lieve Lau en Ber, ik vind het fantastisch dat jullie mijn paranimfen zijn. Onwijs bedankt voor jullie steun!!

Lieve Tjal, grote broer, en natuurlijk Anneloes, het is bijzonder om te zien hoe jullie groeien, privé en op het werk. Ik hoop, maar weet eigenlijk wel zeker, dat jullie dat altijd zullen blijven doen. Geniet van wat je doet en van elkaar!

Lieve mam en paps, ook al heb ik altijd geroepen dat ik dat sentimentele gedoe van je ouders bedanken maar niks vind, ga ik het nu toch doen. Zonder jullie was ik namelijk nooit aan deze reis begonnen. Jullie onvoorwaardelijke steun waardeer ik enorm. Zelfs nu ik besloten heb mijn reis niet voort te zetten binnen de cardiologie, staan jullie volledig achter mijn keuzes en helpen jullie mij de beste beslissingen te maken. Ik hoop dat ik nog vaak gebruik mag maken van jullie adviezen. Ik kan jullie nooit genoeg bedanken.

Lieve Marc, lieve schat, of we nu tientallen of honderden kilometers uit elkaar woonde, jij hebt me altijd gesteund en altijd een luisterend oor geboden als er wat was met mijn promotie. Woorden schieten dan ook te kort om je te bedanken. Ik vind het heerlijk om, inmiddels al een paar jaar, met je samen te wonen en geniet van je steun en hulp bij alles wat ik doe en wil doen. Ik ben super trots op wat jij doet en weet zeker dat je altijd succesvol zal zijn. Ik hoop dat we samen nog veel avonturen zullen beleven!

Financial support for the printing of this thesis was generously provided by:
The Erasmus University Rotterdam
Cardialysis
Chipsoft
Boehringer Ingelheim B.V.
Abbott/ St. Jude Medical
Servier Nederland Farma B.V.
Department of Experimental Cardiology of the Erasmus Medical Center
MarcEdwards Menswear